Electron microscopy characterisation of *in vivo* collagen and mineral ultrastructures, their development and pathologies

Michał Kłosowski

Submitted for the fulfilment of the degree of Doctor of Philosophy (PhD), Imperial College London

Department of Materials and Engineering

Imperial College London

Author's Declaration

I am the author of all the work presented in this thesis. Research was conducted in the Department of Materials at Imperial College London. Part of the work presented here has been published or accepted for publication:

M.M. Kłosowski, A.E. Porter, S.J. Shefelbine and D.W. McComb, Analytical Electron Microscopy of Bone and Mineralized Tissue, Handbook of Imaging in Biological Mechanics, CRC Publishing, 2014, accepted.

Copyright Declaration

The copyright of this thesis rests with the author and is made available under a Creative Commons Attribution Non-Commercial No Derivatives licence. Researchers are free to copy, distribute or transmit the thesis on the condition that they attribute it, that they do not use it for commercial purposes and that they do not alter, transform or build upon it. For any reuse or redistribution, researchers must make clear to others the licence terms of this work.

Acknowledgements

Many people had contributed to successful completion of the work presented here. Firstly, I would like to thank my Supervisors: Dr. Alexandra Porter, Dr. David McComb and Dr. Sandra Shefelbine. Their expertise, enthusiasm and tremendous support guided my steps on the tough path of research and discovery.

I am very grateful to all members of Electron Microscopy team at Imperial College: Dr. Mahmoud Ardakani, Mrs. Ecaterina Ware, Dr. Liam Spillane, Dr Eva Mcguire, Dr. Angela Goode, Dr. Catriona McGilvery and Dr. Vaso Tileli; and Dr. Robert Williams at Ohio State University. They showed me the ropes, so I could sail on my own.

I would like to thank Dr. Suwimon Boonrungsiman and Dr. Raffa Carzaniga for sharing their knowledge about preparation and characterisation of biological samples, and all the tricky handling of resins, stains and liquid nitrogen. And to Dr. Shu Chen, who added few useful tools to my chemical toolbox. And to Dr. Robert Friederichs and Naiara Rodriguez Florez for sharing their expertise in preparation and examination of bioceramics at the bulk scale.

I would like to thank fellow students from Imperial College London and Ohio State University, especially Jim, Kharissa, Rob and Samartha, for sharing dark and bright experiences of PhD life in academia.

Special thanks are directed to the whole Titan team: Angela, Bey, Catriona, Eva, Hannah, Liam and Shu for much needed tea, lunch breaks, extracurricular activities and every bit of support I received.

I would like to express my gratitude to my Mum, Dad and Grandma for your wholehearted love, unwavering support and belief that my research will save the world. And last but not least, a most exceptional thanks to Kasia – for nags and hugs. For sharing your life with me, thank you.

Abstract

The investigation of the nanostructure of mineralised tissues is challenging due to the intrinsic complexity of the hierarchical biocomposites and heterogeneity of biological samples. Despite numerous transmission electron microscopy (TEM) studies investigating a variety of mineralised tissues, details of the collagen-mineral ultrastructure and the origins of collagen and mineral formation are not fully understood. Analytical scanning transmission electron microscopy (STEM), combined with electron energy-loss spectroscopy (EELS), has the potential of identifying bone composition at a very high spatial resolution. We used these techniques to investigate the *in vivo* mineralisation process, and to probe the structural/compositional origins of bone-related pathologies at high spatial resolution.

High-pressure freezing/freeze substitution (HPS/FS) methods were employed to preserve features of mineralisation process, specifically the structure and chemistry of the mineral and collagen phases and the distribution of diffusible mineral ions. The application of STEM-EELS in the biomineralisation studies is, however, limited, partially due to the absence of an EELS library of mineral and collagen standards.

We developed an EELS spectra collection of biominerals (hydroxyapatite, carbonated hydroxyapatite, beta-tricalcium phosphate and calcite) so that biominerals can be identified by composition and coordination environment. For the first time, an extensive collection of all major elemental edges (phosphorus, carbon, calcium, oxygen) is presented and compared. We then used this library to characterise *in vivo* mineralisation processes.

We examined turkey tendon, which calcifies with age, in order to understand the mineralisation process. We identified chemical and structural signatures representative of the non-, poorly and well mineralised tissues. In particular, a chemical signature of pyridine-based compounds was identified and a protocol was developed to assess changes in the nano-scale chemistry of the collagen-mineral matrix in disrupted tissues. We observed a change in the oxidation state of pyridine-based compounds in the collagen fibrils, which most likely occurs pror to nucleation. Mineral ions (calcium, phosphate) were delivered into the collagen matrix, either in the form of amorphous calcium phosphate vesicles or by diffusion from the

body fluids. We are first to show *in vivo* that the mineral nucleated in the gap region of collagen fibrils in the form of ellipsoidal grains of amorphous calcium phosphate, which transformed into crystalline apatite with time. Inside the collagen fibril, pyridine-based compounds changed their oxidation stage prior, or during, the mineralisation process.

We also compared healthy and abnormal (osteogenesis imperfecta or OI) mice tissues to reveal defects in the fibril architecture and mineral chemistry in the OI model. Abnormal tissues were capable of producing collagen fibrils with a characteristic banding pattern, typical for the normal collagen. However, the diameter of the abnormal fibrils was lower. Moreover, in OI-affected tissues, large regions of disorganised fibrils were seen. Defects in fibril formation have previously been predicted by bulk chromatographic and modelling studies. The morphology and crystallinity of mineral in healthy and abnormal tissues were similar. In contrast, a much stronger signal, characteristic of carbonate ion presence, was observed in the EELS spectra taken from the mineral in the OI tissue.

More generally, the library of biominerals, identification of early *in vivo* mineralisation patterns, and identification of alterations in disease, demonstrate that STEM-EELS provides a method to identify chemical and structural features present within mineralising with unprecedented spatial resolution. Understanding the mechanisms of bone mineralisation and the nature of the collagen-mineral interaction will help in determining the source of bone's toughness at the molecular level.

Table of Content

AUTHOR'S DECLARATION....2

COPYRIGHT DECLARATION....2

ACKNOWLEDGEMENTS....3

ABSTRACT....4

TABLE OF CONTENT....6

LIST OF ABBREVIATIONS....11

1. INTRODUCTION: BONE STRUCTURE AND FUNCTIONS....13

2. LITERATURE REVIEW: COLLAGEN AND MINERAL ORGANISATION....18

2.1. Collagen and its arrangement in bone....18

2.1.1. Collagen chemistry....19

2.1.2. Collagen molecule structure....21

2.1.3. Collagen fibril structure....21

2.1.4. Collagen crosslinking....24

2.1.5. Collagen fibril 3D organisation....30

2.2. Apatite....32

2.2.1. Mineral at the macro-scale....33

2.2.2. Chemistry and crystallography of bone apatite....33

2.2.3. Bone mineral at the nano-meter scale....36

2.3. Mineralisation and collagen-mineral interfaces....36

2.4. Electron microscopy of mineralising tissues....39

3. MATERIALS AND METHODS....43

3.1. Sample preparation of tissues for nano-scale characterisation....43

3.2. Fundamental techniques of electron microscopy....50

3.2.1. Basics of electron microscopy....50

3.2.2. Overview of electron interactions with matter....54

3.2.3. Bright-field imaging....55

3.2.4. Electron diffraction....58

3.2.5. Beam damage....61

3.3. Scanning transmission electron microscopy (STEM)....65

3.4. Chemical analysis....68

3.4.1. Analytical energy dispersive X-ray spectrometry (EDS)....68

3.4.2. Basics of electron energy-loss spectroscopy (EELS)....69

3.4.3. The electron energy-loss spectrum....70

3.4.4. Principal component analysis (PCA)....74

3.5. Titan microscope....75

3.6. Bulk characterisation....78

3.6.1. X-ray diffraction (XRD)....78

3.6.2. Fourier transform infrared spectroscopy (FTIR)....78

3.6.3. Thermo-gravimetric analysis (TGA)....79

4. COMPARISON OF MINERAL STANDARDS PROPOSED TO BE PRESENT IN MATURE HARD TISSUES.....80

4.1. Introduction.....80

4.2. Materials and methods.....82

4.2.1. Production of mineral standards.....83

4.2.2. Bulk pre-electron microscopy characterisation.....84

4.2.3. Electron microscopy characterisation.....86

4.3. Assessment of nano-level chemistry (EELS).....88

4.3.1. Phosphorus $L_{2,3}$-edge.....88

4.3.2. Carbon K-edge.....90

4.3.3. Calcium $L_{2,3}$-edge.....93

4.3.4. Features indicative of beam damage at the oxygen K-edge.....95

4.3.5. Oxygen K-edge.....97

4.4. Discussion & conclusions.....100

5. COMPARISON OF MINERALISING TISSUE ULTRASTRUCTURE AT DIFFERENT TIME POINTS IN A TURKEY TENDON MODEL.....103

5.1. Introduction.....103

5.2. Materials and methods.....107

5.3. Development of the collagen and mineral chemistry and structure over time.....109

5.3.1. Collagen alignment and banding pattern variation with age.....109

5.3.2. The morphology and architecture of mineral crystal variations between poorly and well mineralised regions within all age groups.....114

5.3.3. Crystallinity and phase purity variation with age.....118

5.3.4. EELS analysis of the collagen and mineral....124

5.3.5. Chemical composition of collagen and mineral measured by EDS....141

5.4. Bulk characterisation of turkey tendon (XRD & TGA analyses)....143

5.5. Discussion & conclusions....147

6. COMPARISON OF WILD-TYPE AND OI-AFFECTED TISSUE IN A MOUSE BONE MODEL....152

6.1. Introduction....152

6.2. Materials and methods....155

6.3. Preliminary microscopic examination of wild type and OI bone: morphology and crystallinity of mineral phase present....157

6.4. Nano-meter scale modifications of non-mineralised tail tendon morphology of collagen in wild type (WT) and osteogenesis imperfect (OIM) mouse models....162

6.5. EELS analysis of the chemical composition of the collagen and mineral in wild type (WT) and OI-affected (OIM) models....174

6.5.1. Phosphorus $L_{2,3}$-edge....174

6.5.2. Carbon K-edge....175

6.5.3. Calcium $L_{2,3}$-edge....182

6.5.4. Nitrogen K-edge....183

6.5.5. Oxygen K-edge....188

6.6. Discussion & conclusions....190

7. CONCLUSIONS & FUTURE WORK....194

7.1. EELS analysis....194

7.2. Damage study....195

7.3. Mineral and protein standards.....196

7.4. Mineralised tissue development.....197

7.5. Mineralised tissue disorders.....198

7.6. Final conclusions.....199

APPENDIX.....202

BIBLIOGRAPHY.....205

LIST OF FIGURES.....226

LIST OF TABLES.....239

List of Abbreviations

2D	Two dimensional
3D	Three dimensional
AC	Amorphous carbon
ACP	Amorphous calcium phosphate
AMCP	Calcium dihydrogen phoshate
Al	Alanine
Alys	Lysine aldehyde
BF	Bright field
CCP	Calcium pyrophosphate
CHA	Carbonated hydroxyapatite
DCP	Dicalcium phosphate
DF	Dark field
DOS	Density of states
DP	Diffraction pattern
EDS	Energy-dispersive X-ray spectroscopy
EELS	Electron energy-loss spectroscopy
ELNES	Energy-loss near edge structure
EXELFS	Extended energy-loss fine structure
EM	Electron microscopy
FEG	Field emission gun
FTIR	Fourier transform infrared spectroscopy
FWHM	Full width half maximum
Gly	Glycine
HA	Hydroxyapatite
HAADF	High-angle annular dark field
HAlys	Hydroxylysine aldehyde
HCP	Heptacalcium phosphate
HLKNL	Hydroxylysino-5-ketonorleucine
Hyp	Hydroxyproline
Hys	Hydroxylysine
ICA	Independent component analysis
LH	Lysyl hydroxylase
LKNL	Lysino-5-ketonorleucine
LOX	Lysyl oxidase
Lys	Lysine
NCP	Non-collagenous proteins
OCP	Octacalcium phosphate
OI	Osteogenesis imperfecta
OIM	Osteogenesis imperfecta *murine* type
PCA	Principal component analysis
Phen	Phenylalanine
Pro	Proline
SAED	Selected area electron diffraction
SAXS	Small-angle X-ray scattering

STEM	Scanning transmission electron microscopy
TCP	Tricalcium phosphate
TDHP	Tetracalcium dihydrogen phoshate
TeCP	Tetracalcium phosphate
TEM	Transmission electron microscopy
TN	Non-mineralised turkey tendon
TP	Poorly mineralised turkey tendon
TW	Well mineralised turkey tendon
WT	Wild type
XANES	X-ray absorption near edge structure
XAS	X-ray absorption spectroscopy
XRD	X-ray diffraction
ZLP	Zero loss peak

1.
INTRODUCTION:
Bone structure and functions

During evolution, organisms have developed various external and internal skeletal systems. The human internal skeleton performs a number of tasks: it provides a scaffold for the entire body; it is a vital component of the movement apparatus; and it protects internal organs. In addition to its structural importance, bone also acts as a mineral store and produces blood cells. Any scaffolding material needs to possess particular properties, like stiffness, strength and toughness.

To achieve these characteristics soft, but elastic protein is reinforced with stiff mineral in the mineralisation process. Together these two components form a hard and tough tissue which is able to sustain large stresses and strains. In living systems this process typically occurs through a calcium-derived route. *Mollusca* and *Arthropoda* exoskeletons incorporate mainly calcium carbonates, while *Vertebrae* endoskeletons adapt calcium phosphates as building material [1,2].

Bone, specifically, meets the demands of a scaffolding material in a truly marvellous way by combining a brittle apatite mineral with a soft collagen protein [3]. For human femoral cortical bone the average longitudinal, transverse and shear moduli are 17.9, 10 and 3.3 GPa, respectively, with longitudinal and transverse Poisson's ratios of 0.4 and 0.62, respectively [4]. These values depend on the animal species, age and function of the bone.

To understand the fundamental mechanisms of bone toughness, one has to consider that bone is a hierarchical structure, which derives its remarkable structural and mechanical properties, in many different ways, at each of its structural levels. At the macro-level, the solid cortical bone forms the outer layer, which covers and protects the inner porous trabecular bone (Figure 1.1 A). At the micro-level, bone is built from osteons (Figure 1.1 B, C) formed from

concentric layers of osteocytes (pleated lamelle) around a central vascular canal (Figure 1.1 C, D). Finally, at the nano-level, lamellae can be separated into collagen fibre bundles, which contain finer fibrils made of microfibrils (Figure 1.1 D, E, F).

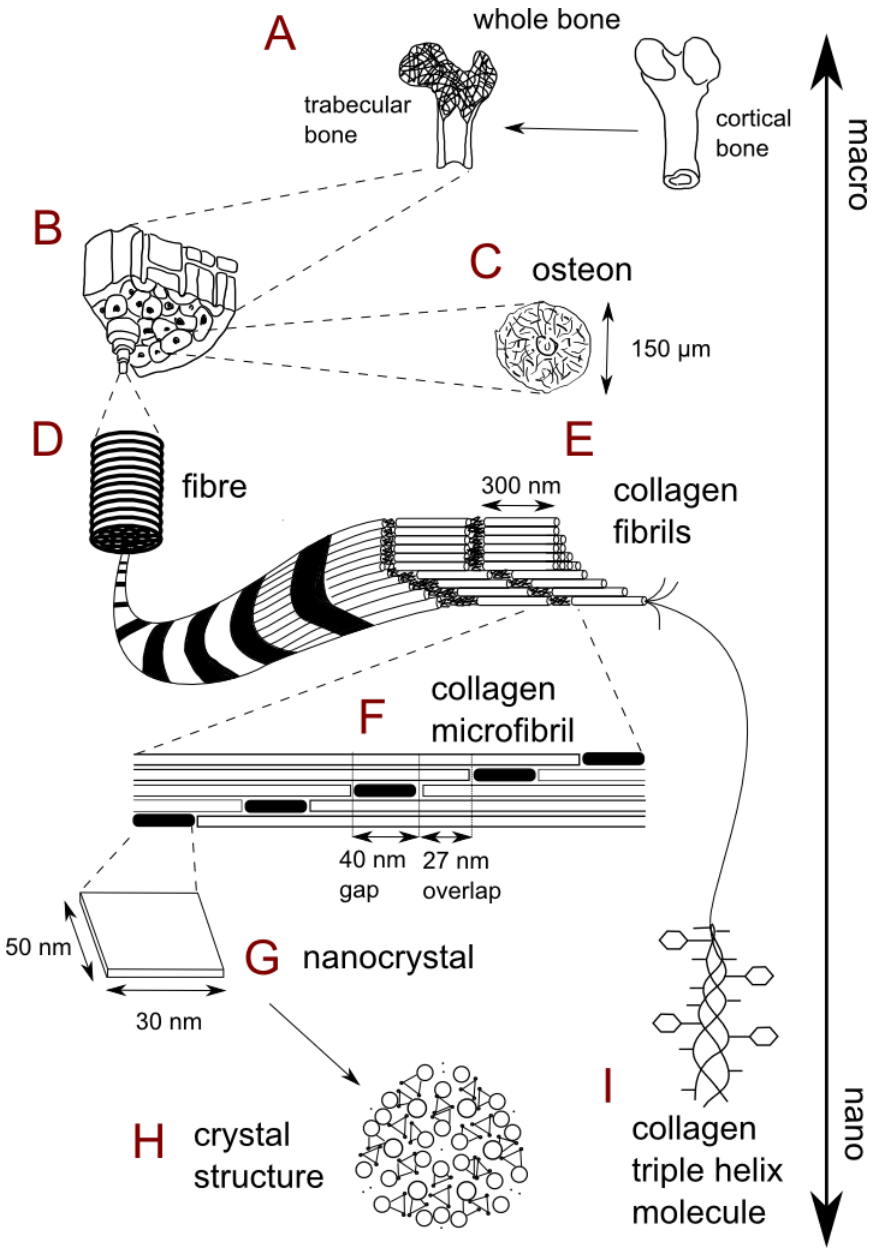


Figure 1.1 The hierarchical structure of the bone. (A) The whole bone sectioned longitudinally to show cortical (shaft) and trabecular bone (end). (B) A wedge of a bone cross-section depicting the osteon distribution in cortical bone. (C) A single osteon. (D) A collagen fibre. (E) Collagen fibrils. (F) Schematic organisation of collagen molecules and apatite mineral inside a microfibril (not to scale). (G) A single apatite crystal platelet. (H) A projection of the atomic structure of apatite. (I) A collagen triple helix molecule (tropocollagen) with side groups and crosslinks. [3]

A microfibril is the most basic structural assembly in bone, which underlays collagen's higher structure.A microfibril is composed of five collagen molecules, with each molecule having three protein chains which are twisted together forming a triple helix (Figure 1.1 E, I). At this level, the most basic interactions between collagen molecules, apatite crystals (Figure 1.1 G, H, I) and other non-collagenous proteins (NCP) take place [5]. The mechanical properties of bone are thought to be derived from the nano-scale collagen-mineral arrangement and the multi-scale hierarchy [6].

Electron microscopy has the capability to examine and characterise the ultrastructure of bone and other mineralised tissues. The structure and chemistry of bone can be examined with a spatial resolution not achievable by other methods, *i.e.* Raman and Fourier-transformed infrared spectroscopy, or X-ray diffraction. Basic transmission electron microscopy (TEM) techniques can be employed to assess a range of ultra-structural features in bone *in vivo*, *i.e.* the collagen banding pattern or the distribution, crystallinity and morphology of mineral crystals. Advanced analytical techniques, such as electron energy-loss spectroscopy (EELS), can be employed for chemical mapping at the nano-meter scale [7]. EELS, combined with scanning TEM (STEM), additionally provides spatially resolved information about the coordination environment and bonding at the collagen-mineral interface. Electron tomography allows three dimensional (3D) visualisation of bone cells and collagen matrix.

With proper preservation methods, intra- and extracellular stages of tissue mineralisation (*i.e.* cell-matrix transport of calcium, mineral nucleation of collagen fibrils, bone resorption) can be mapped. TEM techniques are also utilised in bone implant studies to observe bone-implant interfaces at the nano-meter scale [8–10]. In palaeontology and anthropology, bone fossilisation is studied to unravel the original composition of petrified tissues.

Previous TEM studies made attempts to characterise collagen-mineral ultrastructure and discover the origins of collagen and mineral formation processes through the investigation of longitudinal [11–16] and transverse [17–22] sections of hard tissues, as well as through 3D tomographic reconstructions [10,22–26]. Despite numerous efforts, details of collagen-mineral development and mutual interactions remain unresolved.

The overall aim of this project was to characterise the nanostructure of bone tissue, in particular to identify the chemical nature of the bonding between collagen and the mineral in

bone, and to investigate how the nanostructure and composition of bone change in pathological tissues. In this project, analytical STEM techniques were applied to image the nano-scale structure, and analyse the composition of bone with very high spatial and energy resolution.

Typically in analysis of bone pathologies (such as osteoporosis, rickets, osteogenesis imperfecta, etc.), variations in bone properties are examined at the organ (whole bone) level and at the bulk tissue level. With macro-scale analyses, it is not possible to link changes in mechanical integrity to compositional differences. As collagen and mineral are the basic building blocks of bone, small changes in composition and structure at this level have drastic ramifications on the strength and toughness of bone at larger length scales.

This PhD project has developed analytical STEM methods to assess nano-scale alterations in a mouse model of osteogenesis imperfecta (OI or brittle bone disease). In the process of optimising the protocols, turkey tendons, which ossify at certain stages of development, were used as a model to identify characteristic features of collagen-based tissues and to pinpoint age-related changes in the tissue. Additionally, a range of calcium phosphate and calcium carbonate ceramics, found in biomineralisation processes, was characterised using EELS to create a calibration library of mineral phases, which may be present during calcification.

Application of nano-analytical electron microscopy techniques helps to decipher how alteration in the molecular structure of collagen affects the composition and architecture of the mineral on the collagen template. One of the long standing questions about the origins of bone formation is which functional groups on proteins are responsible for templating nucleation of bone mineral. This question has remained outstanding due to a lack of a technology to analyse functional groups with nano-scale spatial resolution. In this project nano-scale analytical methods were developed to probe bonding at the collagen mineral interface and identify functional groups (e.g. C-O vs. C=O and amino acids *i.e.* proline vs. lysine). The library of ceramic standards and tissue spectra developed in this work combined with application to pathologic bone allow examination of the nano-scale compositional changes with unprecedented spatial resolution. More generally, this analysis could provide new fundamental insights into mechanisms of bone formation, the origins of fracture toughness in bone and the aetiology of bone disease.

2.
LITERATURE REVIEW:
Collagen and mineral organisation

2.1. Collagen and its arrangement in bone

Collagen is one of the most important and most abundant proteins in the animal kingdom. The collagen molecule (or tropocollagen) is a filament composed of three left-handed protein chains, which are twisted together forming a right-handed triple helix (Figure 2.1).

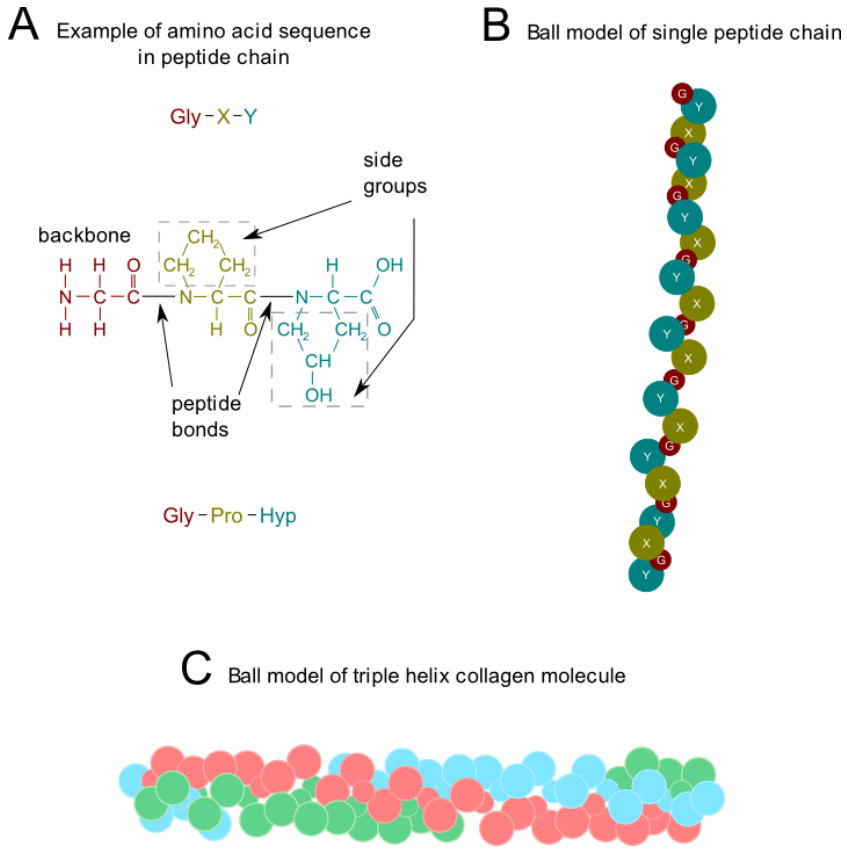


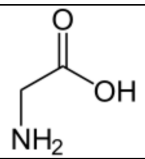
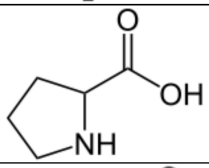
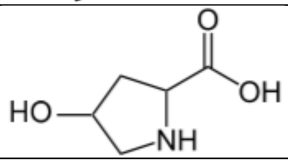
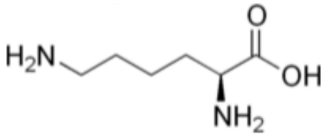
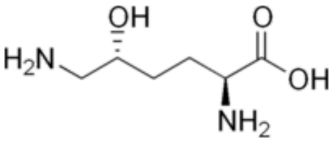
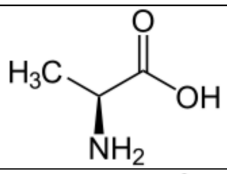
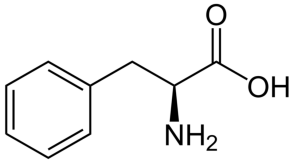
Figure 2.1 Models of collagen structure hierarchy from the basic amino acid sequence to the collagen molecule. (A) Example of Gly-Pro-Hyp amino acid sequence. (B) Ball model of polypeptide chain fragment. (C) Fragment of collagen molecule (tropocollagen) twisted together from three polypeptide chains. [27]

Usually a single polypeptide chain is described by the $[Gly\text{-}X\text{-}Y]_n$ formula, where Gly is glycine, which forms the polymer backbone, X and Y stand for other amino acids and n gives the number of iterations in the chain (Figure 2.1A), thus collagen formation can take many different varieties; so far 28 types of collagen have been discovered [28,29]. The most prominent are type I collagen (found in bone, tendon, ligament and skin) and type II collagen (found in cartilage).

2.1.1. Collagen chemistry

Type I collagen, which is the most common form present in bone, is composed primarily of the amino acids (Table 2.1): glycine, proline, hydroxyproline, lysine, hydroxylysine, alanine and phenylalanine [30]. Polypeptide chains of collagen are formed by assemblies of amino acids in various proportions and sequences (such as glycine-proline-hydroxyproline; Gly-Pro-Hyp) [27]. For many applications (*i.e.* modelling of collagen molecular mechanical behaviour), proline is sufficient as the main substitution component and the collagen structure is approximated as $[Gly\text{-}Pro\text{-}Pro]_{10}$ [31].

Table 2.1 Basic amino acids found in type I collagen peptide chains.

Amino acid	Symbol	Formula	
Glycine	Gly	$C_2H_5NO_2$	
Proline	Pro	$C_5H_9NO_2$	
Hydroxyproline	Hyp	$C_5H_9NO_3$	
Lysine	Lys	$C_6H_{14}N_2O_2$	
Hydroxylysine	Hys	$C_6H_{14}N_2O_3$	
Alanine	Al	$C_3H_6NO_2$	
Phenylalanine	Phen	$C_9H_{11}NO_2$	

Often the X-Y sequence is explicitly given as Pro-Hyp (proline-hydroxyproline, Figure 2.1 A). The Pro-Hyp sequence is the most widespread combination, making up for 10% of the collagen chain [27,31–34]. In addition, computational models indicate that this sequence is the most stable one [35]; the inverse combination Hyp-Pro results in destabilisation of the molecule [36,37]. Pro-Pro and Pro-Hyp sequences are the most common models and are usually adequate to reflect major protein properties. Attempts have been made to establish more detailed standards involving less common amino acids [28,37,38].

2.1.2. Collagen molecule structure

Type I collagen chains are organised into triple-helical molecules, consisting of two α_1 and one α_2 chains. The most distinctive differences between the α_1 and α_2 chains are: shorter length of α_2 chains [27], lower hydroxylation of α_2 proline residues [39] and lack of cysteine rich telopeptides in the α_2 chains [40]. Each chain is composed of around 1000 amino acids residues, which translates to a total length of the molecule of 300 nm [27,28]. While the longitudinal dimension is significant, the diameter of the coiled triple helix chains is 1.5 nm [27,28,41].

The tropocollagen backbone is formed by glycine residues, which are closely packed in the middle of the molecule. Glycine's amide groups N-H form hydrogen bonds with carboxyl side groups C=O of neighbouring amino acid contributing to the inter-chain bonding [27,28]. Additionally, it is essential for helix formation that all the peptide bonds are in the *trans* conformation [28] (Figure 2.2). These two requirements need to be fulfilled in order to hold the peptide chains together in a triple helix structure.

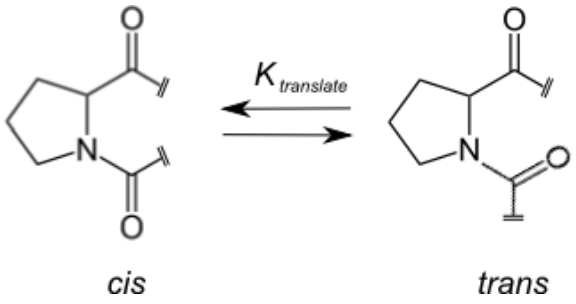


Figure 2.2 Example of proline *cis-trans* isomerisation [28].

2.1.3. Collagen fibril structure

So-called D banding (Figure 2.3, Figure 2.4B), the most characteristic trait of collagen fibril organisation at the nano-level, has been known for over seventy years [11,42]. The D segments are typically about 67 nm in length and vary from 64 to 71.7 nm [43]. These segments are repeated patterns of dark and bright stripes seen in bright field transmission electron microscopy (BF-TEM) images. Petruska and Hodge proposed an explanation of this characteristic of type I collagen by linking it to the arrangement of collagen molecules and mineral deposition within the fibril [44]. In their model, collagen molecules are arranged

parallel to each other to form a distinctive pattern of gaps and overlapping regions. The distinctive periodic contrast visible in BF-TEM images of mineralised bone is related to the presence of mineral crystals nucleating in the gap regions, which create dark regions of contrast caused by high electron scattering. This representation of the collagen structure is known as the quarter-stagger model [44,45].

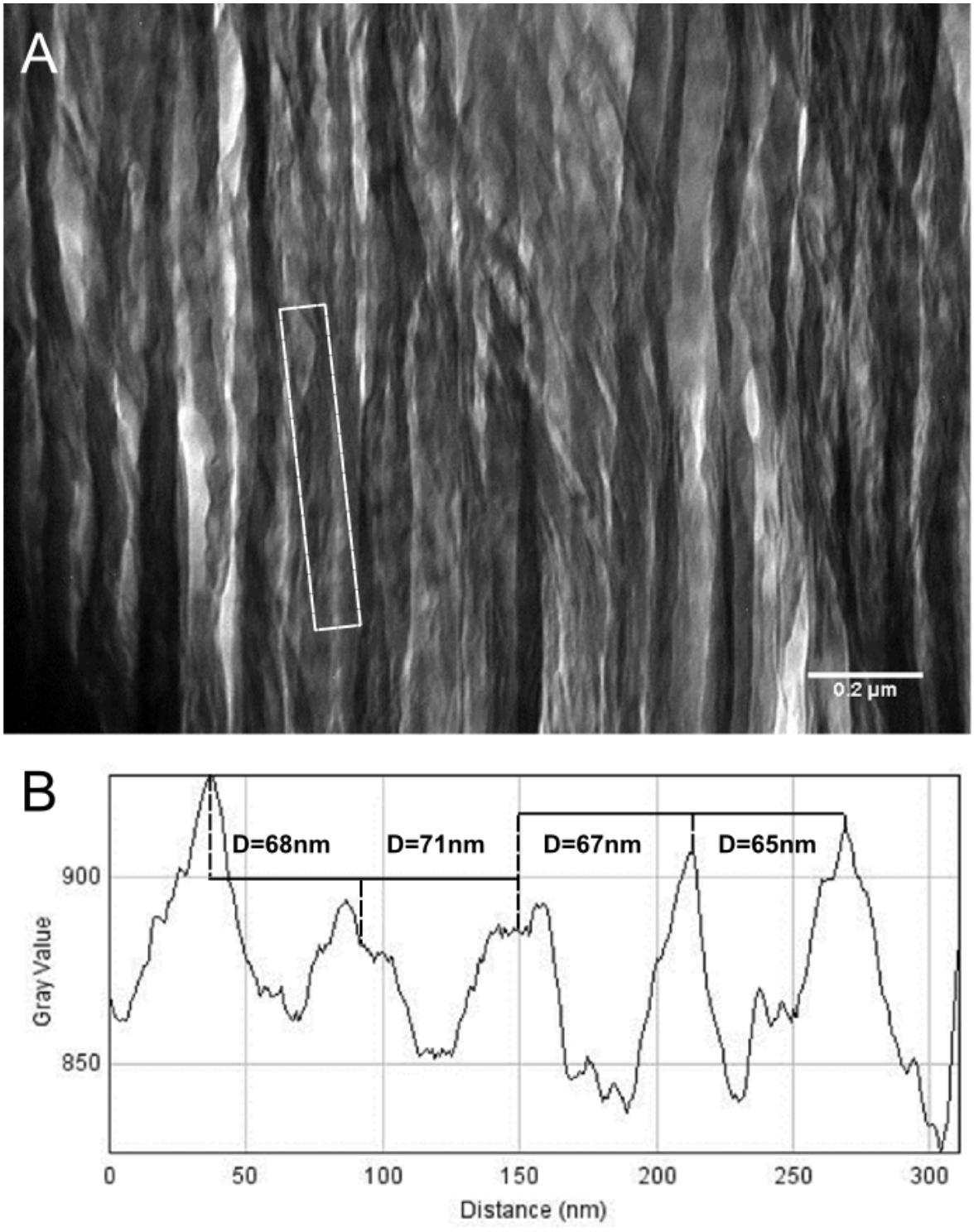


Figure 2.3 An example of banding in mouse cortical bone. (A) Bright-field (BF)-TEM micrograph of a thin, focused ion beam (FIB) milled bone section. Image acquired at 120kV on JEOL 2000FX. (B) Part of the line profile taken from the boxed region in insert A. Four D-periods were plotted with the corresponding periodic spacing ranging from 65 to 71 nm.

The basic building block of a collagen fibril assembly is the microfibril (the simple 2D model is illustrated in Figure 2.4A). The microfibril is a structure composed of five collagen molecules pleated together. Repeated sequences of multiple microfibrils form a fibril. The collagen fibrils display distinct regions: overlap and gap. In the overlap region, the collagen molecules overlap through all cross-sections. In the gap region, one of five microfibril molecules is not present through cross-sections, which creates a gap [41,44,45]. The mechanisms responsible for this self-arrangement are still under investigation [27,28,41].

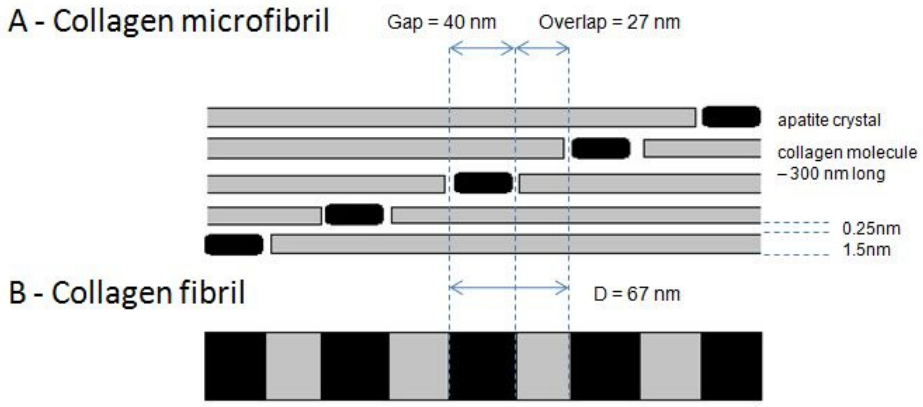


Figure 2.4 Schematic 2D quarter-stagger representation of the collagen microfibril arrangement (A) explaining collagen fibril banding (B). The overlap (with five molecules), and gap (with four molecules) regions, alternately arranged, form a characteristic pattern.

Studies have shown that a similar, but inverted pattern is exhibited in non-mineralised and non-heavy metal stained collagen fibrils [41,43,46]. This inverted contrast is exhibited purely due to the fibrillar arrangement of overlaps, which are made of tightly packed molecules, thus producing darker contrast. Gaps, which contain 20% less molecules than the overlap regions, appear brighter. Heavy metal stained, non-mineralised collagen fibrils also display a sub-banding pattern. The origin of this sub-structure has not been fully characterised [12].

2.1.4. Collagen crosslinking

In the process of fibril assembly, collagen molecules, after arranging in quarter-staggered array, start to develop crosslinks to stabilise their newly formed structure (Figure 2.5). Crosslinks are covalent bonds formed between lysine-based residues in neighbouring

molecules [27,47]. There are two types of crosslink: lysine-based bonds form in overlap regions of fibrils in a head-to-tail fashion, while sugar-based bonds may form at any position in the molecule [48]. Both types of bonds play an important role in contributing to the tissue's tensile strength [27].

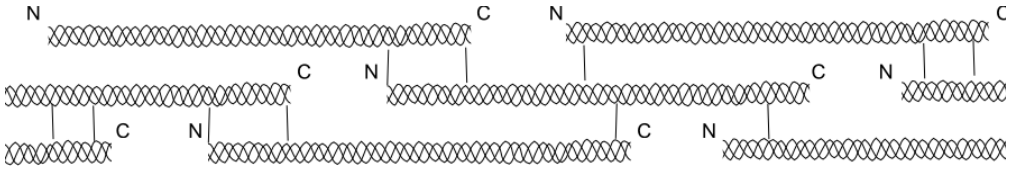


Figure 2.5 Collagen molecules with N- and C-termini labelled. Tropocollagen is organised in a staggered fashion and reinforced with crosslinks. [27,48–50]

Lysine-based crosslink formation starts inside the cell, where the enzyme lysyl hydroxylase preconditions part of the lysine residues, creating hydroxylysine (Figure 2.6). In a subsequent extracellular step, selected residues are oxidised by the action of lysyl oxidase enzyme, which leads to the creation of lysine and hydroxylysine aldehydes (Aly and HAly) [27,48,50]. These modifications open two pathways of further crosslink development: based either on Aly or HAly residues. The Aly residue pathway is characteristic for collagen in adult skin, cornea and sclera. The HAly pathway leading to crosslink formation is predominant in bone, tendon, cartilage, ligament and young skin [27], and is described in Figure 2.7.

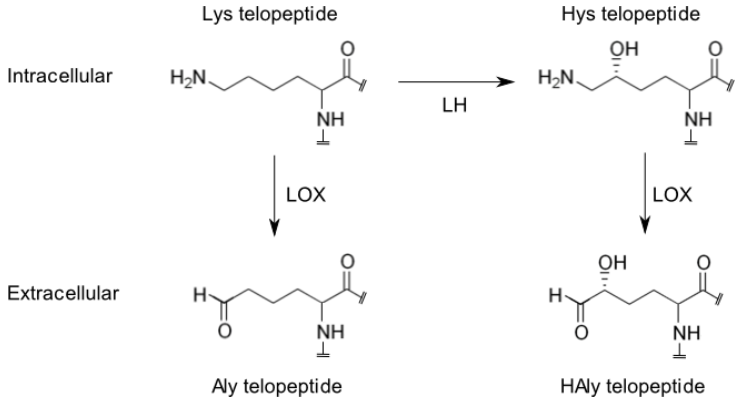


Figure 2.6 Initial intra- and extracellular action of two enzymes leading to creation of lysyl-based aldehydes essential for crosslink development. Inside the cell, lysyl hydroxylase (LH) affects selected lysine (Lys) residues attaching hydroxyl groups to their side chains and thus creating hydroxylysine (Hys). Outside the cell, lysyl oxidase performs further modifications of the Lys and Hys residues resulting in formation of lysine aldehyde (Aly) and hydroxylysine aldehyde (HAly). [27,50]

In the next step of crosslink formation, a Schiff's base is formed in the non-enzymatic reaction between HAly residue and ε-amino group of Hys (or Lys) telopeptide. Secondly the Schiff's base is subject to Amadori rearrangement resulting in creation of hydroxylysino-5-ketonorleucine chain (HLKNL) for Hys branch and lysino-5-ketonorleucine (LKNL) for Lys branch. Afterward, two HLKNL (or LKNL) chains are merged through aldol condensation followed by ring closure. Finally a Hys (or Lys) telopeptide is cut off from the main body effectively creating a mature pyridinoline (or deoxypyridinoline) crosslink. This crosslink formation pathway was proposed by Eyre [51,52]. Alternative pathways have also been proposed [50,53]. However, they all yield to a similar pyridine-based final product. It is still disputed if the mature crosslink binds three [54,55], or just two molecules [56] (Figure 2.8).

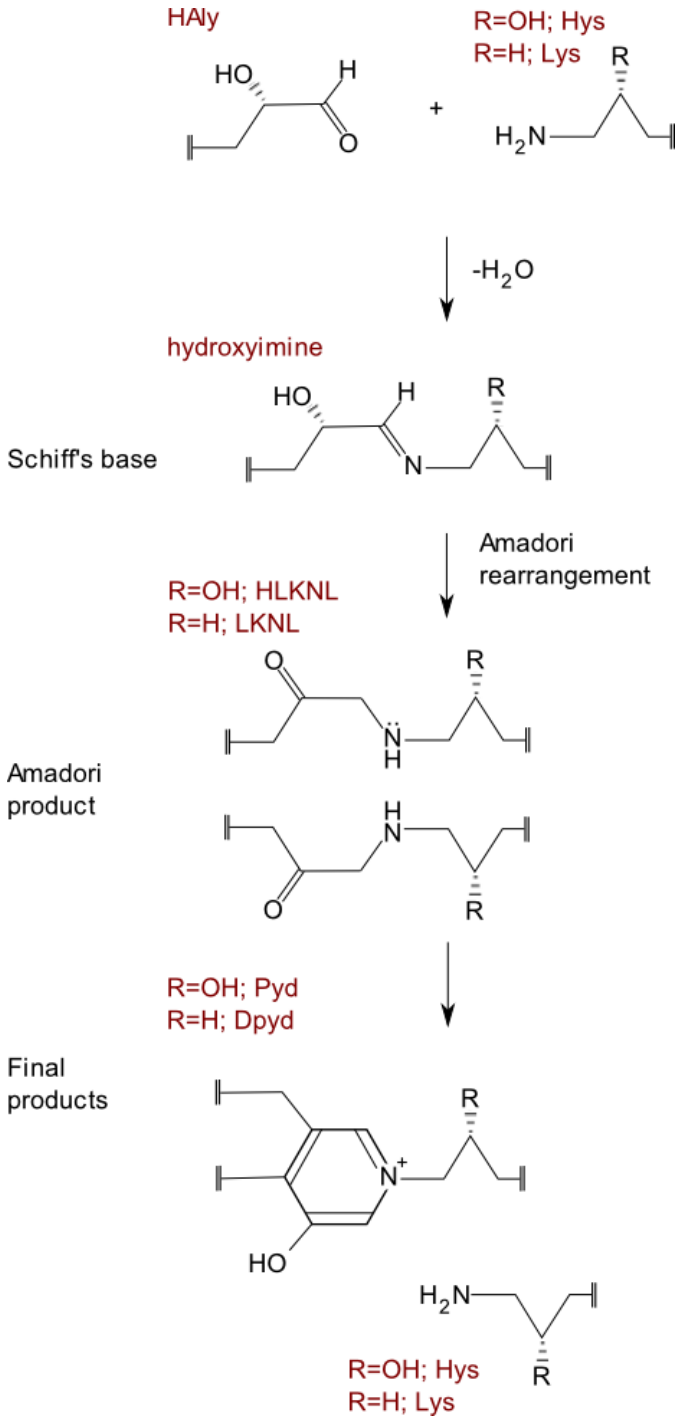


Figure 2.7 Crosslink formation *via* the HAly pathway proposed by Eyre. [50]

Compounds such as the Schiff's base and Amadori product are referred to as immature crosslinks which can undergo further modifications. In the maturation process, bivalent crosslinks slowly transform into more stable, trivalent, non-reducible conformation. Mature crosslinks accumulate and, in effect, their number increase with age. At the nano-meter scale,

this accumulation results in reduced solubility and inhibits collagen fibril remodelling. At the macro-meter scale, stiffening of the tissue can be observed which progressively increases the brittleness and risk of bone fracture [48].

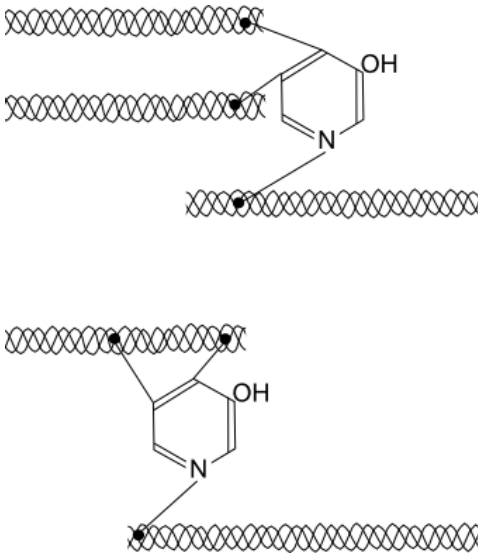


Figure 2.8 Two proposed models of mature crosslink organisation within collagen fibril. [57]

Sugar-derived crosslinks are formed *via* non-enzymatic glycosylation, in addition to enzymatic lysine-based processes described above. Hys and Lys residues are capable of reacting with sugar groups (such as glucose) and may form crosslinks at any length of the molecule (Figure 2.9). In the Maillard reaction, a sugar aldehyde binds with a free amino group creating a Schiff's base, which may evolve into a more advanced glycosylation product (AGE) or degrade into pyrrole-based crosslinks [27,48]. Sugar-derived crosslinks also add to collagen stability and resistance to resorption, but, in excess, cause stiffening and brittleness [48,58].

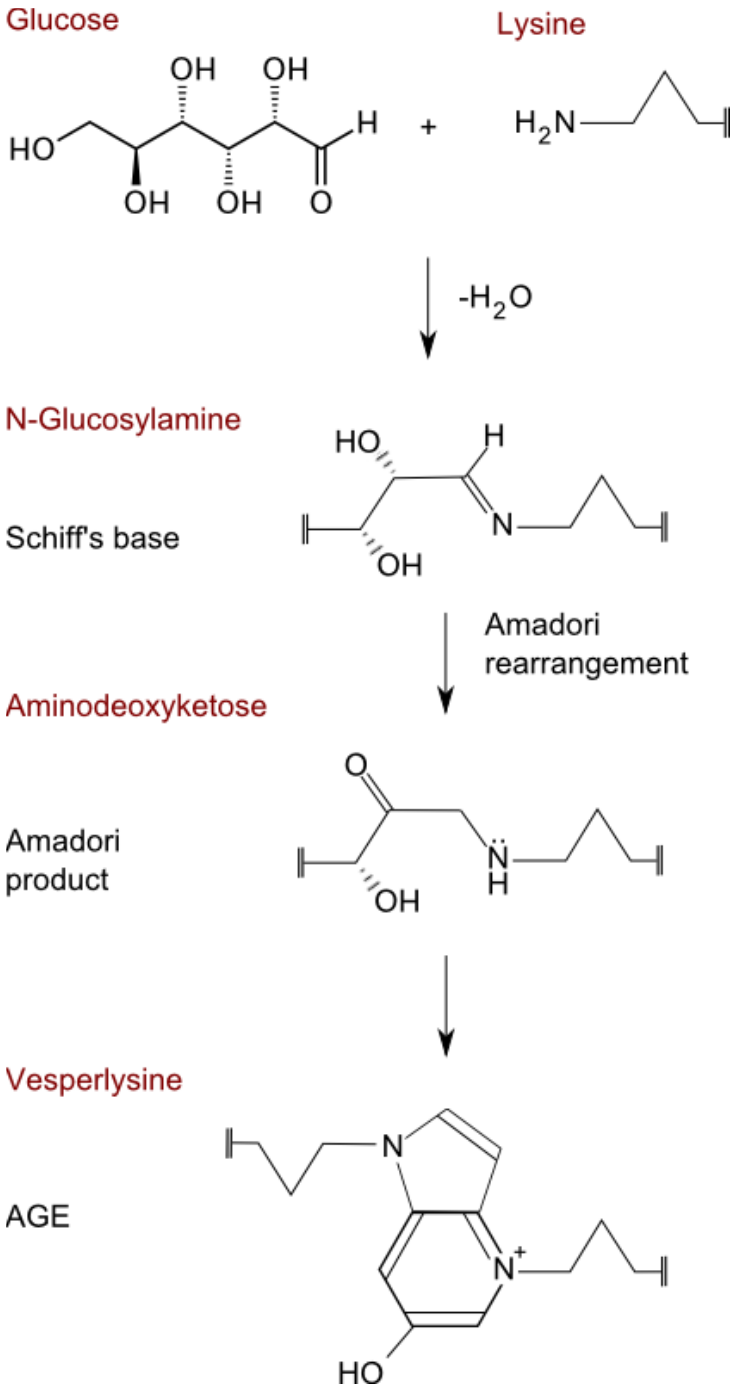


Figure 2.9 Example of glucose-derived saccharide crosslink formation leading to creation of vesperlysine [48].

Interestingly, sugar groups may be also attached to lysine residues on the R position (Figure 2.7) *via* intracellular enzymatic action [27,50]. This substitution is considered as one of factors controlling further growth of collagen fibrils. The bulky sugar side groups affect formation of ordered fibrils by steric hindrance, limiting its diameter [27].

Formation of crosslinks is not only important for defining the fibril stability and mechanical properties, but may also be beneficial for the mineralisation process. Enzymatically-driven crosslinks form in the overlap region, while overlap/gap interfaces are also considered as mineral nucleation sites [59]. Charged residues of lysine-based crosslinks are frequently suggested to be the direct attachment points for mineral [49,60–62]. Other studies suggest that saccharide groups are even more inclined to mineral binding [63]. In both cases, crosslinks possess multiple hydroxyl side groups, which might be shared with hydroxyl-deprived bone apatite [64]. Studies on mineralising turkey tendon show that the lysine hydroxylation process is regulated (independent maturation of telopeptide and helical lysine residues) and the collagen matrix is reinforced (increase of thermal stability) to promote mineralisation [61]. These bulk studies advocate for the need for further investigation of the role that crosslinks play in the fibrillogenesis and in the mineralisation process, as they imply that crosslinking may affect mineralisation process in two ways: directly as nucleation site and indirectly as a collagen matrix regulator. Observations of this system at the nano-meter scale may provide confirmation of these hypotheses.

2.1.5. Collagen fibril 3D organisation

The Hodge-Petruska model is the most favoured model of collagen, probably due to its elegant explanation of the origin of the periodic banding pattern [44]. However, this elementary, two-dimensional model makes some simplistic assumptions, such as straight collagen fibres, which may place in doubt its applicability to the mechanics of three dimensional fibrils *in vivo*. For this reason, researchers are still developing valid collagen fibril models in three dimensions (Figure 2.10) and other models focused primarily on the mechanics of collagen, such as a tube-like [65] or worm-like [66] representations of collagen fibrils.

Landis [67] proposed a simple three dimensional structure made of repeated 2D projections of the Hodge-Petruska model (Figure 2.10A). More recently, Jäger and Fratzl [68] have suggested that the arrangement of mineral particles occurs in alternating staggered layers corresponding to the Hodge-Petruska model, but that the repeated 2D projections form a “tree ring” pattern (Figure 2.10B), similar to the concentric model of collagen proposed by Hulmes *et al.* [69]. Burger *et al.* [70] built their model on a “butterfly” pattern, in which mineral is

randomly distributed over cross-sections (Figure 2.10C), but follows the Hodge distribution in the longitudinal direction. Jantou-Morris *et al.* [21] extrapolated the quarter stagger model into three dimensions, similar to Landis, but shifted slightly each consecutive layer and added a novel mineral crust around the fibril (Figure 2.10D), which was neglected by previous models. Alexander *et al.* [71] offered a model based on the recent study by Orgel [41], in which collagen molecules are not represented as straight lines as in other models, but twisted and tilted forming a complicated pleat (Figure 2.10E). In this model, mineral can be aligned in several different ways and the best possible orientation can accommodate up to 40% of the total mineral in bone. The Alexander *et al.* model stands in agreement with several studies describing intrafibrillar/extrafibrillar mineral deposition ratio as approximately 30/70 [72–74]. The combination of last two proposed models provides an interesting, and not overcomplicated representation, of the problem, but still lacks a structural validation.

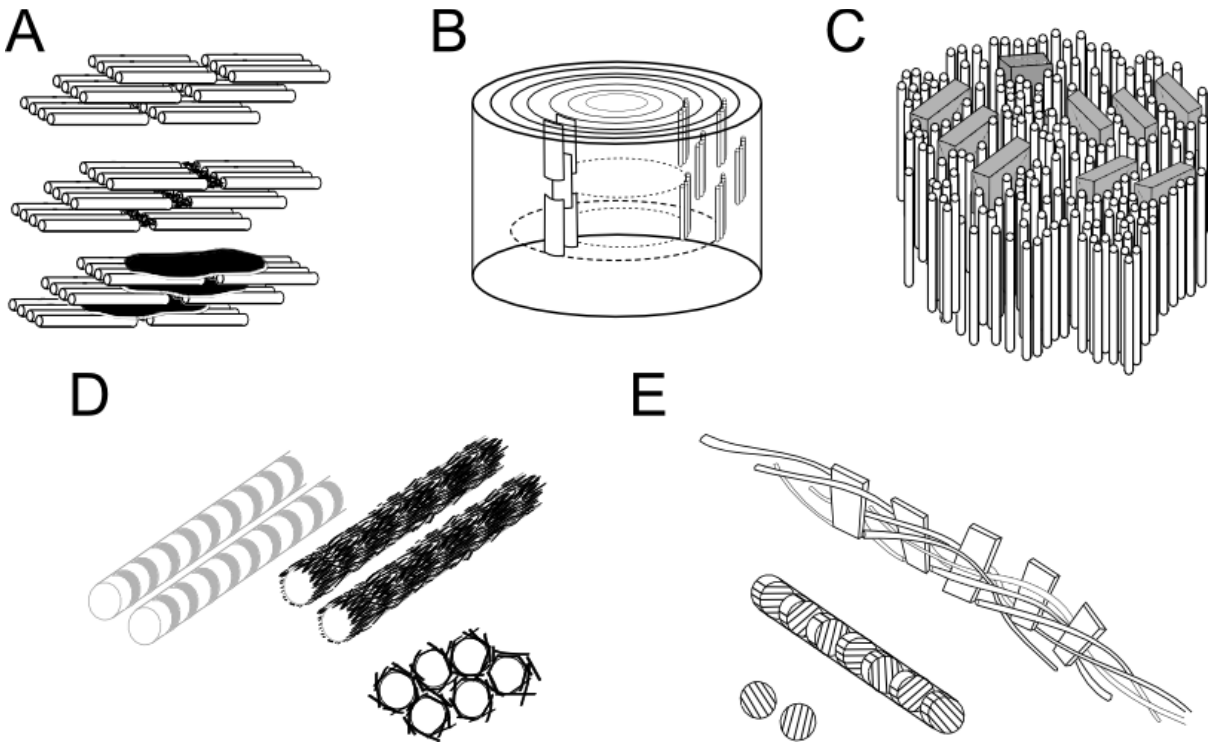


Figure 2.10 Various structural models of collagen fibril. (A) Landis model. Collagen molecules and apatite crystals arranged in Hodge model fashion. Top to bottom: collagen fibrils alone, collagen fibrils with mineral nucleating in gaps, mineral growing from gaps between fibrils [67]. (B) Jäger and Fratzl model. Apatite platelets (absent) and collagen molecules arranged in concentric layers [68]. (C) Burger *et al.* model. Apatite crystals (grey) randomly distributed among the collagen molecules (white) [70]. (D) Jantou-Morris *et al.* model. Extrafibrillar mineral crust formed around fibril [21]. (E) Alexander *et al.* model. Bent collagen molecules with various crystal alignments. The crystals align separately in each gap [71].

2.2. Apatite

Tissues, like bone or dentin, are often known as "biomineralised materials" due to their characteristic nanostructure composed of organic elements, such as proteins, and inorganic mineral. The inorganic part of such material is commonly indicated as a "biomineral". Bioapatite is the most widely encountered mineral of this type and can be found in bone, dentin, enamel, morbid calcifications, and as a fossil in sedimentary formations. This biomineral displays a wide variability in its structural organisation, and therefore also in its properties.

2.2.1. Mineral at the macro-scale

There is a significant diversity in the composition of bone, dentin and enamel, corresponding to the different functions of these tissues. Rogers *et al.* [75] and Skinner [76] reported that the mineral component of bone ranges from 45 to 70 wt.%, with the organic component (mainly collagen) representing 45-20 wt.%, respectively, and the remaining 10 wt.% being water. Similar values have been measured in dentin. Compositional similarity and absence of remodelling make dentin a frequently used bone model. In contrast, in enamel, over 90 wt.% is apatite [3]. Such changes in composition have a great impact on the material's properties, resulting in higher brittleness in hard tissues with greater mineral content [3]. The strength, toughness and stiffness of biomaterials are partially based on their chemical composition, which are related in the simplest way to the collagen-mineral ratio [3].

Variation in the collagen-mineral ratio is not only observed between different tissues, but depends on other factors. In bone, the collagen-mineral ratio depends on the species and function of the bone and age. These differences can be illustrated by comparing a sheep and a mountain goat. A mountain goat's leg bones require more flexibility, so they have higher collagen content. By contrast, the leg of a sheep acts mainly as a support, so the mineral content is higher [75,77]. A higher collagen-mineral ratio correlates with lower brittleness, but also implies a less stiff structure [3].

2.2.2. Chemistry and crystallography of bone apatite

Bone apatite is calcium-phosphate based mineral. Similar calcium phosphate minerals are encountered in both biological and geological materials [78]. In tissues, the mineral phase is responsible for their overall stiffness, and also for calcium storage and homeostasis.

The basic formula for apatite is usually written as $Ca_5(PO_4)_3X$, or as $Ca_{10}(PO_4)_6X$, to indicate the ions in the crystal unit cell. X is referred to as the calcium-channel ion and is most commonly a hydroxyl group (OH^-), a fluorine (F^-) or a chlorine (Cl^-).

It is extremely rare to find pure hydroxyapatite (HA; $Ca_5(PO_4)_3OH$) in living organisms, and trace elements and substitutions, such as Na^+, CO_3^{2-} etc., are very common. HA unit cell dimensions are: a=b=9.4 Å and c =6.87 Å, with unit cell angles: $\alpha = \beta = 90^o$ and $\gamma = 120^o$ [78–

80]. The atomic organisation within the unit cell is shown in Figure 2.11. Ten calcium atoms are distributed along two different sites. Four of Ca^{2+} ions are arranged parallel to the c-axis in coordination to neighbouring oxygen atoms (the Ca_I position), while the remaining six Ca^{2+} ions are organised in alternately inverted triangles, forming channels parallel to the c-axis (the Ca_{II} position), which accommodates hydroxyl groups. Finally, each of six phosphorus atoms is arranged in coordination to the four neighbouring oxygen atoms in a tetrahedral fashion [79].

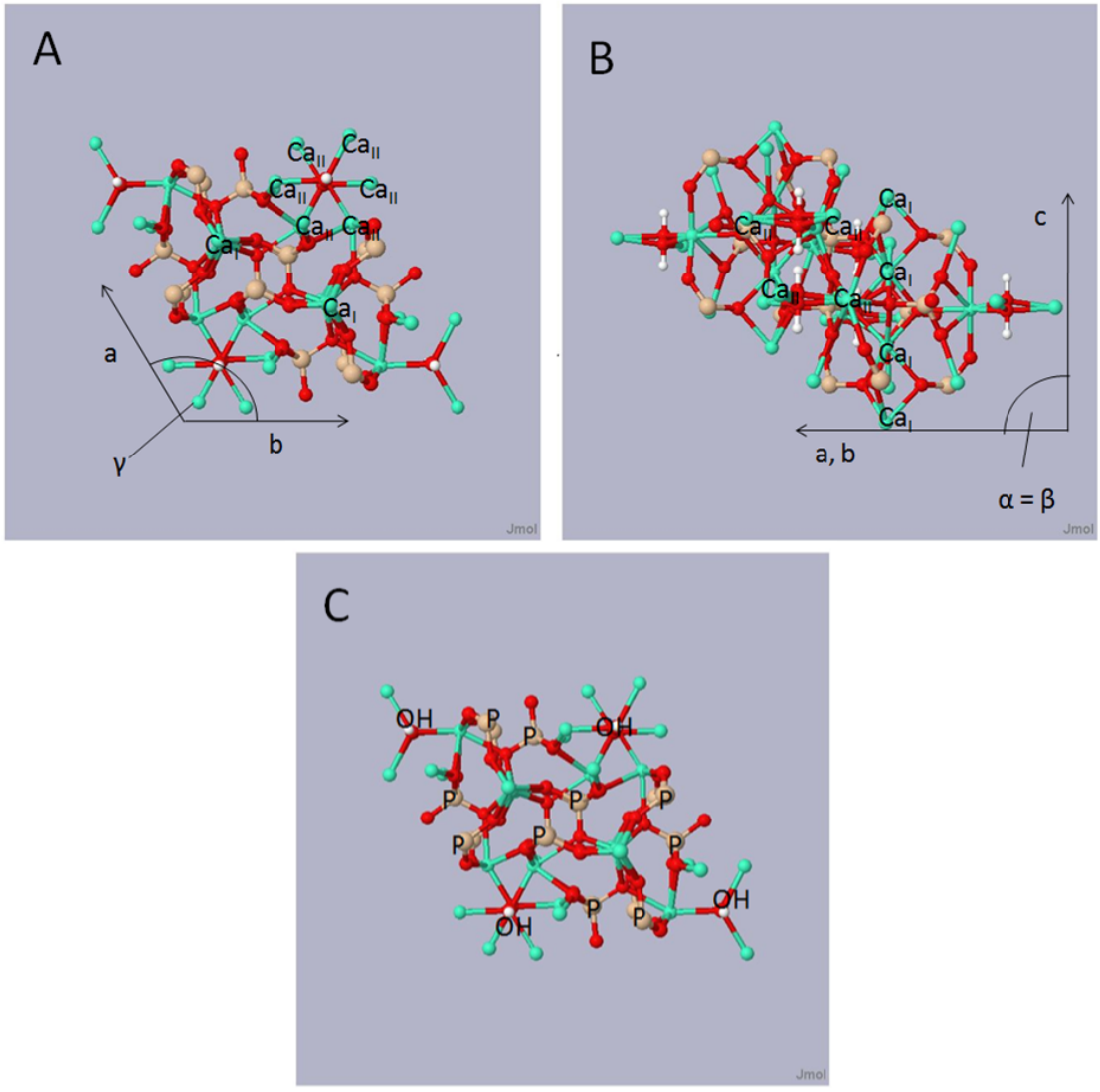


Figure 2.11 The atomic structure of two unit cells of hydroxyapatite with labelled Ca_I and Ca_{II} sites; O = red, Ca = green, P = orange, H = white; a, b, c – unit cell dimensions; α, β, γ – unit cell angles. (A) A view on the (001) plane. (B) A view on the (-110) plane. (C) A view on the (001) plane indicating the P and OH

sites. This structural model is based on work of Posner *et al.* [81] and was acquired from The United Kingdom Chemical Database Service [82].

The apatite crystal lattice accommodates many ionic impurities. There are three sites (Figure 2.11), where the substitutions may occur: the first site in which calcium ions can be replaced by cations such as Na^+, K^+, Mg^{2+}, Fe^{2+}, Zn^{2+}, Pb^{2+} or Sr^{2+} [3]; the second site in which channel hydroxyl groups OH^- can be replaced by F^-, Cl^- and CO_3^{2-} [3] or even become vacant [6,64]; the third site in which phosphate groups PO_4^{3-} can be replaced by CO_3^{2-}, SO_4^{3-} or HPO_4^{2-} [3]. The presence of these substitutions in the crystal lattice may cause changes in the dimensions of the unit cell and affect crystallinity and solubility of the mineral [83].

The incorporation of CO_3^{2-} ions in the HA lattice is especially important and represents up to 6 wt% of bone apatite [3]. It is suggested that substitution has a great impact on the properties of apatite. Due to their dimensions, triangular shape and charge, carbonate ions cause disruption of the crystal lattice which may act as a crystal growth limiting factor [3,84,85]. The carbonate content tends to increase with age [86–89], but Fourier transform infrared spectroscopy (FTIR) studies suggest that elevation in the carbonate ion concentration may be also observed in early stages (up to fourth week) of mineral development during fracture healing [6,90].

Modifications of the carbonate content in bone apatite are not only age-dependent, but might be also very site specific. Differences in carbonate content have been found between cortical and trabecular bone [91]. Variations in carbon content were found even within the osteon [92]. There is also evidence of changes in carbonate chemistry between fractured and intact tissue [93]. Lower carbonate content in the damaged regions of bone was connected with apatite dissolution and removal of carbon-containing mineral from the rupture. Increased solubility of carbonated apatites might be connected with microstrains developing in crystal lattice [94].

CO_3^{2-} substitutions can occur at two different sites. OH^-- CO_3^{2-} exchange is known as an A-type substitution; PO_4^{3-}- CO_3^{2-} exchange is known as a B-type substitution. The latter type appears to be the preferred substitution in tissues [95], due to the lower temperature requirement [96]. *In vivo*, the usual A/B ratio is 0.6-0.9 [95] which reduces with age as levels of B-type carbonate increase [97]. In tissue, also a third carbonate species (C-type) can be

found, which is described as an unstable, surface carbonate; its presence is especially pronounced in young bone [98].

2.2.3. Bone mineral at the nano-meter scale

The mechanical properties of bone are highly dependent on the collagen-mineral packing and their interfaces at the nano-scale. Apatite mineral fills the spaces between collagen molecules in the fibril, as well as extra-fibrillar space. There has been extensive discussion about the crystal morphology in the collagen matrix and whether their shape is plate- or needle-like. Much controversy surrounds the morphology of the apatite crystals *in vivo*. The dispute between supporters of needle-like and plate-like geometry has been reconciled in favour of the plate-like morphology [99]. The impression of needle-shaped crystals originated from observations of platelets oriented edge-on, instead of *en-face* [19,99]. The apatite platelet in mature bone is on average 15-200 nm long, 10-80 nm wide and 2-7 nm thick [19,99]. Crystals tend to be deposited along the collagen fibrils with the c-axis of the crystals parallel to the long axis of the collagen fibrils [80,100,101].

2.3. Mineralisation and collagen-mineral interfaces

Mineralisation of hard tissues is a complex process, which is dependent on the concentration and distribution of ions, the arrangement of collagen molecules, and the localisation of nucleation sites. The mechanisms of bone mineralisation are still strongly disputed.

Before maturation into apatite, bone mineral evolves through different phases. Processes, by which the chemistry of the mineral develops over time during bone formation, remain largely unexplained and are highly controversial. Tricalcium phosphate (TCP), octacalcium phosphate (OCP) and amorphous calcium phosphate (ACP) are most often considered as immature phases in apatite development *in situ* [102], *in vitro* [103] and *in vivo* in turkey tendon, fish bone and enamel models [104–106]. However, other calcium phosphate phases are also studied in the context of biomineralisation (Table 2.2) [107]. The calcium/phosphate ratio varies within different phases. Hydroxyapatite, with Ca/P=1.67 ratio, is the most stable calcium phosphate phase. Deviation from the stoichiometric value of results in an increase in solubility and an increase in the possibility of recrystallisation [107]. In bone, Ca/P ratio varies strongly from 1.3 to 2.1 [16].

Table 2.2 Calcium phosphate biominerals considered in mineralisation process, or as synthetic bone replacements and their corresponding Ca/P ratios.

Ca/P	Formula	Name	Abbr.
2.0	$Ca_4O(PO_4)_2$	Tetracalcium phosphate	TeCP
1.67	$Ca_{10}(PO_4)_6(OH)_2$	Hydroxyapatite	HA
1.50	$Ca_3(PO_4)_2$	Tricalcium phosphate (α,β,γ)	TCP
1.33	$Ca_8H_2(PO_4)_6 \bullet 5H_2O$	Octacalcium phosphate	OCP
1.0	$CaHPO_4$	Dicalcium phosphate	DCP
1.0	$Ca_2P_2O_7$	Calcium pyrophosphate (α,β,γ)	CPP
0.7	$Ca_7O(P_5O_{16})_2$	Heptacalcium phosphate	HCP
0.67	$Ca_4H_2P_6O_2O$	Tetracalcium dihydrogen phosphate	TDHP
0.5	$CaH_4(PO_4)_2$	Calcium dihydrogen phosphate	AMCP

In situ and *in vitro* studies of mineral precipitation in simulated body fluids [102,108], on bioactive substrates [109,110], in tendon collagen [59,111], and in cell cultures [103] have provided insight into mineral evolution in the collagen matrix. Characterisation of mineral development *in vivo* presents a much greater challenge. Multiple studies have been conducted at various levels of tissue hierarchy: in the bulk of bone tissue [112], at the micro-meter scale (above micro-meter resolution) in fish bone [106], and at nano-meter scale in enamel [105,113] and fish bone [22]. However, little is known about the initial composition and organisation of premature calcium phosphate phases and their further development into apatite. Furthermore, a lack of the knowledge exists about the distribution of these phases within and surrounding the collagen *in vivo*.

One of bone mineralisation models proposed is that a local increase of Ca^{2+}-PO_4^{3-} accumulation activates the mineralisation process and the formation of pre-nucleation clusters on the collagen surface [1,108,114]; others emphasize the role of specific, charged nucleation sites (*i.e.* lysine residues) [17,59,114] or pre-mineralisation modifications of collagen matrix organisation (*i.e.* due to maturation of crosslinks) [61].

Crystal nucleation *in vivo* can occur both in the intra-fibrillar gaps and in the extra-fibrillar space [13,23,67,115,116]. These two processes are thought to be independent and can be observed simultaneously in different parts of the same sample. On the basis of *in situ* studies, specific agents are believed to promote particular types of mineralisation [59,108,117]. For

example polyaspartic acid or fetuin stimulates intra-fibrillar nucleation [59], while polyacrylic acid stimulates extra-fibrillar formation [117]. The formation of mineral could also be driven solely by collagen with no support from non-collagenous proteins (NCPs) [59,118]. It is speculated that strong bonding between the positively-charged domain at the gap/overlap region of the collagen fibril and the negatively-charged surface of the apatite complex [59,111] could confirm previous observations of mineral nucleation in the gap region *in vitro* [115]. Some studies suggest that hydroxylysine or lysine residues in collagen molecules are the direct nucleation sites for the mineral [49,60–62], but other possible sites (*i.e.* arginine and polysaccharide) with similar charge distribution have also been identified [62,63]. The crystal plane orientation of the mineral nucleating in the collagen matrix has an influence on the mechanics of the system [119]. In natural systems, the direction of (002) crystal planes of hydroxyapatite (crystallographic c axis and long axis of the crystal) is oriented preferably parallel to the long axis of collagen fibril [6,100].

There have been only few attempts to map the elemental distribution within the collagen fibrils and extrafibrillar space surrounding them, in bone and dentin. Higher intensities of phosphorus, calcium and oxygen in gap region (compared to the overlap region) were reported by scanning transmission electron microscopy and electron energy-loss spectroscopy (STEM-EELS) experiments in mouse bone and elephant dentin [21,71]. There is also more intense carbon signal in the overlap than in the gap regions [21,71]. The carbon and nitrogen signal is attributed to the presence of collagen. Interestingly, examination of mineral-deficient bone revealed an elevated nitrogen signal in gap region, which has a lower collagen content [71]. Similar findings have been reported for transverse sections of elephant dentin, where an elevated nitrogen concentration was also found in the extra-fibrillar space [21]. Investigation of the chemistry of the transverse bone sections is a quite novel approach and it is presumed this approach may lead to new findings of the chemistry of the collagen-mineral interface. In both Alexander and Jantou's studies, the presence of nitrogen is consistent with the regions in which the mineral forms. The source of nitrogen, however, is still unexplained. The latter investigation also showed both nitrogen and carbon peaks at the collagen-mineral interface [21]; it remains unexplained if these carbon-nitrogen peaks are related to mineral, collagen or other proteins. There are reports that a carbonated mineral surface might display improved collagen-mineral bonding in presence of water, since infiltration by water molecules leads to

the creation of multiple hydrogen bonds on the mineral-collagen interface [120]. Water molecules also help with stress shielding, where water movement disperses some energy [119,120].

Major steps have been made over the past four years to explain the fundamental mechanisms of bone nucleation, and the source of its toughness, originating from collagen-mineral interactions at the molecular level. However, the full chemical nature of the interface between the mineral and proteins remains largely unknown.

2.4. Electron microscopy of mineralising tissues

Electron microscopy is an indispensable technique allowing examination of bone's structure at the lowest levels of hierarchy. It has been utilised in bone studies for over 70 years [11]. Electron microscopy allows direct observation of the nano-meter scale features, such as:

- structural changes in the collagen fibrillar matrix, *i.e.* the banding and sub-banding patterns;
- the spatially resolved chemistry, crystallinity and morphology of mineral phases, *i.e.* the time- and site-dependent transformation from immature phases to carbonated crystalline apatite;
- the combined collagen-mineral ultrastructure, *i.e.* the distribution of the mineral crystallites and their alignment in relation to collagen fibrils.

Analysis of bone is extremely challenging to conduct. The progression of mineralisation in bone can be observed only prenatally or antenatally in the region of growth plate. In mineralisation studies, models such as dentin or tendon are frequently used. Dentin has a similar chemical composition to bone, but does not remodel, which makes *in vivo* studies easier to conduct [121,122]. Cell culture models for *in vitro* studies use osteoblast cultures to observe collagen fibrillogenesis and mineralisation [103]. For *in situ* studies of mineralisation, highly aligned, non-mineralised collagen fibrils, extracted form tendon, are utilised [59]. Recent analytical TEM studies of bone and other mineralisation models are presented in Table 2.3.

Table 2.3 Recent (2010-2012) TEM studies of bone mineralisation.

Title, year & authors	Findings	Model	EM techniques
The nano-morphological relationships between apatite crystals and collagen fibrils in ivory dentine, 2010, Jantou-Morris *et al.*[21]	Elemental maps of longitudinal and transverse sections; a low resolution EELS library (P, C, Ca, N, O, low loss) for dentin.	*In vivo*, elephant dentin	TEM, STEM, EELS
The role of collagen in bone apatite formation in the presence of hydroxyapatite nucleation inhibitors, 2010, Nudelman *et al.*[59]	Identification of the mineral nucleation sites close to the collagen C-termini, mineralisation controlled by polyaspartic acid.	*In situ,* horse tendon collagen	TEM, electron tomography
Bone mineralization proceeds through intracellular calcium phosphate loaded vesicles: a cryo-electron microscopy study, 2011, Mahamid *et al.*[123]	Formation of intracellular disordered calcium phosphate mineral vesicles.	*In vivo,* mouse bone	TEM, selected are electron diffraction (SAED), energy dispersive X-ray spectroscopy (EDS)
Minerals and Aligned Collagen Fibrils in Tilapia Fish Scales: Structural Analysis Using Dark-Field and Energy-Filtered Transmission Electron Microscopy and Electron Tomography, 2011, Okuda *et al.*[22]	Low magnification elemental maps (C, Ca, O) of longitudinal and transverse sections. A 3D reconstruction of the extrafibrillar mineral.	*In vivo,* tilapia fish scales	TEM, SAED, energy filtered TEM, electron tomography
Linking Microstructure and Nanochemistry in Human Dental Tissues, 2012, Srot *et al.* [122]	An EELS library (P, C, Ca, N, O, low loss) for enamel and dentin averaged over large regions; a beam damage study.	*In vivo,* human dentin and enamel	TEM, STEM, EELS, EDS
The role of intracellular calcium phosphate in osteoblast-mediated bone apatite formation, 2012, Boonrungsiman *et al.* [103]	Formation of the intracellular mineral vesicles secreted into the extracellular matrix.	*In vitro,* osteoblast cell culture	TEM, STEM, EELS
The nanometre-scale physiology of bone: steric modelling and scanning transmission electron microscopy of collagen-mineral structure, 2012, Alexander *et al.*[71]	Elemental maps of longitudinal sections of bone, calcium phosphate grains attached to poorly mineralised collagen fibrils.	*In vivo,* mouse bone	TEM, STEM, EELS
Mineral Distributions at the Developing Tendon Enthesis, 2012, Schwartz *et al.*[124]	Low magnification elemental maps of longitudinal sections of the bone-tendon interface.	*In vivo,* mouse bone and tendon	TEM, STEM, EELS

Electron microscopy also has potential to resolve spatially compositional variation, the coordination environment, oxidation state and bonding in the collagen matrix, *i.e.* the distribution of the mineral nucleation and crosslink sites. However, no studies have been able to analyse the mineral-collagen interface or crosslinks. This analysis is challenging (and was thought to be impossible), because spatially resolved analysis of a beam sensitive material (*i.e.* protein) requires difficult optimisation of the experimental conditions. Also an adequate sample preparation needs to be employed in order to preserve the chemistry and structure of collagen and mineral (including the distribution of diffused ions), simultaneously.

Characterisation of the mineral-collagen interfaces, the mineral ion distribution during mineralisation and collagen crosslinks would provide information about nano-meter scale details of the mineralisation process in bone and bone pathologies. Knowledge about the most direct interactions between the basic building blocks of bone can be utilised to guide improved engineering of artificial tissue or drugs targeting diseased tissues.

3.
MATERIALS AND METHODS

3.1. Sample preparation of tissues for nano-scale characterisation

Preparation is the first step in facilitating characterisation of different structures present in mineralising tissues and bioceramics. Since mineralisation events occur frequently at the length scale of the collagen fibrils [15], preparation methods must preserve the nano-scale architecture and chemistry of the tissue. Transmission electron microscopy (TEM) studies are performed in a high vacuum environment; this requirement is particularly troublesome in the case of biological samples, which are hydrated *in vivo*. As dehydration is a necessary step to conduct EELS analysis of the tissues, it is a very challenging to preserve the native state of biosamples.

For preparation of TEM samples from soft, non-mineralised or poorly mineralised, tissues, including mouse tail and turkey leg tendon, two embedding protocols were optimised (Figure 3.1).

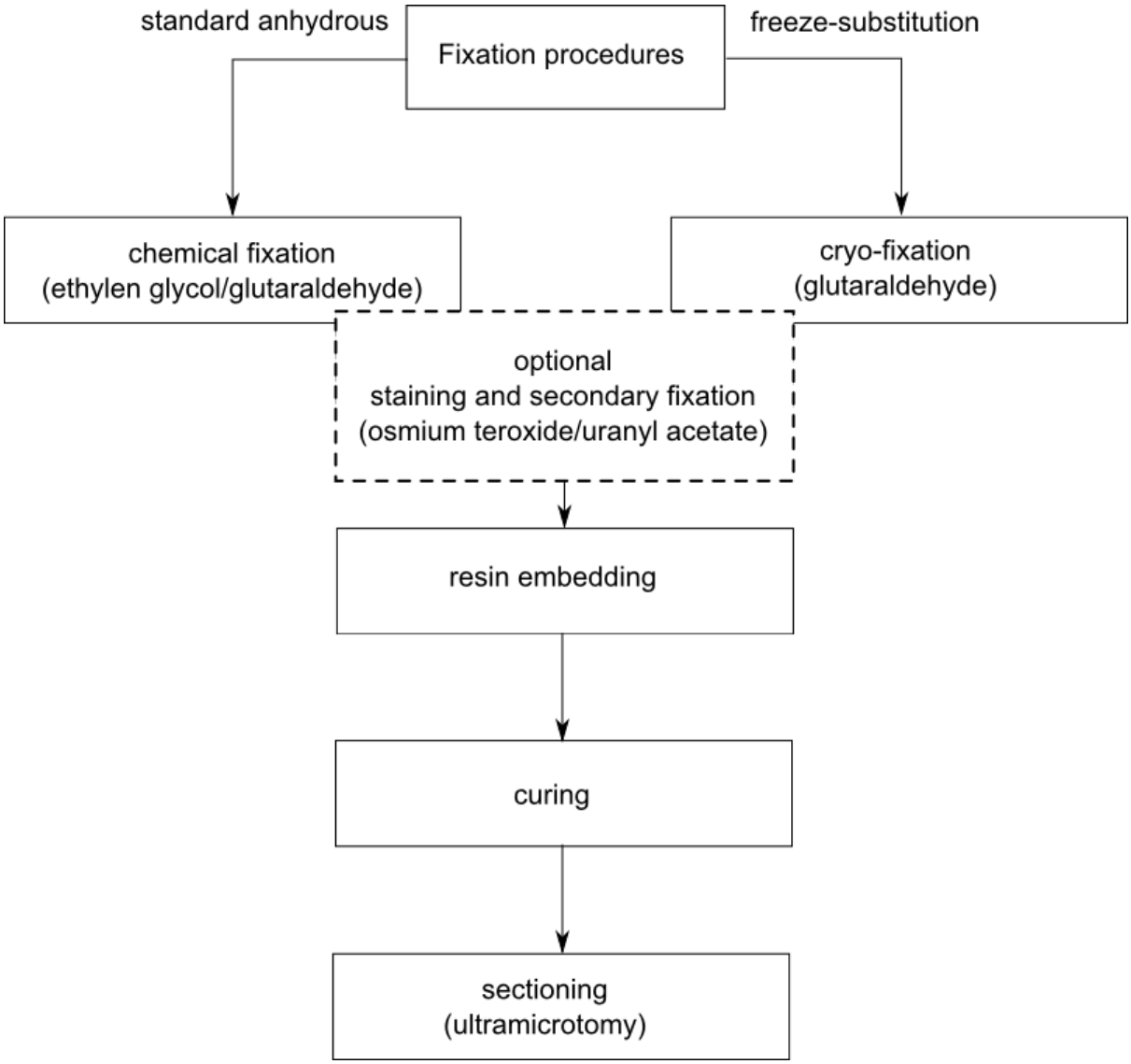


Figure 3.1: A flow chart showing the embedding procedure.

The **standard anhydrous method** is the most common procedure used for preparation of mineralised tissues. This method is the only method that preserves mineral chemistry and crystallinity. Combined with chemical fixation, it also produces preservation of the structure of collagen in bone and dentin [9].

A pure **chemical tissue fixation** conserves cell membranes, collagen fibrils and their banding pattern. Aldehydes (*i.e.* glutaraldehyde or formaldehyde) are used to crosslink the amino acid groups in proteins. To increase the contrast in the biomaterial and enhance the fixation (Figure 3.2), heavy metal stains (*i.e.* osmium tetroxide and/or uranyl acetate) are added.

Strong oxidants, like osmium tetroxide, bond to unsaturated carbon bonds in lipids. Fixation is followed by dehydration in pure ethanol and embedding in a plastic epoxy resin.

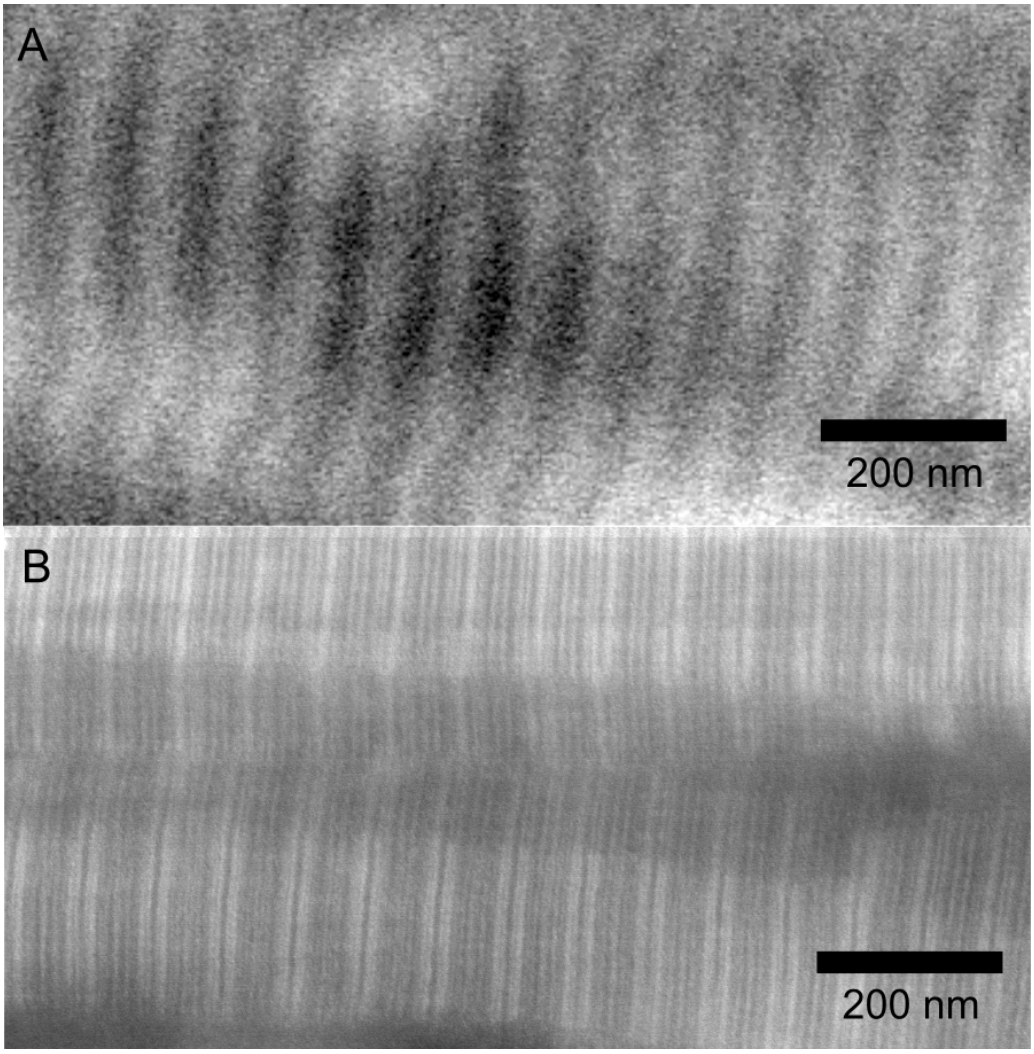


Figure 3.2 Representative ADF-STEM images of non-stained and bulk stained collagen fibrils. (A) An 11 week old, non-stained turkey tendon collagen. (B) An 8 month old, bulk stained mouse tail tendon collagen.

Shrinkage and collapse of fragile structures of proteins should be expected after the chemical fixation process. Room temperature chemical fixation alone is also not sufficient to preserve the original mineral structure and composition. A high amount of water, which activates conversion of amorphous calcium phosphate into a crystalline phase, is introduced in the preparation process. An initial dehydration step is necessary to remove any water, which may

dissolve the mineral and trigger the crystallisation process, from the sample using graded ethanol or ethylene glycol solutions.

In mineralising tissues, a range of calcium phosphate phases have been discovered. The precursor phase is described as amorphous calcium phosphate (ACP) [125,126,123]. In an aqueous environment, the unstable ACP transforms rapidly into a poorly crystalline carbonated apatite [127,128]. This transformation depends on the temperature and pH of the environment [129]. In comparison to a hydrated environment, the ACP stability increases in acetone solutions and ACP becomes stable in 100% acetone [127].

An anhydrous preparation protocol can be applied to prevent any changes in the crystallinity or chemistry of bone mineral phases from occurring. In the first step, dissected tissues are immersed in the dehydration agent, usually ethylene glycol. The organic components are not fixed during the dehydration process, but the crystallinity and chemistry of mineral is conserved. Studies of bone and HA implants used the anhydrous protocol to prepare samples for high-resolution TEM and diffraction analyses [9,130].

To preserve the ultrastructure of the organic phases in the dehydration process, aldehyde fixatives in anhydrous solutions may be added to crosslink the proteins. However, the distribution of diffusible ions is not preserved, when room temperature preparation methods are used. In order to simultaneously fix the apatite chemistry, the distribution of diffusible ions and the structure and chemistry of the proteins, methods, like rapid freezing and freeze-substitution, need to be employed.

Freeze-substitution preserves the chemistry of the mineral and the collagen, simultaneously [131–133]. A standard protocol has been developed for preparation of collagen and other biological materials [59,133].

A typical procedure starts with rapid freezing (**cryo-fixation**), in which specimens are exposed to a very low temperature, using liquid nitrogen. The specimen is frozen fast enough (within milliseconds) to capture biological events. For example, the rapid freezing procedure enables capture of fibrillogenesis process in chick embryo tendon [134], which is difficult to observe in chemically fixed tissues. However, during rapid freezing at ambient atmosphere,

ice crystals, which can damage the fine structure of the sample (*i.e.* disrupt cell membranes), may form.

To avoid ice damage, a **high pressure freezing** technique is often used. In this approach, small samples (<1mm thick) are rapidly frozen at high pressures (*i.e.* 210MPa). In these conditions, the melting point of water is decreased to -22°C, which helps to produce water super-cooled to -92°C [135] and different ice phases (Figure 3.3). Ice II and III are denser and grow less rapidly than ice I formed at the normal atmosphere. Vitrification is performed at a cooling rate of -1°C/ms [136]. When the sample is cooled from two sides, the maximal depth of vitrification is estimated to be 50µm [137,138]. However, the actual vitrification depth depends on the thermal properties of the sample [133].

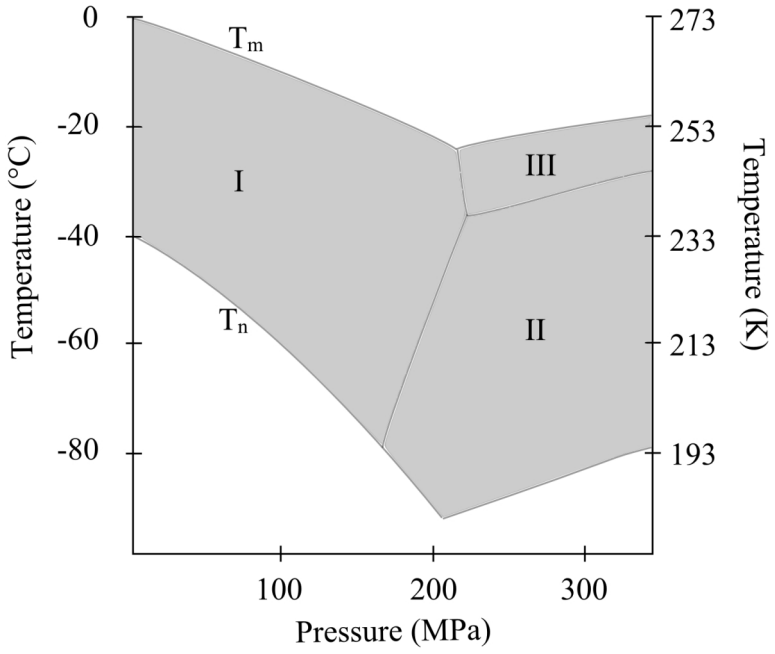


Figure 3.3 Part of water phase diagram showing the melting point (T_m) and the homogeneous nucleation temperature (T_n) as a function of pressure. At 210 MPa, the melting temperature is at a minimum as well as the nucleation temperature. The possibility of supercooling is maximized. At high pressure (i.e above 200 MPa), water crystallizes as ice II and III, rather than ice I.

Samples prepared by high pressure freezing or cryo-fixation can be sectioned and imaged in the TEM at liquid nitrogen temperature. This approach was utilised to study biomineralisation in fish [126] and mouse bone [123]. However, frozen hydrated bone is very

susceptible to electron beam damage. For this reason, examination of bone chemistry is extremely challenging in the TEM.

Rapid freezing of the sample is usually followed by **freeze-substitution**, in which amorphous ice is replaced with an anhydrous solvent. Ice and super-cooled water are gradually replaced by acetone or methanol solution at -90°C to avoid osmotic stress in the samples nanostructure [139]. The anhydrous solutions often contain chemical fixatives and/or staining agents, which fix and stain with the sample while the sample is warmed to the room temperature [136]. At -70°C, the lipid membranes are stained with osmium tetroxide [140], and, at -40°C, proteins are crosslinked with glutaraldehyde [141]. A combination of high-pressure freezing (HPS) and freeze-substitution (FS) preserves the distribution and chemistry of diffusible ions in the tissue. This approach facilitates accurate mapping of both, the chemistry of bone mineral and collagen and also the distribution of diffusible ions. Recently HPF/FS method has allowed the study of cell-mediated transport of calcium ions into the extracellular matrix [103].

The HPS/FS method is not completely anhydrous (1% of water is introduced) [103], although the amount of calcium phosphate crystallised during preparation is significantly lower than in case of a standard chemical fixation procedure. To study the crystallinity of the mineral phases, the anhydrous preparation method is needed. In general, multiple preparation methods must be used in parallel to fully appreciate artefacts produced during each preparation procedure.

Embedding using an epoxy resin provides mechanical support during preparation of thin sections. The embedding procedure is identical for the anhydrous and freeze-substitution methods and is performed at room temperature. This is a time-consuming (1 week) procedure involving daily changes of the embedding medium under vacuum to promote a slow infiltration of tissues with resin.

For TEM studies, sections (50-150nm thick) are prepared using an ultramicrotome. **Ultramicrotomy** is a well-established preparation method of electron transparent sections, which is particularly useful for biological specimens [142]. It involves physical cutting of the specimen with a glass or diamond knife, to produce ultra-thin sections. Each section is floated

onto a distilled water surface, in order to restore its original size and shape distorted by compression during slicing, and to protect the section from mechanical damage. The knife edge is often positioned at 6° to the sample to make the transition of the section smoother. However, this exerts more pressure on the knife edge and in some cases may crumple the sample. The specimen is collected onto a carbon coated 300 mesh copper grid. Swift removal (<10s) of sections from water needs to be performed to prevent the mineral in the sample from dissolving [130].

Hard tissues containing mineral, such as bone and highly mineralised tendon, do not need to be embedded for additional mechanical support. As alternative to ultramicrotomy, **focused ion beam** (FIB) **milling**, can be employed in order to avoid mechanical damage induced during ultramicrotomy [121]. In FIB sectioning, a beam of incident ions is used to mill thin sections of the sample. There are several advantages of FIB method over ultramicrotomy: chemical treatment of material may be avoided and a smaller number of preparation steps is required, and thickness can be controlled with 10 nm accuracy. Samples for FIB sectioning are often air dried without any fixative. This approach does not preserve the distribution of diffusible ions or the original chemistry of the collagen and mineral. However, in FIB milled thin films mechanically undisturbed tissue architecture can be observed (Figure 3.4).

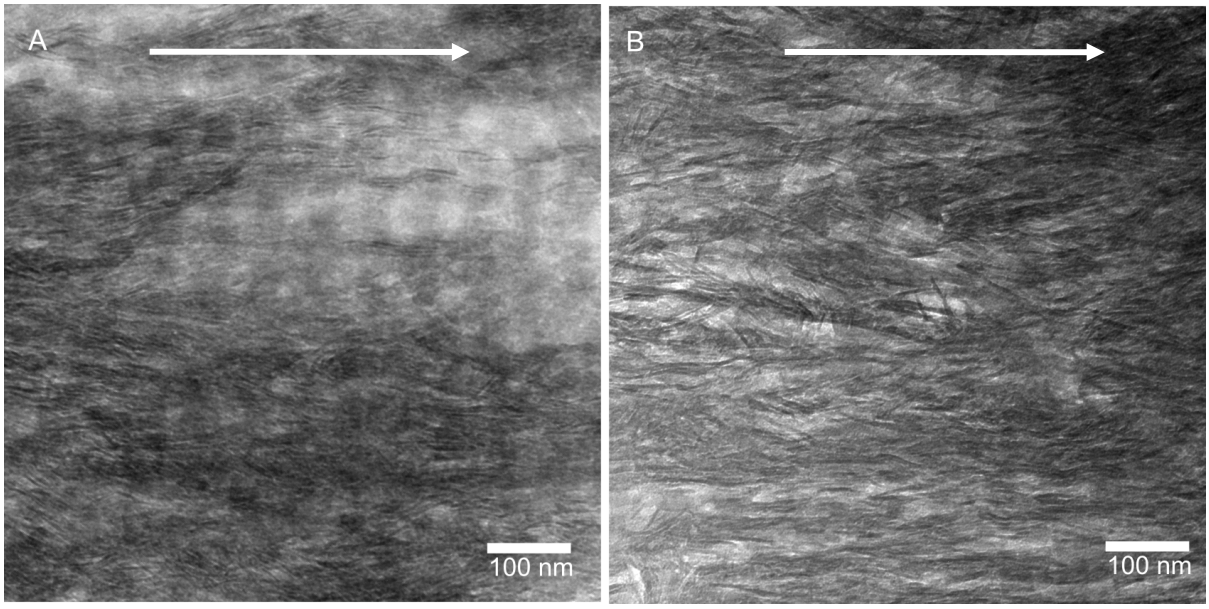


Figure 3.4 Bright-field TEM images of unstained mouse bone sectioned by (A) ultramicrotomy and (B) FIB milling. White arrows indicate the direction of the fibrils. In ultramicrotomed section, the majority of

mineral crystals is aligned along the fibrils. In FIB milled section, the orientation of crystals is less homogeneous.

In FIB milling, a gallium ion source is used to create the incident ion beam. In this procedure, high velocity ions interact with material generating damage by collision and dislocation of native atoms caused by momentum transfer. As a result, each ion produces a surge of secondary events, such as atom movements and electron release. Due to these incidents, the interacting ion loses energy and, if it is not back-scattered, in time, it will impregnate into the material. To avoid charge accumulation in non-conductive biological materials, which decreases the image quality and causes the beam to drift during milling, specimens are coated in a conductive material, in order to disperse the electrons. If the sputtered material is not entirely extracted by the vacuum system, this material can be re-deposited in the area of interest reducing the quality of obtained section. Ion implantation and re-deposition issues are inherent challenges in FIB milling.

3.2. Fundamental techniques of electron microscopy

In order to investigate the structure and chemistry of tendon and bone samples, transmission electron microscopy was employed.

3.2.1. Basics of electron microscopy

In basic principles of electron microscopy, the sample is illuminated with electron beam, controlled by set of electromagnetic lenses. The electron beam is created by the electron gun, usually in a form of heated tungsten/LaB_6 filament or sharp tip, or a more sophisticated field emission gun (FEG).

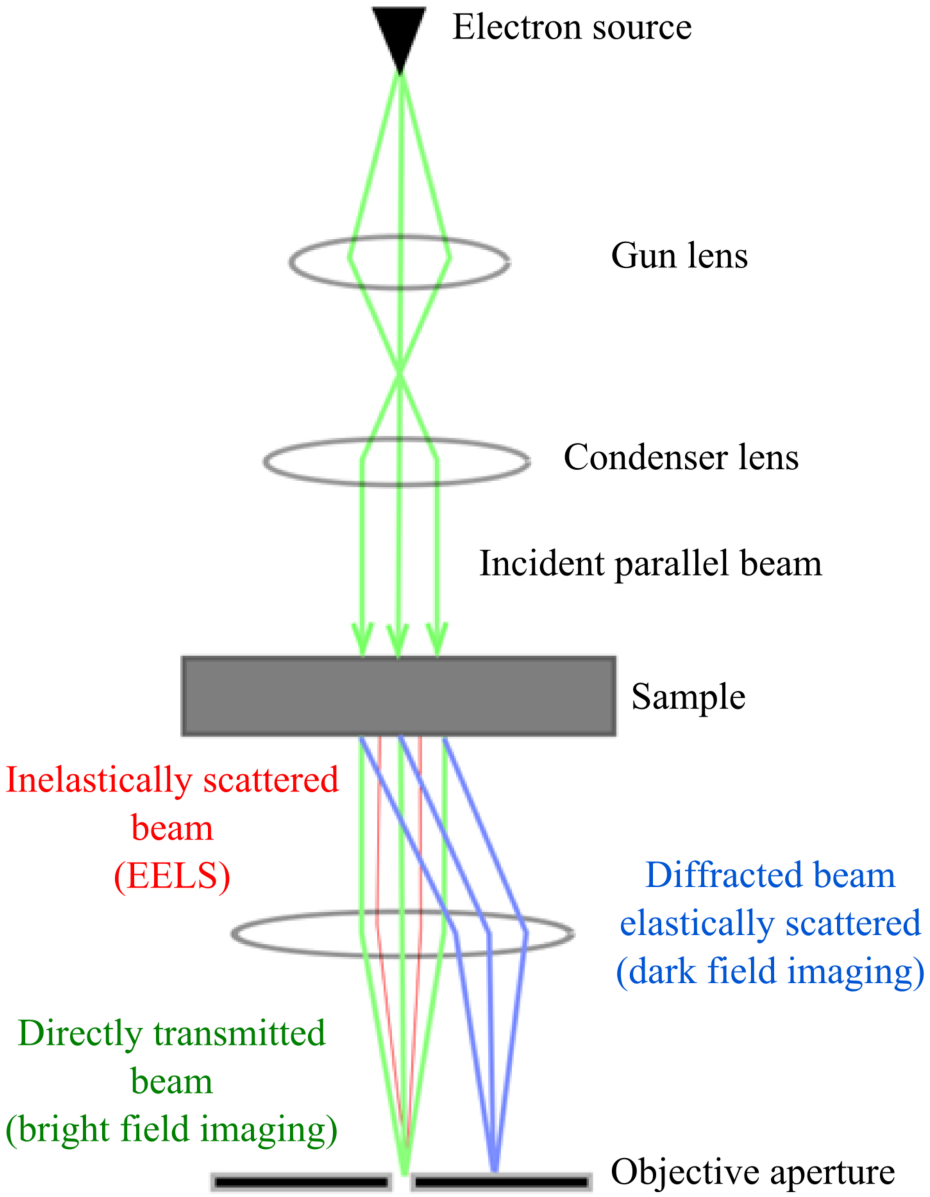


Figure 3.5 Schematic of a conventional TEM.

There are two methods of image acquisition in TEM. In bright field (BF) imaging only directly transmitted non-scattered electrons are collected to generate the image (Figure 3.5 - green beam). In dark-field (DF) imaging, the scattered electrons are collected. This means regions which scatter electrons at selected diffraction angles appear brighter in the image, whereas regions which do not scatter electrons or scatter them at different angle appear

darker. A low-resolution DF image can be obtained by positioning the objective aperture around a given diffraction spot (Figure 3.5 - blue beam), while a high-resolution dark field image can be obtained by centring the objective aperture and tilting the beam to set the diffracted beam parallel to the optic axis [143].

The main factors limiting the resolution of the acquired images are the diffraction and imperfections of lenses. The diffraction limit is the ultimate constrain to the resolution of system. Due to the finite size of lenses, rays are diffracted at the edges of lens. This phenomenon causes spreading of a point into a disk. In perfect system (with no aberrations), the resolution is defined by Rayleigh criterion. In approximation, two points cannot be resolved if the incline in the intensity profile between two given points is less than 20%.

Three types of lens aberrations need to be considered in electron microscopy: astigmatism, chromatic and spherical aberrations. Non-uniformity of the lenses magnetic field is responsible for **astigmatism (**Figure 3.6B**)**, resulting in elongation of circular objects into elliptical shapes. This aberration may be adjusted using stigmators in condenser and objective lenses. The astigmatism in the diffraction pattern may be corrected with a projector lens.

Lenses with **chromatic aberration** focus low energy electrons more strongly than those with higher energy (Figure 3.6C). In consequence, point objects appear as disk of radius r_c:

$$r_c = C_c \frac{\Delta E}{E_0} \beta$$

Equation 3.1

Where C_c is the chromatic aberration factor for given lens, ΔE is the decrease of initial electron energy E_0 and β is the collection semi-angle of the lens. The effect of this aberration has a great impact on the TEM image, where electrons loose a significant amount of energy during the interactions with sample.

Finally, lenses with **spherical aberration** (Figure 3.6D) overfocus off-axis electrons in the image plane, creating disk of radius r_s:

$$r_s = C_s\beta^3$$

Equation 3.2

Where C_s is the spherical aberration factor for given lens and β is the collection semi-angle of the lens. Spherical aberration has an impact on the image quality in the TEM, where defects in objective lens degrade the final image, and in STEM, where it causes probe spreading.

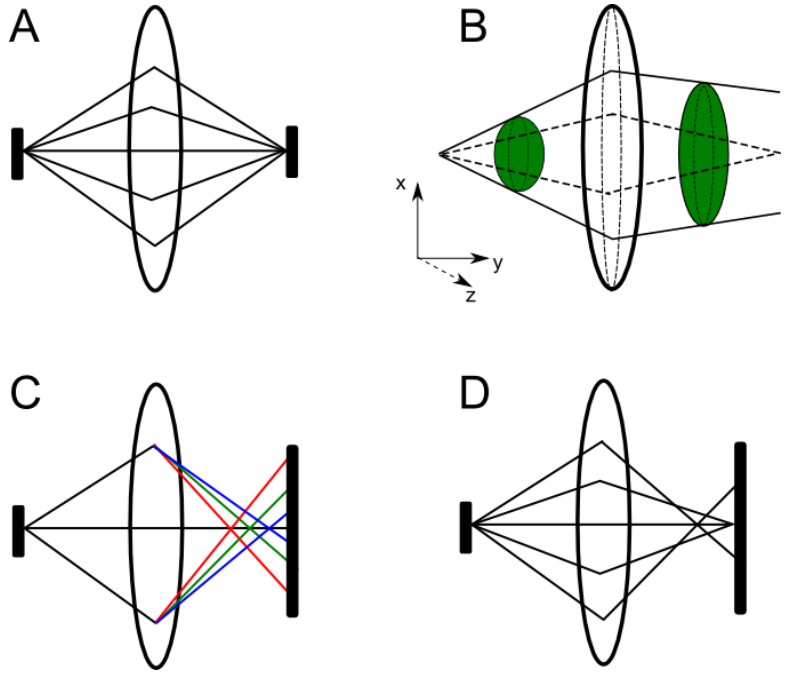


Figure 3.6 Schematics of perfect and aberrant lenses. (A) A perfect system focusing a point source into point. (B) Astigmatism – the lens spreading a round object into ellipsoid. (C) Chromatic aberration – the lens focusing electrons according to their energy. (D) Spherical aberration – the lens overfocusing off-axis electrons.

Contemporary microscopes are often fitted with aberration correction systems. For example, Scherzer showed that round lenses have positive C_s. By use of non-round lenses, C_s can now be corrected so that higher order aberrations become the limiting factor. A corrector after the specimen will correct C_s in TEM, while a corrector before will correct it in STEM. This topic is also addressed later in section 3.5.

3.2.2. Overview of electron interactions with matter

The fundamental imaging technique used in many studies of hard tissues is known as conventional TEM, where a parallel electron beam is transmitted through a thin specimen section (usually 50-100nm) producing an image or a diffraction pattern. Depending on the properties of the sample, the incident beam electrons can be transmitted directly through a thin layer, or interact with the material by elastic, or inelastic, scattering events (Figure 3.7).

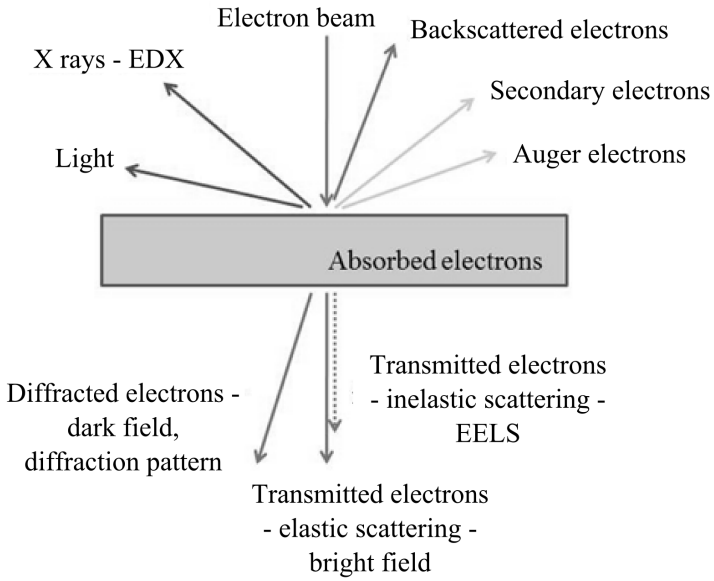


Figure 3.7 Schematic showing electron-sample interactions used in electron microscopy imaging and analysis [143].

Scattering events are also categorised as coherent and incoherent to reflect their wave nature. Elastic scattering events are usually coherent, especially in thin, crystalline materials and at low angles (1-10°), and become more incoherent at higher angles. Inelastic scattering events are incoherent in most cases and occur at very low angles (>1°).

Scattering events can be used to determine the elements present in the sample, their chemical organisation and crystal structure. While these events provide useful information about the material studied, only a small portion of the incident electrons interact with sample; the majority of them pass through the section unaffected.

Majority of atomic scattering for electrons can be describe as the Fourier transfer of the electrostatic potential, which goes to the Rutherford limit at higher angles. Electrons scattered to high angles (>50 mrad) in electron-nucleus collisions are described by Rutherford scattering. As this phenomenon is highly dependent on the atomic number *Z* (Equation 3.3), the originating contrast is less susceptible to changes caused by thickness changes. This allows for a preliminary assessment of the elemental composition of the sample. The probability of an electron scattering to high angles in the interaction with the nucleus is given by nucleus total scattering cross-section $\sigma_{nucleus}$.

$$\sigma_{nucleus} = 1.62 \times 10^{-24} \left(\frac{Z}{E_0}\right)^2 \cot^2 \frac{\theta}{2}$$

Equation 3.3

Where Z is atomic number, E_0 is electron energy, and θ is the scattering angle in mrads.

Electrons interacting inelastically with the electrons in the sample are typically deflected to small angles (<10 mrad) and lose only small quantity of their initial energy. These electrons can be utilised in electron energy-loss spectroscopy (EELS) to study the chemical composition and bonding within the specimen (see section 3.4). Inelastic scattering events may also produce X-ray radiation, whose energy signature can be employed in energy-dispersive X-ray spectroscopy (EDS) to assess basic sample chemistry.

3.2.3. Bright-field imaging

To understand the origin of contrast in bright-field (BF) TEM imaging, electron interactions in the sample should be examined more closely. The probability of a single electron interaction with given material is described by the interaction cross-section σ. The probability of an interaction event of a single electron with single, isolated particle can be described by following formula [143]:

$$\sigma = \pi r^2$$

Equation 3.4

Where r is the effective radius of interacting particle, which can be electron or nucleus, in the sample and can be represented as follows [143]:

$$r_{electron} = \frac{e}{V\theta}$$

Equation 3.5

And

$$r_{nucleus} = \frac{Ze}{V\theta}$$

Equation 3.6

Where e is the electron charge in coulombs, V is the accelerating voltage in volts and θ is the scattering angle in mrads. Equation 3.4, Equation 3.5 and Equation 3.6 show that electrons with a higher energy are less likely to be scattered. It is more probable that electrons are scattered to higher angles by the atomic nuclei, than by the electron shells of the atoms. Further, higher scattering cross-sections are observed for heavier elements.

The probability of an interaction event for a single electron passing through a given material can be expressed by the total scattering cross-section Q_T in relation to density ρ and thickness t of the sample [143]:

$$P = Q_T t = \frac{A_o \sigma_T \rho t}{A}$$

Equation 3.7

Where A_o is Avogadro's number, σ_T is the total interaction (elastic and inelastic) cross-sections and A is the atomic weight.

In biological electron microscopy, mass-thickness contrast can be partially explained by Equation 3.7. The contrast in bright field imaging originates from variations in mass and

thickness, which results in darker appearance of regions with higher density and thickness (Figure 3.8). To enhance this contrast, the objective aperture is used, which filters an angular array of electrons. Electrons, which are not scattered, or are scattered to comparatively small angles, participate in the creation of the image, while electrons scattered to higher angles, are blocked.

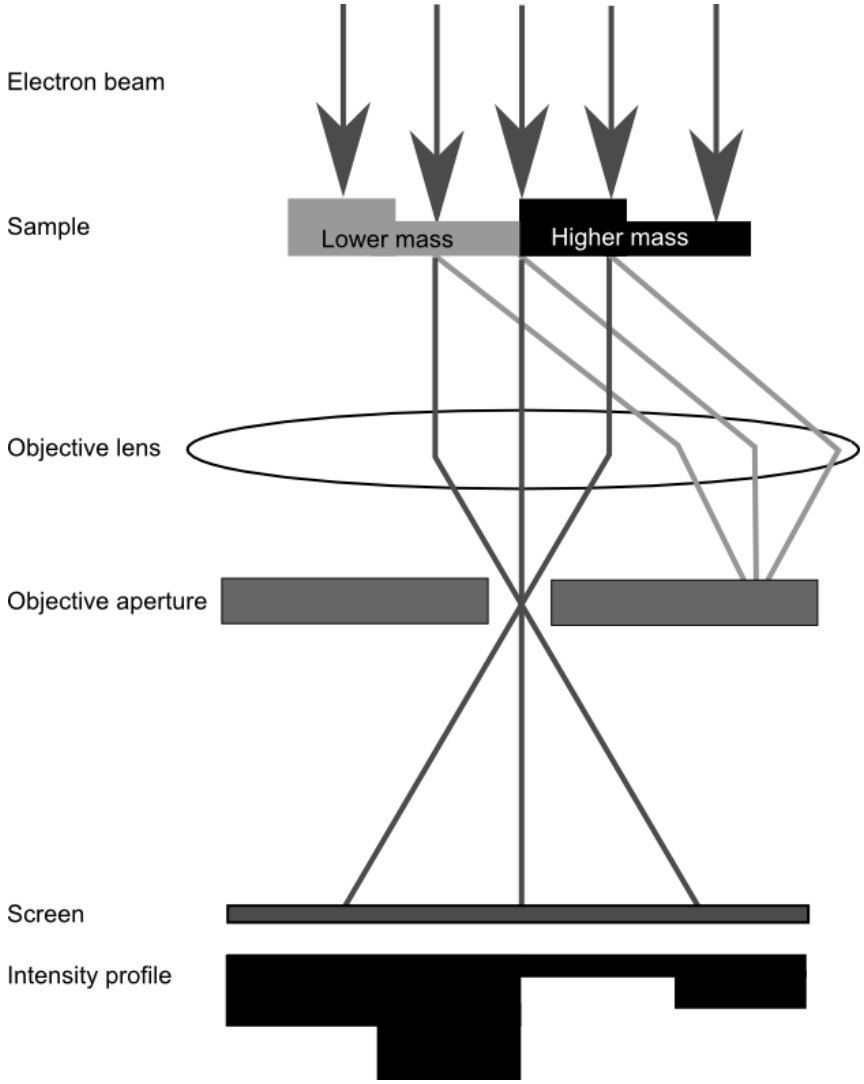


Figure 3.8 Illustration of the mass-thickness effect on image contrast in bright field TEM. The objective aperture enhances contrast by removal of strongly scattered electrons.

3.2.4. Electron diffraction

Electron diffraction is used in electron microscopy to reveal information about crystal structure (and its defects) in the material. The images and diffraction patterns (DP) can be correlated revealing spatial changes in crystallography (Figure 3.9).

Selected area electron diffraction (SAED) can be applied to examine the crystallography of the tissue. The electron beam is limited by a diffraction aperture to illuminate a circular region (typically 100-200nm in diameter). The majority of electrons travel through the sample without being diffracted, creating a bright central spot (covered with the beam stop on Figure 3.9), while the rest of the electrons are diffracted by various crystal planes, producing a range of rings and arcs. Such patterns are characteristic of the polycrystalline materials. The electron beam illuminates large quantities of small crystals and the resulting pattern is a superposition of individual, single crystal patterns. An ordered distribution of crystals results in a pattern consisting of spots or small arcs, while disorganised crystals produce ring structures. [143]

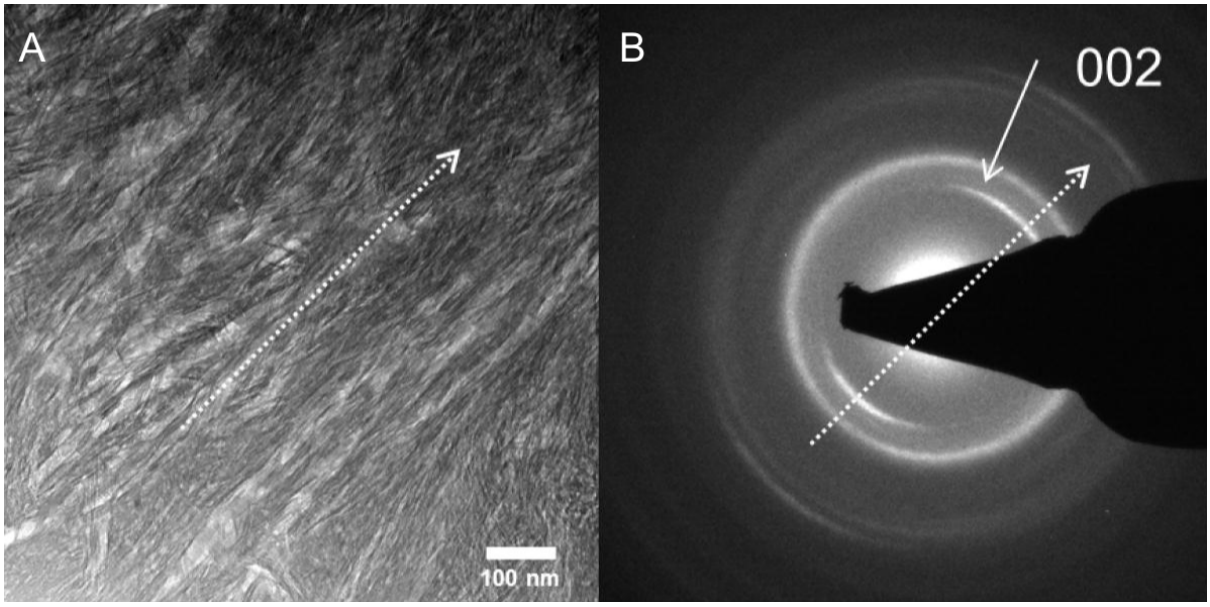


Figure 3.9 (A) Bright-field image of mouse bone and (B) the corresponding diffraction pattern showing arcs resulting from diffraction from the (002) crystal planes of hydroxyapatite indicating the alignment of the crystals (dotted arrow). The central spot in (B) is covered by the beam stop to increase contrast and protect the camera from over-saturation.

When electrons interacting with the sample are scattered and interfere constructively, a diffraction pattern is formed. This effect only occurs for monochromatic incident waves at characteristic angles (Figure 3.10), specifically, when two interfering waves satisfy the Bragg condition. The requirement to satisfy Bragg's law only applies to crystalline materials. [143]:

$$n\lambda = 2d \sin \theta_B$$

Equation 3.8

Where n is an integer of diffraction order, λ is the wavelength of the incident beam, d is the spacing between two atomic planes and θ_B is the semi-angle between incident plane wave and scattered plane wave.

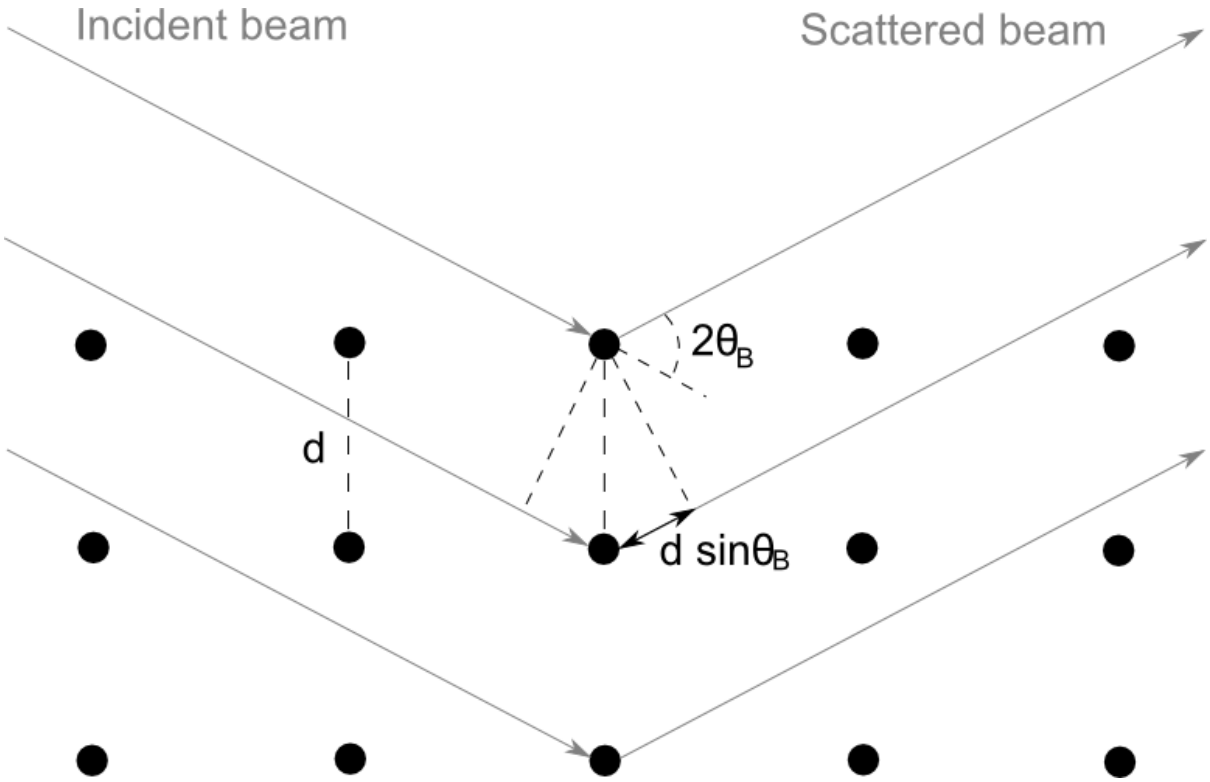


Figure 3.10 Schematic showing the scattering of an incident electron wave in a crystal lattice. The black spheres represent lattice points [143].

To project the diffraction pattern on the screen, the back focal plane of the objective lens needs to be adjusted to become the object plane of the projector lens (Figure 3.11). The objective lens remains fixed. It is the first projector lens that changes from imaging to diffraction mode.

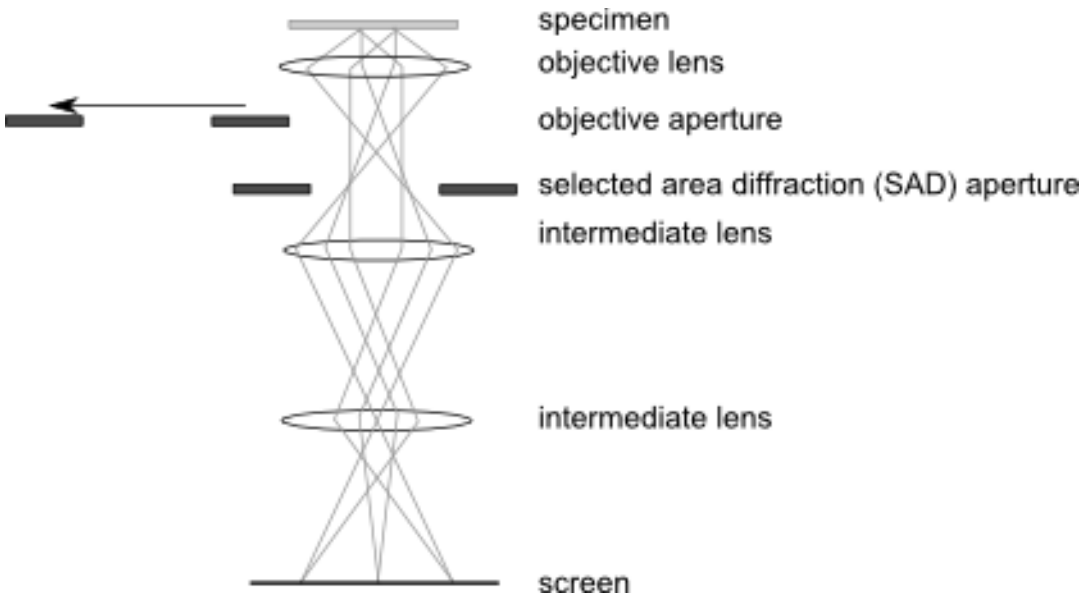


Figure 3.11 Schematic showing the TEM microscope operation in diffraction mode. The objective aperture is removed [143].

Electron diffraction patterns provide information about the mineral phases present in the mineralised tissue, and the degree of atomic order and organisation of the crystallites in collagen matrix [103]. Diffracted beams may be also utilised in dark-field (DF) microscopy to map the distribution of mineral phases.

3.2.5. Beam damage

Although electron interactions in the sample are the source of important information about its structure and chemistry, they can also cause disruption of the basic structure. In other words, a specimen may undergo modifications, sometimes severe, during imaging and analysis. Bone and other mineralising tissues are extremely susceptible to beam damage (Figure 3.12). This susceptibility to radiation damage makes even imaging of bone a challenging task, requiring a careful, but fast approach, especially when one aims to obtain high-resolution data and compositional information.

Depending on the experimental conditions, several different electron beam damage events may occur. Both elastic and inelastic interactions between the electron beam and a specimen may cause damage to the specimen, resulting in structural and chemical changes. There are two main damage mechanisms: radiolysis and knock-on damage.

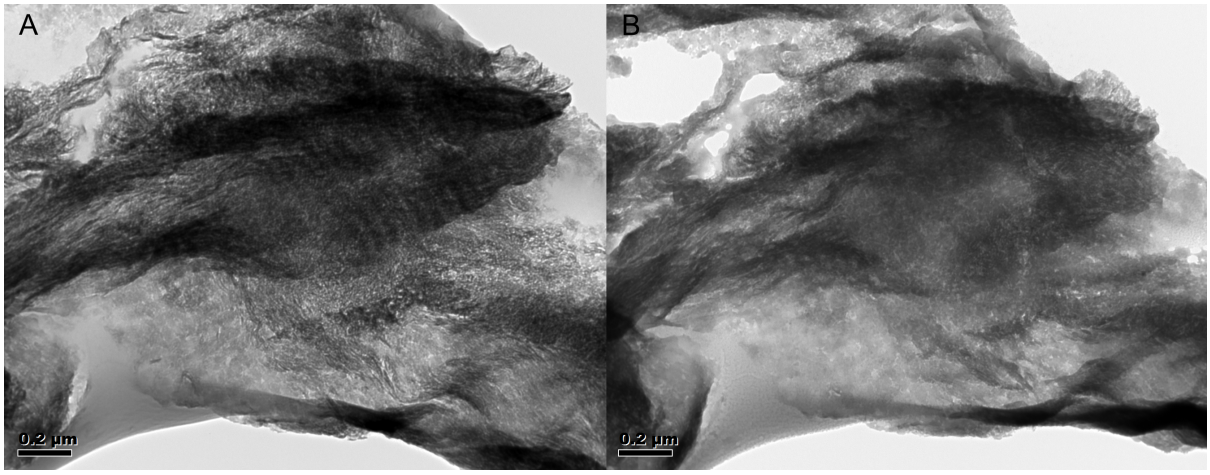


Figure 3.12 BF-TEM image of 22 week old mineralised turkey tendon before (A) and after exposure (B) to the electron beam at 200kV. The electron dose was not recorded in this experiment. The region of interest was exposed for several minutes. After prolonged exposure to the electron beam radiation, the distinctive banding pattern (A) is lost (B), possibly due to amorphisation of the crystal structure.

Radiolysis: Radiolysis occurs when the incident electron beam causes the breakage of chemical bonds through inelastic electron-electron events. This effect is particularly pronounced in organic compounds such as polymers and biological samples [144]. The breakage of the primary polymer chains changes the structure of material, resulting in mass loss. The breaking-off of side chain molecules leaves reactive free radicals, which may react and crosslink to form a new structure. In the TEM, mass-loss of the specimen can be seen as thinning of the specimens and eventually the drilling of a hole through the specimen. Radiolytic damage can also lead to the loss of the crystallinity of a polymer. This damage mechanism can be minimised by operating at a high accelerating voltage (e.g. 300 kV) as this will decrease the probability of electron interaction and energy transfer to the sample. Also, electrons accelerated through a high potential have a high velocity and, as a consequence the electron spends less time in a given volume. Therefore operating at a high voltage minimizes the probability of electronic interactions occurring between incident electrons and the sample. However, it also lowers the probability of elastic scattering, resulting in reduction of mass-thickness/diffraction contrast.

It has also been suggested that radiolysis is partially a temperature dependent process [144]. Specimen heating is also a problem in the TEM, particularly for specimens which have a low thermal conductivity, such as organic materials. When incident electrons collide with

electrons in the specimen, they can transfer energy to the specimen, and most of the transferred energy ends up as heat in the specimen. However, specimen heating does not depend solely on the thermal conductivity of the sample. Even heat-resistant materials might be easily damage, if the thermal conductivity and connectivity of all elements of the sample holding system (sample-film-grid-holder) are poor. Heating damage can be minimised by using a high accelerating voltage and by reducing the specimen thickness, by carbon coating or by liquid nitrogen cooling [144].

As for many other polymer materials, bone is susceptible to radiolytic damage as it is a poor heat and charge conductor. Therefore, illuminating a thin section of bone, gradually heats the sample, which leads to bond-excitation and finally to break-down of sample structure. Prolonged exposure to electron beam radiation may cause amorphisation, not only of polymer chains, but also of the apatite crystals. These changes can lead to formation of new compounds: apatite can reorganize into CaO and phosphate can transform into phosphide, once the total electron dose exceeds 10^8 electrons/nm^2. [145]

One type of damage is particularly visible when bone sections are examined using the STEM probe and often referred to as “hole drilling”. This ionisation event is a special case of radiolysis. The electron beam excites oxygen atoms bound to the structure of bone. Once the oxygen atoms are released, either as free radicals or O_2 molecules, they form a “bubble” inside the sample. The growing “bubble” may finally burst from the surface of the thin section, creating a void in the sample. This effect may be minimised by reducing electron dose or coating the sample with a thin carbon coating.

Knock-on damage: Displacement damage occurs when the electron beam transfers energy sufficient to knock out an atom from its atomic site leading to the generation of a vacancy, this affects the crystalline perfection of the materials. The threshold energy required for this event to occur is dependent on the material being studied. In TEM, knock on damage is usually not expected to occur at accelerating voltages of >100 kV, unless a specimen contains hydrogen atoms or other light elements [144]. Knock-on damage occurs at higher voltages. To minimize knock-on damage, operation should be carried out using an incident beam with kinetic energy lower than the threshold displacement energy of the material. If a higher energy is used, then the electron dose (electron/nm^2) should be minimised. For the atoms on

the specimen surface, the threshold energy for displacement is lower. The surface atoms are free to leave the specimen and do not have to be displaced into interstitial sites, they are usually ejected from the specimen into vacuum. In severe cases, this may lead to hole drilling. This mechanism is called sputtering and

In the most severe cases accumulation of damage processes described above may lead to physical rupture of thin sample film. This effect is particularly pronounced in two cases: when the sample was not dehydrated thoroughly and water residues, heated by electron beam, erupt from sample, or when there is a significant discrepancy in electrostatic charges on sample surface increased by electron beam [144]. To avoid these problems, the sample may be illuminated by a low dose electron beam or plasma cleaned [146]. These procedures not only gently remove water residues and even charge distribution, but also reduced the effect of carbon contamination. Carbon contamination is not strictly a damage process, but it may hinder the quality of data obtained, especially when STEM-EELS techniques are used. Mobile, charged carbohydrates on the sample are attracted by electron beam; in effect regions exposed to beam grow thicker with additional carbon layer.

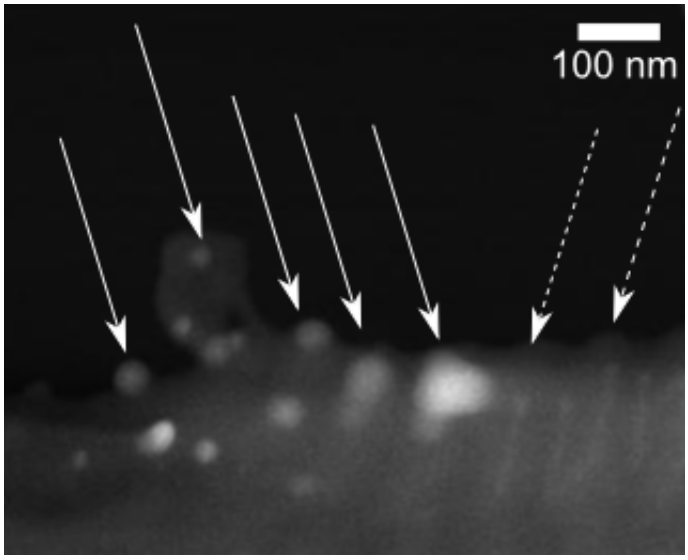


Figure 3.13 Effects of free carbohydrate accumulation on non-mineralised collagen of a 14 week turkey tendon. Clusters (solid arrows) are formed by a stationary beam. Lines (dashed arrows) are formed during collection of EELS line profiles.

3.3. Scanning transmission electron microscopy (STEM)

In STEM, the electron beam is focused into a probe, which is scanned through a selected region. The probe size, which defines STEM resolution, depends on the quality of the source and the microscope lens system. STEM images are acquired with the microscope in diffraction mode. The signal arises from an array of convergent beam electron diffraction patterns acquired for each pixel in the image [147]. In order to maintain the same convergence of the electron beam on the sample, the STEM probe must not tilt or change direction when scanned and the beam must be scanned parallel to the optic axis throughout the scan. This action is maintained by two sets of scan coils (Figure 3.14).

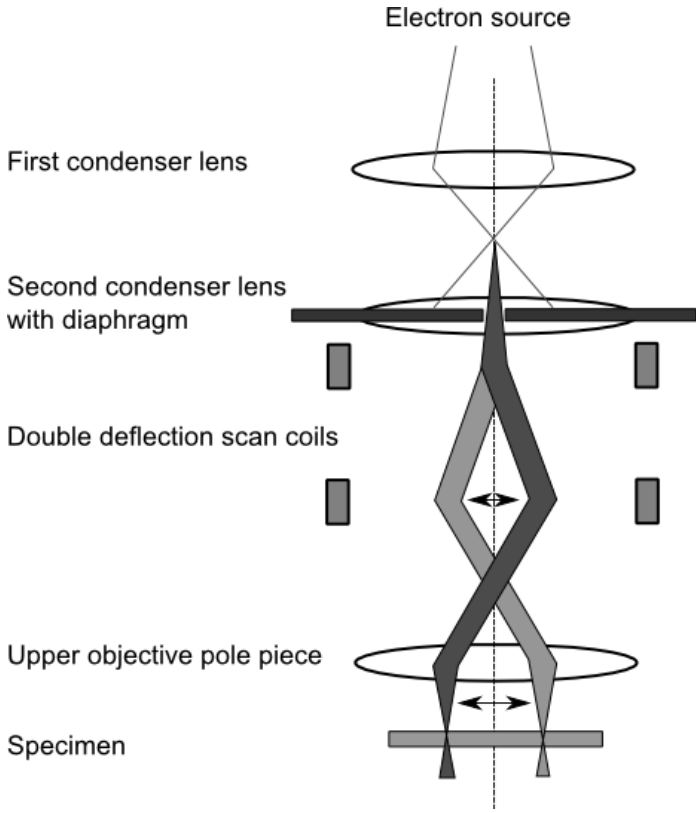


Figure 3.14 Schematics of an operating STEM probe, rastering across the specimen. The beam is scanned and kept parallel to optic axis (dashed line) by deflection coils [143].

In TEM, images are formed using a parallel beam. This allows a fast acquisition, but gives little freedom in the angular conditions used for imaging. In STEM, electrons are collected by a set of detectors placed beneath the specimen. This setup allows collection of differently scattered electrons, but is more susceptible to factors such as noise, and scan distortions.

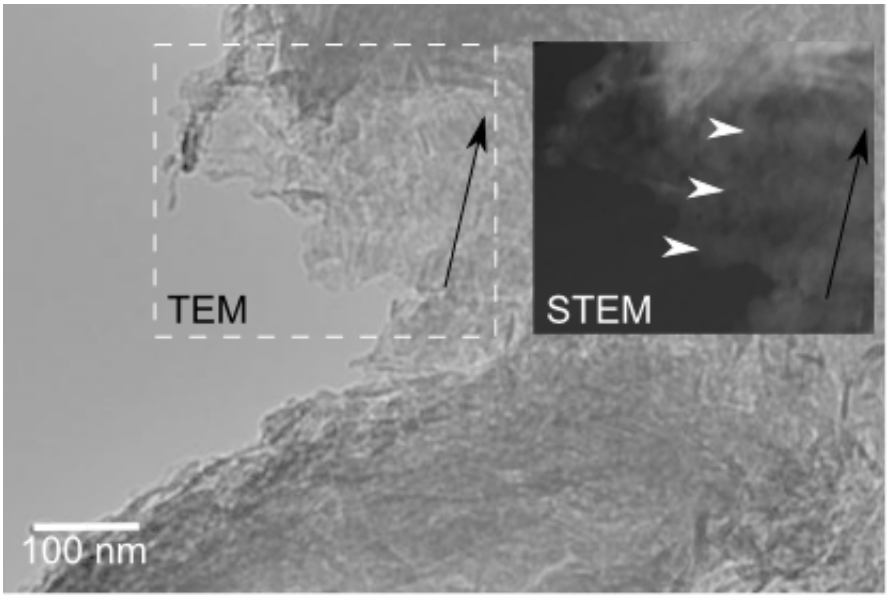


Figure 3.15 Comparison of the same region of 14 week turkey tendon imaged in TEM and STEM mode. In TEM image banding is hardly visible parallel to the arrow. In STEM mode, banding (along the black arrow) is more visible. White arrow heads point the gap regions. The collection angles have been adjusted to angles characteristic for mineral diffraction.

There are three detectors present in the Titan, which can acquire signals simultaneously: a BF detector recording electrons directly transmitted or scattered at small angles (<10 mrad), an annular dark field (DF-ADF) detector recording electrons scattered at 10-50 mrad angles and a high-angle annular DF (HAADF) recording electrons scattered to higher angles (>50 mrad). Actual angle values of collected electrons will also depend on the selected camera length.

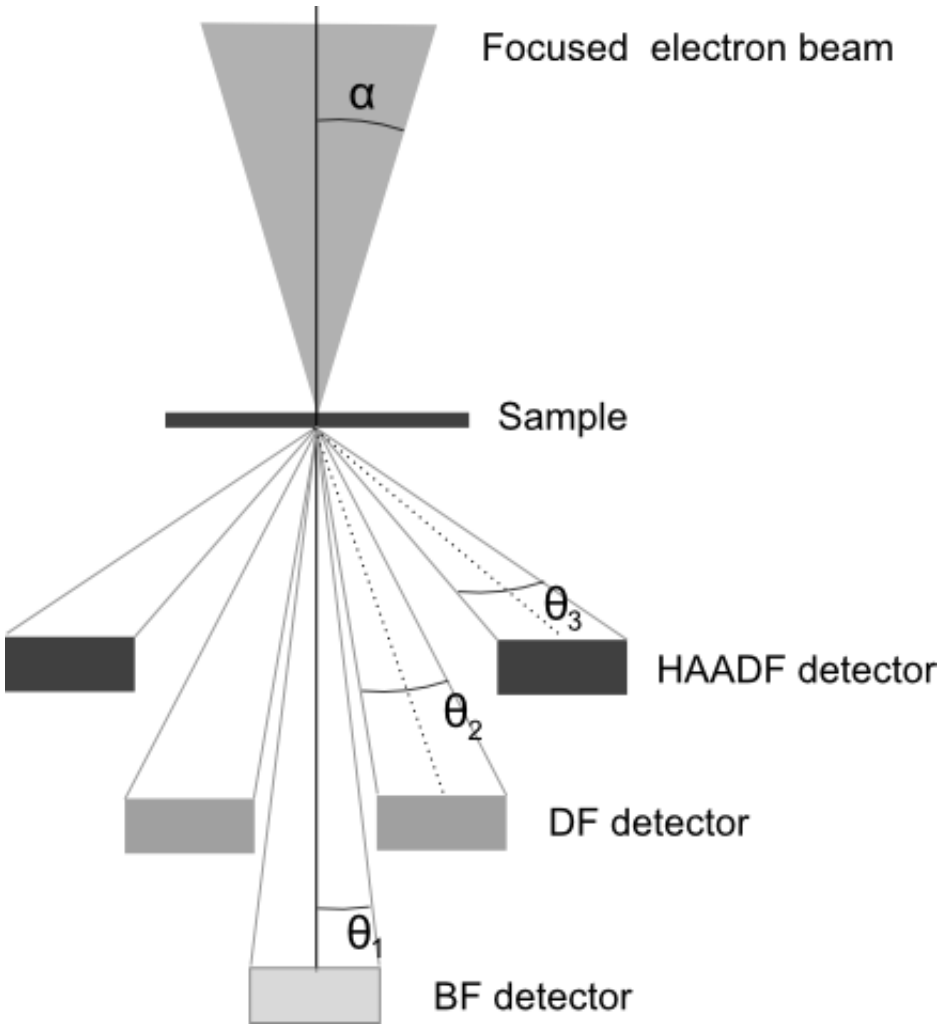


Figure 3.16 Schematic showing STEM detectors collecting electrons scattered at different angles [143]. α is the probe convergence angle. θ_1, θ_2 and θ_3 are the collection angles of respective detectors. Detectors are often mounted on retractable strips to allow access to other tools, such as the EELS spectrometer.

There are few advantages of STEM over conventional TEM. The electron dose, to which sample is exposed during acquisitions, can be easily controlled as the exposure time and the region selected are managed by user. The image resolution is affected by the condenser system, but not the projection system. The significance of no post-specimen lenses controlling the beam is that electrons have a much wider range of energies after interactions with the sample, which would result in bigger chromatic aberrations. Comparison of images collected from different detectors provides preliminary information about sample, as different contrast mechanisms contribute to each mode unequally. BF mode is dominated by mass-thickness contrast, while ADF benefits from diffraction contrast. HAADF mode reduces the

effect of diffraction contrasts, as the high-angle detector collects mainly Rutherford-scattered electrons (Z contrast).

3.4. Chemical analysis

3.4.1. Analytical energy dispersive X-ray spectrometry (EDS)

Electron microscopy provides alternative techniques to assess sample chemistry.

The most straight forward, easy to perform and interpret technique is EDS. This method utilises X-rays produced when excited electrons fall from the outer shell into a vacant core shell vacancy (emptied as a result of prior inelastic scattering event) [143]. The quantised energies of emitted X-rays are characteristic of their parent atom, which allows identification of elements. Spectral peaks are relatively easy to observe as the background originating from braking radiation (Bremstrahlung) is minimal. However, there are also some challenges in the interpretation of recorded spectra. Artificial peaks may be observed, which are caused by imperfections in the detection (internal fluorescence peaks, escape peaks) and processing (sum peak) systems. Ennui in the EDS especially excels in detection of heavy elements as the probability of emitting X-rays (instead of ionising the atom) increases with the atomic number Z. This probability is known as the fluorescence yield ω and is given as [143]:

$$\omega = \frac{Z^4}{a + Z^4}$$

Equation 3.9

Where *a* is a constant characteristic for the atomic shell (*i.e.* 10^6 for K shell).

Low fluorescence yields limit the suitability of EDS for detection of light elements. There also are other limitations, such as low effectiveness of the detector and low energy resolution. These obstacles might be particularly troublesome when beam sensitive materials, such as tissues, are under investigation. To achieve more complete information about sample's chemistry and bonding environment, techniques such as EELS need to be applied [148].

3.4.2. Basics of electron energy-loss spectroscopy (EELS)

EELS detects excitation events that cause changes in the kinetic energy of electrons as they interact with the specimen. Analysis of such events yields information about the atomic composition, crystallography and energy-band structure. Fast electrons, which suffered some energy-loss during interaction with the sample, are collected by a spectrometer placed below the STEM detector system. The spectrometer consists of a drift tube fitted with a magnetic prism deflecting, and dispersing, electrons filtered through the entrance aperture (Figure 3.17). Effectively, electrons with the same energy are brought to focus at the dispersion plane and electrons of different energies are dispersed at different positions. Next, electrons travel through a multipole optical system and are projected onto a detector (either CCD or photodiode). The quadrupole lenses of the post-tube optics may project either the spectral image (EELS) or a magnified image of the sample created from electrons selected by the slit (energy-filtered TEM). However, aberrations (astigmatism) may be introduced in the process. Sets of sextupole and octupole lenses are responsible for the correction purpose. Finally, EELS spectra are plotted as a distribution of electron counts versus their energy-loss. [7,143]

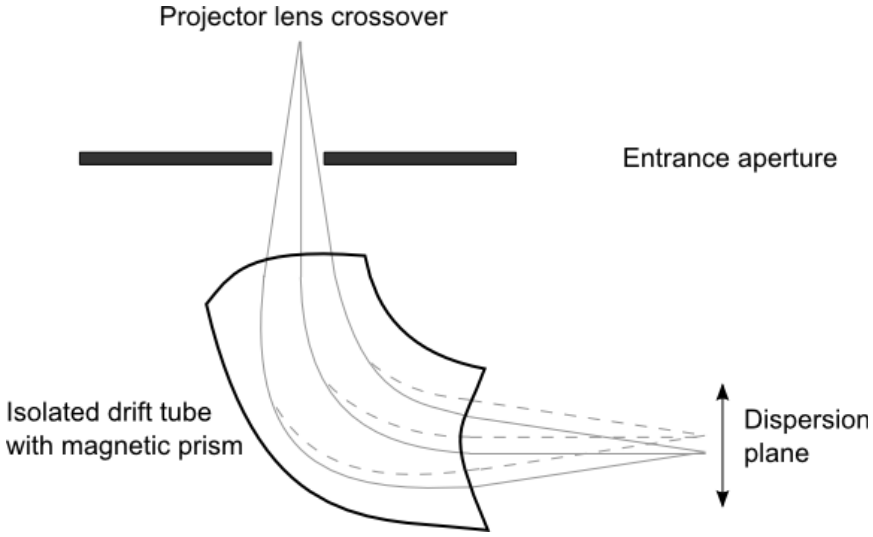


Figure 3.17 Schematic of the EELS spectrometer. The magnetic prism deflects electrons according to the energy of the electrons. Slower electrons are deflected to higher angles (dashed line) than faster ones (solid line). [143]

3.4.3. The electron energy-loss spectrum

There are three main regions characteristic to energy-loss spectrum (Figure 3.18). The first, most intensive peak known as **zero loss peak** (ZLP) is attributed to electrons transmitted through the sample without energy-loss (or with a negligible loss of energy). The full width half maximum (FWHM) of ZLP is considered as a measure of the energy resolution of the spectrometer.

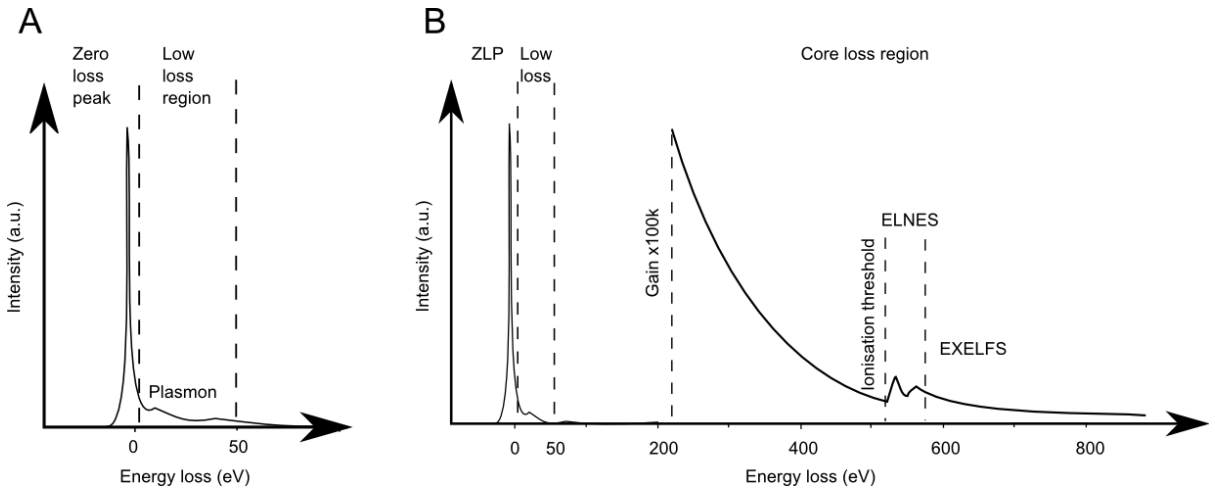


Figure 3.18 Schematics of electron energy-loss spectra. (A) Zero loss peak and low loss region with features arising from plasmon scattering. (B) Extended spectrum with core loss region. The intensity of the core loss structures is relative low in comparison to the 0-50eV region. The structure of the core loss edge is presented by an example of an oxygen-K edge. Core edges are labelled according to their corresponding ionised shell (K – 1s, L – 2s/2p, M - 3s/3p/3d, N – 4s/4p/4d/4f and O).

The region expanding from ZLP to 50 eV, known as the **low loss region,** is composed of peaks created by electrons, whose energy-loss is characteristic to excitation of the sample's valence electrons to vacant states above the Fermi level. In general, plasmon peaks represent collective oscillations of valence electrons [149]. Analysis of the ZLP and low loss region provides information about sample thickness [7]. In quantitative analysis, the low loss region is used in deconvolution processes to account for multiple scattering in the core loss region. Typically, a log-ratio method is used to assess the relative thickness t/λ:

$$\frac{t}{\lambda} = \ln\left(\frac{I_t}{I_0}\right)$$

Equation 3.10

Where t is the sample thickness, λ is the mean free path, which depends on materials chemistry and incident electrons energy (λ is reciprocal to Q_T, Equation 3.7), I_t is the total area under spectrum (usually only ZLP and low loss region are considered) and I_0 is the area under ZLP. Estimation of the relative thickness is not only important in quantitative studies, but is essential for selection of optimal regions of interest. A perfect sample for EELS should have t/λ factor of 0.3-0.5. Low values correspond to low signal-to-noise ratios, while high value indicates a strong contribution to the spectrum from multiple scattering.

Finally, the **core loss region (**>50 eV) exhibits ionisation edges created by excitation of inner shell electrons to vacant states. As the ionisation energies are characteristic of specific elements, the chemical composition of specimens can be determined both qualitatively and quantitatively. Additionally, changes in the valence of the atom (due to alteration of binding energies) might be reflected in small shifts of the energy onset of the ionisation edge. For example, core shell electrons of an ionised atom will have a higher binding energy than in a neutral atom. In effect, corresponding core edge will shift to higher energies.

The fine structure of edges depends on the atomic transition matrix, which describes basic shape arising from atomic physics, and the density of unoccupied states function (DOS), which is susceptible to alterations in the bonding environment.

Excited electrons are more probable to reside in particular vacant energy states. The probability to occupy a certain state is reflected in higher intensities observed at specific energy losses [7]. The DOS describes the interactions between atoms resulting in the bonding formation. The intensity of a peak *I(E)* corresponds to the probability of an electron to occupy given state and increases with the number of vacant states *ρ(E)*(DOS):

$$|I(E)| = \frac{d^2 I}{d\Omega dE} = |M(E)|^2 \rho(E)$$

Equation 3.11

Where $|M(E)|$ is the transition matrix element:

$$|M(E)| = \frac{2\gamma}{a_0 q^2} |\langle f|exp(iq \cdot r)|i\rangle|$$

Equation 3.12

Where γ is the relativistic factor, a_0 is the Bohr radius, q is the momentum transferred to the atom, r is the coordinate of the fast electron and $|i\rangle$ and $\langle f|$ are the initial and final state of the electron wave-functions. The exponential part can be expressed as:

$$exp(iq \cdot r) = 1 + i(q \cdot r) + \ldots$$

Equation 3.13

When Equation 3.13 is included in Equation 3.12, the first component converts to zero due to orthogonality of the initial and final state wave-functions. To observe electron transitions, the second component must be non-zero, which requires the initial and final states to have different symmetries. This condition is reflected in dipole selection rule.

The DOS is highly localised (changes of states are confined to particular atoms) and symmetry-projected (transitions are governed by the dipole selection rule $\Delta l = \pm 1$, so core s state electron transit to p-like states and p state electron to s- or d-like states). As final states and core holes have a limited life time, fine features are subject to energy broadening ΔE_t described by the uncertainty principle [7]:

$$\Delta E_t \approx \frac{\hbar}{\tau}$$

Equation 3.14

Where τ is state lifetime. This energy condition describes the energy resolution required to resolve a given state.

There two sub-regions considered in analysis of these fine structures. The energy-loss near edge structure (ELNES) spans 50eV from the ionisation threshold. The region from 50eV onwards is considered to be extended energy-loss fine structure (EXELFS). As ΔE_t increases with distance from the ionisation edge, the EXELFS features are usually damped and hard to resolve. In the excitation process, the incident electron may deliver more energy than required to excite a core shell electron above Fermi level to the first vacant state. Excited electron with additional energy of few eV will be scattered multiple times, which gives origin to ELNES. Excited electrons with greater energy will be scattered once causing EXELFS formation. Structures further from the ionisation edge are more damped and broader. This spectral broadening depends on the limited lifetime of the final states. The broadening increases with the excitation energy above the ionisation threshold and originates from energy lost by electrons in transitions to the final state.

ELNES originates from plural scattering events and depends on the bonding environment. EXELFS arises from single scattering events and depends on the local atomic arrangement [143]. This study focuses on the examination of near edge structures.

Core loss structures are overlaid on a background arising from multiple scattering and extended tails of previous peaks and edges. Before actual analysis, the background signal needs to be removed by subtraction of a power-law fit from the region (ideally 50eV-wide) preceding the edge of interest. In this process, one must be careful to avoid creation of artefacts. Consecutive analysis of refined edges frequently involves computer modelling and

comparisons with reference spectra. However, EEL fine structure is often complex and its interpretation should not be considered as trivial.

3.4.4. Principal component analysis (PCA)

PCA is a multivariate statistical analysis (MSA), which can be employed in the analysis of EELS spectra [150,151]. PCA is used to reduce the original large datasets (i.e. spectral images) by calculating a minimal number of principal components (variations of the EELS signal) necessary to construct a new dataset containing all significant information. No prior knowledge about the dataset is required. The PCA approach assumes that the original data might be expressed by a linear sum of a finite amount of specific characteristics. These characteristics can be retrieved from the original data matrix D and approximated by two smaller matrices: score S and loading L^T, where T means a matrix transpose (Equation 3.15). Decomposition of the original data matrix is performed *via* singular value decomposition (SVD) eigenanalysis [151]. Each row of data matrix D is an original spectrum and each row of loading matrix L^T contains a principal component known as an eigenspectrum (abstract spectral characteristic uncorrelated to other rows). The score matrix S contains the coefficients (spatial magnitudes) of corresponding eigenspectra in the loading matrix L^T.

$$D_{((x,y),E)} = S_{((x,y),n)} \times L^T_{(E,n)}$$

Equation 3.15

Where x and y are the dimensions of the original spectral image (in pixels), E is the number of energy channels and n is the number of principal components (eigenspectra).

Eigenspectra with low coefficients usually represent the experimental noise and can be discarded. The dataset reconstructed from the dominant eigenspectra will exhibit the characteristic signal in the original spatial and energy resolution. This property makes PCA a very efficient noise filtering technique. Further information about the processing algorithms can be found in the literature [150,151].

Independent component analysis (ICA) [152] is a processing method based on PCA principles, which aims to identify the real components of the original signal mixture. Finding the real components depends on “contrast functions”, which indicate the highest degree of

componential independence. Algorithms used in the present study were described in detail in the work of de la Pena *at el.* [153,154].

3.5. Titan microscope

The majority of work presented in this thesis was performed on FEI Titan microscope, which is a TEM/STEM instrument.

In comparison to standard electron sources (LaB_6, tungsten), the Titan's thermal FEG is capable of producing electron beam with smaller energy spread (0.7 eV on average [143]) and higher current density. A Wien-filter monochromator located below the FEG performs further energy filtering, which leads to additional reduction of energy spread (up to 0.1 eV) and increase in beam coherence. More details of this instrument can be found in [155].

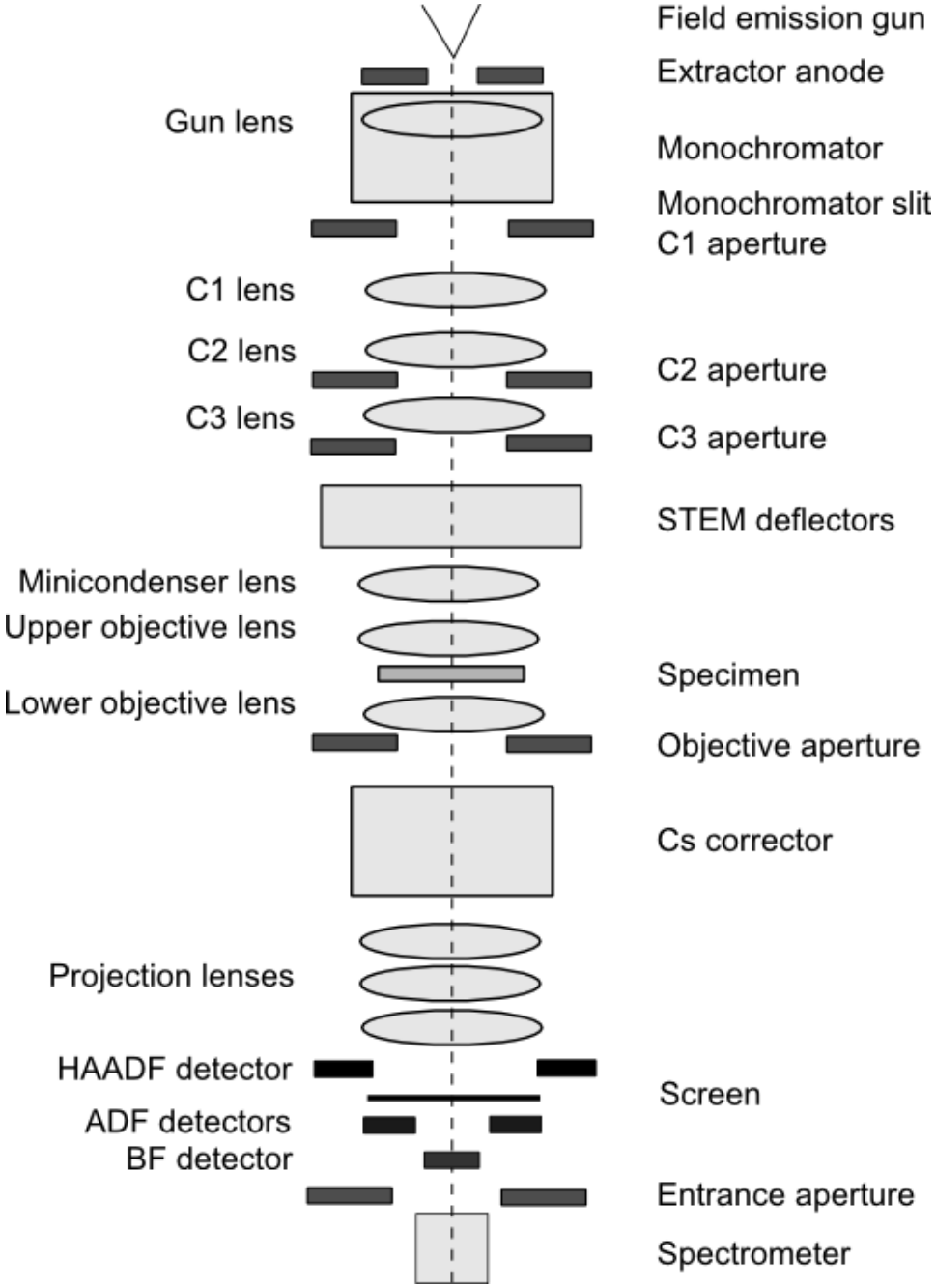


Figure 3.19 Schematics of Titan microscope.

Titan's illumination system consist of six lenses: gun lens, three condenser lenses (C1, C2, C3), minicondenser and objective lens (Figure 3.19). Unlike a typical condenser system consisting of two lenses, Titan has a triple condenser lens system with double zoom, which provides better control over beam parameters. The beam current is maintained by C1-C2 zoom, while beam width and convergence angle are regulated by C2-C3 zoom. [156]

Also the objective lens functionality differs from the standard one. There is a twin lens system in the pre-specimen sector, consisting of the mini condenser and upper objective lens, and the lower objective lens in the post-specimen sector. The minicondenser compensates the upper objective lens and the upper objective lens is responsible for creating parallel illumination in TEM mode (minicondenser on) and for focusing the probe in STEM mode (minicondenser off).

To address the problem of spherical aberration, an image-corrector (C_s) is placed below sample compartment (i.e. corrects the lenses in the projector system). Inhomogeneous behaviour of off-axis electrons arising in round lenses according to Scherzer theorem [157] is reduced by configuration of two hexapole electromagnetic fields.

Table 3.1Typical Titan settings and parameters used in the present study.

	TEM	STEM-EELS	STEM-EELS monochromated
Acceleration voltage	300kV		
Extraction voltage	4.5kV		
Emission current	65 μA		
Image correction	15-23 mrad		
Condenser apertures	C1 = 2000 μm C2 = 150 μm C3=2000 μm	C1 = 2000 μm C2 = 50 μm C3=2000 μm	C1 = Slit1 C2 = 150 μm C3=50 μm
Spot size	3	9	15
Camera length		48-60 mm	
Convergence angle		8-10 mrad	
Collection angle		12-14 mrad	
Energy resolution		0.6.0.7 eV	0.2-0.4 eV

3.6. Bulk characterisation

Bulk characterisation of selected samples was performed on the tissues. Specifically, X-ray diffraction (XRD), Fourier transform infrared spectroscopy (FTIR) and thermogravimetric analysis (TGA) were executed to measure the purity, chemistry and crystallinity of the mineral.

3.6.1. X-ray diffraction (XRD)

XRD utilises elastic X-rays scattering (Thompson scattering) to identify the crystal structure of the material. Constructive interference of X-rays interacting with an ordered crystal lattice results in formation of the diffraction pattern, as described by Bragg's law (see section 3.2.4). The peak positions (diffraction angle), intensities and widths provide information about phases present in the material, their compositional ratio and the average crystal grain size [158].

The presence of amorphous material, a relatively low crystallinity and a variety of phases present in the material result in peak broadening and overlapping making the examination of tissues a non-trivial task [159]. In this study, XRD was applied to confirm the phase purity of the bioceramic standards, and identify and compare mineral phases present in turkey tendon.

3.6.2. Fourier transform infrared spectroscopy (FTIR)

Phenomena, in which infrared light is absorbed by different molecules at characteristic (resonant) frequencies, lay at the basis of FTIR. In FTIR, reflections of a multi-frequency beam illuminating the sample are recorded *via* set of mobile mirrors known as a Michelson interferometer. Absorption-to-wavelength spectra are reconstructed from raw frequency-mirror position data, by application of a common Fourier transform algorithm. [160]

The FTIR spectrum provides information about the chemical structure and bonding environment of molecules in the sample. FTIR is particularly suited for identification of carbonate, phosphate and hydroxide bonding environments and the ratios between their different phases. The ability to discern between different bonding characteristics was employed to identify the ratios of different carbonate substitutions in carbonated HA.

3.6.3. Thermo-gravimetric analysis (TGA)

In TGA, specimens are incinerated using constant temperature gradient and weight changes are recorded as components are burnt out. In mineralised tissues, water (T<260°C), organic matter (T=260-600°C) and carbonate residues in apatite (T=600-850°C) are removed [159]. The high temperature also changes the remaining mineral content, for example by: transformation into different phases, growth in crystal size, and increase of crystallinity and equidimensionality [161]. TGA was performed to confirm that the turkey tendon samples' mineral/protein ratios increased with age and to compare mineral composition of the turkey tendon.

4.
COMPARISON OF MINERAL STANDARDS PROPOSED TO BE PRESENT IN MATURE HARD TISSUES

4.1. Introduction

For several decades hydroxyapatite $Ca_{10}(PO_4)_6(OH)_2$ has been used as the closest approximation of the biomineral present in *Vertebrae* mineralised tissue [101,162,163]. Hydroxyapatites are the most common phase present in natural systems; however, there are other forms of apatite that contain ionic substitutions (e.g. carbonate, fluorine, sodium, potassium etc.). The composition of the mineral may vary between tissues (e.g. bone, dentin, enamel, calcified tendon) [164], with age [97], as a function of the mineralisation stage [106] and as a result of diseases, such as osteogenesis imperfecta [165,166]. Modifications in apatite chemistry are present as substitutions into the lattice (e.g. carbonate or fluorine ion substitutions), and as different calcium phosphate phases (e.g. β tricalcium phosphate (TCP) vs. HA) [21,106]. Compositional variations between, and within hard tissues, may control mechanical properties such as the hardness or fracture toughness of each biomineral [167]. For example, disruption to mineralisation processes may have significant implications in altering the mechanical properties of diseased tissues. In the bone of mice suffering from osteogenesis imperfecta (OIM bone), high remodelling rates resulted in less mature crystals and therefore less carbonate substitution [168].

Characterisation of minerals in tissues not only provides insight into disease states, but is also beneficial to synthetic bioceramics research, where biocompatibility, bioactivity (e.g. resorption or cardiovascular response), material properties and mineral nucleation are of paramount importance [169–172]. Apatites with various dopants (carbonate, silicon and fluoride), beta-tricalcium phosphate and various mixtures of them are among the most popular bone-like bioceramics made for medical applications [170–172]. These minerals are often used as a connective material between implants and bone or as a porous synthetic bone

graft to reconstruct fractures; they are designed as a regeneration enhancer for bioactive bone growth.

Optimisation of the bioactivity of bioceramics, requires precise control over their chemistry. Subtle changes in the chemical composition, e.g. as a result of the form of ionic substitutions, and phase purity leads to alteration in bioactivity [173–175]. Nano-scale modifications in the chemistry of these bioceramic implants have a direct impact on mechanical and chemical properties of the surrounding bone. For example, phase changes and changes in the local atomic order at grain boundaries of apatite crystals affects mineral dissolution and the ability of carbonate and silicate substituted HA to integrate with the surrounding collagen matrix [9,130]. Other surface changes may promote or demote creation of sacrificial layers, an important factor in mechanisms stopping fracture propagation [176].

A full analysis of coordination environment within these materials and whether the ions substitute into the HA lattice, or not, will improve our understanding of mechanisms controlling their bioactivity, which will open the door for synthesis of more bio-adaptive ceramics to replace diseased or fractured tissues.

One of the challenges of probing the bioimineralisation process is the ability to identify mineral compositions at the nanometer scale during tissue formation and tissue disease. Acquisition of this information is the first step in facilitating characterisation of different phases present in tissues and bioceramics. Since mineralisation events frequently occur at the length scale of the collagen fibrils [15], it is critical that compositional information is acquired with nanometre scale spatial resolution.

X-ray absorption spectroscopy (XAS) is one of the most common methods used to characterise biomineral chemistry at the nanometer scale. X-ray absorption near edge spectroscopy (XANES) provided a new insight into the chemical environment of biominerals and mineralised tissues [177–181]. While XAS studies provide a very high energy resolution, its spatial resolution is not adequate to resolve features below 15nm [182–184]. Although the average sized (100nm long, 50nm wide, 5nm thick [19,99]) crystal platelets could be examined, investigation of smaller (5-10nm) features such as inter-crystal spaces, grain boundaries and protein-mineral interfaces are below the spatial resolution limit of this method.

At present, scanning transmission electron microscopy (STEM) combined with electron energy-loss spectroscopy (EELS) is the only technique capable of achieving molecular scale resolved information about the chemistry and coordination environment of minerals. Previous studies have attempted to identify spectral fingerprints from bioceramics using STEM-EELS [110,185]. However, these studies did not consider carefully the relative susceptibility of biominerals to radiation damage in the electron microscope, which may make the results unreliable [110].

In addition, previous studies focused on selected edges rather than comparing edges of all characteristic elements present in the mineral. Here we apply electron energy-loss spectroscopy (EELS) to discriminate between different bioceramic standards. Our library of calcium phosphate and calcium carbonate bioceramic implant materials has been chosen for the phase purity and commercial relevance of each material. These calcium phosphates were also selected as these materials are likely to be present in bone tissue at different stages of mineralisation [106] and/or are relevant in clinically enhanced mineralisation.

Calcium carbonates were examined to determine if carbonate ion substitution in the HA lattice is detectable with EELS. The near-edge core loss spectra of phosphate, carbon, calcium and oxygen were acquired and analysed for various forms of biomineral. A careful damage study was conducted in order to observe changes in the spectra that result from damage.

4.2. Materials and methods

A range of standards was investigated to represent the calcium-containing minerals suggested to be present in calcified tissues [21,162] or bioceramics enhancing bone growth [9,130]. These minerals are pure hydroxyapatite (HA), carbonated hydroxyapatite with carbonate substituted for hydroxyl and phosphate groups in various ratios (CHA), beta-tricalcium phosphate and two polymorphs of calcium carbonates (CC): calcite (CAL, the main phase in the CC standard) and impurity found in calcite (IMP, observed in small quantity in the calcite standard) (Table 4.1).

Table 4.1 List of standards used in the EELS study. Mineral standards were prepared by Dr. Robert Friedrichs (Cambridge University).

Mineral name and formula	Abbreviation	Notes
Hydroxyapatite $Ca_{10}(PO_4)_6(OH)_2$	HA	As precipitate and heated to 1200°C
Carbonated hydroxyapatite $Ca_{10}(PO_4)_{6-x}(CO_3)_x(OH)_{2-y}(CO_3)_y$	CHA	Ca/P=1.76, heated to 800°C, A/B = 0.099
		Ca/P=1.74, heated to 900°C, A/B = 0.168
β-tricalcium phosphate $Ca_3(PO_4)_2$	bTCP	Heated to 1100°C
Calcium carbonate $CaCO_3$	CAL – calcite IMP – impurity	Sigma Aldrich 239216, ACS Reagent >= 99.0%, main phase – calcite, impurity - aragonite-like phase discovered during present study

4.2.1. Production of mineral standards

HA with a Ca/P ratio of 1.67 was synthesised using a wet precipitation method described by Akao and Jarcho that involves a reaction between $Ca(OH)_2$ and H_3PO_4 where the pH is kept above 10.5 using aqueous ammonia [186,187]. $CaCO_3$ (Sigma Aldrich ACS reagent grade 239216) was decarburised over night at 960°C then cooled under vacuum. The resulting CaO was hydrated in deionised water to form $Ca(OH)_2$, then H_3PO_4 aq (85 v/v % Fisher Scientific) was diluted in deionised water and was added at a rate of 5 $ml.min^{-1}$ to the $Ca(OH)_2$. Upon completion the mixture was aged overnight then vacuum filtered. The resulting filter cake was dried then ground in an alumina crucible.

A mixed AB-type CHA was produced *via* a sodium free wet chemical precipitation reaction first described by Gibson & Bonfield [188]. Ca/P ratios of 1.76, 1.74 and 1.72 were

considered. Similarly to HA, $Ca(OH)_2$ was formed and CO_2 gas was bubbled through deionised water until the pH dropped to around 4 then H_3PO_4 aq. (85 v/v % Fisher Scientific) was added. This solution was added at a rate of 5 $ml.min^{-1}$ to the $Ca(OH)_2$ solution. No pH control was necessary as the pH remained above 10.5.

A fraction of the apatite mineral standards were heat treated: at 1200°C in air (HA) or 800-1000°C in a wet CO_2 environment (CHA) for 2 hours. The other fraction was investigated as-precipitated.

Beta-tricalcium phosphate (bTCP) precursors were formed through combination of $Ca(OH)_2$ and H_3PO_4 in an aqueous environment with a Ca/P ratio of 1.5. This mixture was aged, dried and heated to 1100 °C for 4 hours to produce bTCP [189].

4.2.2. Bulk pre-electron microscopy characterisation

The phase purity of heat-treated powders was investigated with X-ray diffraction (XRD). Powder XRD scans were performed using a Phillips PW1050 diffractometer with monochromatic Cu K-α x-rays operating at 40 kV and 40mA. 0.5° divergence and anti-scatter slits, a 10 mm mask and a 0.2mm-receiving slit were used. Scans used a 0.05° step size and a sweep rate of 1° 2θ/min. Phillips HighScore plus software was used to identify phases in the heat-treated CaP powders. International Centre for Diffraction Data (ICDD) powder diffraction files of HA 09-0432, α-TCP 29-0359, β-TCP 70-2065, CaO 37-1497, tetra calcium phosphate (TTCP) 25-1137 and calcium carbonate (calcite-CAL) 85-1108 were considered during phase analysis.

XRD revealed that all mineral standards were phase pure (Figure 4.1). The only phase present in heat treated HA and CHA was hexagonal HA (09-432). bTCP (70-2065) did not contain any α-TCP or HA impurities. The as received $CaCO_3$ from Sigma Aldrich was purely calcite phase (85-1108).

One should keep in mind that the estimate of the bulk phase purity might give an error of 2-6% [190]. This inaccuracy in the bulk phase purity may lead to the observation of various phases at the nanometre scale, like aragonite impurities in calcite estimated as 100% pure by XRD.

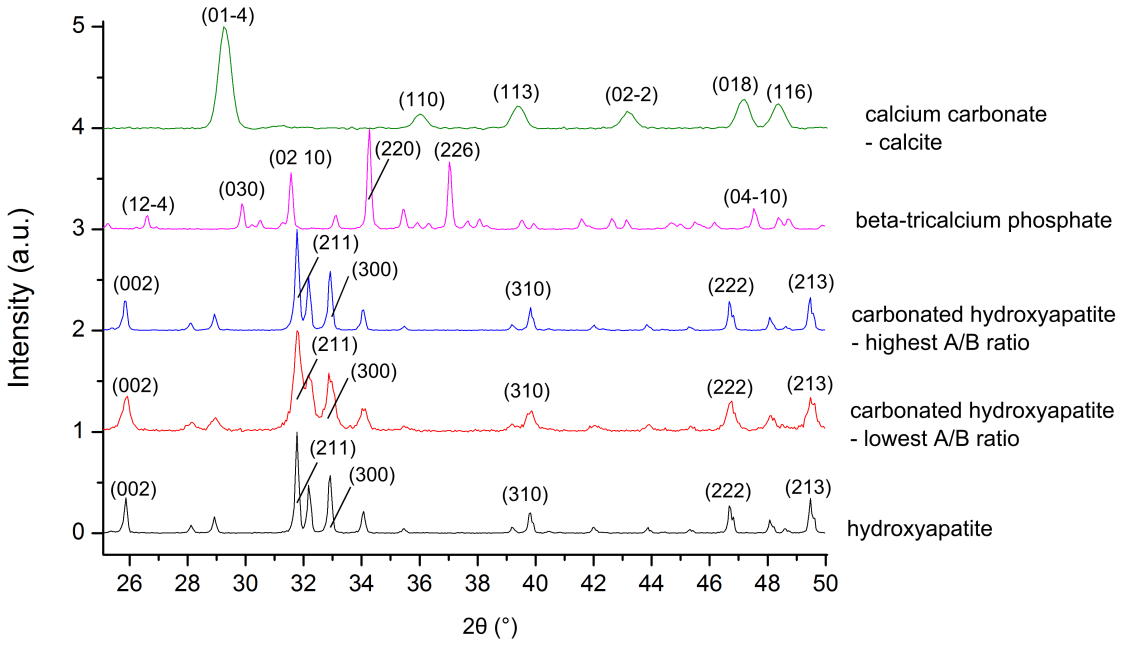


Figure 4.1 Representative XRD patterns of selected mineral standards used in STEM-EELS studies. The lower crystallinity shown in carbonated HA (lowest A/B ratio) is due to the lower heat treatment temperature and lower Ca/P ratio.

Carbonate groups in hydroxyapatites can occupy two possible positions; hydroxyl (A-type) or phosphate (B-type) group substitution [95,191]. Several variants of CHA were produced in order to obtain a high and low A/B type carbonate ratio to reflect clinical findings that A/B ratio varies in bone between species [95].

To determine the substitution sites of carbonate doping in the HA lattice, apatites were examined with FTIR (Perkin Elmer Spectrum 100 spectrometer), and A/B ratio was estimated as the ratio of areas of peaks corresponding to A and B substitutions [192]. CHA standards with the highest and lowest A/B ratio were selected to represent extremes of carbonate substitutions (Figure 4.1, Table 4.2).

Table 4.2 A/B ratios in ascending order for CHA produced using various Ca/P and heat treatment temperatures. The two extreme A/B ratios were used in the TEM-EELS study.

Ca/P ratio	Temperature (°C)	A/B ratio

1.76	800	0.099
1.76	900	0.1
1.74	900	0.127
1.76	1000	0.146
1.72	900	0.154
1.72	800	0.163
1.74	800	0.168

4.2.3. Electron microscopy characterisation

For TEM investigation, mineral powders were dispersed in 100% ethanol and then transferred onto copper 300-mesh grids coated with a lacy carbon film as a support (Agar Scientific Ltd.).

The specimens were examined on the FEI Titan 80-300 field emission, C_s corrected electron microscope fitted with a Gatan Tridiem electron energy-loss spectrometer. The instrument was operated at the accelerating voltage of 300kV and the emission voltage of 4500V, conditions frequently used to study mineralised tissues in order to minimise radiolysis damage [21,103]. For EELS analysis, the microscope was aligned in STEM mode with condenser aperture set to 50µm and spot size 9 selected with camera length of 60mm, corresponding to convergence and collection semi-angles of 8 and 12 mrad, respectively. The core loss signal was acquired in 10 second acquisitions with sub-pixel scanning. Beam parameters were optimised to ensure the total electron dose for the specimen would not exceed 10^4 electrons/nm^2 [193]. Each spectral image was collected with energy resolution of 0.6-0.7eV using an energy dispersion of 0.05eV/channel. This energy dispersion was selected to spread the noise over a larger number of channels. To further improve signal-to-noise ratio,

spectra from neighbouring pixels were added, limiting the effective spatial resolution to 10 nm. Also the dark current correction was applied manually from a reference collected after the acquisition of a spectrum.

Zero loss peaks (ZLP) were collected from the regions of interest to estimate the sample thickness. As the operated microscope did not have a dual beam system an absolute calibration from the ZLP was limited and spectra were calibrated to their characteristic peaks based on the literature. Unfortunately this approach limits the possibility to study chemical shifts.

For the purpose of the damage study, doses higher than 10^4 electrons/nm^2 were tested [193]. Samples were exposed to dose of 10^3 electrons/nm^2 per second. The signal was acquired in 1s increments for a total time of 120s.

A power law background subtraction was performed on all acquired edges and resulting spectra were normalised and calibrated to the characteristic peaks (for details see appropriate edges).

For the examination of impurities in the calcite sample, where overlapping structures of carbon film and mineral were observed in the carbon K-edge, a principal components analysis (PCA) approach was applied to separate superpositioned spectra [194]. In PCA, original spectra are decomposed into a set of orthogonal spectra. These spectra are weighted according to their contribution to the original spectrum, while spectra not showing any significant features can be discarded as noise. Finally the data set may be reconstructed from spectra carrying valuable information. For this processing Hyperspy open source software was used [154]. Specifically, an independent component analysis (ICA) was used. ICA is a processing method based on PCA principles, which aims to identify the real components of multiple original signals mixture. Finding the real components depends on the selection of "contrast functions". Contrast functions indicate the degree of componential independence, and the most independent components are considered as the original signals.

4.3. Assessment of nano-level chemistry (EELS)

No significant differences in EELS spectral features were observed between hydroxyapatite and hydroxyapatite sintered in 1200°C. No significant differences in EELS spectral features were observed between various carbonated hydroxyapatites (type A or B substitution). Representative hydroxyapatite spectra were labelled as HA, and representative carbonated apatite spectra were labelled as CHA.

4.3.1. Phosphorus $L_{2,3}$-edge

EELS data from the phosphorus-containing minerals (no calcium carbonates) are shown in Figure 4.2. The phosphorus $L_{2,3}$-edge displayed three main peaks in the energy-loss near-edge structure (ELNES): peaks A, B and C at ~138, ~141 and 146-149 eV, respectively. These features preceded a broad peak D at ~160 eV. Phosphorus spectra were normalised and aligned to the first peak A, which was set to an energy-loss of 138 eV based on the literature [195].

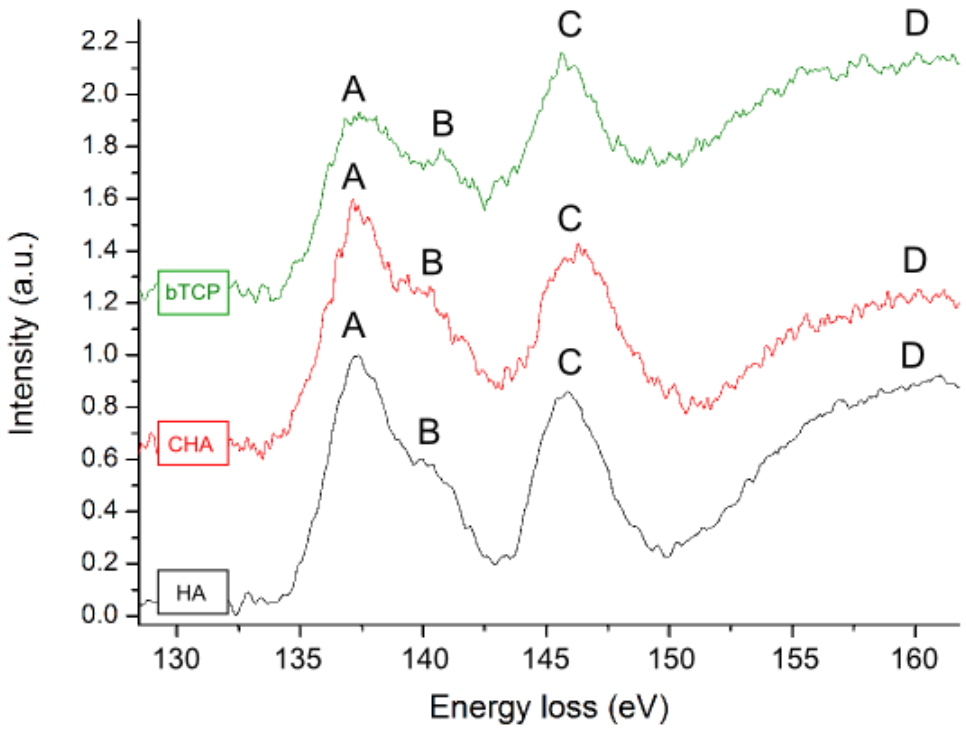


Figure 4.2 Phosphorus $L_{2,3}$-edge structures of hydroxyapatite (HA), carbonated hydroxyapatite (CHA) and beta-tricalcium phosphate (bTCP). All phosphate-containing minerals displayed a characteristic pattern of two main peaks: peak A and peak C, followed by a broad peak D.

Background subtractions of phosphorus $L_{2,3}$-edge were performed with a pre-edge (10eV) window. The confidence of fit of the subtraction window was limited by the intensity of signal at lower energies of the spectra and experimental noise, which created artefacts in the spectra, which hinder the application of a wider fit.

Peak A can be assigned to transitions from the phosphorus 2p core states to unoccupied states of p-like symmetry [195]. Monopole transitions (p-to-p state) are not allowed by dipole selection rule. However, if a hybrid sp^3 (combination of 3s and 3p state) state is formed, the dipole selection rule can be satisfied by transitions to the s-like component of this state [196]. Additional mixing with hybrid sd^3 states may further increase the transition probability [196,197]. By analogy, peak B has been attributed to transitions from 2p state to p-like final states that arise due to mixing of calcium d-states [195]. Peak C is formed by electrons

excited to d-like states [195,198]. Peak D, with a maximum at ~160 eV, is attributed to a cross section maximum of 2p state excitations and multiple scattering [198].

There was no significant difference in the phosphorus $L_{2,3}$-edge from phosphorus-containing minerals shown on Figure 4.2.

4.3.2. Carbon K-edge

Carbon K-edge spectra of carbonated minerals were normalised and aligned to the carbonate peak D (Figure 4.3), which was set to an energy-loss of 290 eV, based on the literature [177]. The amorphous carbon spectrum (AC) of the carbon film was collected in the same acquisition as the calcium carbonate spectra. AC spectrum was normalised to peak A of CHA.

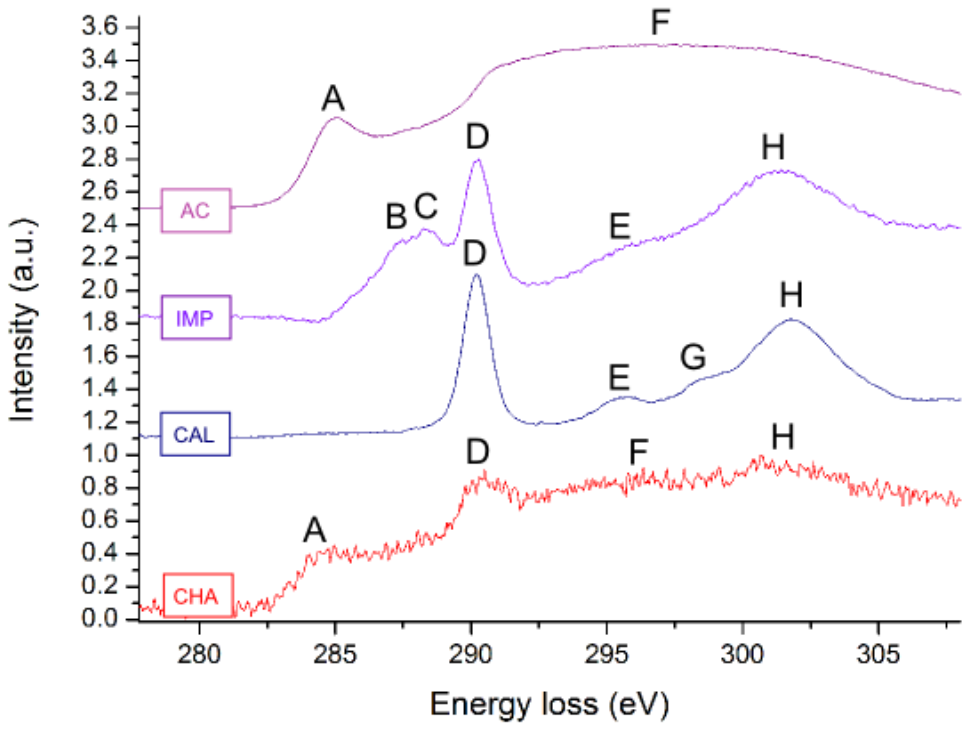


Figure 4.3 Carbon K-edge structures of carbonated hydroxyapatite (CHA), calcite (CAL), an impurity (IMP) and amorphous carbon (AC). The carbonate-containing minerals (CHA, CAL, IMP) display a

sharp peak D at 290 eV and a less intense peak H at 302 eV. The IMP edge was obtained *via* ICA (Figure 4.4).

The spectrum from calcite, $CaCO_3$ (CAL, Figure 4.3) was consistent with the literature [199] and exhibited a distinct, sharp peak D at ~290 eV, less intense peaks E and G at ~296 eV and ~298 eV, respectively, and a broader peak H at ~302 eV.

The CAL standard was nominally a 99% pure phase calcite. Impurities detected in the study exhibited EELS spectra with characteristics similar to aragonite. Apart from aragonite-like features, these spectra showed additional peaks typical for organic compounds. Impurity particles were found exclusively on the support film. Therefore spectra acquired from impurities represent a superposition of amorphous carbon film and unknown phase spectra, and were analysed using ICA.

In Figure 4.3, IMP was the spectrum obtained *via* the ICA blind source separation method [153], which extracts a full spectral signal of each individual phase present in the examined region. Original spectrum and extracted spectra are presented on Figure 4.4. We assumed that the original signal was a mixture of two signals. After application of ICA, the first spectrum obtained exhibited features consistent with an amorphous carbon film, while the second spectrum exhibited features, which allegedly represent the unknown calcium carbonate phase signal. Similar results were obtained by subtracting the amorphous carbon spectrum from the original spectrum.

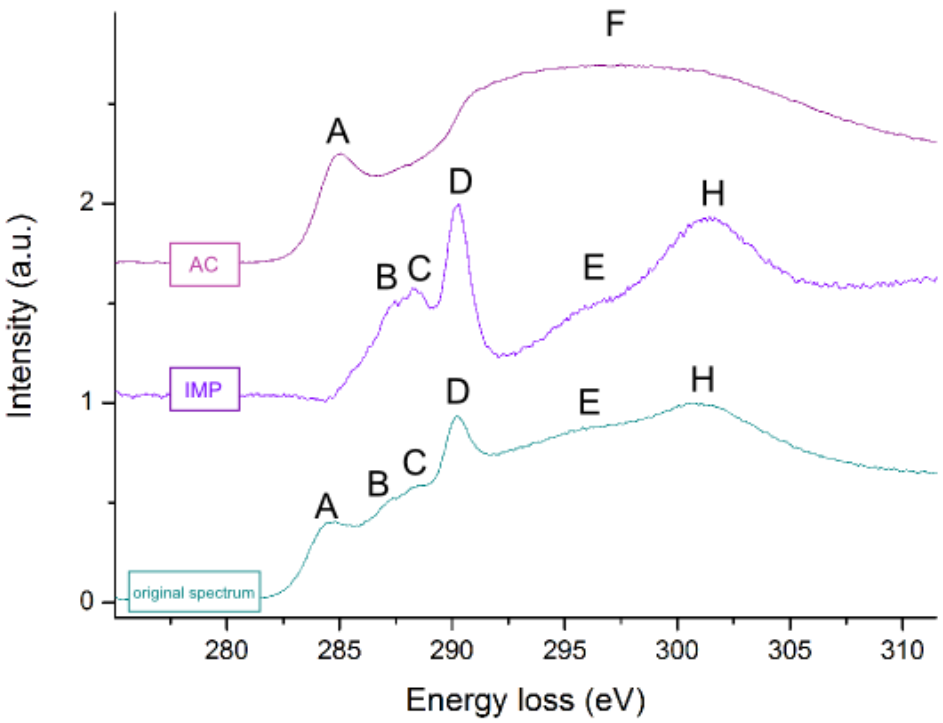


Figure 4.4 The original calcite impurity carbon K-edge spectrum acquired from a crystal grain deposited on an amorphous carbon film, accompanied by the amorphous carbon film (AC) and impurity (IMP) spectra reconstructed by the ICA method.

The impurity spectrum (IMP), in comparison to calcite (CAL), displayed additional double peaks B and C at ~287 and ~288 eV, respectively. Peaks E and G, seen in calcite, were barely visible in the impurity spectrum and peak H was shifted towards lower energies.

Peaks B and C observed in the impurity were assigned to 1s→π*states transitions of carboxyl and carbonyl groups, which are often connected with organic material in XANES studies [200–202]. Previous EELS studies of aragonite and calcite did not record peaks B and C [199], while XANES studies show the presence of peaks B and C, and attributed their origin to the surface contamination or surface states [203]. In the present study, the presence of peaks B and C might be also an artefact of the ICA signal processing.

The most distinct peak in calcium carbonates (D at ~290eV) originated from core 1s transitions to the vacant π*-A states of CO_3 groups [177,204]. Peaks E (CAL, IMP) and G

(CAL) were assigned to carbonate 1s→σ*-C and π*-C transitions [178,203]. Peak H resulted from the main 1s→σ*-A transitions [178,203].

Carbonated HA (CHA) exhibited four peaks: A at ~285 eV, D at ~290 eV, F at ~297 eV and H at ~302 eV. The low signal-to-noise ratio of CHA carbon K-edge arose from an effect of a relatively low carbonate content and the low dose exposure condition used. Pure calcium phosphates (HA and bTCP) exhibited no carbon signal or a weak signal corresponding to amorphous carbon, which could be attributed to impurities introduced during preparation of standards or accumulation of mobile carbohydrates originating from the carbon support film (data not shown). The amorphous carbon (AC) film spectrum was added to Figure 4.3 as an example of amorphous carbon impurities recorded in pure calcium phosphates spectra (HA, bTCP). The amorphous carbon edge consisted of two peaks a sharper one A at 285 eV, characteristic for core electron transitions from 1s to vacant π*states, and a broad peak F at ~297 eV, characteristic for 1s→σ* transitions in the carbon-carbon bonding environment [204].

Peak D is a peak characteristic of the presence of carbonate ions (Figure 4.3) [204,205]. Analysis of the carbon K-edge alone is not sufficient to distinguish between calcium carbonate and carbonated hydroxyapatite [179], as the carbonated hydroxyapatite spectra hold a strong resemblance to edges collected from calcite and aragonite and may be approximated as a superposition of features visible for amorphous carbon and calcite. The presence of the D peak provides a good confirmation of carbonate ions in the material.

4.3.3. Calcium $L_{2,3}$-edge

Calcium $L_{2,3}$-edge spectra were aligned and normalised to the peak B, which was set to an energy-loss of 348 eV based on literature [180].

The calcium $L_{2,3}$ ELNES (Figure 4.5) consisted of two principal sharp peaks: B at ~348 eV and D at ~350 eV , corresponding the spin-orbit split L_3 and L_2 edges, respectively [206,207]. In calcite (CAL), two additional, smaller peaks A and C were observed at ~346 and ~350 eV, respectively.

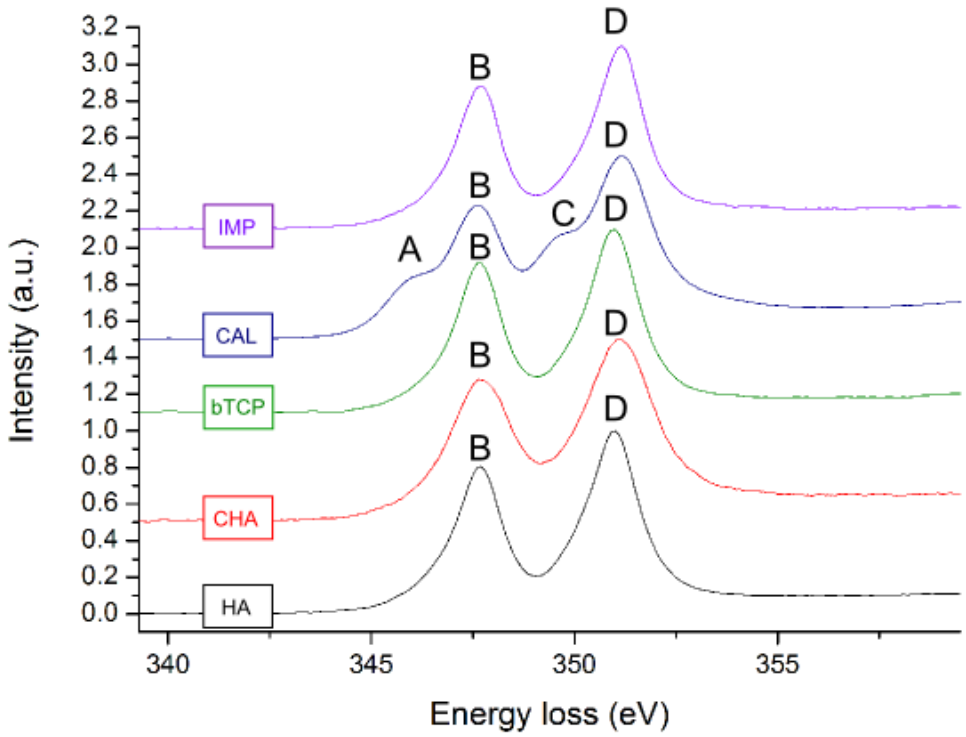


Figure 4.5 Calcium $L_{2,3}$-edge structures of hydroxyapatite (HA), carbonated hydroxyapatite (CHA), beta-tricalcium phosphate (bTCP), calcite (CAL) and impurity (IMP). All specimens displayed two peaks B and D characteristic to calcium L-edge. All minerals containing carbonate groups showed a small shift of peak D towards higher energies in comparison to pure calcium phosphates (HA, bTCP). Only CAL displayed additional peaks A and C characteristic of multiplet splitting.

In the calcite spectrum each of the principal peaks (B, D) was split, creating additional, smaller peaks (A, C), as a result of the crystal field splitting [7,181,199]. These features were observed in the calcite spectrum due to the highly symmetric calcium coordination environment. In calcite, calcium atom is in octahedral configuration with six oxygens; in aragonite, calcium is positioned in irregular environment of nine oxygens; in apatites, calcium atoms occupy two positions: one in coordination with nine oxygen atoms (Ca1), other with seven (Ca2) [181]. In apatites (HA, CHA) and impurity found in calcite, the d orbitals experienced more complex splitting resulting in finer peaks than that seen in calcite. This may result in numerous, finer peaks, which are unresolved here due to insufficient energy resolution.

Although XANES experiments showed a calcite-like split for CHAs, aragonite [181] and even HA [105], we did not observe these features. Nevertheless, some CHA species showed a slight broadening of the FWHM (around 0.3 eV), which may indicate the multiplet splitting [7,181].

Most examined minerals did not exhibit significant modifications in the calcium $L_{2,3}$-edge. Only calcite displayed distinctive features (A, C), which are characteristic of multiplet splitting.

4.3.4. Features indicative of beam damage at the oxygen K-edge

Observations of damage-related changes in the structure of the oxygen K-edge are presented prior to the discussion of the intact O K-edge structures, as the damage peak X was used to align oxygen spectra.

Changes observed in the oxygen K-edge structure are connected with two damage events. In the first event, minerals exposed to total electron doses above 10^4 electrons per nm^2 exhibited a characteristic peak X at ~530 eV. In the second event, calcium phosphates exposed to doses above 10^5 electrons per nm^2 showed the transformation of the oxygen K-edge structure into spectra consistent with calcium oxide features.

For doses exceeding 10^4 electrons per nm^2 [193], many minerals exhibit strong peak X at 530 eV (HA damaged, CAL damaged, Figure 4.6). Peak X is a sign of damage induced by formation of O_2 oxygen molecules [208] or other forms of oxygen radicals, like OH or CO, and is a good marker of early damage modifications of sample's chemistry. Some studies interpreted the X peak damage signal as the hydroxyl group or a marker of the presence of water [110,185]. However, Garvie questioned this approach and showed that a direct relation between hydroxyl or water presence and a damage signal cannot be derived [193]. The positioning of peak X does not vary with different minerals, which makes it a good calibration marker.

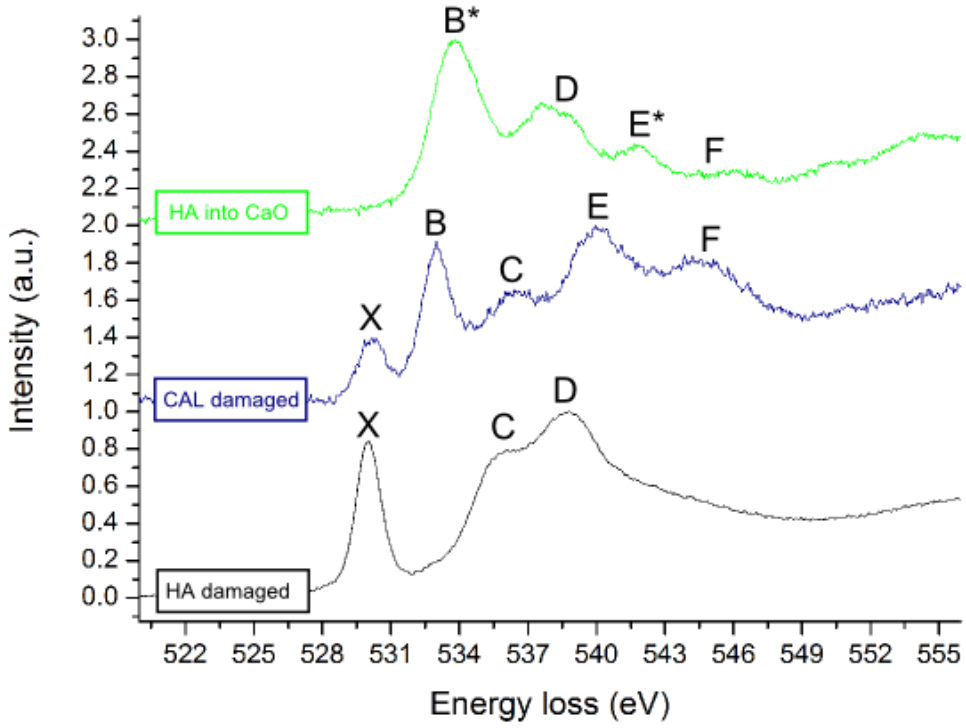


Figure 4.6 Damage markers seen in the oxygen K-edge. CAL (calcite) and HA (hydroxyapatite) display an additional peak at 530 eV when exposed to an electron dose above 10^4 electrons/nm^2. The spectrum obtained from HA exposed to an electron dose above 10^5 electrons/nm^2 (HA into CaO) is consistent with CaO spectra presented in the literature [209]. CaO exhibits new peaks marked as B* and E*. The origin of oxygen K ELNES is discussed in section 4.3.5.

Hydroxyapatite transforms into calcium oxide after prolonged exposure to the beam radiation [210]. This transformation occurs in apatites exposed to an electron dose exceeding 10^8 electrons per nm^2 [145]. We observed electron radiation induced damage in the HA and CHA oxygen K-edge for samples exposed to much lower doses (above 10^5 electrons per nm^2). During the transformation, formation of peaks B* and E* (HA into CaO, Figure 4.6) and decrease of peak C are observed (HA damaged, Figure 4.6). The final structure of the oxygen K-edge transformation (HA into CaO, Figure 4.6) was consistent with a pattern attributed to calcium oxide found in the literature [209].

As biominerals are prone to degrade under specific beam conditions, precautions need to be taken to preserve its structural and chemical integrity. Prolonged beam exposure leads to

modifications, such as breakdown of elemental bonds, formation and reconstruction of voids and transformations into other compounds [211].

The oxygen coordination is sensitive to beam-induced modifications, which makes it an excellent marker for the low dose damage. A total dose of 10^4 electrons per nm^2 is sufficiently low to avoid the radiation damage observed in biominerals. Nevertheless, we recommend monitoring of the oxygen edge to minimise the possibility of an unintentional damage.

4.3.5. Oxygen K-edge

Oxygen spectra were aligned using the damage peak X (see section 4.3.4), which was set to an energy-loss of 530 eV based on the literature [193]. First undamaged signal was acquired, and then acquisition was continued until a peak at 530 eV started to form. Spectra were normalised to the most intense peak of each individual spectrum.

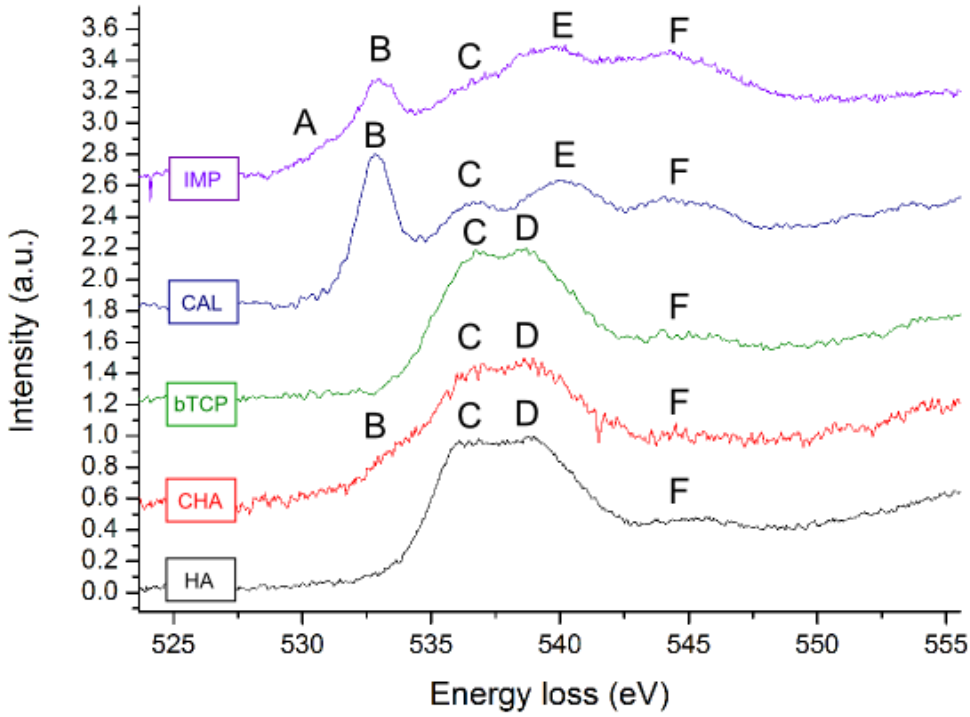


Figure 4.7 Oxygen K-edge structures of hydroxyapatite (HA), carbonated hydroxyapatite (CHA), beta-tricalcium phosphate (bTCP), calcite (CAL) and impurity found in calcite (IMP). Calcium carbonates

(CAL, IMP) display a characteristic peak B. Calcium phosphates (HA, CHA, bTCP) display a characteristic double peak C-D.

All phosphorus-containing minerals examined (HA, CHA, bTCP, Figure 5) exhibited a characteristic double peak C-D at ~537 and ~539 eV, respectively. On the high energy shoulder of peak D, a small peak F was positioned at ~545 eV. Carbonated HA exhibited an additional, low-energy shoulder B at ~533 eV.

Calcium carbonates (CAL & IMP) exhibited a pronounced peak B at ~533 eV followed by smaller peaks C, E and F at ~537, ~540 and ~545 eV. Although calcite and aragonite-like impurities showed a similar distribution of peaks, the intensity of particular peaks fluctuated. Namely, the intensity of B peak was relatively lower in IMP, while E was the highest in IMP. The impurity spectrum also displayed shoulder A at ~531 eV. The oxygen K-edge of IMP was consistent with the aragonite spectra reported in the literature [199].

Literature on the oxygen K-edge configuration in calcium-containing minerals is limited. Transitions of core 1s electrons to molecular vacant π*states of carbonate are responsible for the formation of peak B, while 1s transitions to vacant σ*states result in formation of E peak at approximately 540 eV [212].

EELS and XANES studies on metal oxides suggest peaks C and D to originate from transitions to hybrid 3d calcium/2p oxygen orbitals (π* and σ*, respectively) [213,214]. Similarly, peak E and F would represent transitions to higher energy hybrid states 4s- and 4p-like [213,214]. In oxides, separation of peaks C, D, E and F should be consistent with peak separation seen in metal $L_{2,3}$-edges (calcium peaks A-D). However, such consistency was not observed in the minerals examined here, which suggested a more complex hybridisation of oxygen orbitals. For example, formation of peak D may be also attributed to hybrid phosphorus-oxygen orbital transitions, as this peak is observed only in phosphorus-containing minerals.

Previously, Gregori *et al.* [215] proposed that the pronounced presence of peak C is characteristic of HA, while a decrease in the intensity of peak C indicate presence of bTCP. We detected presence of both peaks in HA, CHA and bTCP. No significant variation in the C/D intensity ratio was observed.

In CHA, the C-D double peak is preceded by a broad shoulder B at ~533 eV (Figure 4.7). This shoulder corresponds to the calcium carbonates (CAL, IMP) initial shoulder and peak seen in the EELS spectra. Shoulder B observed in CHA has a low intensity, which might be attributed to relatively low amount of carbonate present in the crystal lattice.

The oxygen K-edge structure changes most significantly between minerals allowing discrimination of examined ceramics. The oxygen signal can distinguish between calcium phosphates and calcium carbonates. The presence of carbonate in carbonated HA (CHA) is confirmed by formation of peak B at 533eV (Figure 4.7).

4.4. Discussion & conclusions

We have shown that EELS can be used to detect the presence of carbonate ions in the apatite lattice and can be utilised to differentiate between calcium carbonates and apatite, by comparing the carbon and oxygen K-edges edges. Observation of EELS spectra did not reveal any features, which might indicate the carbonate substitution sites (*i.e.* preference for the A or B site) in carbonated apatite (CHA).

Discrimination between calcium phosphates (HA, CHA, bTCP) and calcium carbonates (CAL, IMP) can be performed directly *via* observation of the oxygen K-edge (Figure 4.7). The oxygen edge also provides sufficient information to discriminate between carbonate polymorphs: calcite and impurity found in calcite. EELS was also capable of detecting small amounts of carbonate present in HA by observation of the carbon and oxygen K-edge features. However, we were not able to distinguish between HA and bTCP.

Calcium phosphates exhibited the presence of a characteristic double peak at ~537 and ~539 eV and the absence of a strong peak at ~533 eV, which is characteristic of calcium carbonates. Calcium carbonates might be discriminated by the presence (CAL) or absence (IMP) of the peak at ~537 eV. The presence of carbonated HA can be confirmed by mutual observation of the peak at ~290eV in the carbon K-edge and the double peak at ~537 and

~539 eV in the oxygen K-edge. CHA also displays a shoulder at ~533 eV in the oxygen edge.

In contrast, the phosphorus and calcium L-edges displayed only subtle modifications between the selected bioceramics, such as peak shifts. Changes in the separation of peaks might originate from alterations in the bonding environment caused by the differences in crystal structures and/or the presence of dopants (Figure 4.2, Figure 4.5). Due to a small magnitude of shifts and significant contribution of noise observed in phosphorus and calcium edges, these results should be treated with caution.

The main limiting factor in EELS studies of biominerals is their relative susceptibility to beam damage, like oxygen ionisation. Some studies neglected the importance of damage study [110]; studies, which do consider damage, do not report the acquisition conditions in a reproducible manner [122]. Here, we described the most characteristic damage markers observed in the oxygen K-edges and their threshold conditions. Selection of appropriate experimental conditions is crucial to reduction of possible damage, while maintaining a high signal-to-noise ratio in the same time to distinguish between different species.

Investigation of smaller features and/or mapping fine changes in the edge structure is very challenging even with the beam conditions optimised according to the guidelines presented in this chapter. If a satisfying signal-to-noise ratio could not be achieved for an electron dose below the damage threshold, the PCA processing methods may be employed to filter the noise component out and enhance the original signal.

If the examination of small structures (<10nm) is not the primary objective, the most effective way to minimise damage is to raster the beam over large areas (i.e. 100x100nm^2). Each data pixel should be collected within a small timeframe to minimise the electron dose. Next, spectra obtained from each pixel should be added to increase the signal-to-noise ratio. As the information about the spatial distribution of various components will be lost, this approach will be most suitable to investigate the bulk of mineralised tissues.

Electron interactions may cause damage and should not be neglected in work with EELS. As more and more studies recognise the significance of damage issues and undertake appropriate measures to prevent them, they are often omitting to report the most reproducible

experimental conditions [122], such as electron dose, fluence or current, which can be directly connected to damage processes and easily monitored. Beam damage can be minimised by adjusting microscope settings (i.e. voltage, electron dose, exposure time) to operate below the damage threshold of material. We have reported these instrumental values here and established some operating guidelines for performing EELS on calcium-based ceramics.

EELS is an optimal technique capable of revealing chemical changes in bioceramics at the nano-scale level. Application of this method opens the possibilities for development of more detailed mineralisation models and will be useful in studying of tissue/implant interfaces *ex vivo*. The understanding of the time-dependent evolution of mineral chemistry and morphology in tissue will help in designing more biocompatible ceramics for bone grafting. Similarly, knowledge about nano-scale changes introduced into pathological tissues will result in therapies targeting the origins of the disease rather than just the macro-scale symptoms.

5.
COMPARISON OF MINERALISING TISSUE ULTRASTRUCTURE AT DIFFERENT TIME POINTS IN A TURKEY TENDON MODEL

5.1. Introduction

For over 50 years, turkey leg tendon has aroused interest as a biomineralisation model [216]. Turkey tendons start to ossify from the 11th week of the turkey's life. The ossification proceeds in the tarsometatarsal joint region at the bone-tendon interface and progresses towards proximal regions [217], to reach full mineralisation at 22nd week (Figure 5.1). Age- and site-specific evolution of mineral make turkey tendon an interesting model to study stages of the biomineralisation processes in collagen type-I tissues

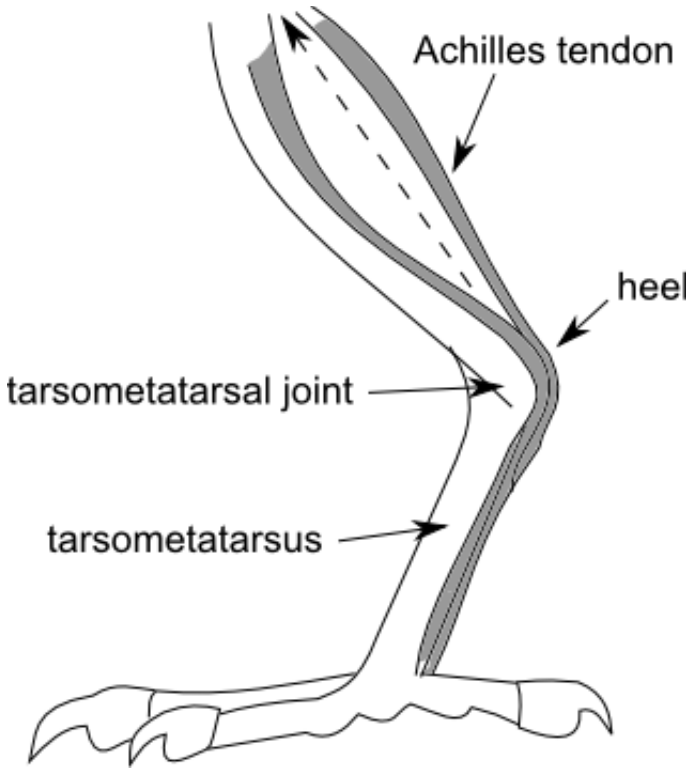


Figure 5.1 Schematics showing a turkey leg with tendons (grey).The mineralisation front proceeds in the direction indicated by the dashed arrow.

In turkey tendon, collagen fibrils grow in diameter with age [218]. Over time, the number of immature crosslinks decreases and mature pyridinoline crosslinks are formed [61]. These changes are correlated with an increase of the matrix activity of metalloproteinase (MMP) and an increase of collagen thermal stability of collagen type I [61].

The mineralised tendon, observed by light microscopy, is composed of fibres fusing into irregular, over 100µm-wide beams [104,219]. At the nano-meter scale, non-mineralised, partially and fully mineralised regions can be encountered in close vicinity [13]. The mineral encountered in turkey tendons, in the early mineralisation stage, is described as amorphous calcium phosphate (ACP), and the mineral in the advanced mineralisation stage is described as crystalline apatite [104].

There are two types of mineral formation observed at the early stage of mineralisation in turkey tendon. In the first type, large (~150nm in diameter), extracellular, amorphous mineral vesicles transforming into globules, granules or clusters of misaligned crystallites are observed [23,104,220]. It is suggested that vesicles attach to the collagen fibril and form

mineral globules, which act as a mineral store [18] as disorganised crystallites align within the collagen fibrils [220]. In the second type of mineral formation, groups of small (10-20nm long), scattered crystal grains are seen on the surface of the collagen fibrils [114,220]. It is not clear if these two formations are different stages of one mineralisation process, or reflect two different mineralisation pathways. Similarly, it is not clear in what form mineral is delivered to the collagen matrix: diffused ions, amorphous calcium phosphate vesicles or globules of disorganised apatite crystals.

There is a significant inconsistency in the nomenclature and description of these mineral formations in the literature. In the present study, 'vesicle' refers to a phospholipid sphere containing amorphous mineral precursors. 'Globule' refers to a large (50-150nm in diameter) mineral formation or aggregate. 'Grain' refers to a small (10-20nm) mineral formation.

Fully mineralised turkey leg tendon exhibits characteristics comparable to bone and dentin, including:

- a banding and sub-banding pattern within the collagen fibrils [13,219];
- c-axial alignment of mineral crystals along the collagen fibrils [164,221,222];
- nucleation of plate-like crystals in the gap regions of the collagen fibrils [116,220,223];
- mineral growth into intramolecular spaces in the collagen fibrils [24,220];
- an extrafibrillar crust formed from the most mature mineral crystals [17,224];
- strain-stress curves showing bone-like mechanical responses [68,104].

Demineralisation studies showed that the growing mineral has a strong impact on the collagen ultrastructure [224]. Longitudinal, previously mineralised regions lost or exhibited only a faint and disorganised banding pattern, whilst non-mineralised regions did not show any change in banding pattern [224].

Despite similarities described, it is not conclusive that mineralisation processes in tendon and bone are identical [68]. The chemical composition of collagen and mineral are usually

assessed by bulk methods, and the detailed, site-specific chemistry at the nano-meter scale is still poorly understood. In particular, changes in the chemistry of the bone-tendon and proximal-distal tendon transitional regions require further investigation [225]. Similarly, changes with age observed in the bulk chemistry of collagen and other proteins were not related to their arrangement and structure at the nano-meter scale [61].

In this chapter, the evolution of collagen-mineral ultrastructure and compositional variations as a function of age are characterised in the turkey tendon model and compared across three age groups; in particular, the chemical, crystallographic and morphological evolution of the mineral phase over time and the chemical and structural evolution of the collagen fibrils, especially in context of the crosslink formation, are examined.

Specific aims are:

- to develop methods of the nano-scale imaging and analysis of hard tissue using a turkey tendon model and to employ these methods in the characterisation of mineralised fibrils;
- to assess the suitability of turkey tendon as a bone mineralisation model;
- to image and analyse the distribution and chemical nature of the nucleation sites in collagen fibrils and relate their functional group to that of crosslinks;
- to characterise the chemistry and morphology of the primary mineral assemblies and observe their growth at three different time points;
- to characterise the age-dependent changes in mineral composition *in vivo*; especially to observe changes in the levels of carbonate substitution in extra- and intrafibrillar spaces.

5.2. Materials and methods

To characterise the collagen and mineral development, tissue samples of Achilles tendon were collected from turkeys of three age groups, which are predicted to reflect different

mineralisation stages: early (11-week old), intermediate (14-week old) and advanced (22-week old) [61,218]. Fresh Achilles tendon samples (Norfolk White breed, all females) were acquired from the farmer. Turkey tendon samples for TEM were prepared by both, HPF/FS and anhydrous methods, to ensure the adequate preservation of mineral and collagen in tissue. The tissues were not post-stained. Embedded material was sectioned, using an ultra-microtome.

Rapid (1^{o}C/ms) cryofixation of 0.5mm-thick samples was performed in a Leica EM Pact2 machine under high pressure (2100 bars) with 1-hexadecene used as cryo-preservative. The substitution of ice by acetone solution (3% glutaraldehyde) was performed at -90°C. After 8h, the temperature started to rise steadily, until it reached 0°C in 18h. Finally, two 15min acetone washes were performed on the samples, before they reached room temperature.

In the anhydrous preparation method, small (5mm length) pieces of turkey tendon tissue were fixed and dehydrated in ethylene glycol and 3% glutaraldehyde in acetone for 24h. Fixation was followed by three 10min washes in pure ethanol and then by three 10min washes in acetone used as a transitional solvent.

For the first three days, samples were immersed successively in 1:3, 1:1 and 3:1 resin:acetone solutions for 24h. The resin was prepared from a mixture of 2.645ml of Quetol651, 3.762ml of nonenylsuccinic anhydride (NSA), 1.305ml of methylnadic anhydride (MNA) and 0.168ml of benzyldimethylamine (BDMA), (Agar Scientific, Dorset, UK). Finally, samples were placed in pure embedding resin for 7 days allowing full infiltration under vacuum. The resin was changed daily. After eight days, the samples were moved into the curing oven and heated at 60^{o}C for 48h.

An ultramicrotome PowerTome XL with an ultra 45^{o} Diatome diamond blade was used to prepare thin (70 nm) sections of embedded samples. An automated procedure was employed with cutting speeds of 0.1-1 mm/s. A specific cutting speed was selected to allow sufficient time for relaxation of a section of material taken from the bloc face. The knife was set to a 6^{o} angle to the front of specimen.

Bright-field TEM and SAED of turkey tendons were performed on JEOL2000FX and Titan TEMs operated at 120kV and 300kV, respectively.

STEM-EELS experiments were conducted on the Titan, using a Gatan Tridem EELS spectrometer. In STEM mode, a 50µm condenser aperture, spot size 9 and a 48mm camera length were used to optimise the signal-to-noise ratio. In these conditions, the collection semi-angle was 14mrad and the probe convergence semi-angle was 8mrad. The core loss signal was acquired in 10-second exposures with sub-pixel scanning and total electron doses below 10^4 electrons/nm^2 to prevent electron beam damage. Spectra were collected with an energy resolution of 0.6-0.7 eV, using an energy dispersion of 0.05-0.1 eV/channel. For these settings, the effective pixel size for the spectra was 10nm.

After background subtraction, spectra were aligned to the characteristic (usually first) peak and normalised to the most intense peak. To create intensity profiles and maps, a 20eV-wide window from the edge onset was integrated for each pixel.

Electron tomography acquisitions of the intrafibrillar mineral were taken at 2° steps from -50° to 50° on the Titan in HAADF-STEM mode (collection angles 161-681nm). 3D reconstruction was performed, using Inspect 3D processing software (FEI, Netherlands), and visualised, using Amira 3D software (Mercury Computer systems, France). A threshold Voltex projection was used to represent the bulk of intrafibrillar mineral. A solid isosurface was used to represent individual mineral platelets.

EDS spectra were acquired on the JEOL200FX, using Oxford Instruments INCA EDS system. The Ca/P ratio in turkey tendon was estimated from spectral intensities of selected elements using the Cliff-Lorimer equation [143]:

$$\frac{C_{Ca}}{C_P} = K_{CaP}\frac{I_{Ca}}{I_P}$$

Equation 5.1

Where K_{CaP} is the Cliff-Lorimer factor determined by atomic numbers, X-ray absorption and fluorescence within the sample, X-ray detector, accelerating voltage and processing methods; C_{Ca}/C_P is the calcium-to-phosphorus weight or atomic ratio, and I_{Ca}/I_P is the calcium-to-phosphorus intensity ratio. The K factor was calculated from a series of 20 phase pure hydroxyapatite standard spectra (received from Prof. Serena Best, Cambridge University).

For bulk X-ray diffraction (XRD) and thermo-gravimetric analysis (TGA) characterisation, dissected turkey tendons of all age groups (11, 14 and 22 week old) were defatted in chloroform/ethanol solutions (2:1 for 48h, then 1:2 for 48h) and dehydrated in ethanol (70%, 80%, 90% and 100%; 30min each). Tissues were ground using an agate pestle and mortar with addition of acetone to produce a fine powder. Only one sample from each age group was processed as the present study was focused on the nano-scale characterisation.

The XRD patterns were collected from prepared powders using a PANalytical® XRD XPert Pro diffractometer operated at 40 kV and 40 mA. XRD data were acquired for 2θ angles from 20° to 60°. A step size of 0.0334° and acquisition time of 52 seconds per step were used. After XRD, the samples were incinerated using a STA 449 C Jupiter thermo-microbalance (Netzsch-Gerätebau GmbH). Samples were heated to 800°C with 10°/minute step. After TGA, a second XRD acquisition was conducted and results were compared with the initial patterns.

5.3. Development of the collagen and mineral chemistry and structure over time

5.3.1. Collagen alignment and banding pattern variation with age

Examination of the turkey tendon revealed that tissues at different stages of mineralisation may be found within the same section, regardless of the age of given specimen. Figure 5.2 shows bright-field TEM images of regions of non-mineralised and mineralised turkey tendon collagen of all three age groups, respectively.

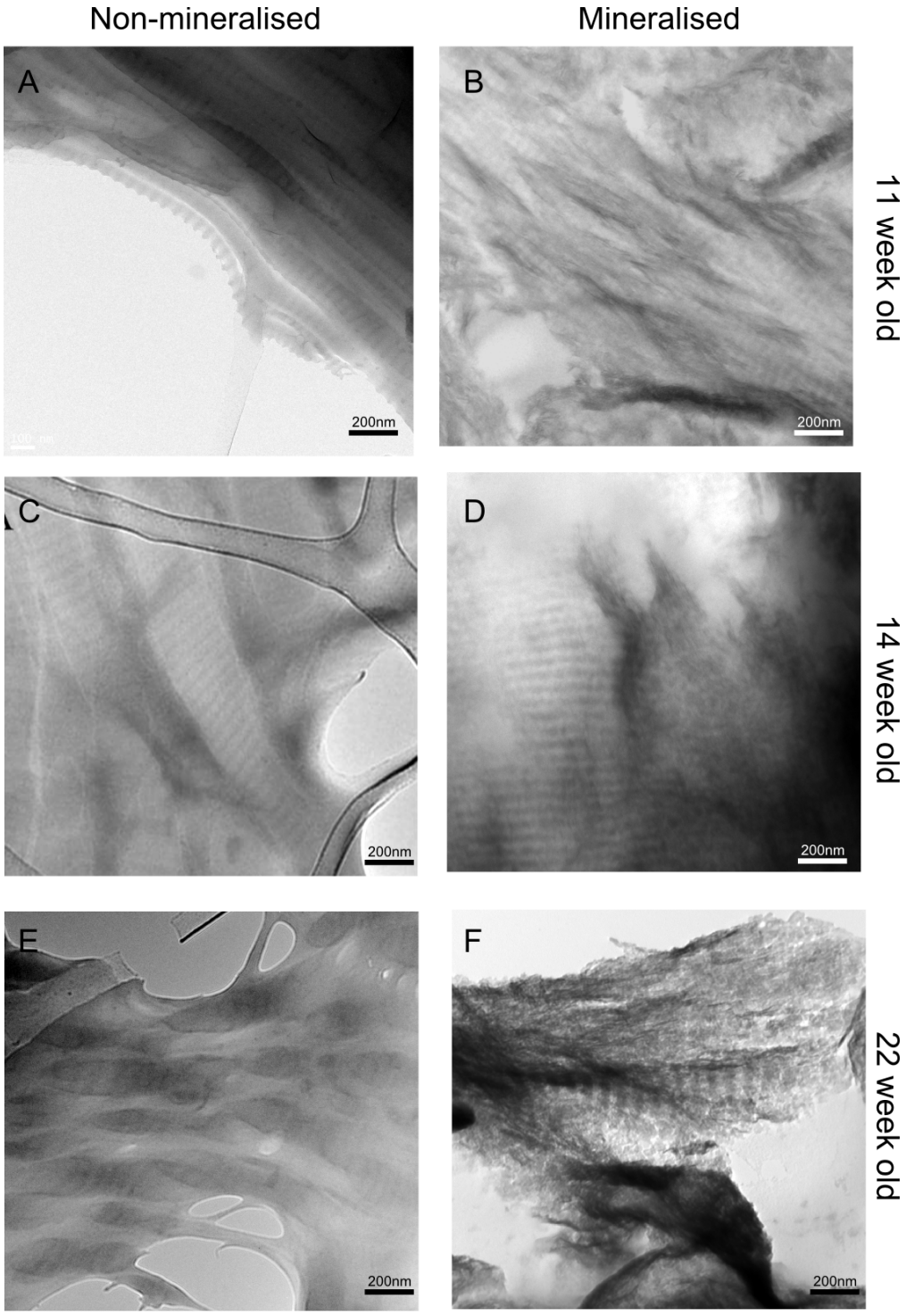


Figure 5.2 Bright field TEM images of non-mineralised (A, C, E) and mineralised (B, D, F) turkey tendon. In non-mineralised tendon, the darker contrast arises from the overlap region, which contains overlapping collagen molecules. In mineralised tendon, the darker contrast arises from the gap region, which contains mineral crystals.

Unstained tendon collagen forms regular fibrils exhibiting a clearly visible banding pattern in regions without mineral present (Figure 5.2A, C, E). Measurements of the distance between bands in turkey tendon were taken using Digital Micrograph software by taking the profiles of regions exhibiting a periodic banding pattern. Estimation of the fibrils' periodicity included measurement of the length of the gap-region, overlap-region and whole period of the collagen arrangement taken from 150 profiles. Analysis of intensity profiles drawn on long axis of fibrils (non-mineralised and mineralised) showed consistency with the characteristic D-banding (D≈67nm) pattern for collagen type I found in mineralised tissues[43,44].

For comparison of sections prepared by the freeze-substitution and the anhydrous method, 22 week old turkey tendons were selected as the mature tissue should exhibit less structural variation than a developing one. Comparison of the two methods revealed a small amount of shrinkage in the tissues preserved by the anhydrous method (Table 5.1). This might be an effect of the preparation method or may also be attributed to natural diversity in tissues. One needs also to consider the shrinking effect of electron beam on the tissue. However, the imaging conditions were identical in all acquisitions.

Non-mineralised and mineralised sections prepared by freeze-substitution showed less variation than mineralised tissues prepared by the room temperature, when the whole banding period was considered (Table 5.2). Variations seen in the gap and overlap distance can be attributed to a measuring error, originating from a weaker contrast transition in collagen devoid of mineral reinforcement. However, within the standard deviation, these differences are not significant.

Table 5.1 Length of gap, overlap, their sum and period measured separately in freeze-substituted (FS) and room temperature embedded (RT) 22 week old turkey tendon.

	Gap (nm)		Overlap (nm)		Sum (nm)		Period (nm)	
	FS	RT	FS	RT	FS	RT	FS	RT
Mean	40.2	39.6	29	27.3	69.2	66.9	66.8	65
St.dev.	3.6	3.8	3.2	3.3	4.5	5	4.8	4.5
Mode	38.9	37.3	27.1	28.8	69.3	66	66	64.3
Median	40.5	40.6	28.8	27.1	69.3	67.7	67.7	66.1

Table 5.2 Length of gap, overlap, their sum and period measured separately in non-mineralised and mineralised regions 22 week old turkey tendon, prepared by freeze-substitution.

	Gap (nm)		Overlap (nm)		Sum (nm)		Period (nm)	
	Mineral	No mineral	Mineral	No mineral	Mineral	No mineral	Mineral	No mineral
Mean	40.2	38.8	29	28.8	69.2	67.7	66.8	66.2
St.dev.	3.6	3.8	3.2	3.7	4.5	4.9	4.8	4.1
Mode	38.9	37.3	27.1	30.5	69.3	69.4	66	67.7
Median	40.5	38.9	28.8	28.8	69.3	67.8	66	66.1

Investigation of the transverse sections of turkey tendon showed that the fibrils are bundled together in a 1-2μm fibre wrapped by collagen. This external wrapping is formed from collagen fibrils aligned perpendicular to the long axis of the fibre. Figure 5.3 A-C shows this arrangement of collagen matrix in 14 week old turkey tendon.

These structures were detected in mineralised parts of tendon and were cross-compared with non-mineralised regions of tendon, where same structures have been identified (Figure 5.3D). Features seen in the non-mineralised tissue are smaller (especially when cross-sections through the fibres are seen) and less organised. Observations of smaller, less mature features in non-mineralised regions agrees with the hypothesis that the collagen matrix in turkey tendons needs to develop and reorganise itself before the mineralisation process starts [61].

The size of fibril cross-section varies from 50 to 1000 nm (100 fibrils measured). Smaller fibrils are often densely packed and each individual fibril is surrounded by a mineral crust (with less mineral inside), while larger fibrils are fully mineralised. This may suggest that the larger fibrils originate from an assembly of smaller fibrils fused in a calcification process.

Preparation of thin (70 nm) sections by ultramicrotomy may cause damage to sample film (darker lines going top-down on Figure 5.3A are knife marks). Some features on the micrographs are harder to distinguish not only because of the knife damage, but also because of the carbon support grid (Figure 5.3B, C, D), which contributes to contrast within thinner sections.

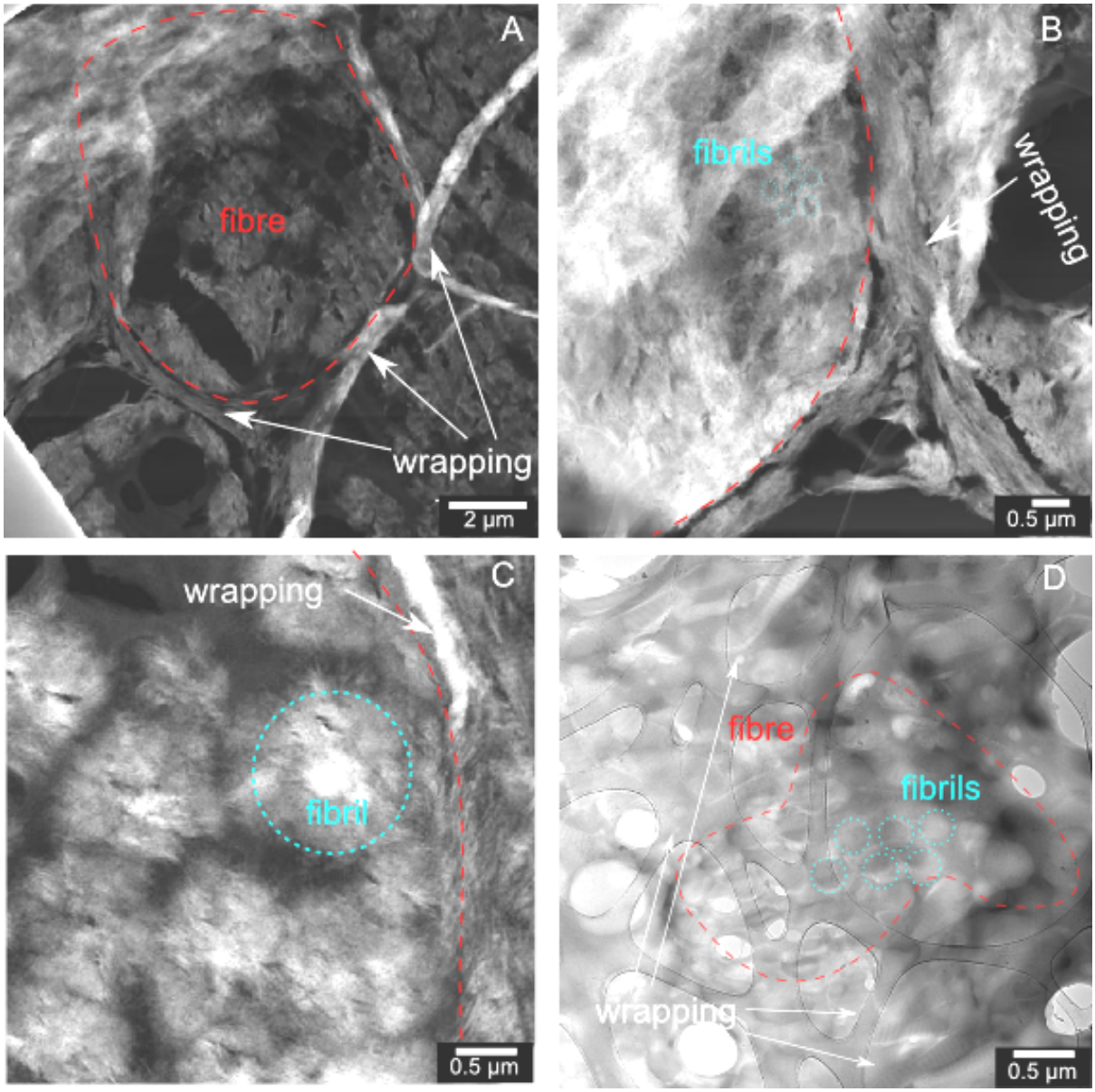


Figure 5.3 Transverse structure of mineralised (A, B, C in ADF-STEM) and non-mineralised (D in BF-TEM) regions of 14 week old turkey tendon imaged at different magnifications. Fibres (red, dashed regions) are built from smaller fibrils (blue, dotted regions) and wrapped into collagen sheets formed from collagen fibrils arranged perpendicular to the long axis of fibre. A faint periodic banding pattern is visible in the wrapping region in B, C and D.

5.3.2. The morphology and architecture of mineral crystal variations between poorly and well mineralised regions within all age groups

In **poorly mineralised regions**, circular or ellipsoidal grains were found (Figure 5.4), which resemble the mineral nucleation clusters described in *in situ* [15] and *in vivo* [71,114,220]

studies of the bone mineralisation process. The grains are usually aligned in the gap regions of collagen fibrils, forming larger clusters, or along the surface of the fibril. These formations are very sensitive to beam damage and can be easily obliterate during the imaging process which would make 3-D tomographic imaging very challenging.

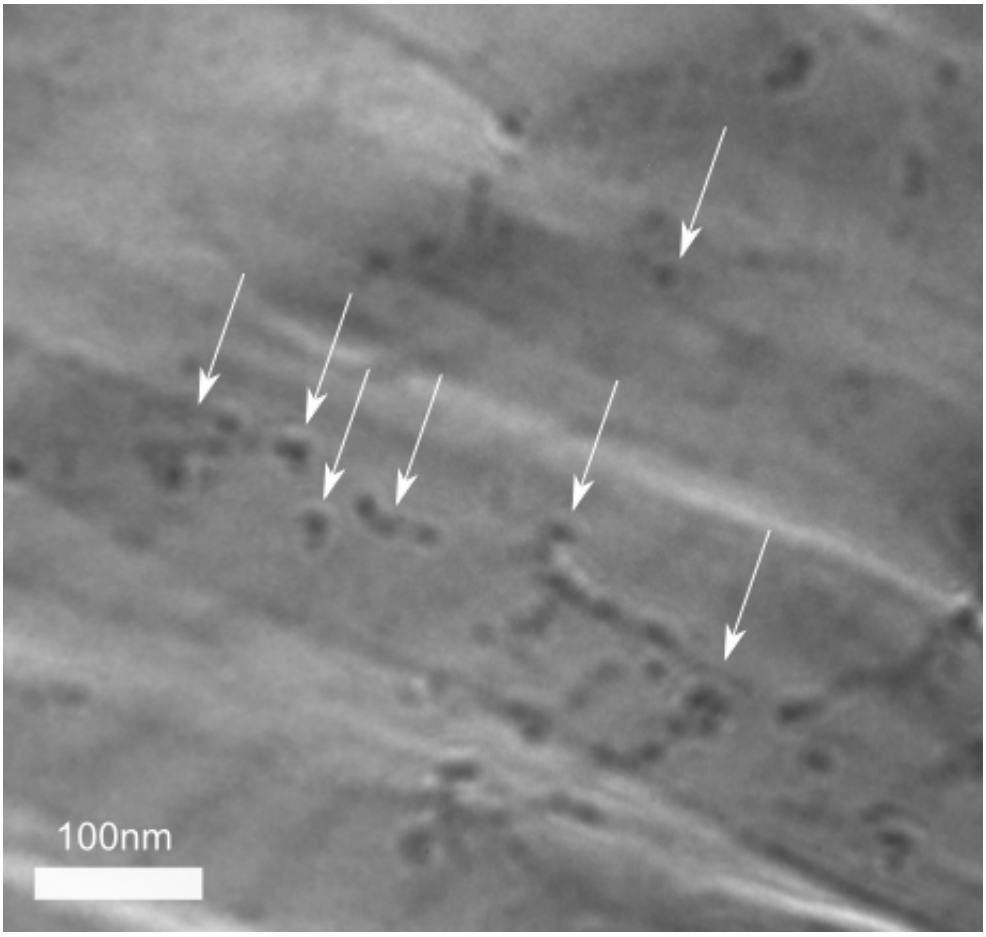


Figure 5.4 Bright-field, mass-thickness contrast TEM image of grains (indicated by arrows) associating with 11 week old turkey tendon. Grains form larger agregates and align along the gap region and along the surface of the collagen fibril.

In **well mineralised regions** of tendon, fully developed plate-like mineral crystals were found in turkey tendons of each age group (Figure 5.5). This observation has also been made in TEM studies of bone [99]. Areas of misaligned (with respect to the c-axes of fibrils) mineral crystals were often observed at the early mineralisation stage [23,220]. In the present study, globules containing misaligned apatite crystals were observed only in well mineralised parts of tissues (Figure 5.5). Mineral crystals were visible on 2D micrographs either as sharply contrasting needle-like objects or less contrasting platelets (Figure 5.6). An electron

tomography study (Figure 5.7) confirmed that all crystals develop into plate-like form and the needle-like shape of crystals seen in 2D images when plate is observed en face or edge-on, respectively.

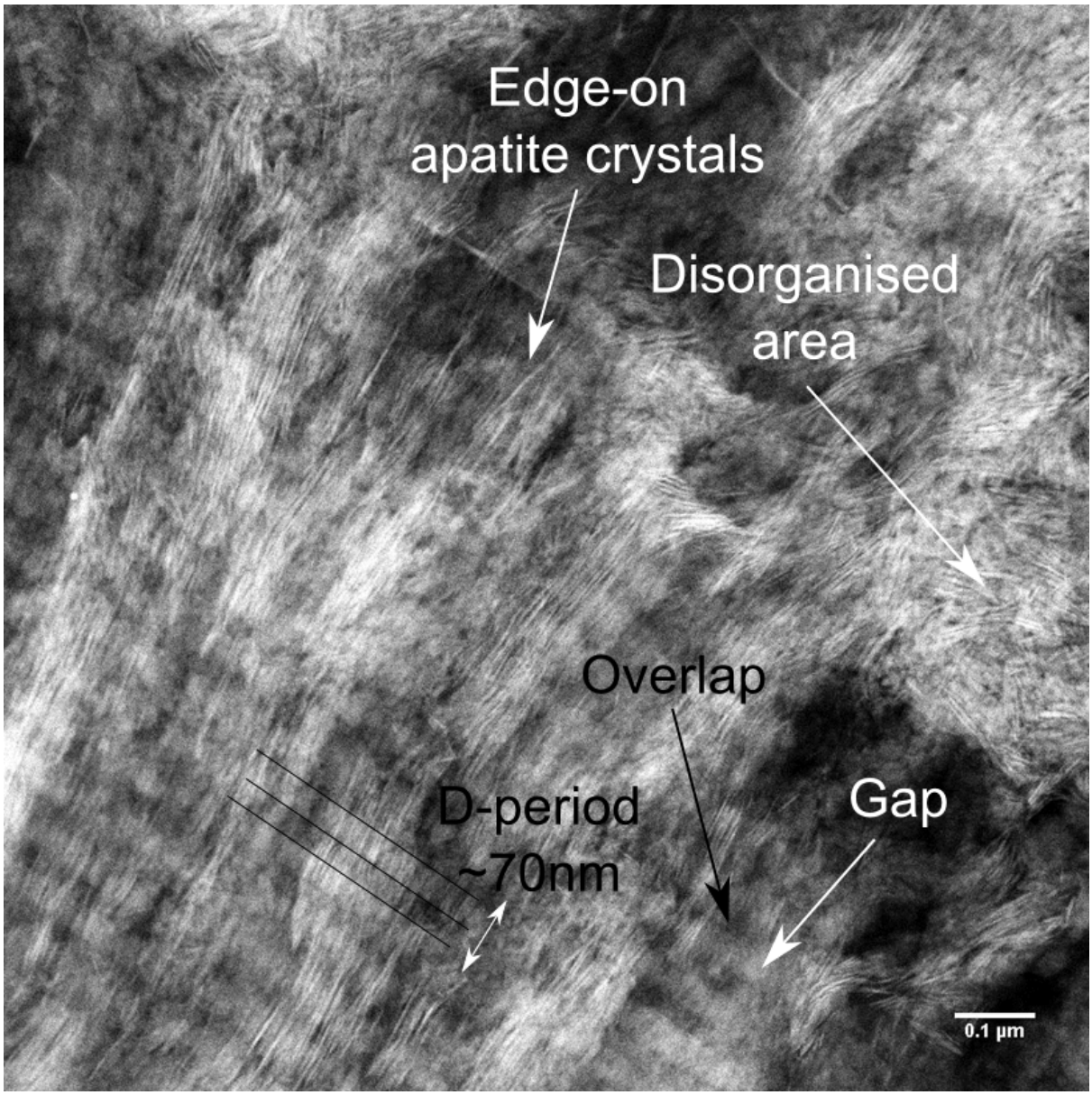


Figure 5.5 ADF-STEM image of 22 week old turkey tendon displaying features characteristic of mineralising tissues. Banding pattern with characteristic periodicity is clearly visible. The needle-like (edge-on) crystal are superimposed on banded regions. The long axes of the needles followed the long axes of the collagen fibrils. Disorganised areas were also observed, where crystals do not follow the collagen orientation, but instead form disordered globules.

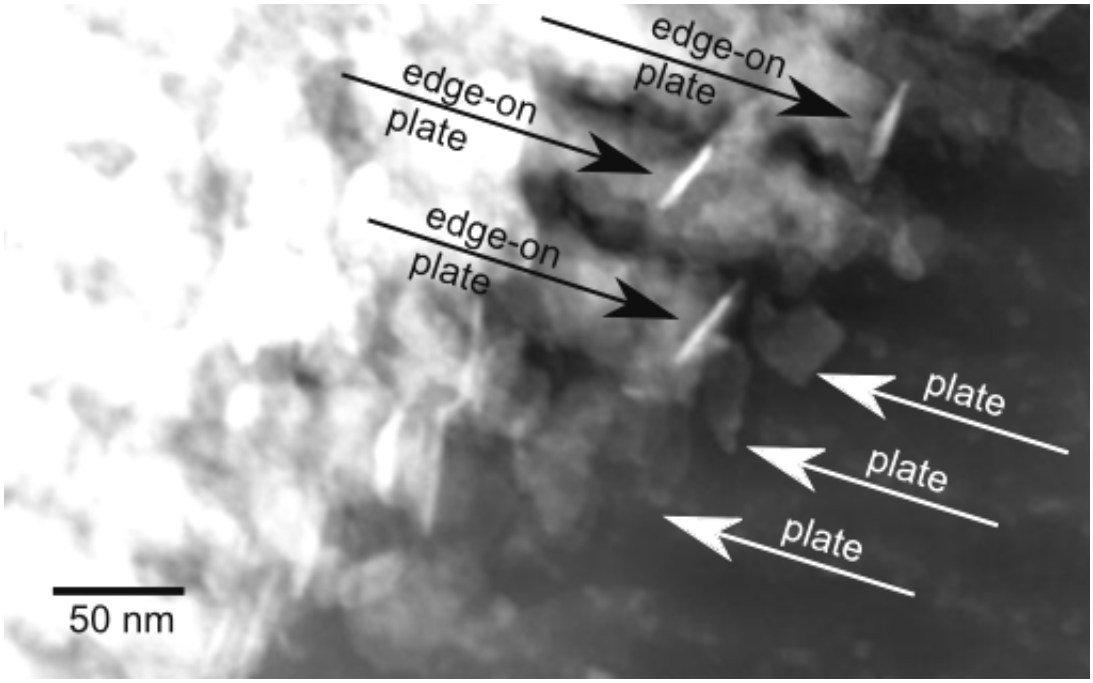


Figure 5.6 14 week old turkey tendon microtomed and imaged in ADF-STEM mode on the Titan at 300kV. The tissue cut at an oblique angle to the fibril plane revealed (possibly due to rotation of some crystals) plate-like mineral crystals and a needle-like crystals which are probably platelets oriented edge-on.

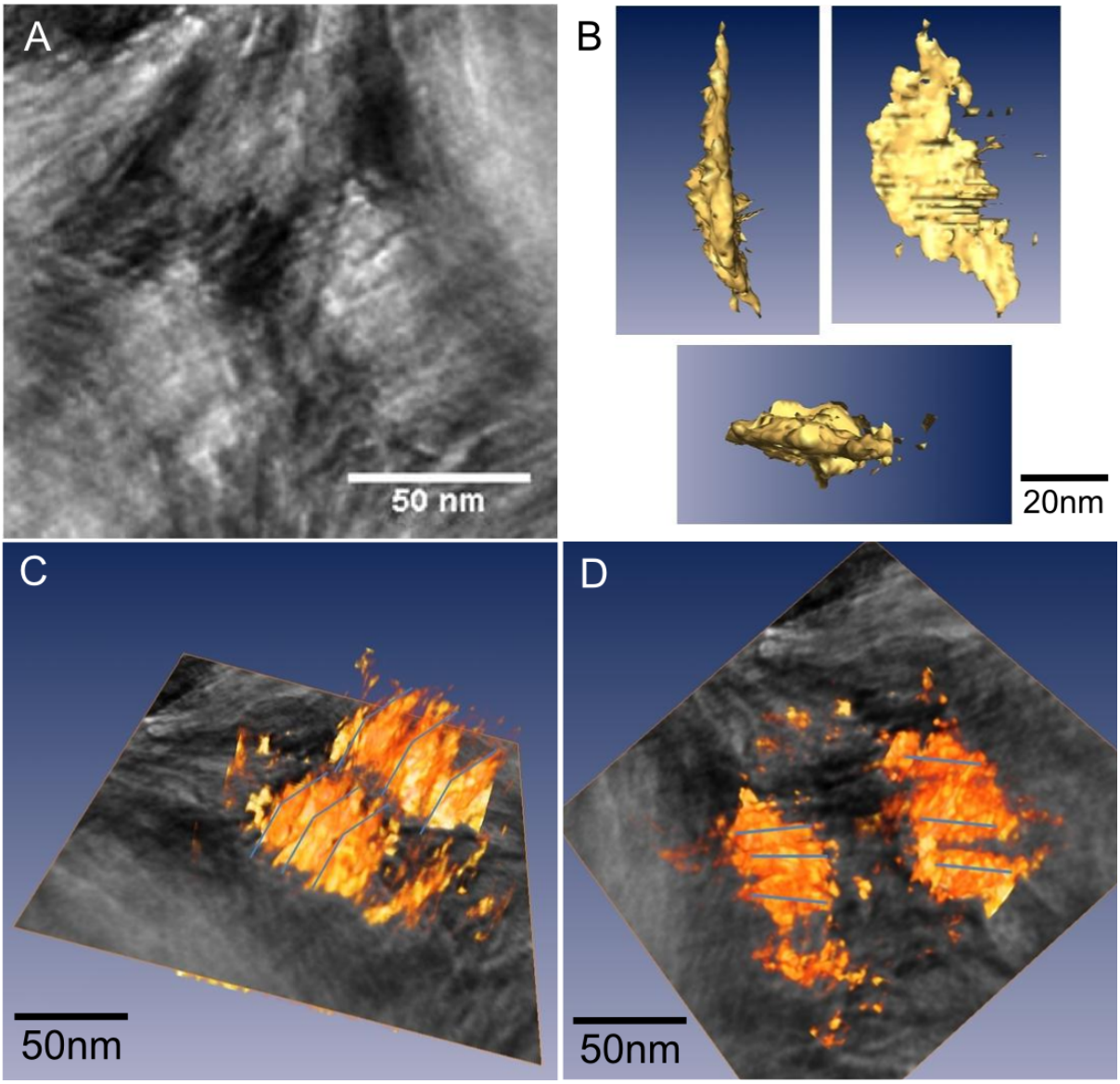


Figure 5.7 Tomographic reconstruction of a mineral plate inside the gap region of turkey tendon. Acquisitions were collected in STEM-HAADF mode from the 22 week turkey. (A) An orthogonal section through a segment of a reconstructed volume showing a fragment through a banded fibril. (B) A mineral platelet (thresholded and segmented) from within the gap region. (C, D) Reconstructed plates superimposed on slide A. The edges of the plates are marked with lines.

5.3.3. Crystallinity and phase purity variation with age

Diffraction patterns from non-mineralised and mineralised turkey tendons of all age groups (Figure 5.8, Figure 5.9), obtained *via* SAED, were cross-compared with a hydroxyapatite standard (Figure 5.10). Details about the standards are given in Chapter 4. SAED patterns are also comparable with XRD spectra collected from the bulk of the tissues (Figure 5.25, Figure

5.26). The major peaks were indexed and presented in Figure 5.9. Not all of the peaks visible in turkey tendon were observed in the HA standard. The absence of peaks in the HA standard pattern may be attributed to a random organisation of apatite crystals in the powder, as some of the reflections are highly dependent on crystal orientations. In turkey tendon, the crystals showed a high degree of texturing connected with the fibril alignment. The most distinct features are the (002) and (004) arcs, confirming that the favoured orientation along long axis of collagen fibril is in (001) direction. Diffraction patterns could only be obtained from regions with crystals present and regions devoid of crystals showed patterns characteristic to an amorphous material (Figure 5.8).

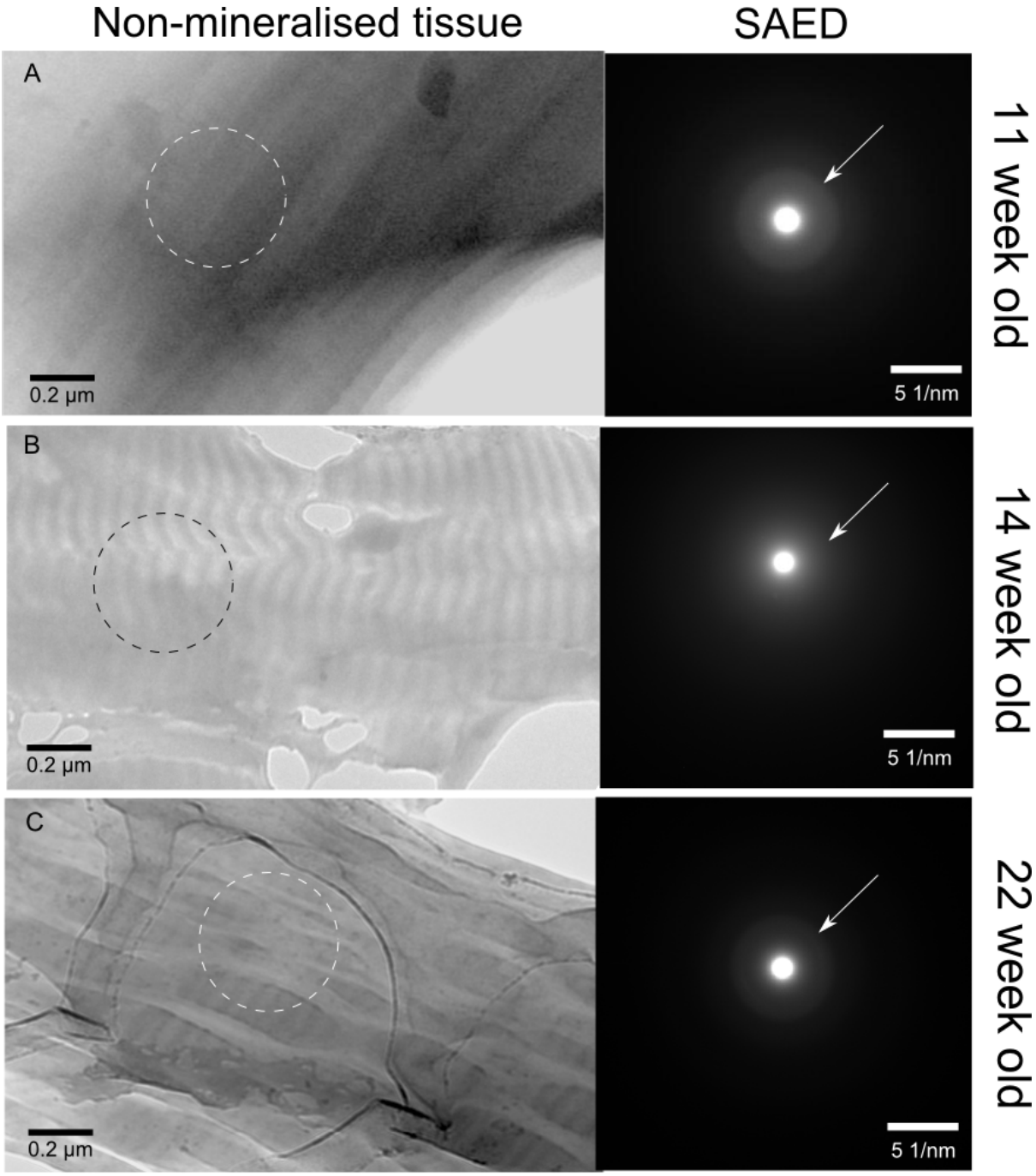


Figure 5.8 TEM image of banded collagen fibrils from non-mineralised regions of 11, 14 and 22 week old (A, B, C, respectively) turkey tendon (left) and corresponding diffraction patterns (right) collected from selected region (dashed circle) consistent with amorphous material.

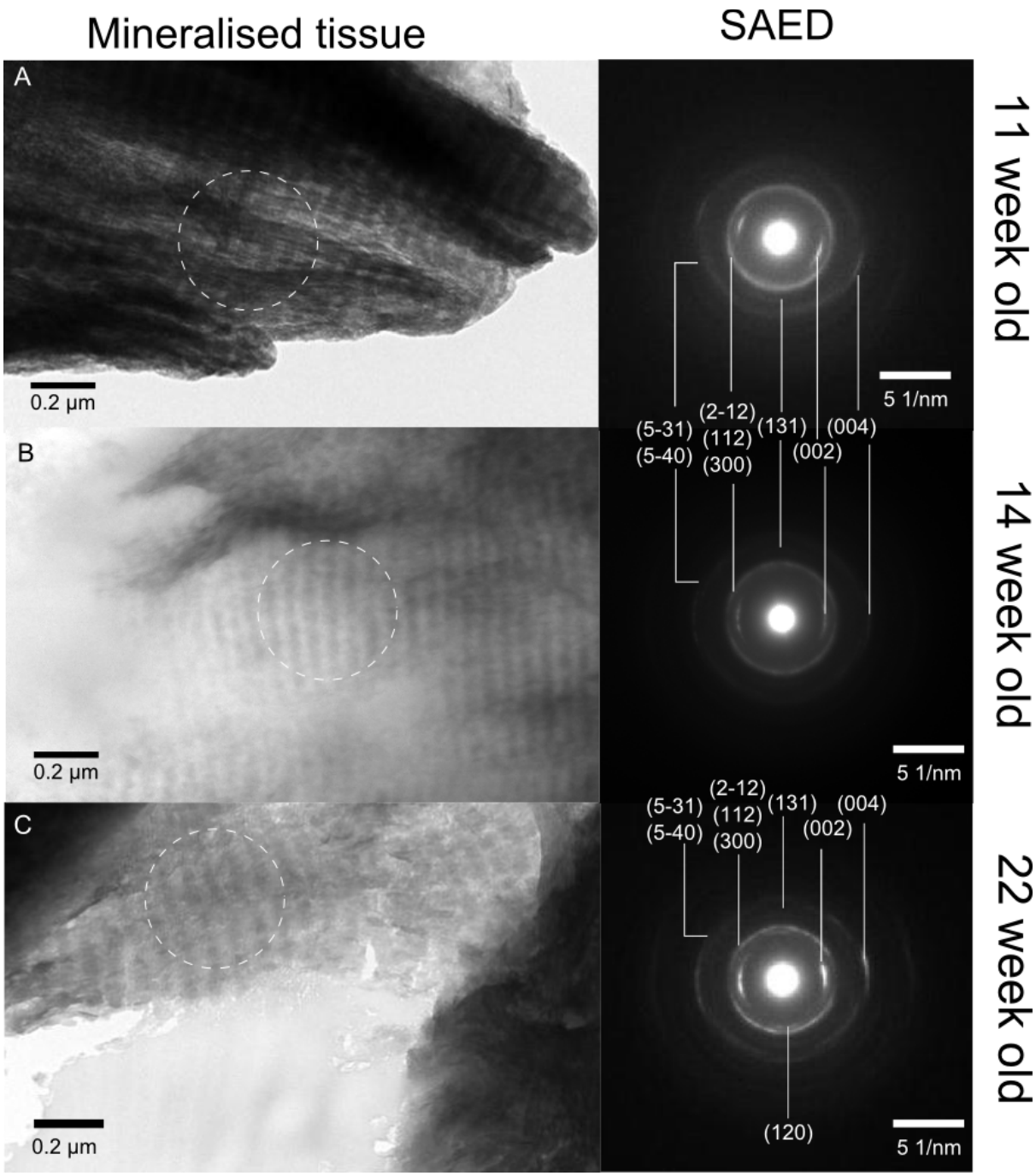


Figure 5.9 TEM images of mineralised turkey tendon (left) and corresponding SAED patterns (right; with major plane reflections indexed) collected from regions defined by the dashed circles in their corresponding images.

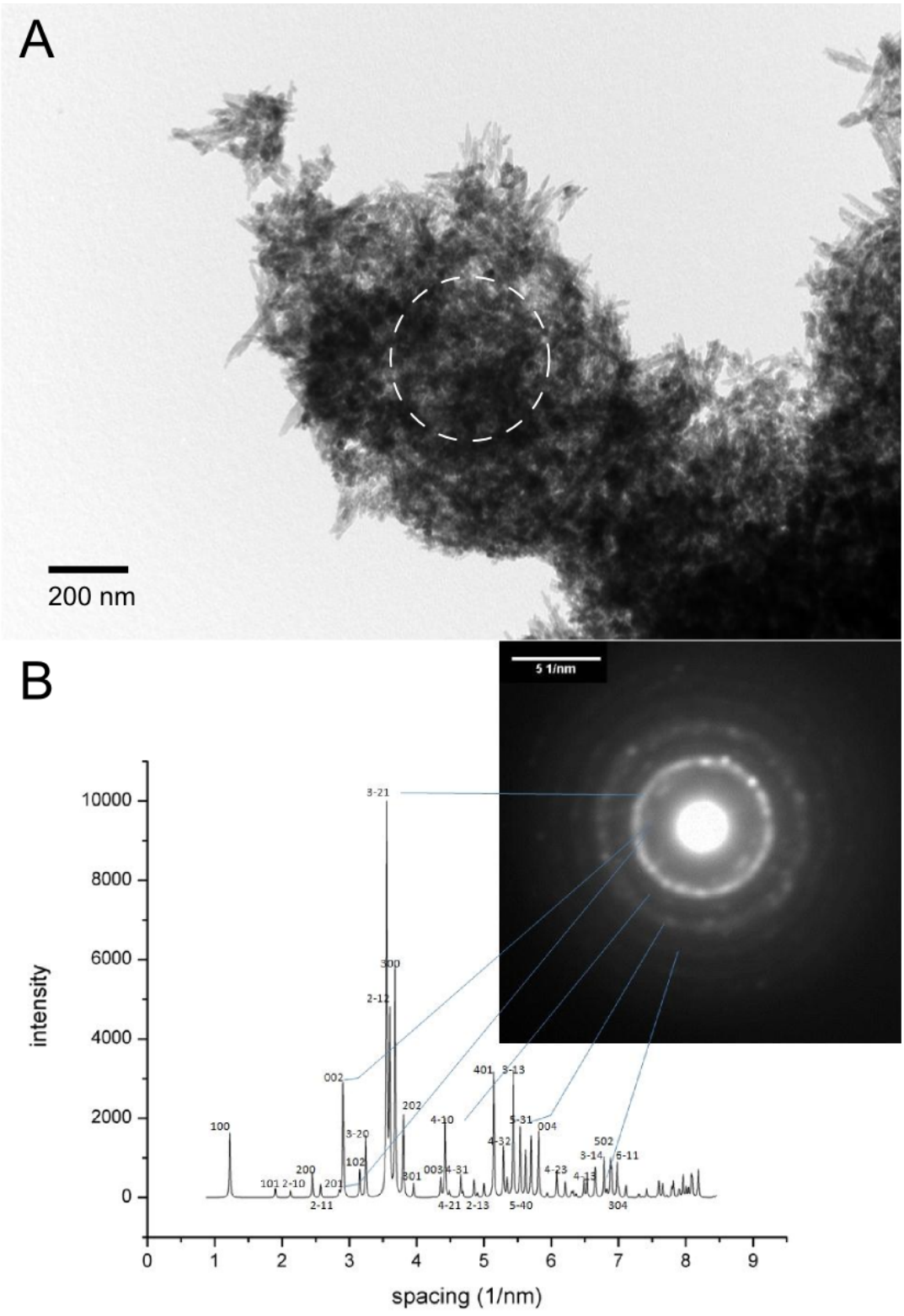


Figure 5.10 (A) TEM image of synthetic hydroxyapatite crystals. Needle-like crystals are randomly distributed in the clusters. (B) A SAED pattern obtained from selected region (dashed circle in A) indexed using a hydroxyapatite standard.

A preliminary assessment of the turkey tendon mineral and collagen revealed that turkey tendon development is very heterogeneous and regions at different stages of development can be found in each age group. Although turkey tendon calcifies with age, the actual mineralisation front is very inhomogeneous (Figure 5.11). Mineralised and non-mineralised regions (Figure 5.2) could be found in multiple locations on a single section; however, transition between these regions is often very sharp (*i.e.* there is no border region, which could be described as developing - Figure 5.11). Three types of regions at different stages of mineral development were identified in turkey tendons of all age groups: non-mineralised regions, poorly mineralised regions, and well mineralised regions.

Observations of these three regions in tissues of each age group lead to the conclusion that comparison between ages using the turkey tendon model is not ideal for studying how mineralisation of collagen changes as a function of the age of the turkey, but interestingly does highlight that mineralisation events occur very heterogeneously over time within this tissue. Nevertheless, examination of turkey tendon at different stages of mineralisation within all tissues examined (11, 14, 22 weeks), revealed details about how the architecture and chemical composition of the tissue change during the early stages of tendon mineralisation. For the EELS analysis, only spectra from selected non-, poorly and well mineralised regions from within all of the tissues were acquired.

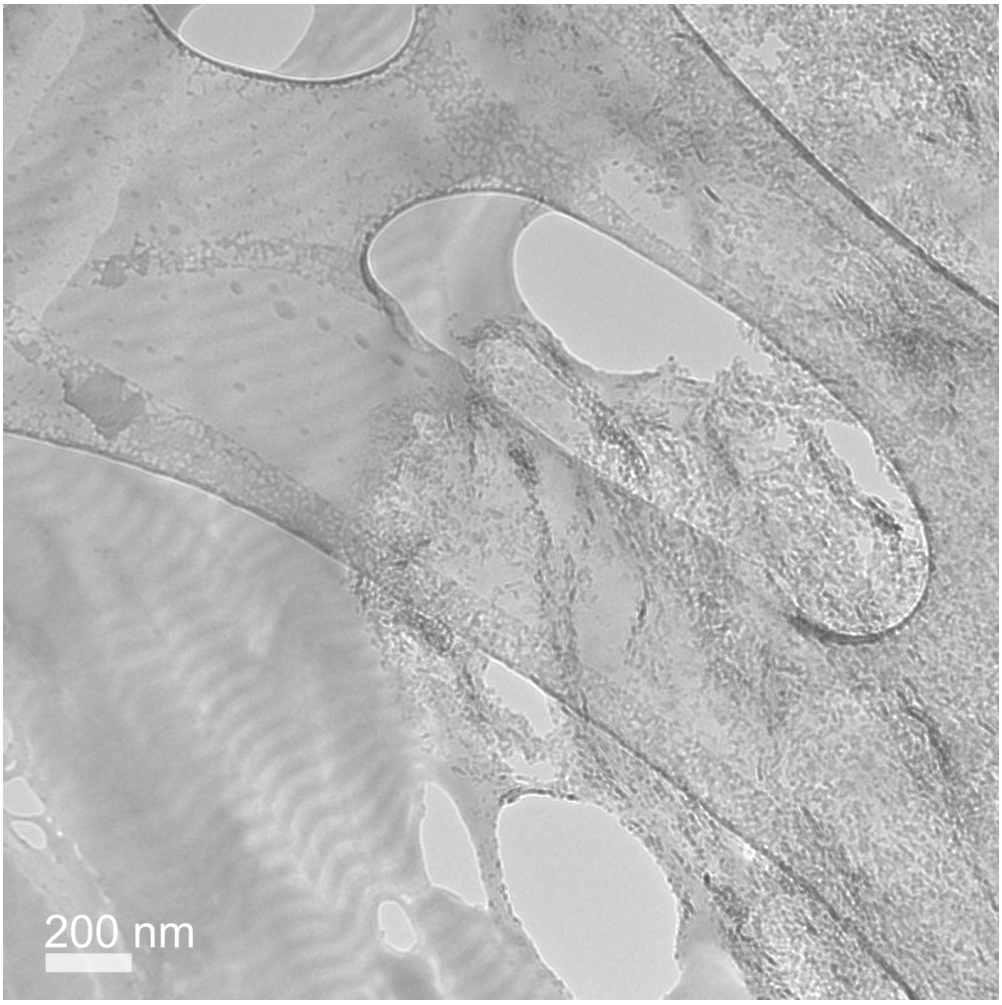


Figure 5.11 BF-TEM image of a 14 week old turkey tendon showing the transition from non-mineralised (left) to mineralised (right) regions.

5.3.4. EELS analysis of the collagen and mineral

In the **non-mineralised regions** (TN; Figure 5.12), only collagen fibrils could be seen. No mineral grains or crystals were seen. SAED patterns of these regions did not show any crystal plane reflections. There were no elements characteristic of calcium phosphate mineral visible in the EELS spectra of these regions. Collagen fibrils could be identified by the simultaneous presence of carbon, nitrogen and oxygen signals.

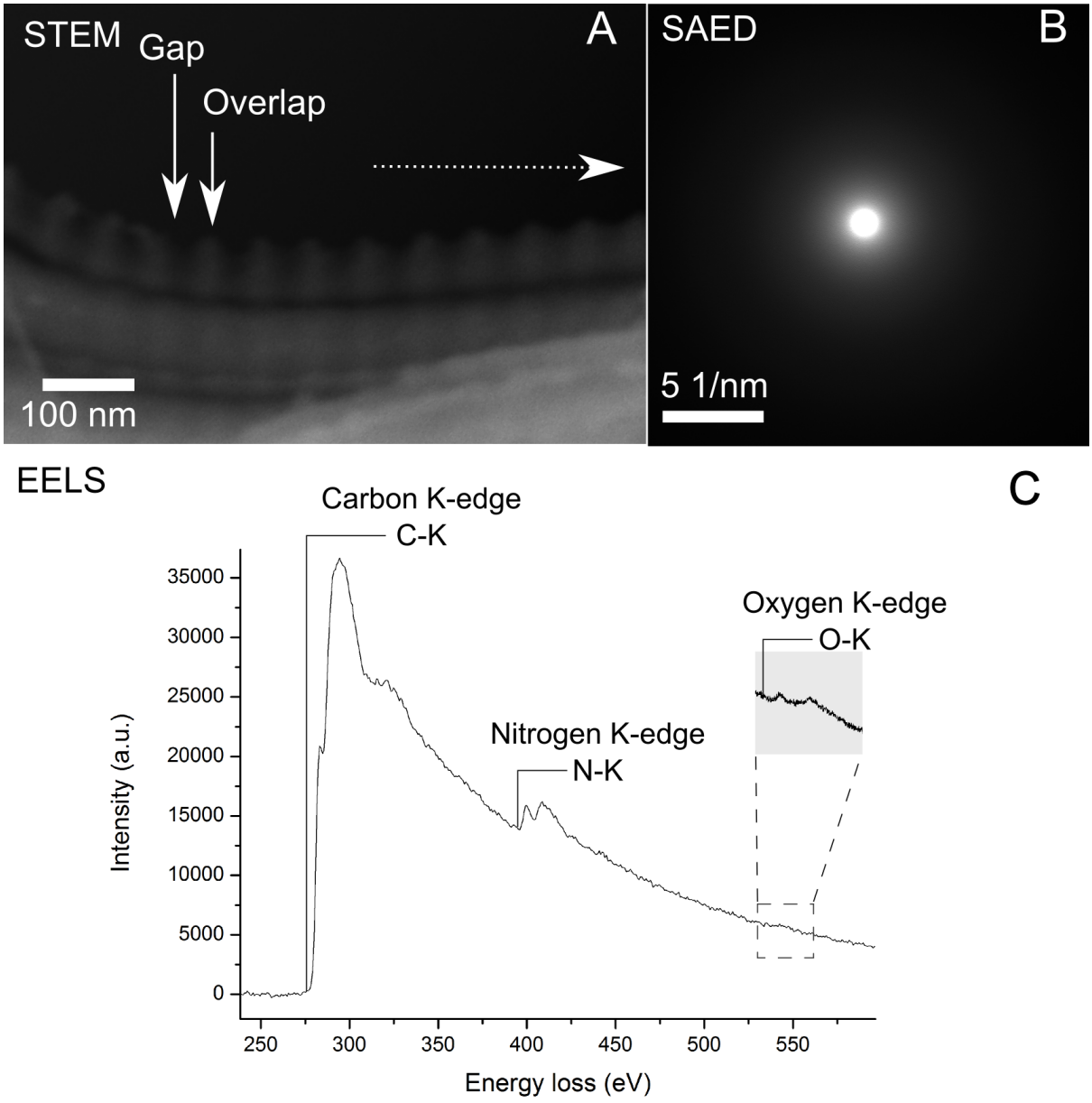


Figure 5.12 Representative features seen in non-mineralised regions taken from a 14 week old turkey (TN). (A) ADF-STEM image shows banded fibrils with mineral absent. Dotted arrow indicates the direction of the periodic banding pattern. (B) SAED shows a diffused halo characteristic of amorphous material. (C) An EELS spectrum of a non-mineralised turkey tendon collagen fibril showing characteristic carbon (starting at 285 eV), nitrogen (at 400 eV) and oxygen (at 530 eV) edges.

Poorly mineralised regions (TP; Figure 5.13) display morphology characteristic of non-mineralised fibrils. The gap regions appear brighter in ADF-STEM acquisitions. Crystals could not be seen; instead diffuse, elongated shapes were visible, which might be mineralising calcium phosphate grains (Figure 5.13A). SAED patterns taken from the poorly

mineralised regions did not show any presence of a crystalline structure (Figure 5.13B). EELS detected mineral elements (calcium, oxygen) in the gap and overlap regions of the collagen fibril, however, at very low intensity (Figure 5.13C, E, F). An increase in the calcium signal was observed from the ellipsoidal grains and larger globules. On Figure 5.14, intensity maps of calcium present in regions with globules and grains are shown. Features suggesting presence of phosphorus were also observed; however, these features were difficult to resolve due to the signal-to-noise ratio (Figure 5.13D). On Figure 5.15, regions of poorly mineralised tissue show the presence of larger globules (A) and small needle-like mineral formations (B). Significantly diffused SAED pattern collected from this region (B, insert) did not show presence of crystalline structures. The absence of crystalline SAED patterns might be explained by the relatively low signal, arising from the mineral grains, or by damage of developing crystal structures by the electron beam. However, the latter possibility is unlikely as tissues were always imaged under conditions to reduce electron beam damage.

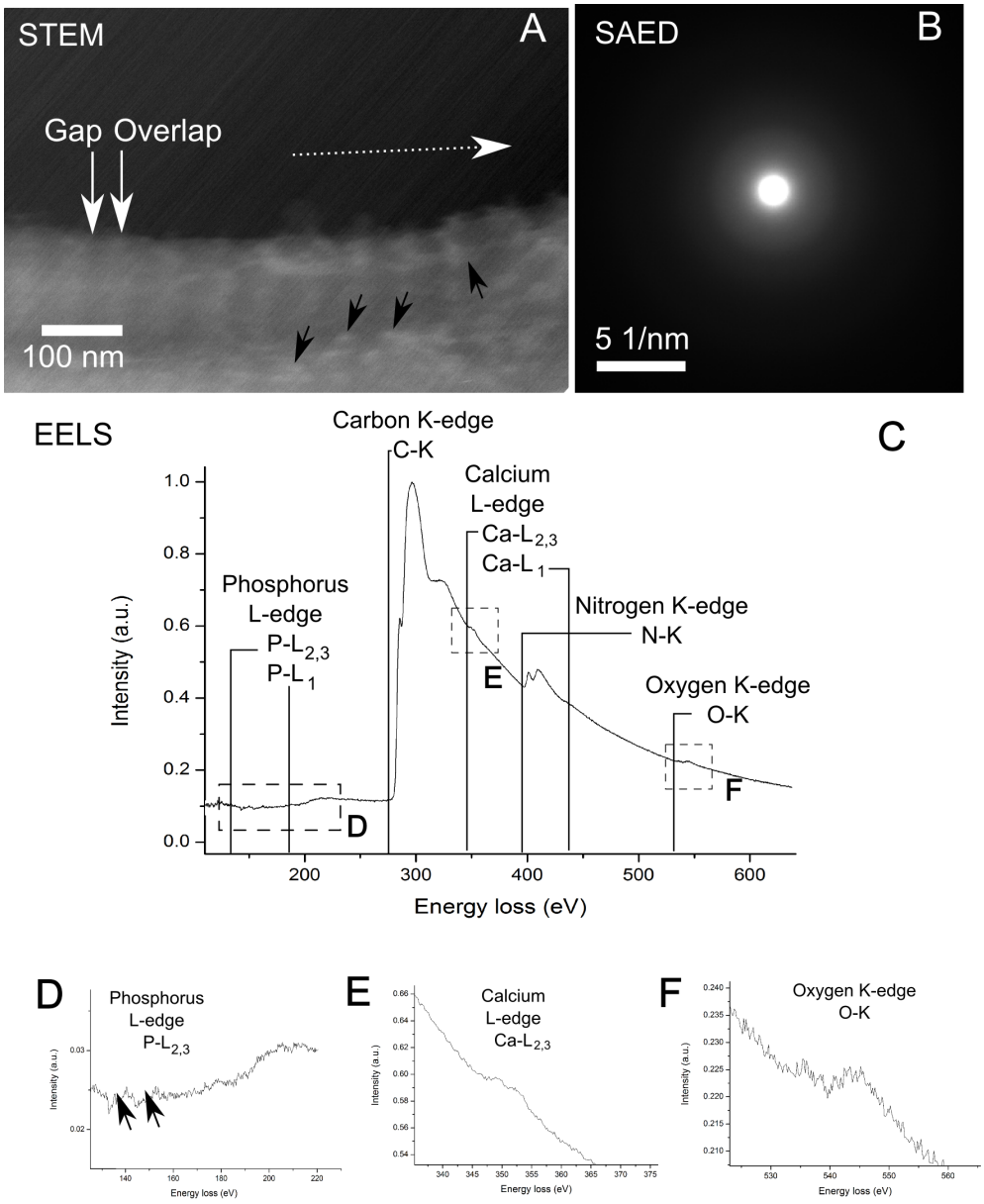


Figure 5.13 Representative features seen in the poorly mineralised regions taken from a 14 week old turkey (TP). (A) ADF-STEM image shows banded fibrils with ellipsoidal grains (black arrows). In regions with these grains, the banding contrast is difficult to resolve. The dotted arrow indicates the direction of banding. (B) SAED taken from the fibril shows a diffused halo attributed to amorphous material. (C) EELS spectrum shows presence of carbon (starting at 285 eV), calcium (E, at 345 eV) nitrogen (at 400 eV) and oxygen (F, at 530 eV) edges. The phosphorus signal (D) could not be properly examined due to the poor signal-to-noise, but irregular features (black arrows) in the spectrum between 130-160eV suggest presence of phosphorus.

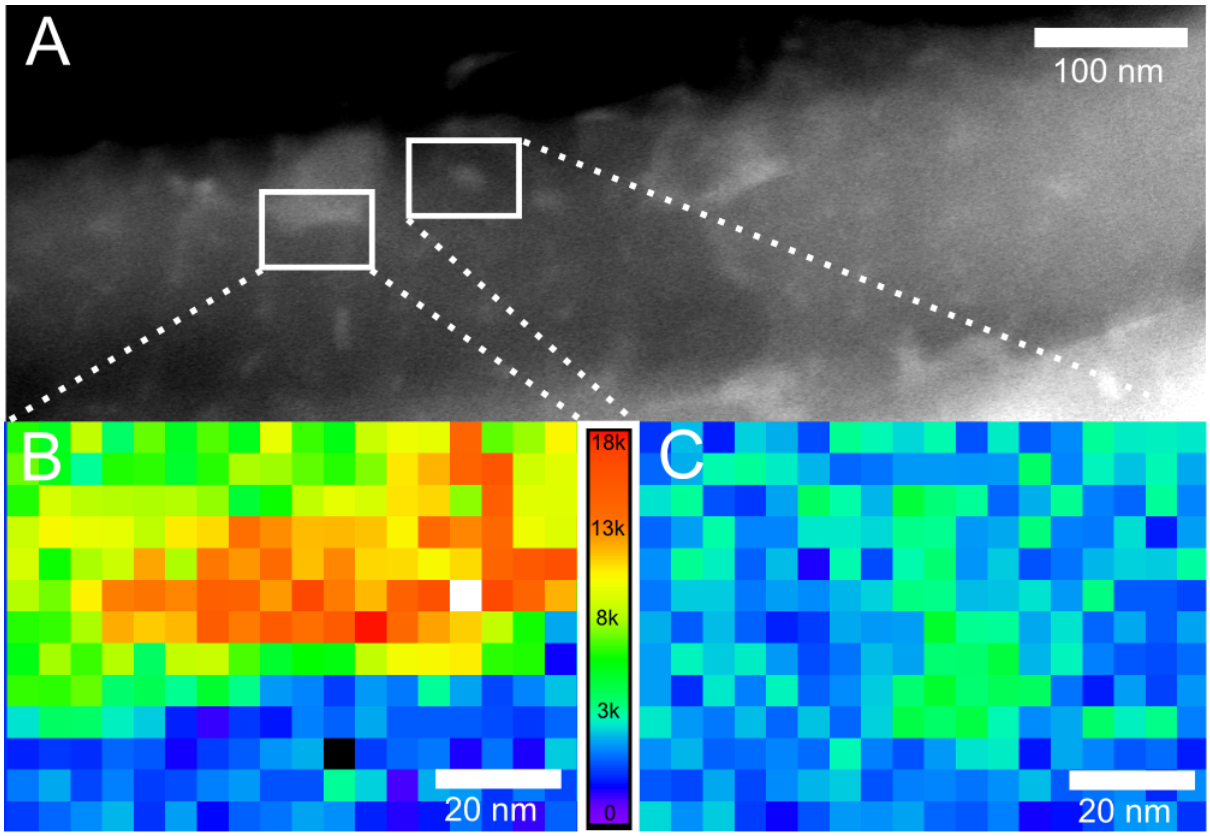


Figure 5.14 (A) ADF-STEM image of a poorly mineralised fibril showing calcium-containing globules and grains. False-colour calcium intensity map (a.u.) of (B) a large globule and (C) a single grain. Regions with higher intensities of the calcium signal are "hotter" (red and orange), while regions with low intensities are "colder" (blue and violet).

In poorly mineralised regions (Figure 5.15) at a more advanced mineralisation stage, large globules (diameter 46.1±13.8nm, n=47), are seen (Figure 5.15A), as well as needle-like crystallites (Figure 5.15B). SAED diffraction patterns display a texture characteristic of amorphous material. A diffuse ring in the diffraction pattern is attributed to the formation of multiple similar planes, here labelled as (2-12) plane in apatite.

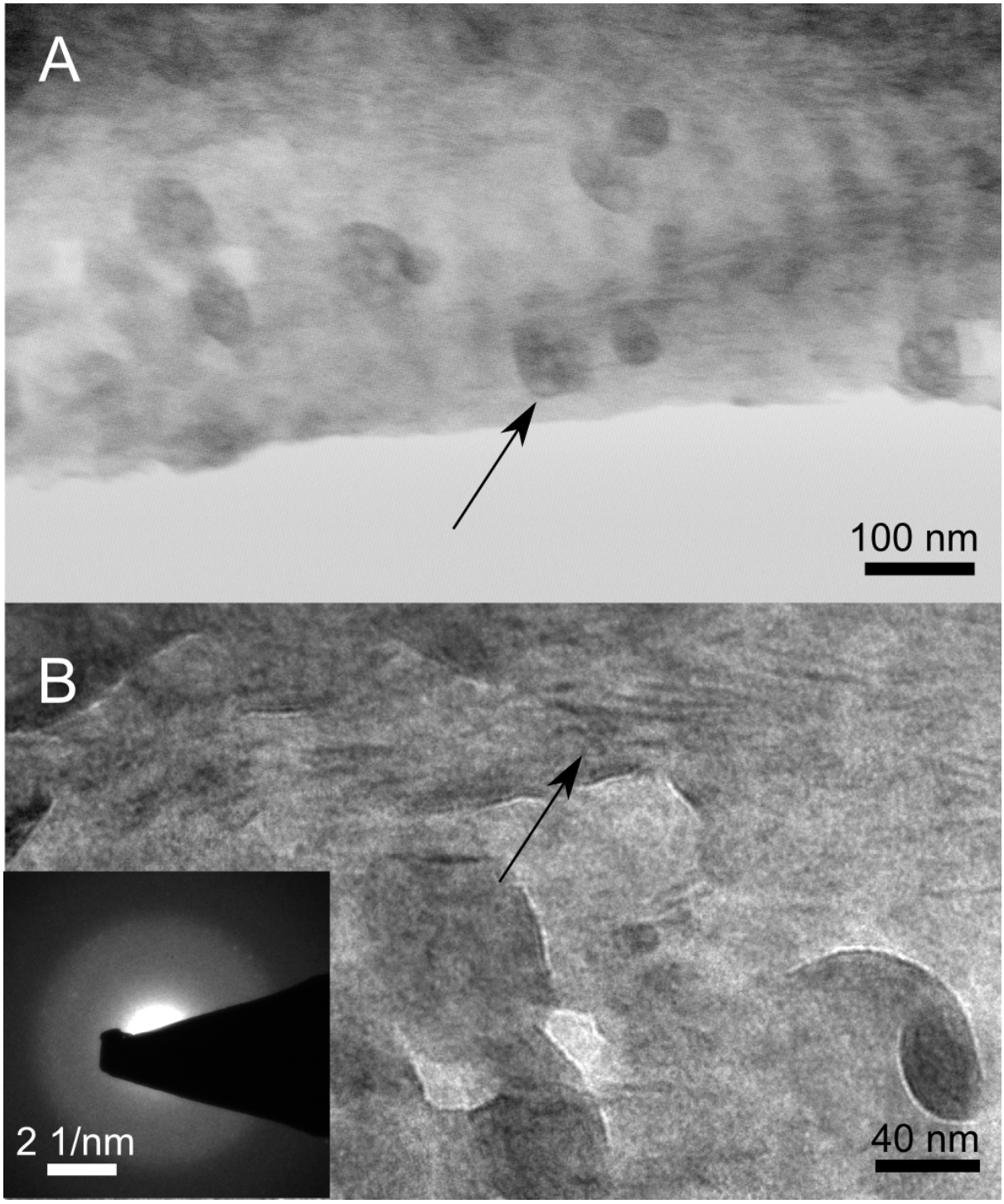


Figure 5.15 TEM images of a poorly mineralised region of 14 week old turkey tendon showing (A) large globules and (B) needle-like grains. The insert shows the corresponding SAED pattern characteristic of an amorphous material.

In the **well mineralised** regions (TW; Figure 5.16), crystals are visible and their crystallinity was confirmed by SAED patterns. These regions display strong EELS peaks for mineral elements (phosphorus, calcium). All well mineralised parts of tendon showed the presence of phosphorus, carbon, calcium, nitrogen and oxygen.

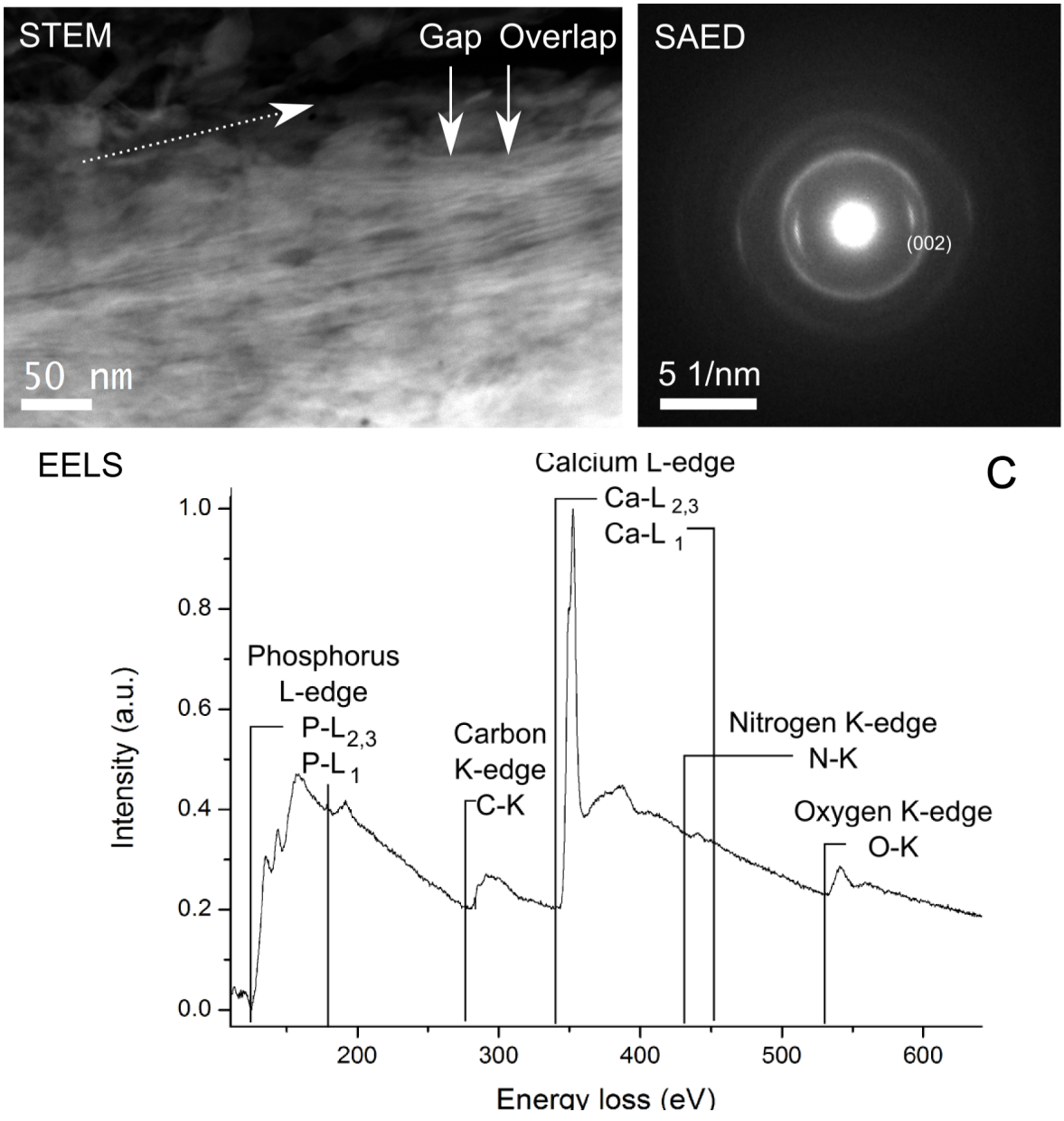


Figure 5.16 Representative features seen in well mineralised regions taken from 14 week old turkey (TW). (A) ADF-STEM image shows banded fibrils with needle-like crystals. Dotted arrow indicates the direction of banding. (B) SAED acquisition shows a ring pattern typical for apatite. The (002) plane reflections are indexed. (C) EELS spectrum shows the presence of phosphorus (starting at 125 eV), carbon (at 285 eV), calcium (at 345 eV), nitrogen (at 400 eV) and oxygen (at 530 eV) edges.

5.3.4.1. Phosphorus $L_{2,3}$-edge

Phosphorus spectra were normalised and aligned to the first peak A, which was set to an energy-loss of 138 eV based on the literature [195]. Phosphorus features, seen in well mineralised regions (TW), were compared to spectra collected from hydroxyapatite and carbonated hydroxyapatite (HA and CHA, Figure 5.17; see also Chapter 4). In each spectrum, four peaks were identified: A at ~138eV, B at ~141eV, C at ~146eV and D at ~160eV.

Peaks A and C arise from transitions from occupied phosphorus 2p states to unoccupied states of p-like and d-like symmetries, respectively [195]. Peak B arises due to transitions to p-like states mixed with calcium d-states [195]. Peak D is attributed to a cross section maximum of 2p state transitions and multiple scattering [198].

The phosphorus edge observed in the well mineralised regions (TW) did not exhibit any deviations from the standards (HA and CHA). No features characteristic of the phosphorus $L_{2,3}$-edge could be resolved in non-mineralised regions, and the signal observed in poorly mineralised regions is difficult to observe due to poor signal-to-noise ratio and the subtraction window could not be confidently fit to remove the background, possibly due to presence of a silicon signal at ~101eV ($L_{2,3}$-edge). The presence of silicon may be attributed to the contaminations from the PVC storage boxes. To avoid this problem in further studies, cardboard boxes should be used.

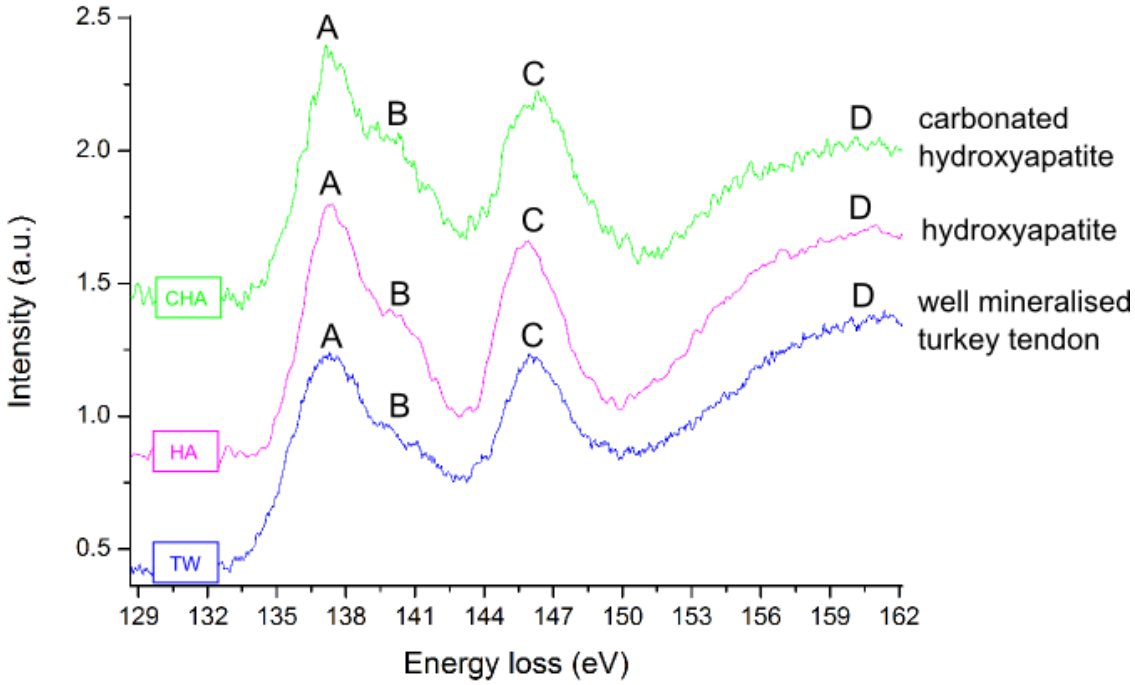


Figure 5.17 The phosphorus $L_{2,3}$ near edge structures of 14 week old well mineralised turkey tendon (TW) and the characteristic standards (HA – hydroxyapatite, CHA – carbonated HA). All turkey tendon patterns were consistent with patterns recorded for hydroxyapatite and carbonated hydroxyapatite. Turkey tendon regions in non-mineralised and in poorly mineralised regions did not exhibit a fully resolved phosphorous signal and have been omitted for clarity.

5.3.4.2. Carbon K-edge

Carbon K-edges of non-mineralised and mineralised collagen fibrils (Figure 5.18) were compared with carbon K-edges of the amorphous carbon (AC) and carbonated hydroxyapatite (CHA).

Carbon spectra were normalised and aligned to the first peak A, which was set to an energy-loss of 285eV, based on the literature [226]. Spectra of non-mineralised (TN) and poorly mineralised (TP) regions exhibit three characteristic peaks A at ~285eV, B at ~286eV and a broad structure E above ~292eV. Some spectra of well mineralised regions (TW2) show additional peaks C and D at ~287 and ~290eV, respectively.

Peak A is assigned to 1s-π* C-C transitions [204]. Assignment of peak B is not straightforward. X-ray absorption spectroscopy (XAS) has shown that the peak in this region arises from carbon or carbonyl groups in an aromatic conformation [200,201,227,228]. Any of these configurations may be attributed to presence of aromatic rings, possibly in nucleic acids, like phenylalanine and tyrosine, or in collagen crosslinks. Other XAS studies attributed peak B to 1s-π* C-C transitions in a nitrated carbon structure [229]. Such conformation could be connected with collagen crosslinking or could confirm the presence of amino acids. In the present study, the peak at ~288 eV associated with 1s-π* C-N transitions [229] was not observed.

There is a variation in spectra collected from the well mineralised regions. In some regions (represented by TW2), peak C and D were observed. Theses peaks are difficult to resolve and interpret. Peak C can be attributed to 1s-σ* C-H transitions in an aliphatic [230] or a diamond-like bond [231], 1s-π* C=O transitions in peptide bonds in carbonyl [227,231] or amidyl [230] and 1s-π* C=O transitions in carboxyl [230]. As features at this position could not be fully assigned, their relation to the mineral-collagen bonding, amino acids or crosslinking is very speculative. Spectrum TW2 shows also a fine structure D, which is characteristic of carbonate 1s-π*-A transitions [177,178]. This feature is clearly visible in the carbonated HA standard (CHA). All spectra exhibit a broad peak E assigned to 1s-σ* C-C transitions [204].

The overall shape of the carbon edge, characteristic for the amorphous carbon, has been attributed to the carbon structure damaged by the electron beam [122]. Srot *et al.* observed amorphisation of carbon structure after prolonged exposure to the electron beam. However, changes in the carbon edge features were connected with the disappearance of the oxygen signal. In the present study, the oxygen signal was still visible after acquisition of carbon spectra. In the report of Srot *et al.* [122], the tissue was not embedded. In the present study, the amorphous-like shape of carbon edge possibly originates from the embedding resin, which partially obscured less intense features of collagen fibrils. Pure resin spectra were identical with amorphous carbon (AC) spectra (data not shown).

All carbon edges collected from turkey tendon start with double peaks A and B (Figure 5.18) characterised previously as arising from the collagen fibril. The carbon edge of the poorly

mineralised region (TP) exhibit strong resemblance to patterns collected from non-mineralised fibrils (TN); also in regions with mineral crystals, similar patterns were acquired (TW1). Typically, the carbon edges of the well mineralised fibril (TW2, Figure 5.18) show peaks characteristic for mineral, *i.e.* a carbonate peak at ~290 eV, and additional peak of unclear origin at ~287eV.

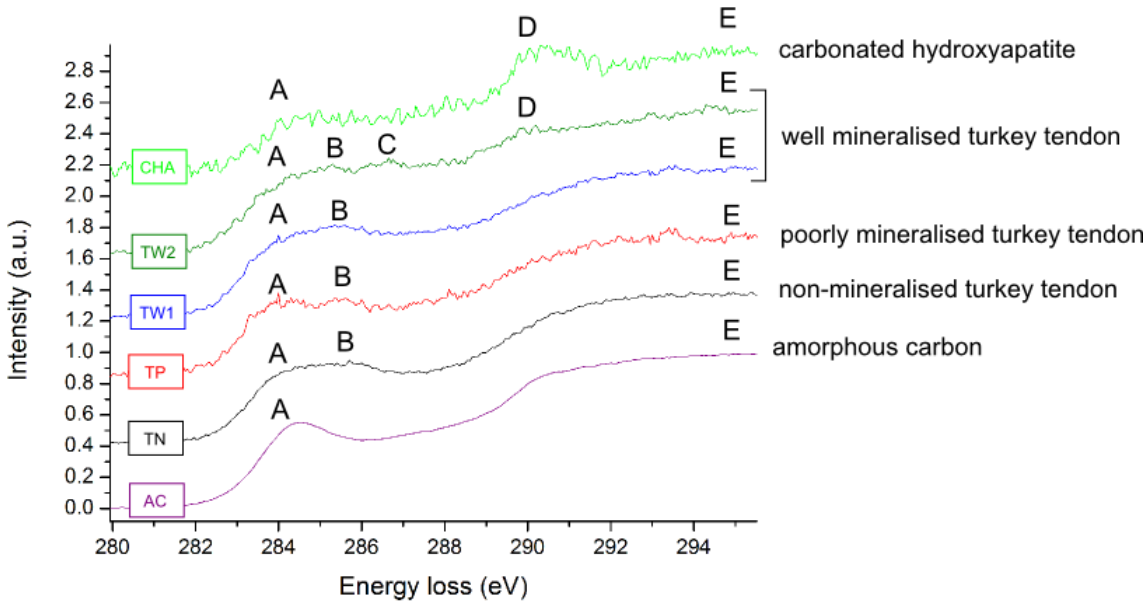


Figure 5.18 The carbon K near edge structures of turkey tendon fibrils (collected from 14 week old specimen), carbonated HA (CHA) and amorphous carbon (AC). The amorphous carbon (AC) spectrum is consistent with spectra collected from resin and carbon film. The AC spectrum has two peaks: a smaller peak A at ~284 eV and a broad peak E above 292 eV. Spectra collected from turkey tendon (TN, TP, TW1, TW2) display an additional peak B at ~286 eV. The mineralised regions show also a formation of peak C at ~287 eV (TW2). In some acquisitions, (TW2), a carbonate peak D at ~290 eV is seen.

5.3.4.3. Calcium $L_{2,3}$-edge

The calcium signal was not observed in non-mineralised regions of sample. In mineralised tissues, as in the case of the mineral standards, two peaks were observed A at ~348eV and B at ~351eV (Figure 5.19). Calcium spectra were aligned and normalised to the peak A, which

was set to an energy-loss of 348 eV based on literature [180]. Sharp peaks A and B are characteristic of the crystal splitting of 2p states.

The calcium $L_{2,3}$ edge did not show significant variations in the shape (Figure 5.19). The calcium signals recorded in the poorly (TP) and well (TW) mineralised regions are consistent with mineral standards (HA, CHA). In the poorly mineralised regions, the calcium edge has a very low intensity, so any additional features are obscured by noise.

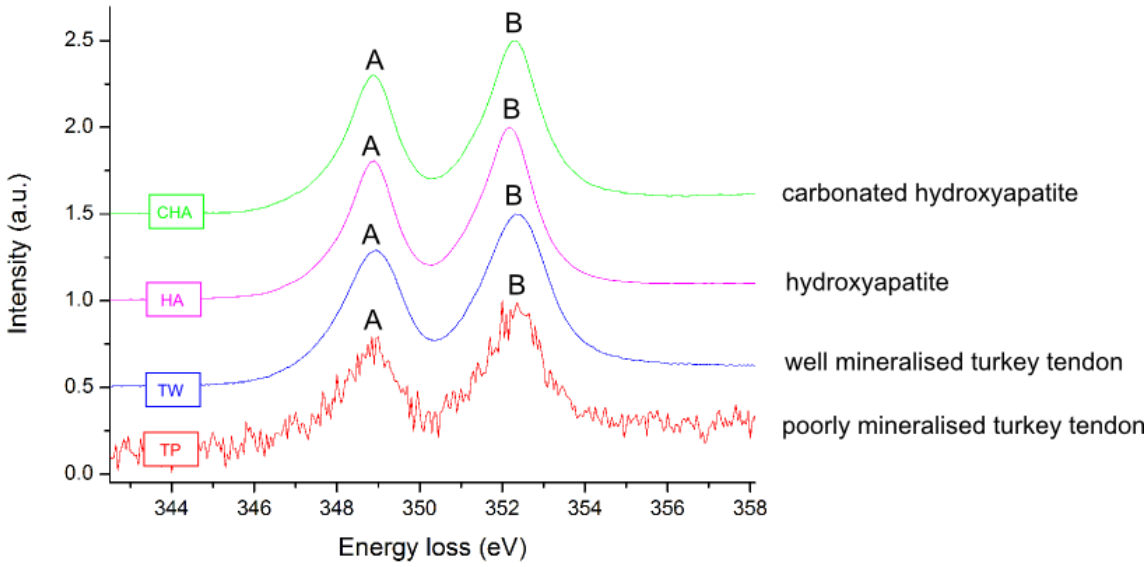


Figure 5.19 The calcium $L_{2,3}$ near edge structures of 14 week old mineralised turkey tendon (TP, TW) and hydroxyapatite (HA) and carbonated HA (CHA) standards. All calcium edge spectra exhibit two characteristic white line peaks: A at ~348 eV and B at ~351 eV.

5.3.4.4. Nitrogen K-edge

The nitrogen signal is used to confirm the presence of protein, and as such, this element was not observed in any of the mineral standards. In the nitrogen K-edge, three peaks were observed: A at ~400eV, B at ~401eV and C at ~408eV (Figure 5.20). Nitrogen spectra were aligned using calcium $L_{2,3}$-edge calibration and normalised to the most intense peak of the nitrogen edge. The calibration of energy scale of non-mineralised regions was confirmed by observation of the zero loss peak before and after the acquisition.

Non-mineralised and poorly mineralised fibril spectra (TN1, TN2, TP) displayed two peaks A and C (Figure 5.20). In well mineralised tissues (TW1, TW2), the nitrogen K-edge shows an additional peak B. There is a significant difference in the intensity of peaks A and B.

Peak A may be attributed to 1s-π* transitions characteristic for nitrogen in an aromatic ring, especially pyridine [228,232–234], which is essential part of collagen crosslinking. Peak B might be connected with oxidised pyridine [228,232], 1s-π* transitions in the nitrated carbon structure [229,233] or 1s-π* transitions in glycine amide groups (C=ONH) [235]. The broad peak C is attributed more generally to 1s-σ* transitions in amino compounds [228].

Spectra of the nitrogen edge collected from non-mineralised (TN1, TN2) and poorly mineralised (TP) fibrils are comparable. Spectra collected from the well mineralised tissues (TW1, TW2) display a clear separation in two peaks: A at ~400 eV and B at ~401 eV. This split may show energy shifts between 1s-π* transitions in pyridine and oxidised pyridine, respectively [232]. A broad peak C corresponding to 1s-σ* transitions in the amino groups is also observed.

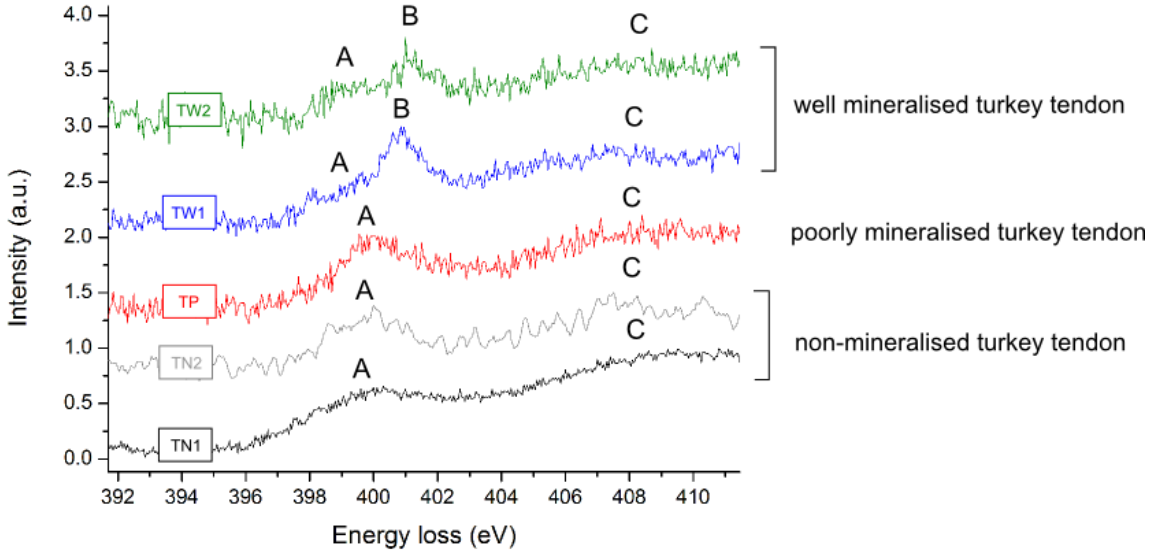


Figure 5.20 The nitrogen K near edge structures of non-mineralised (TN) and mineralised (TP, TW) 14 week old turkey tendon fibrils. In the nitrogen spectra, three peaks can be observed: A at ~400 eV, B at ~401 eV and a broad peak C at ~408 eV.

5.3.4.5. Oxygen K-edge

The oxygen K-edge of non-mineralised and poorly mineralised regions displays two peaks: A at ~532eV and E at ~543 eV (TN, TP, Figure 5.21). Oxygen K-edges in the well mineralised (TW) regions show strong, apatite-like features: a double peak C-D at ~537 and ~539 eV, respectively and a weak peak F at ~545 eV. Mineralised tissues also display smaller features A and E, which are fully resolved in spectra of non- and poorly mineralised regions.

Oxygen spectra of mineralised regions were aligned using peak D, which was set to an energy-loss of 539eV (see section 4.3.4). The calibration of energy scale of non-mineralised regions was confirmed by observation of the zero loss peak before and after the acquisition. Spectra were normalised to the most intense peak of each individual spectrum.

Peak A is attributed to 1s-π* C=O transitions in carboxyl or amide groups [228,230]. The shoulder B in carbonated HA was attributed to 1s-π* C=O transitions in carbonate and peak C to 1s-π* calcium-oxygen transitions [213]; however, in mineralised tissues, there is an overlap of signal coming from protein. Peaks characteristic of organic polymers should form

in 530-536eV region [228], which correspond to position of peaks B and C. In organic material, features at the B position originate from 1s- σ* transitions in C=ONH or COOH groups [228,235], and features at the C position originate from 1s-π* O-H transitions in COOH [235] or 1s- σ* transitions in C-O-C or O-C-N groups [228].

The assignment of peak D is speculative. Possibly it originates from transitions to calcium-oxygen or phosphorus-oxygen orbitals in mineral [213]. In organic material, the broad structure E is attributed to 1s- σ* transitions in O-H groups, while the higher energy shoulder F comes from 1s- σ* transitions in C-O groups [228,235]. In mineral, the assignment of peak F is also not clear. In oxides, peaks of similar energy-loss are connected transitions to 4s- and 4p-like states in calcium-oxygen bonds [213].

Spectra recorded in non-mineralised (TN) and poorly mineralised (TP) regions could be attributed to amino acids, most probably glycine [235], which is the most common acid in the collagen chain. In well mineralised tissue (TW), spectra are dominated by strongly resolved apatite-like features (peaks C, D and F), but features characteristic of organic polymers may also be seen. Formation of peak A could be attributed to the presence of proteins, especially glycine, and shoulder E is relatively more intense in tissues than in mineral standards.

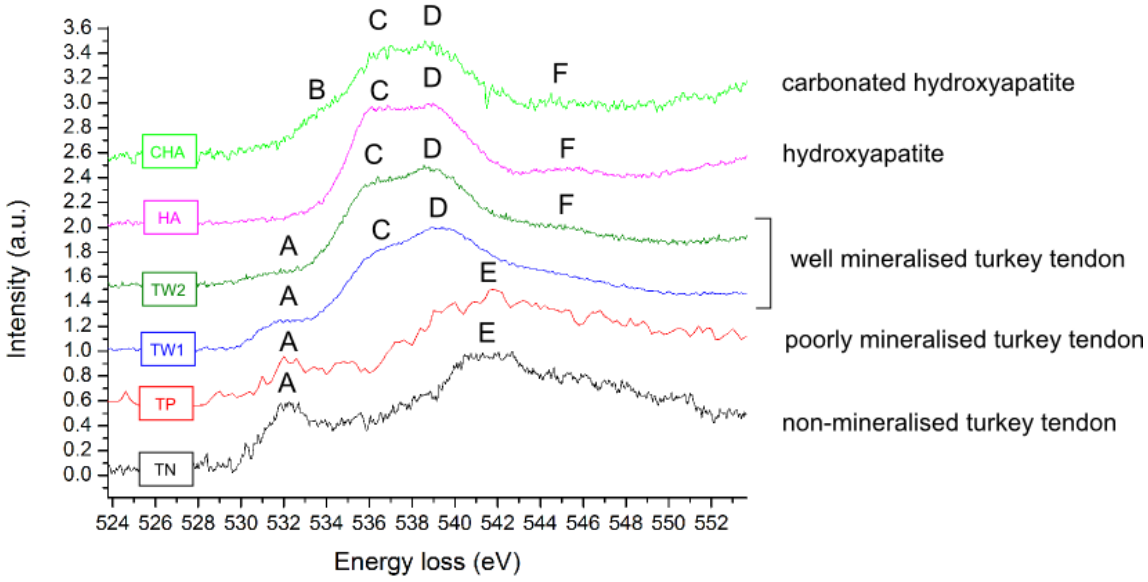


Figure 5.21 The oxygen K near edge of non-mineralised (TN) and mineralised (TP, TW) 14 week old turkey tendon fibrils, and hydroxyapatite (HA) and carbonated HA (CHA) standards. In mineralised tissues, a mixture of features characteristic of the mineral and collagen can be seen.

5.3.4.6. Elemental mapping

Investigation of longitudinal and transverse regions of the non-mineralised fibrils did not show any changes in chemistry between gap and overlap regions (A, Figure 5.22), and between intra- and extrafibrillar regions (B, Figure 5.22), other than in the intensity of the signal. Carbon, nitrogen and oxygen edges were usually intense in the overlap region of longitudinal sections and in the intrafibrillar region of transverse sections.

Regions of longitudinal and transverse sections of the well mineralised tissues show only changes in the intensity of the signal rather than modifications in the edge structure. Phosphate, calcium and oxygen signals were more intense in regions with visible mineral grains or crystals, usually in the gap region of longitudinal sections (C, Figure 5.22), and in the intrafibrillar regions of transverse sections (D, Figure 5.22).

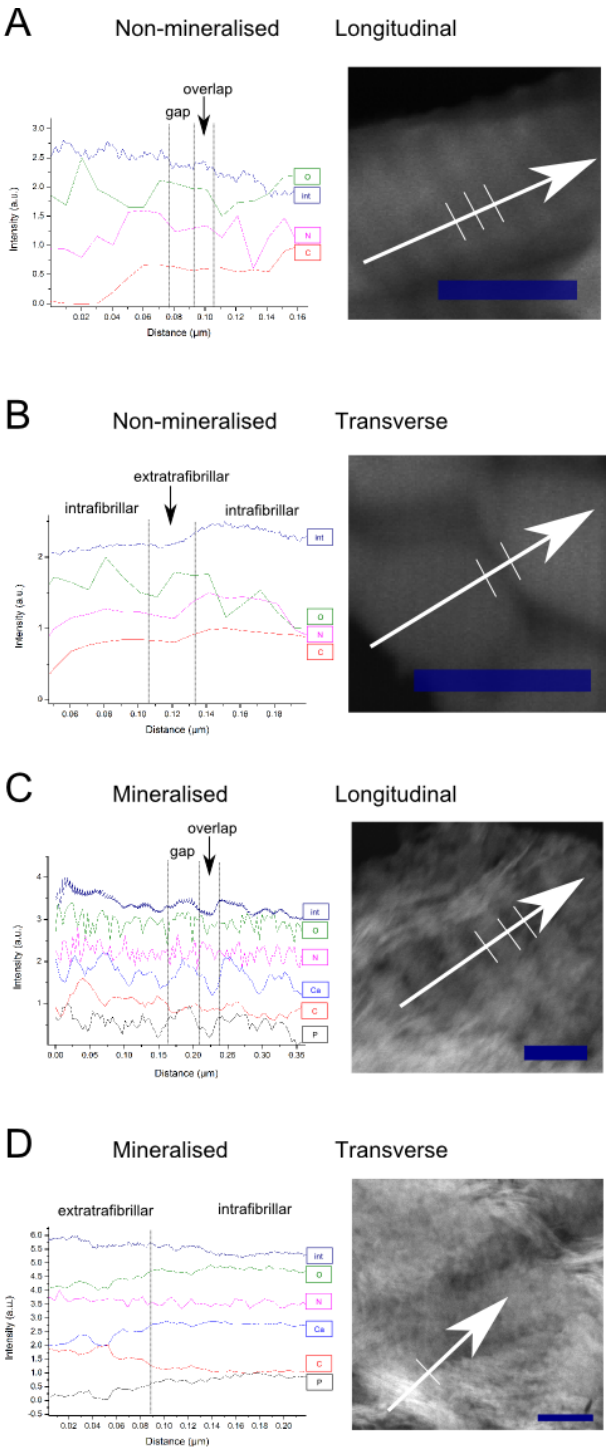


Figure 5.22 Representative normalised intensity line profiles (white arrows;) of elemental signals (phosphorous $L_{2,3}$, carbon K, calcium $L_{2,3}$, nitrogen K, oxygen K) and intensity of ADF-STEM micrographs (int). Profiles were collected for 14 week turkey tendon. Scale bar (blue)=100nm. Arrow heads are consistent with the direction of X axis on the plots and line markers on arrows correspond to the border lines on particular plots.

Nano-scale analysis of bonding between interfaces between the mineral and collagen was limited here. Changes in the elemental edge structures were very subtle and difficult to resolve. To resolve the details of the fine structure at the spatial resolution higher than 5 nm, a higher quality signal needs to be produced. However, any increase in electron dose may cause damage to the observed structure. Application of low loss methods in future studies may overcome this limitation.

Jantou-Morris *et al.*[21] and Alexander *et al.* [71] showed compositional variations across banding in the mineralised tissues, elephant dentin and mouse bone, respectively. It is possible that the developing collagen-mineral matrix in turkey tendon is less organised or organised in a different fashion than in bone and dentin. This difference in the compositional distribution may result in harder to resolve elemental maps. On the other hand, Jantou-Morris and Alexander studies did not report the electron doses used in their experiments. Doses used in the studies of Jantou and Alexander might have been higher than in present study, and tissues they used were more mineralised and therefore probably much more stable than turkey tendon.

5.3.5. Chemical composition of collagen and mineral measured by EDS

The nano-scale characterisation did not reveal the progression of mineralisation with age of the tissue. To confirm that selected specimens exhibit age-related variations reported in previous studies, bulk characterisation methods (EDS, XRD and TGA) were employed.

The calcium/phosphorous ratios present in the specimen were assessed using EDS. EDS spectra of mineralised turkey tendons from each age group showed a similar signal (Figure 5.23) with carbon, nitrogen, oxygen, phosphorous and calcium peaks. The intensities of the trace elements peaks were always close to the background noise level and were not specific for any age group. For each age group, spectra from 20 different regions were collected.

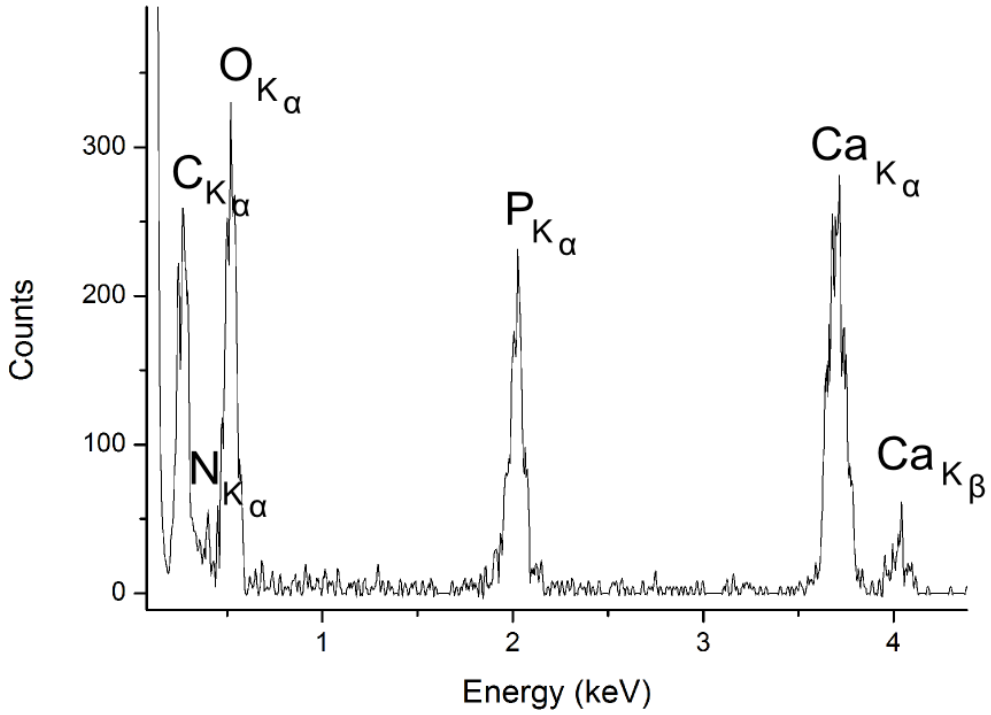


Figure 5.23 Representative EDS spectrum collected from mineralised turkey tendon showing carbon, nitrogen, oxygen, phosphorous and calcium peaks. The spectrum was collected from the 14 week old turkey tendon.

During mineral maturation, the Ca/P ratio increases, which might indicate transformation of mineral from a less stable phase like octacalcium phosphate to a phase or incorporation of carbonate ions, which more resembles stoichiometric HA. In turkey tendon, the bulk Ca/P ratio increased with age towards values observed in HA. This suggests either a presence of a single, homogenously developing (but different at each time point) mineral phase or a presence of multiple, mixed mineral phases. The former supposition is more plausible as diffraction patterns collected from respective regions show dominance of an apatite-like phase.

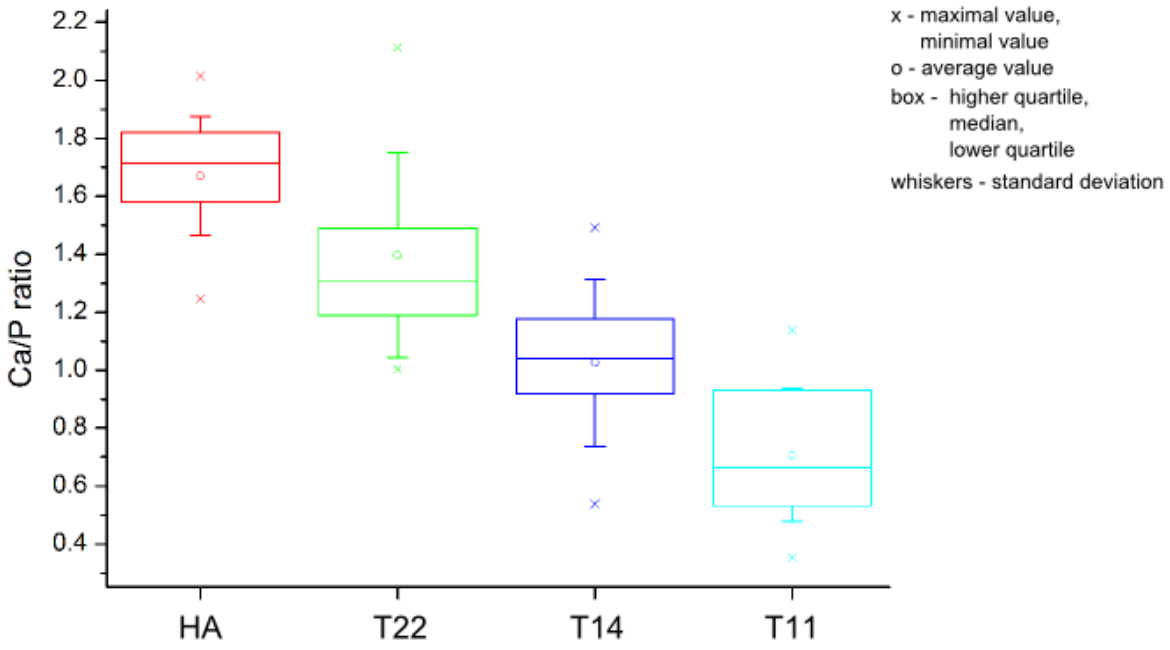


Figure 5.24 Changes in Ca/P ratio between turkey tendon (T11 - 11 week old, T14 - 14 week, T22 - 22 week) and hydroxyapatite standard (HA). The Ca/P ratio increases with age towards values characteristic for hydroxyapatite.

5.4. Bulk characterisation of turkey tendon (XRD & TGA analyses)

XRD spectra collected from the turkey tendon powders of each age group (11, 14, 22 week) exhibit strong similarities to each other (Figure 5.25, Figure 5.26). The distribution of major peaks in each sample was almost identical and consistent with the standard hydroxyapatite data. Only one sample from each age group was examined in the bulk study.

Generally, in non-heat treated turkey tendon samples (Figure 5.25), peaks are broad and difficult to resolve. In younger turkeys, peak broadening is higher and peak resolution is poorer. These differences are the effect of higher collagen protein content and presence of amorphous mineral phases in the juvenile tendons [236]. With age this variance decreases and the older crystals can be more easily indexed as apatite, as peaks become sharper. An additional HA peak at ~29.5° (012) is seen in samples before incineration.

Incinerated turkey tendon spectra still show the presence of amorphous material as peak are not as well resolved as in the case of the hydroxyapatite spectra. A sharpening of the peaks in

turkey tendons was observed, *i.e.* a broad peak at 50.5-52° in Figure 5.25 corresponding to (213), (321), (410) and (402) planes split into four separate, sharp peaks after incineration (Figure 5.26). After thermal processing, the turkey tendons exhibited a more apatite-like crystallography.

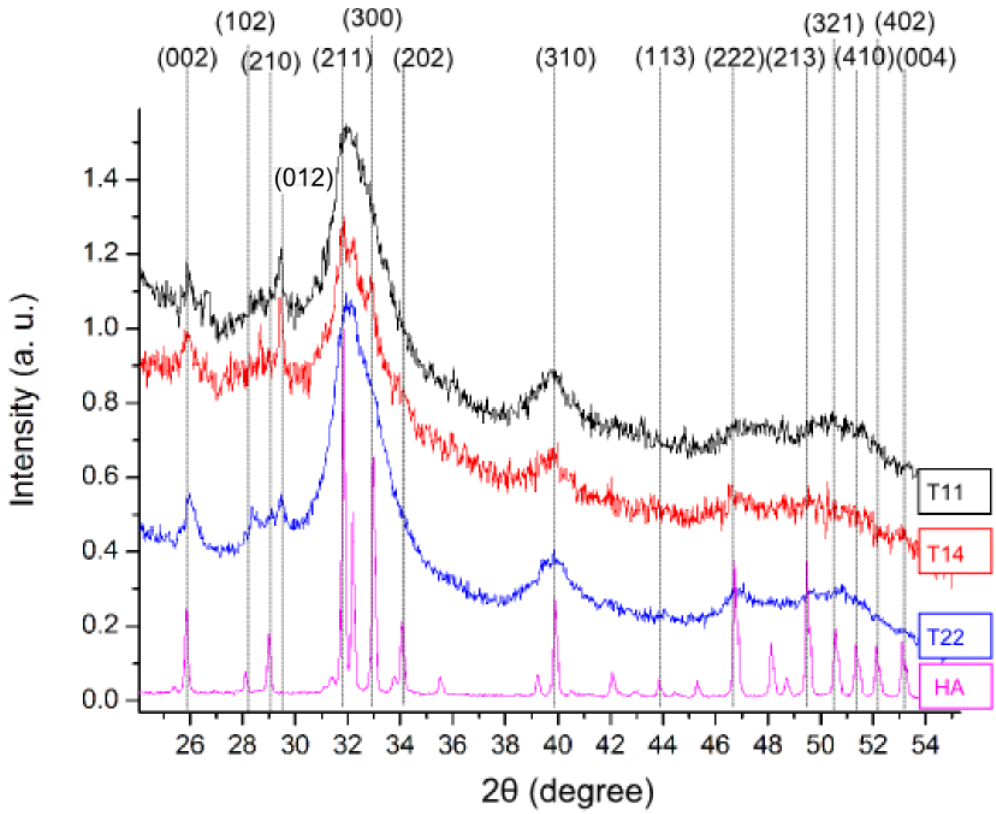


Figure 5.25 XRD spectra of the ground turkey tendon powders (T11 - 11 week old, T14 - 14 week, T22 - 22 week) before TGA. The major peaks are labelled, showing corresponding crystal plane indices.

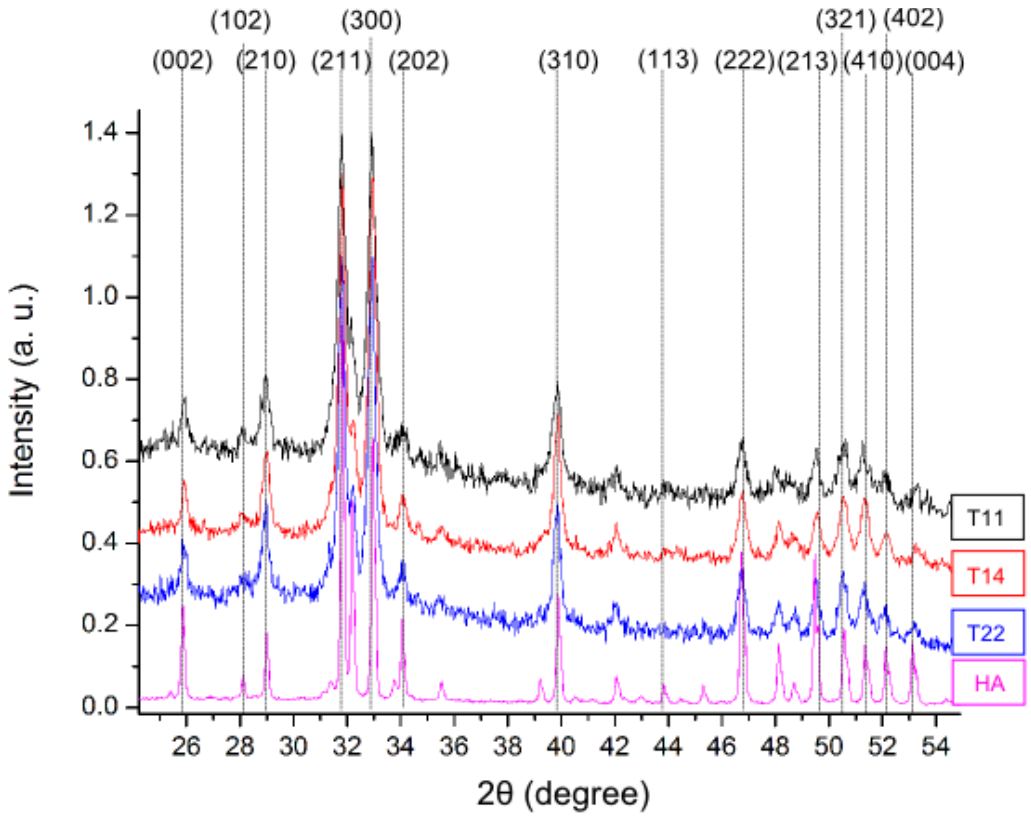


Figure 5.26 XRD spectra of the incinerated turkey tendon powders (T11 - 11 week old, T14 - 14 week, T22 - 22 week) and the hydroxyapatite standard. The major peaks are labelled with corresponding crystal plane indices.

Mineral precipitating in turkey tendon exhibits broad diffraction peaks distributed similarly to apatite. This peak broadening is not surprising, even in the most advanced mineralisation stage, turkey tendon has a high protein content, which is much higher than bone. On average the amount of protein is doubled in the tendon in comparison to bone (40.2±1.9 wt%), but tendon and bone have similar water (16.1±6.7 wt%) and carbonate content (1.56±0.45 wt%). In tendon, like in bone, the total amount of carbonate increased with age (Table 5.3)

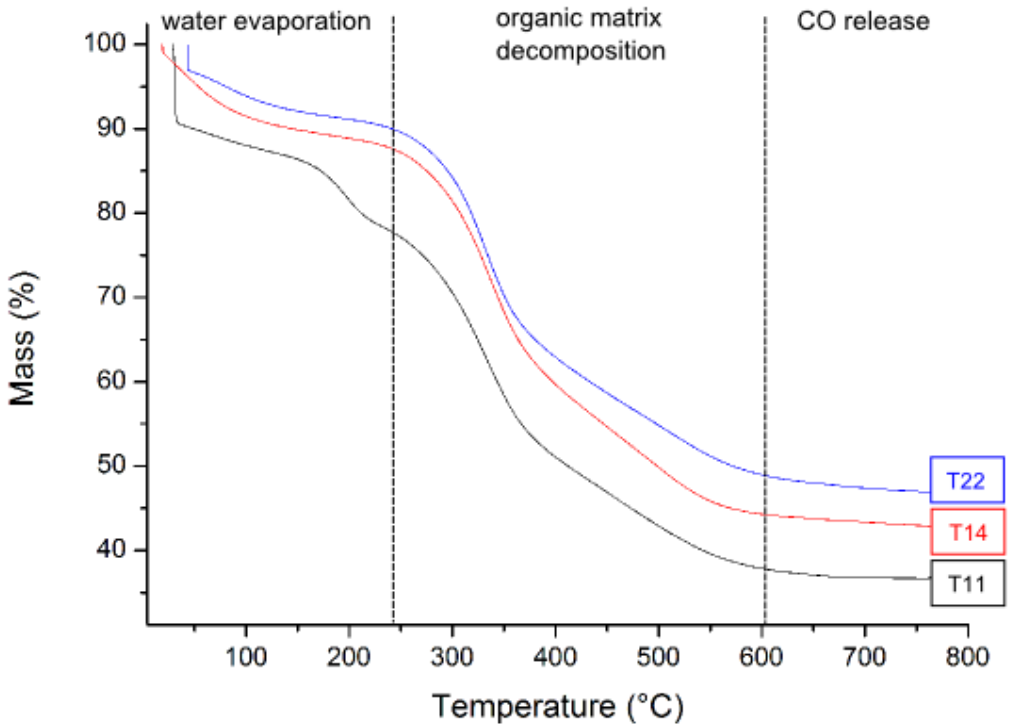


Figure 5.27 Percentage mass reduction of incinerated the tissue samples: three turkey tendons (T11 - 11 week old, T14 - 14 week, T22 - 22 week).

Table 5.3 Weight percentage of water, protein and carbonate content in examined samples

Sample	Water (wt%)	Protein (wt%)	Carbonate (wt %)
T11 – 11 week turkey tendon	23.76	38.38	1.19
T14 – 14 week turkey tendon	13.52	42.19	1.44
T22 – 22 week turkey tendon	11.04	39.98	2.06

5.5. Discussion & conclusions

This study presents a method of differentiation between non-mineralised and mineralised tissues at three consecutive stages of development (before, during and after mineralisation) on the nano-meter scale. The chemical and structural composition of turkey tendon varies between region of different mineralisation stage (non-mineralised, poorly mineralised and well mineralised). These three types of regions were classified on the basis of their morphology assessed *via* micrographs, crystallography assessed *via* SAED and chemistry assessed *via* STEM-EELS.

In non-mineralised regions (consisting of collagen only), no morphological, crystallographic or chemical indicators of the mineral presence could be observed. In poorly mineralised regions, diffuse, elongated, calcium-containing grains become visible. However, SAED patterns did not reveal the presence of any crystalline structure. In well mineralised regions, well-defined crystals can be easily observed. Well mineralised regions produce SAED patterns and EELS signatures comparable with carbonated apatite. Comparison of these three regions described above give an important insight into the evolution of the mineral and collagen during tendon calcification. This classification was also important for interpretation of EELS data.

Changes in the EELS spectra were observed between three types of regions described above. Most significant modifications were observed in the carbon, nitrogen and oxygen K-edges. In the carbon K-edges of all regions, peak at ~286eV, characteristic to aromatic carbon structures, was seen. Additionally, in well mineralised region two new peaks at ~287 and ~290eV appeared. Three peaks were assigned to transitions in carbonyl/carboxyl groups and to transitions in carbonate, respectively. The presence of those peaks might be related to changes in collagen during mineralisation and to nucleation of the mineral. In the nitrogen K-edge, fine structure, which was attributed to pyridine in non-mineralised and poorly mineralised regions, evolves into structure comparable with oxidised pyridine. This transformation seen in the nitrogen K-edge might be an important step in maturation and mineralisation of collagen. In the oxygen K-edge, fine structures in non-mineralised and

poorly mineralised regions are comparable to spectra recorded for proteins [235]. In well mineralised regions, fine structure of protein is overlapped by signal coming from mineral. The phosphorus and calcium $L_{2,3}$-edges did not show significant variation in their shape between different regions. However, an increase in the intensities of these edges was observed. The presence of phosphorus and calcium was not detected in the non-mineralised regions. In poorly mineralised regions, weak signals characteristic of phosphorus and calcium were recorded and in well mineralised regions, very intense signals were detected. As there is a mixing of collagen and mineral phases in the developing tissue, a more holistic approach (observation of edges as a group) might be beneficial to the identification of signal origins and assignation of spectral features to specific chemical structures.

Assessment of turkey tendon chemistry by EELS revealed signatures, which might be characteristic of the presence of nucleic acids with aromatic structures in collagen and/or mature collagen crosslinking. Special interest should be directed towards analysing the carbon and nitrogen edges. The core loss edges show features possibly originating from pyridine-based amino acids and/or crosslinks. With application of monochromated EELS, there is a possibility of further unravelling of the collagen chemical signature and mapping the distribution of aromatic structures in fibrils at different development stages and in diseased tissues.

Carbon, nitrogen and oxygen edges exhibit most significant modifications in their structure between non-mineralised, mineralising and mineralised regions. Literature on modifications of these edges is limited, especially in the context of biomineralisation. This field would greatly benefit from a computation of model features of aforementioned edges and examination of collagen models containing various aromatic structures or analysis of a set of small molecule standards with different functional groups.

The turkey tendon model provides insights into the structure of collagen type-I based tissues. However, it is a challenging model to use to observe the mineralisation process as a function of turkey age, as the mineralisation front was very disperse and regions at different stages of development can be seen in each age group. In contrast, statistically significant variations between different age groups were measured in bulk assessments of the Ca/P ratios, the mineral crystallinity and composition, and the protein content. Our TEM analysis shows that

in each age group, the tissue contains regions at different stages of development, rather than from a homogeneous development of the whole tissue. Stages of mineral development in turkey tendon are fairly straightforward to assess in the bulk of the sample. However, characterisation of mineral development at the nano-meter scale is a challenging task.

If such disorganised development is not an intrinsic attribute of *in vivo* mineralisation process, other models may provide a better insight into how bone mineralises. Fish bone and fish scale models are examined in context of biomineralisation [22,126]. Fin bone calcifies from the roots to the tip, similarly to turkey tendon. Micro-meter scale studies suggest that fish bones mineralisation front is less dispersed than in turkey tendon and might be tracked also on nano-scale level [123].

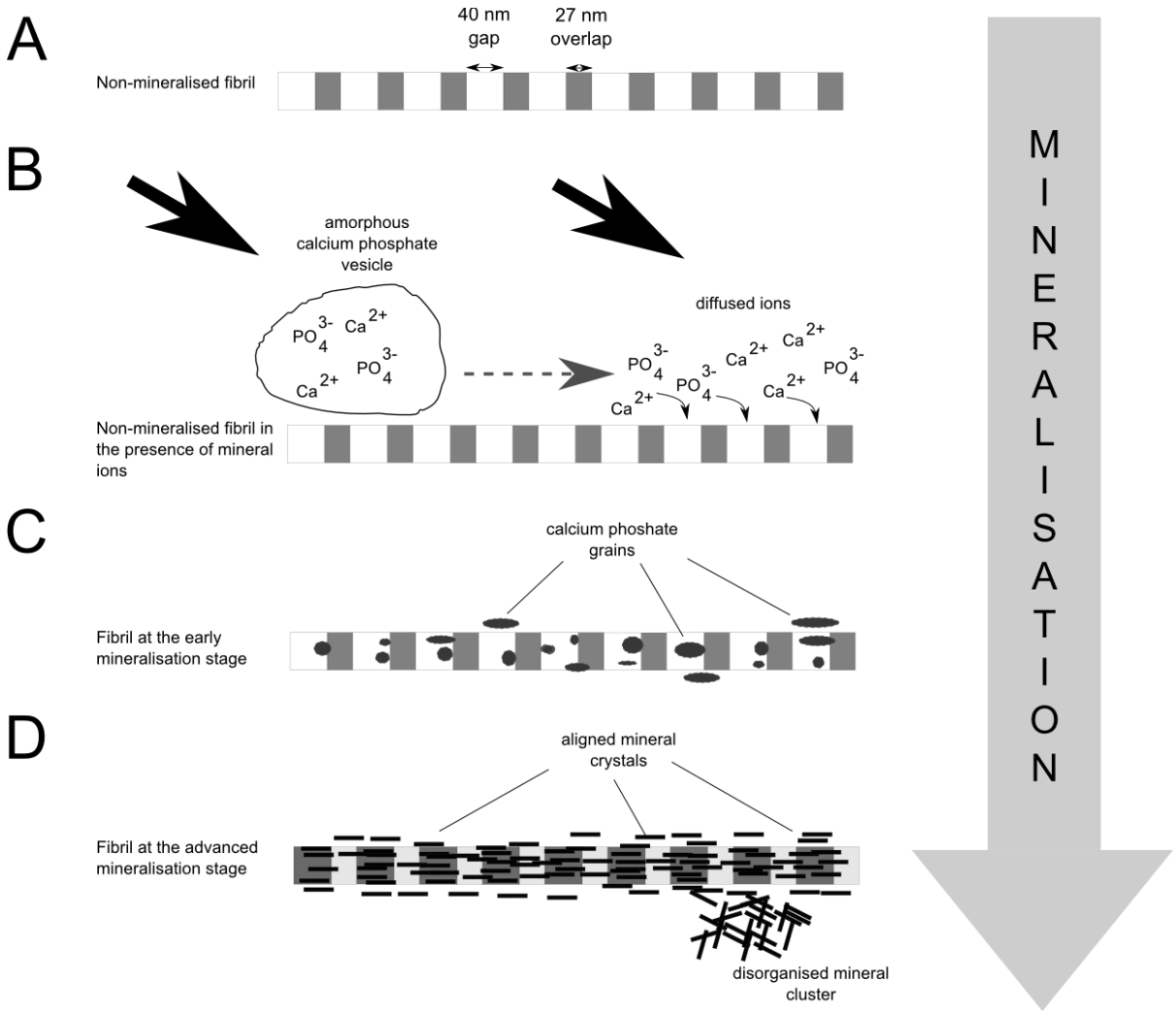


Figure 5.28 Schematic showing the progression of mineralisation based on the turkey tendon model study. (A) A non-mineralised fibril. (B) The mineral ions are delivered into the collagen matrix either as amorphous calcium phosphate vesicles/globules, which dissolve and release the ions, or free ions are transported in the body fluids. (C) Mineral ions start to aggregate forming mineral grains in the gap regions. The periodic banding contrast starts to reverse. (D) Mineral grains crystallise into aligned crystals inside, and outside, the fibril. During development some of the extrafibrillar crystals may lose their alignment and rearrange into disorganised globules.

The *in vivo* mechanisms, by which mineral ions are delivered into the collagen matrix, are still under discussion. It has been suggested that the mineral is delivered from cells to fibrils in amorphous calcium phosphate vesicles or globules of disorganised apatite crystals. In the turkey tendon model used in this study, amorphous calcium phosphate vesicles, which might act as mineral ions supply for fibrillar mineralisation [103], were not observed and mineral globules containing disorganised apatite crystals, which were suggested as the main

mineralisation devices [103,104], could be observed only in the regions at advanced mineralisation Previous *in vivo* observations of disorganised globules of well crystallised mineral in partially mineralised fibrils [18,23,220] could be the artefacts of the non-anhydrous preparation method (*i.e.* mineral crystallisation). However, the presence or absence of mineralising cells in examined region of the animal model used in the present study (turkey tendon) may also have an impact on the distribution and evolution of the mineral [103,123]. An alternative *in situ* model suggests that the mineral nucleation begins, when the body fluids in the vicinity of collagen fibrils are super-saturated with calcium and/or phosphate ions [108].

We hypothesise that mineral ions are delivered into the collagen matrix either *via* saturated body fluids or in globules or vesicles. These mineral ions nucleate and grow in the gap regions of fibrils. Initially, calcium/phosphorus ions form amorphous grains, which crystallise and grow with time. The crystallisation process may occur in the intra- and extrafibrillar regions. Mineral nucleating inside fibrils aligns its crystallographic c-axis parallel to the long axis of collagen. Mineral nucleating outside fibrils usually follows the same alignment, but with limited support from fibrils or in the absence or presence of specific non-collagenous proteins (NCP) extrafibrillar mineral may arrange into disorganised clusters of crystalline mineral [15,237]. These disorganised clusters might be the remnants of globules acting as the precursors to mineralisation.

6.
COMPARISON OF WILD-TYPE AND OI-AFFECTED TISSUE IN A MOUSE BONE MODEL

6.1. Introduction

Osteogenesis imperfecta (OI or brittle bone disease) is a genetic disease causing disruption in type I collagen and thus affects collagen-based tissue. Brittle bone disease is predominantly an inherited disorder, which affects approximately 1 in 10,000 people worldwide [238]. It is caused by a mutation in the genes coding for collagen, the major structural protein in bone. This molecular defect (an alteration in collagen sequence) causes skeletal fragility at the whole bone level (broken bones). However, this pathology is not only limited to bone brittleness. Other common consequences are impaired tendons, loose joints and skeletal malformations [238]. In severe cases this pathology may lead to antenatal death. Changes in OI collagen are associated with alteration of genes responsible for α_1 and α_2 chain expression, usually caused by a point substitution of one amino acid for another. There are over 1500 mutations causing changes in the structure or quantity of expressed collagen [239]. The severity of the disease depends on the location of the mutation in the collagen molecule [238].

In humans, OI mutation causes point modifications of collagen molecules, *e.g.* glycine residues in collagen triple helices are substituted with larger amino acids like cysteine [240]. Such seemingly minor modifications create a significant structural disorder of the collagen fibrils. Nevertheless, this effect seems to be highly dependent on the position of the replaced amino acids in the collagen chain and the most severe pathologies are observed when replacement takes place near the molecule termini [241]. Decreased Young's modulus of the collagen molecules (molecular softening), decreased intermolecular adhesion, and increased intermolecular spacing are observed as results of termini modifications [241].

Osteogenesis imperfecta *murine* (OIM) is a common mouse model of OI that mimics moderate to severe phenotypes in humans. In this mouse model, the natural conformation of two α_1 and one α_2 chains is replaced by a triple-helix consisting of three α_1 chains [242], which leads to poor packing of the microfibrils due to increased intermolecular separation [243,244]. It has been suggested that OIM collagen fibrils are bent and twisted [245], resulting in disruption in the tissue organisation. This hypothesis has been supported by collagen labelling studies (*i.e.* chromatography, polyacrylamide gel electrophoresis) [246,247] and by a molecular modelling of human defects [246,248] and of the OIM mouse model [249]. However, the effects of collagen alternations are heterogeneous, and organised, banded collagen fibrils can also be found in OI tissues [39,250]. The molecular alternations of collagen caused by OI mutations have a great impact on the arrangement of collagen molecules and their packing into fibrils.

Abnormalities in OI are not limited only to collagen matrix organisation, but also affect the interaction interface between the mineral and collagen [245]. Bulk studies of OIM tissue revealed overhydroxylation and overglycosylation of amino acids [60,251,239]. This phenomenon may be related to changes in collagen crosslinking. One of the computational molecular dynamics models predicted that larger distances between OI collagen molecules caused a decrease in the number of lysine-based crosslinks formed [241]; however, levels of pyridinoline crosslinks in human OI are similar to those seen in normal bone [252]. This suggests that sugar-derived crosslinks are responsible for observed increase in the collagen hydroxylation, which potentially has impact on the mineralisation process. A decrease in the number of enzymatic crosslinks and an increase in the number of non-enzymatic crosslinks was observed in OIM model [253]. Additional changes have been also observed in expression of non-collagenous proteins (NCP) in affected tissues [251,254]. The majority of OI studies concentrate on the protein labelling techniques and direct information about spatial distribution of reported malformations at the nano-meter scale *in vivo* is limited.

Previous studies have demonstrated a strong relationship between the overall strength of the material and the molecular orientation and morphology of the mineral crystals. The long axes of crystals in OI tissues exhibit greater deviation from alignment parallel to collagen fibrils [255,256]. There is also a great variation in the shape and size of the apatite crystals [245]. The mineral crystals are smaller, more randomly aligned and distributed in OI bone compared

to healthy bone [245,255–259]. There also have been reports about formation of large bulky crystals and aggregation of small crystals seen in OIM [67,245,259]. These reports are not contradictory. The presence and organisation of small crystals was assessed mainly by small-angle X-ray scattering (SAXS), which is not optimal for detection of structures larger than 50 nm [259]. Hence, there are two groups of crystals: small crystals seen in intrafibrillar regions, and large crystals encountered in extrafibrillar regions [259]. Computational models suggested the actual morphology of apatite crystals may have greater impact on the mechanical behaviour of the tissue than deformations destabilising collagen fibrils [260].

The mineral in OI-affected tissues tends to have lower degree of carbonate (measured by bulk FTIR) content and reduced crystallinity (measured by bulk XRD) [166]. It was proposed that in the bones of OIM mice, high remodelling rates result in less mature crystals and therefore less carbonate substitution [168]. However, different models of the OI disease (BrtlIV) exhibit an increase in the carbonate content, which might suggest that the deviation from the optimal levels of carbonate content have strong impact on the mechanical properties of mineral-collagen composite (increase in brittleness) [261]. Furthermore, studies reporting a decrease in the carbonate content [166,168] used FTIR to assess changes in B-type carbonate in relation to phosphate, but neglected presence of two other carbonate species (A-type and unstable C-type) and the result might not reflect the state of the entire carbonate population. Positioning of the carbonate ion in the crystal lattice is an important factor; investigation should not be limited to only one species of carbonate substitution, but involve all of them, *i.e.* A, B and C substitutions [262]. These uncertainties need to be explained by a more complex study involving a multi-scale, bulk and spatially resolved, examination of specimens from selected disease models.

Changes in structure and chemistry of basic blocks of bone result in modifications at higher hierarchical levels of the tissue organisation. Osteogenesis imperfecta (and the OIM model in particular due to extensive knowledge about its genetic origins and macroscopic consequences) provides an excellent platform for examining the effects of molecular level changes in the nanostructure and composition of diseased bone. In this chapter, the morphological and chemical changes in the collagen fibrils between wild type (WT) and OI mouse models of non-mineralised tail tendon collagen are characterised with nano-meter scale spatial resolution. The crystallinity, morphology and chemistry of the mineral phases

and collagen are also examined and compared between wild type and OIM bones. Specifically, STEM-EELS was used to probe the changes in bonding environment of collagen and mineral, assess formation of crosslinks, their maturation, glycosylation and oxidation states.

The specific aims of this chapter are:

- to validate and improve methods of the nano-scale analysis of bone;
- to characterise the chemistry, coordination environment and morphology of the mature mineral in WT and OIM *in vivo* model, especially to observe changes in the levels of carbonate substitution;
- to characterise the chemistry and morphology of the collagen in WT and OIM using an *in vivo* model, especially to observe changes in the carbon and nitrogen signal in EELS spectra related to presence of aromatic structures in collagen molecules or crosslinks.

6.2. Materials and methods

Femurs of 8 week old OIM and WT mice were dissected, prepared *via* high pressure freezing and freeze-substitution (see sections 3.1 and 5.2), and focused ion beam (FIB) milling without staining. Non-mineralised tail tendon collagen was harvested from mouse tails. Tails were dissected and tendons were pulled out with a surgical needle. Small (1mm) pieces of tendon prepared *via* the freeze-substitution method with osmium staining (0.5% osmium tetroxide in acetone).

A Helios NanoLab™ 50 series DualBeam instrument with gallium ion source was used for preparation of thin bone sections for TEM analysis. Dual beam FIB-SEMs combine an ion beam instrument with a scanning electron microscope (SEM). As ion beam imaging is a destructive method, the use of an electron beam to visualise the sample and minimise possible ion beam damage, is a benefit of this setup. This configuration also allows

visualisation during FIB milling, which helps in producing good quality cross-sections. The FIB is also fitted with a gas injection system, which allows platinum and carbon deposition.

A modified procedure designed by Jantou *et al.* [121] was followed. Silver paint was used to mount bone pieces on a metal support. Before placing the specimen in the FIB compartment, the whole sample was coated with a thin chromium layer using an Emitech coating machine for 1 minute with a current 75mA. In the FIB, a platinum strap was deposited in a two stage process on selected region of interest, in order to protect it from beam damage. Electron assisted deposition of platinum (2kV, 1.4nA; 10(x) x 2(y) x 10(z) μm) was carried out at 0° stage tilt, followed by gallium assisted deposition (30kV, 0.46nA; 17(x) x 2.5(y) x 20(z) μm) at 52° tilt. This procedure is used to avoid additional damage during ion beam deposition. The next steps were carried out at 52° tilt. After platinum deposition, rough parallel trench milling (30kV, 21nA; 25(x) x 10(y) x 6(z) μm) was performed to obtain an outline of the section. Next, a cross-sectional cleaning procedure (30kV, 6.5nA; 3(z) μm; tilt +/- 2°) was applied to obtain a more homogeneous layer. Finally, a lamellae was cut (30kV, 2.8nA; 10(z) μm; tilt 7°) and prepared for lift-out using the OmniProbe tungsten needle. The section was attached to the needle with the platinum strap, the remaining material was cut off and the section was removed from the trench and transported to grid section. The section was fastened to grid finger with platinum (30kV, 93pA; 1(z) μm) and the needle attachment was cut off (30kV, 2.8nA; 10(z) μm). Next, coarse thinning (30kV, 0.46nA; 2(z) μm; tilt +/- 1.5°) was performed, followed by fine thinning (30kV, 93pA; 2(z) μm; tilt +/- 1.2°). Eventually, the remaining platinum layer was removed (5kV, 47pA; 2(z) μm; tilt +/- 1°) to reduce strain on the sample and final polishing (2kV, 28pA; 20(z) nm; tilt +/- 2°) was carried out.

Bright-field TEM and SAED of mouse bone and tendon were performed on JEOL2000FX and Titan TEMs operated at 120/200kV and 300kV, respectively. Lower voltage conditions were tested to examine changes in the mass-thickness contrast and optimise the acquisition conditions.

For non-monochromated STEM-EELS, the C_s corrected, FEI Titan microscope with Gatan Tridem spectrometer was used (Imperial College, UK). Optimal signal-to-noise ratio was achieved using a 50μm condenser aperture, a spot size 9, a 48mm camera length, and 8mrad probe convergence semi-angle. In these conditions, ADF-STEM collection semi-angles range

is 33-181mrad, HAADF-STEM collection semi-angles range is 161-681mrad and EELS collection semi-angle is 14mrad. Total electron doses were kept below 10^4 electrons/nm^2 and sub-pixel scanning was used to minimise radiation damage. The FWHM of the non-monochromated zero loss peak (ZLP) was 0.6-0.7eV. Spectra were collected with the energy dispersion of 0.05 eV/channel.

For monochromated STEM-EELS, the C_s corrected, FEI Titan^3 microscope with Gatan spectrometer was used (Ohio State University, USA). The microscope settings were optimised to mimic the setup of the non-monochromated microscope. The FWHM of the monochromated ZLP was 0.3-0.5eV.

A power law background subtraction (with 30eV window or wider) was performed on all acquired edges. Spectra were usually aligned to the first peak and normalised to the most intense peak (see appropriate edge for details). The calibration of spectra was confirmed with literature and by observation of the ZLP before and after acquisition.

6.3. Preliminary microscopic examination of wild type and OI bone: morphology and crystallinity of mineral phase present

Crystals observed in bone of wild type (WT) and osteogenesis imperfecta (OIM) mouse displayed features similar to those previously described in the literature [99]. Crystals of plate-like shape were aligned with the long axis of collagen fibrils (Figure 6.1). Characteristic needle-like impressions of crystal shapes originate from edge-on observations of platelets. Regions of mineralised fibrils that did not exhibit any banding pattern are present in both, WT and OIM tissues (B, D, Figure 6.2). SAED patterns showed that crystallographic (002) planes of apatite crystals were still oriented parallel to fibrils.

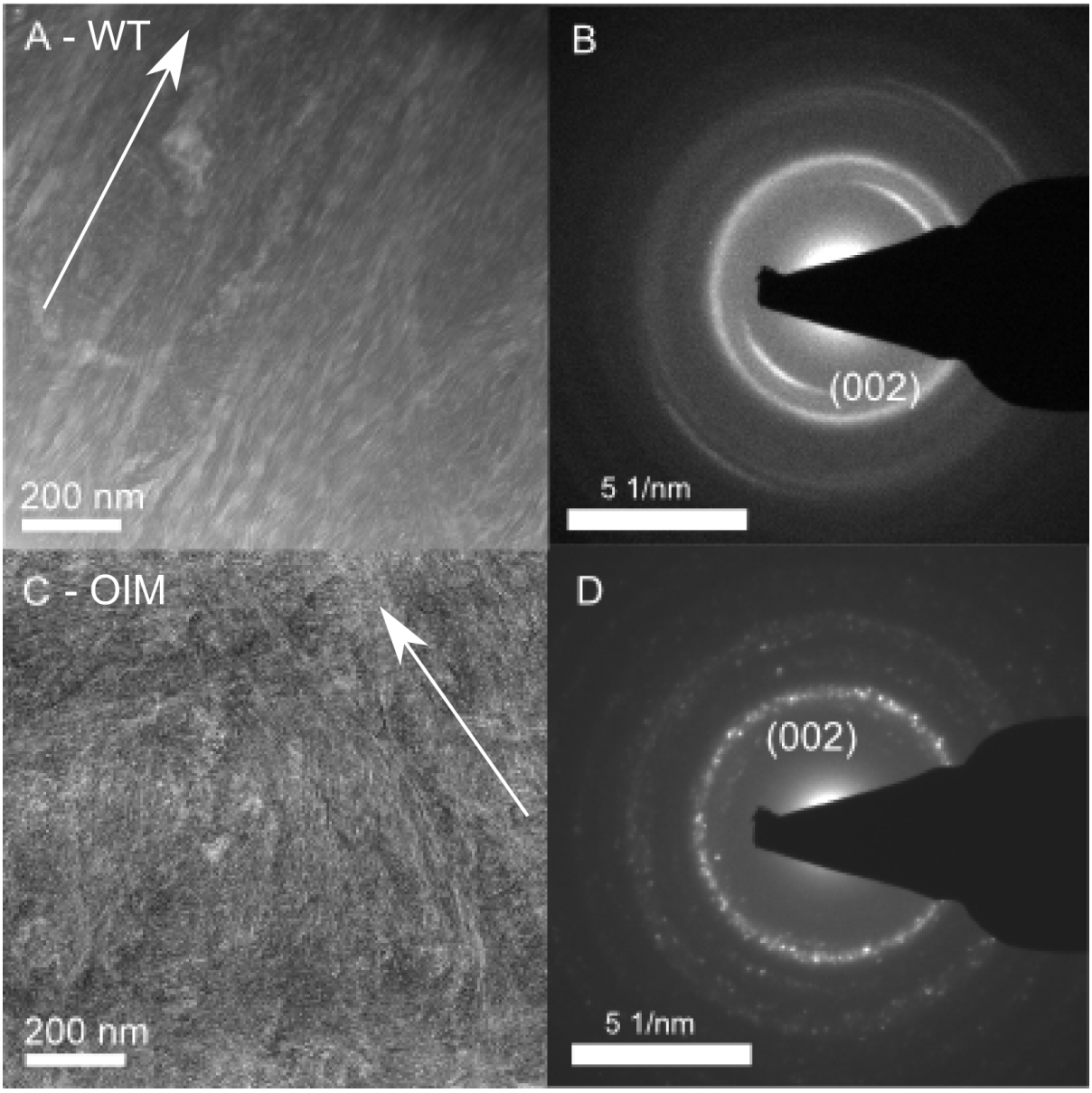


Figure 6.1 Representative BF-TEM images of FIB-milled wild type (A) and osteogenesis imperfecta (C) bone with corresponding SAED patterns (B, D). White arrows indicate the direction of the fibrils. WT regions exhibited a distinctive banding pattern (A) and characteristic arcs of (002) plane reflections from HA in the SAED patterns (B). Banding in OIM tissues is often absent and the fibrils appear disorganised (C), but faint arcs of (002) plane reflections can still be observed (D).

SAED diffraction patterns collected from various regions of WT and OIM tissue exhibited very similar texturing in organised (A, C, Figure 6.2) and disorganised regions (B, D, Figure 6.2). In disorganised regions, the (002) arcs appeared longer and in most extreme cases (B, D,

Figure 6.2), full rings corresponding to (002) reflections in HA could be observed. However, a small degree of order might be still maintained as the ring showed an increase in the intensity in one direction (B, D, Figure 6.2). The orientation of crystals in WT and OIM tissue was assessed by measuring the angles of arcs of the (002) plane reflections of the SAED patterns (Figure 6.3). The mean arc angle was similar in WT and OIM tissues; however, the spread of data was more significant in OIM. These findings are in line with studies showing similar mean values of the periodic banding in WT and OIM, but the OIM has a wider distribution of values [263].

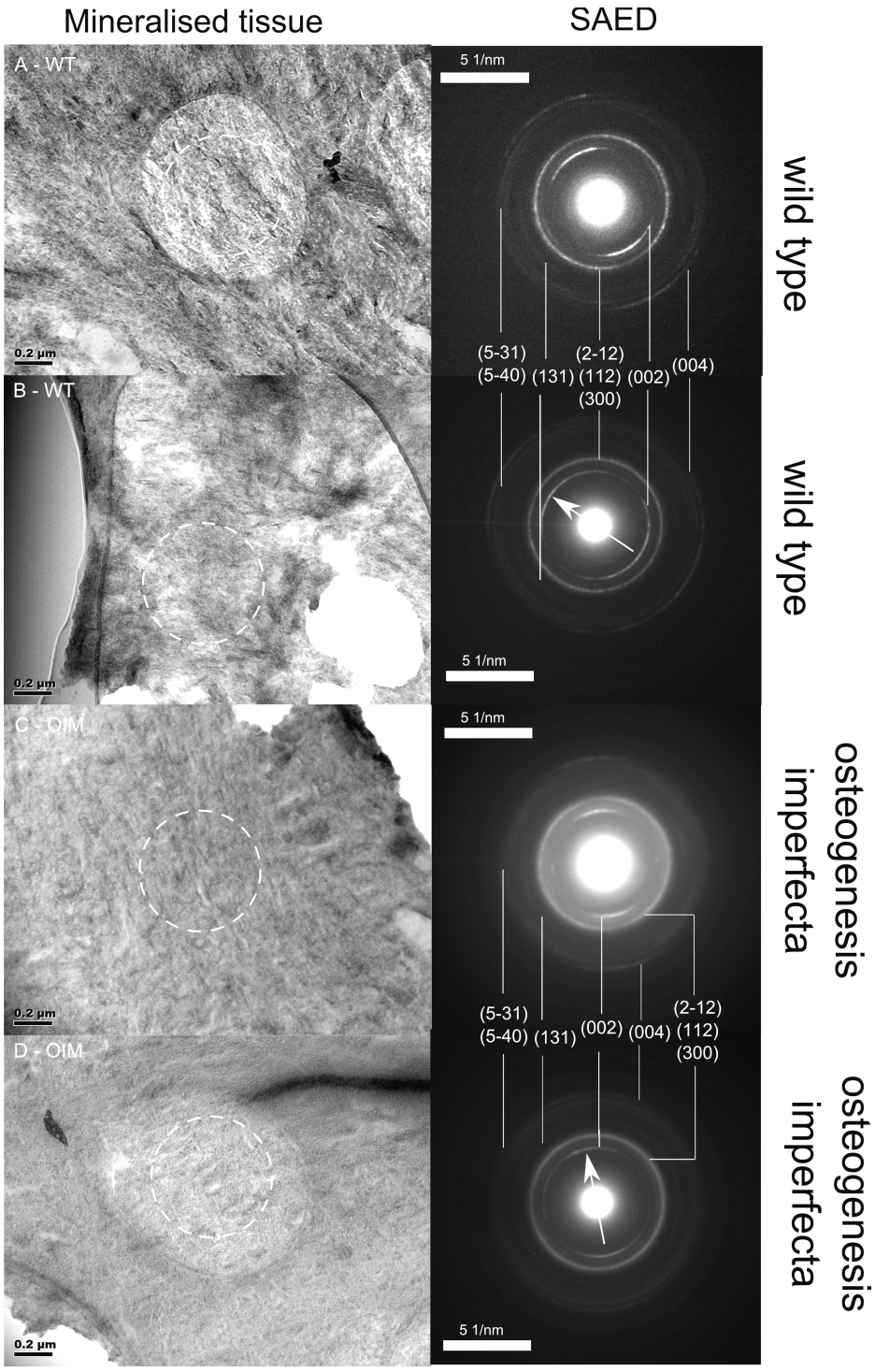


Figure 6.2 Representative BF-TEM images of microtomed wild type (WT, A, B) and OI-affected (OIM, C, D) bone regions with corresponding indexed SAED patterns. Dashed circles show regions without a distinctive banding pattern (A, C), which still show oriented (002) arcs. In the more disorganised regions (B, D), full rings are formed. White arrows on the SAED patterns indicate the most intense regions of rings.

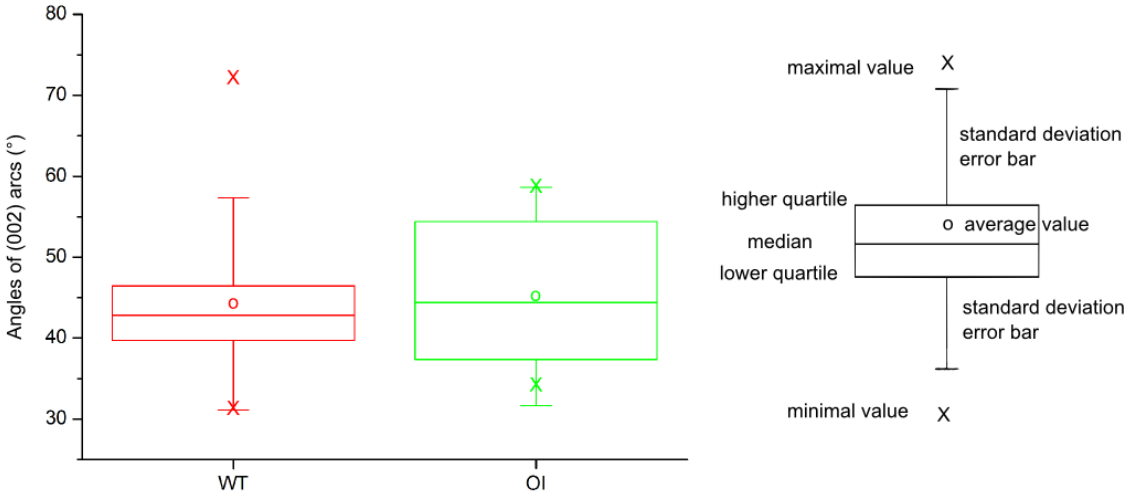


Figure 6.3 Changes in the length of the (002) arcs between wild type (WT) and osteogenesis imperfecta (OIM) specimens (n=30, for each group). WT and OIM arcs have a similar mean length, but the distribution of OIM arc length is much wider.

The orientation of the fibrils is more distorted across the length scale of few micrometres in OIM than in WT tissues [90] (Figure 6.4), which will contribute to disorganisation of fibrils reported at the bulk level [258].

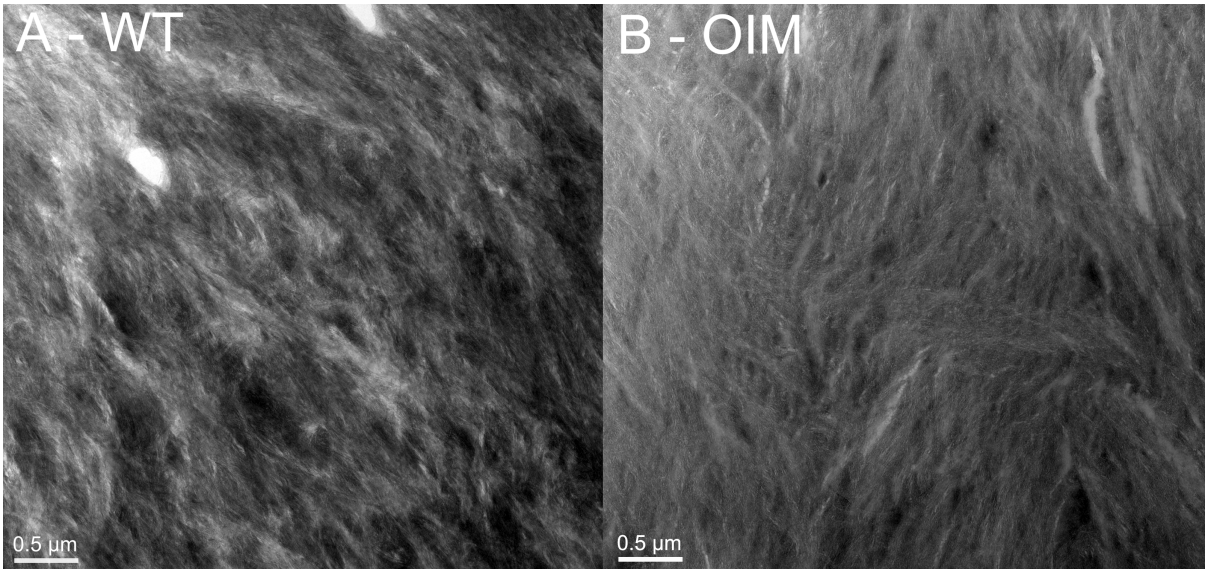


Figure 6.4 Representative BF- TEM images of WT (A) and OIM (B) bone at low magnification. Fibrils in OIM bone appear more totuous and tend to branch and change direction more across smaller length scales than in the control WT tissue. This is a characteristic architecture of 'woven' fibrils.

6.4. Nano-meter scale modifications of non-mineralised tail tendon morphology of collagen in wild type (WT) and osteogenesis imperfect (OIM) mouse models

Non-mineralised tail tendon collagen was used to identify collagen matrix modifications. In both, wild type and OIM collagen, mature fibrils were found. Examination of stained longitudinal sections revealed a sub-banding pattern previously described by Chapman [12] (Figure 6.5). Cross-comparison of these sub-banding features between WT and OIM did not show any significant differences in the length of the gap, overlap and full period (Table 6.1).

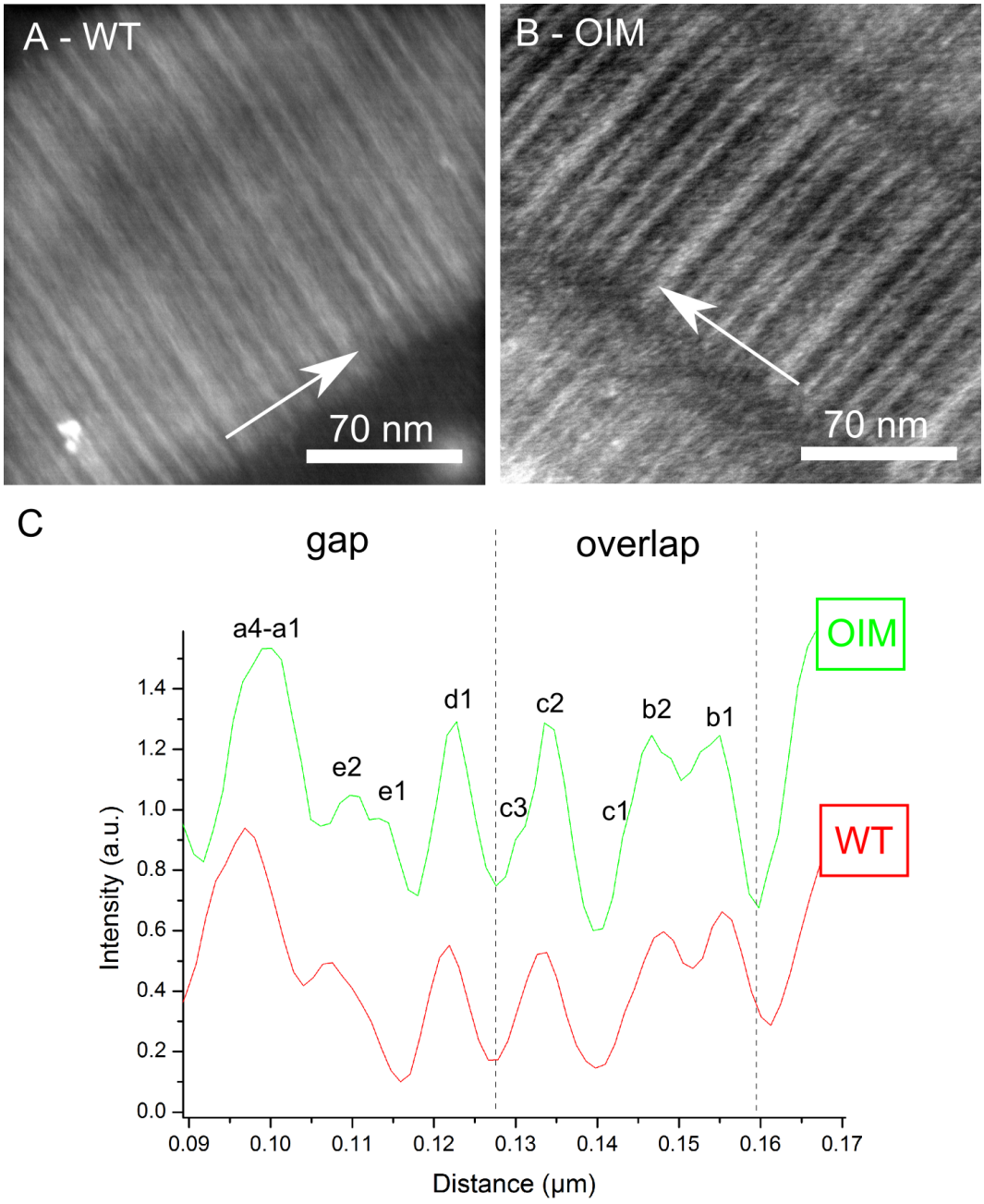


Figure 6.5 Representative ADF-STEM images of longitudinal sections of osmium-stained, non-mineralised tail tendon of wild type (WT, A) and OI-affected (OIM, B) mice with corresponding intensity line profiles (C). White arrows indicate the direction of the line profiles. The sub-banding pattern originates from accumulation of osmium in the bands. Bands are labelled as in work of Chapman [12] and attributed to the gap and overlap regions.

Table 6.1 Length of gap, overlap and the full period measured separately in osmium tetroxide-stained, non-mineralised tail tendon of wild type (WT) and OI-affected (OIM) mice, prepared by high pressure freezing and freeze-substitution (n=20).

	Gap (nm)		Overlap (nm)		Period (nm)	
	WT	OIM	WT	OIM	WT	OIM
Mean	37.8	38.1	27	28.4	64.9	65.6
St.dev.	2.7	1.8	1.2	1.7	2.5	1.7

Investigation of transverse section of mouse tail tendon showed regions composed of circular fibril cross-section (Figure 6.6). The assessment of the cross-sectional area revealed that, while average fibril cross-sections are similar in WT and OIM specimens, OIM fibrils rarely grow to sizes observed in WT tissues.

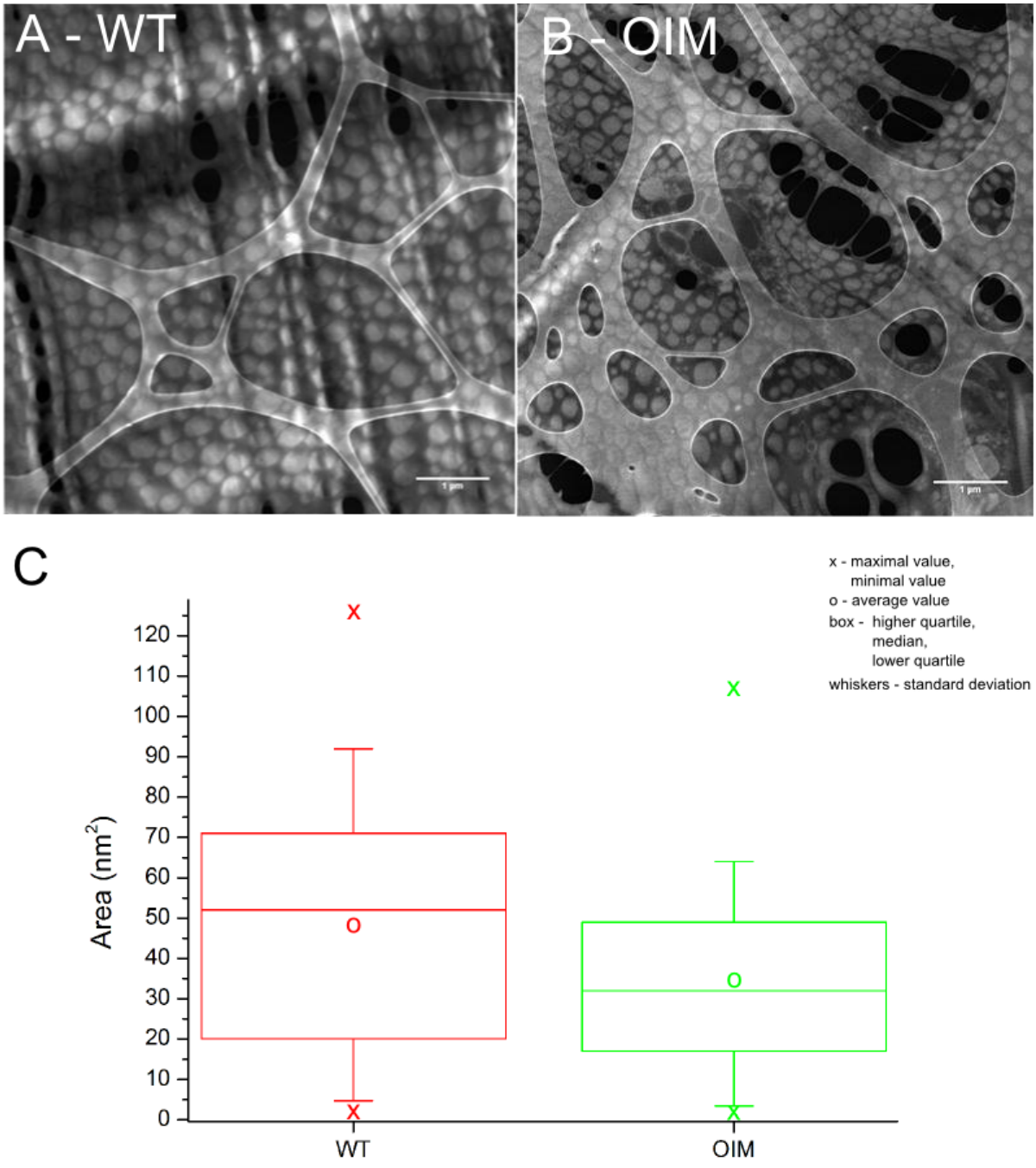


Figure 6.6 Representative ADF-STEM images of transverse sections of mature, osmium-stained, non-mineralised tail tendon of wild type (WT, A) and OI-affected (OIM, B). (C) Comparison of fibril cross-sectional area (n=150).

Disorganised fibrils, as well as mature, fully developed fibrils, are present in OIM (Figure 6.7, Figure 6.8, Figure 6.9, Figure 6.10) and WT (Figure 6.11) collagen. In OIM tissues, regions, with poorly packed, fibrillar structures were encountered more frequently.

Disorganisation of collagen matrix in tail tendon was observed in tendon at two hierarchical length scales: micro- and nano-meter, respectively. At the micro-meter scale, fibrils were loosely packed and kinked fibrils were visible (Figure 6.7). In these regions, formation of many circular and poorly packed assemblies of fibrils was observed (Figure 6.8, Figure 6.9).

In previous reports, similarly deformed fibrils were observed only *in situ* [246]. Modelling studies of collagen molecules in OI model suggest that malformation of collagen triple helices result in kinked molecules, which limit or even prevent formation of a mature fibril [249,264].

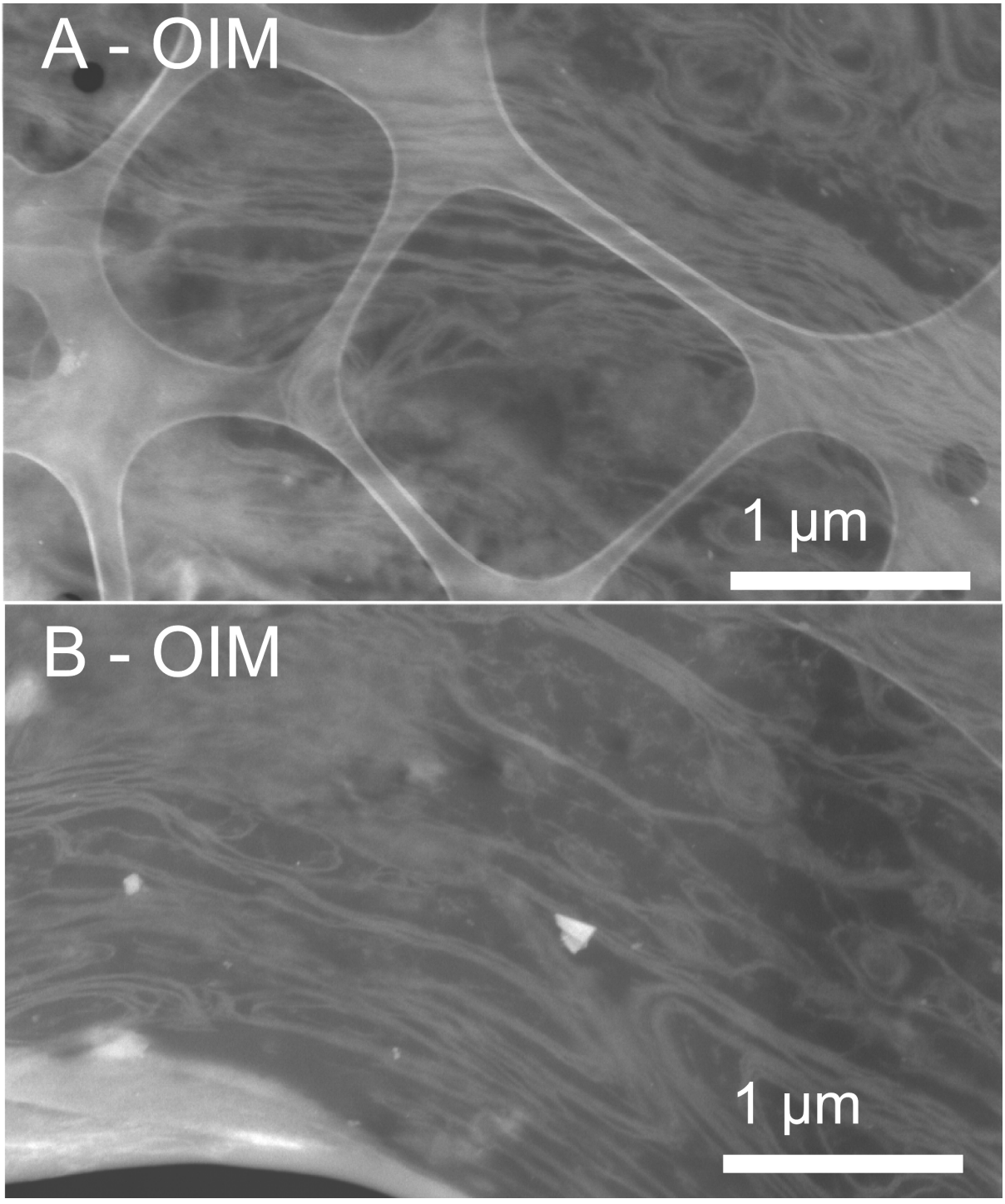


Figure 6.7 Representative ADF-STEM images of longitudinal, irregularly oriented, poorly packed collagen fibrils of OI-affected (OIM) mice. Fibrils are grouped into loose bundles (A) and may bend extensively (B).

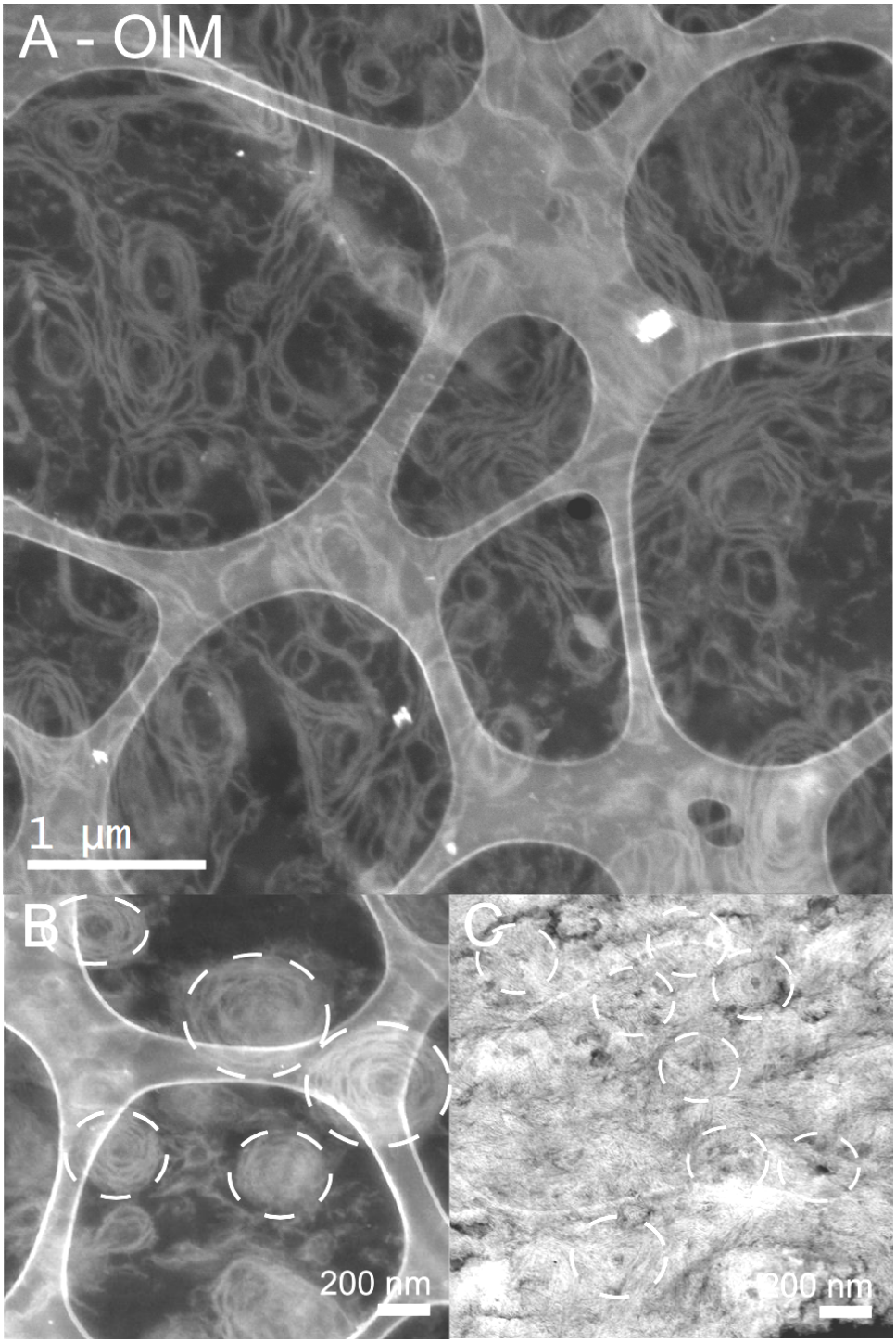


Figure 6.8 Representative ADF-STEM images of disorganised collagen fibrils (transverse sections) of OIM mouse tail tendon showing circular assemblies of collagen (A). Some assemblies seen in non-mineralised tail tendon (B) resemble circular formations seen in mineralised bone (C). Features in the mineralised tissue appear smaller, which suggest that mineral growth might limit the growth of the collagen assemblies.

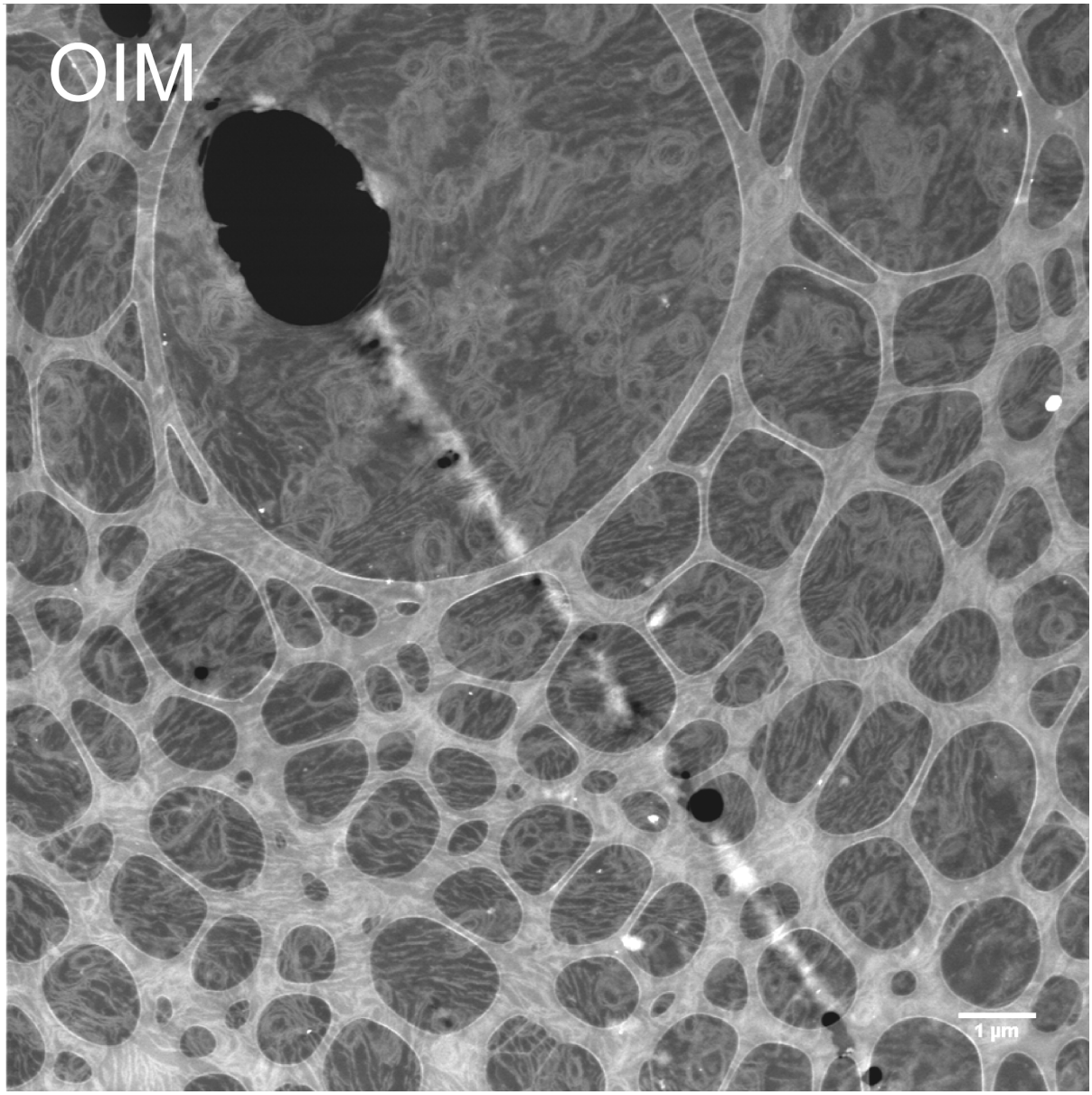


Figure 6.9 Representative ADF-STEM image of loosely packed collagen fibrils and circular collagen assemblies of OI-affected (OIM) mouse tail tendon.

In the second group (at the nano-meter scale), fine sub-fibrils were tightly packed and individual sub-fibrils were difficult to distinguish (Figure 6.10, Figure 6.11A). These disorganised regions appear to consist of finer sub-fibrils (10 nm in diameter), which still display a faint banding pattern (Figure 6.10). Such regions have been observed previously in OI tissues at a relatively low resolution [265]. These tightly packed bundles may develop from loosely packed regions, as deformed fibrils accumulate with time. Features of the tightly packed regions resemble microribbons, which form at the early stages of collagen assembly

[266]. Regions containing such microribbons were also observed in the control WT tissues, but were present in smaller quantities (Figure 6.11B). In WT tissue, circular assemblies or significant kinking of fibrils were rarely observed. The presence of microribbon-like structures in OIM tissues could be an effect of a more intense turnover of the collagen matrix [239]. If these microribbon formations arise due to malformation of collagen, we are the first, who observe the initial steps of the fibril formation process *in vivo* at the high spatial resolution (Figure 6.12).

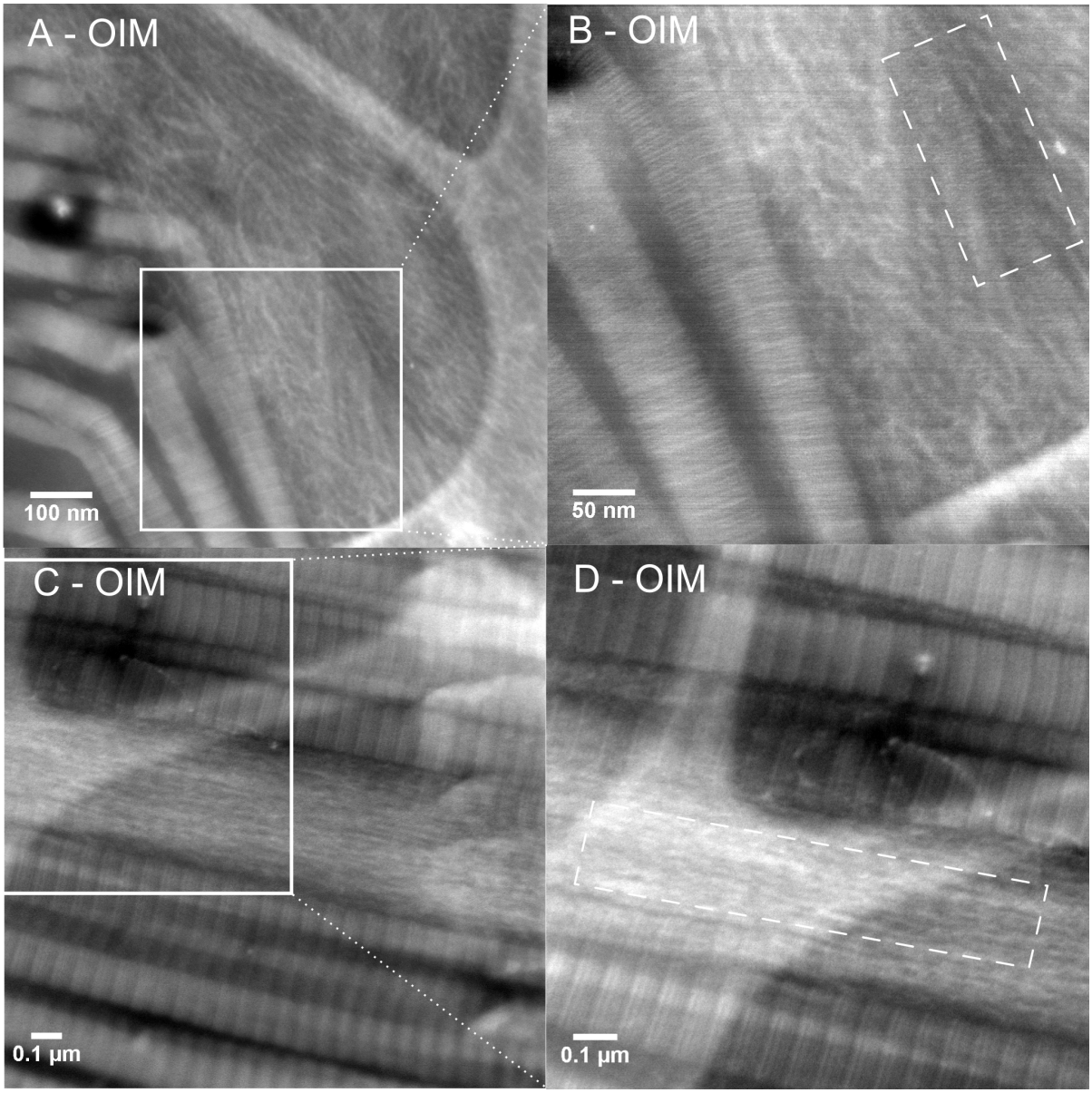


Figure 6.10 Representative ADF-STEM images of longitudinal sections of OIM collagen fibrils. Regions containing mature fibrils coexist with regions of tightly packed microribbons (A, C). In disorganised regions, a faint banding pattern can be observed (dashed boxes, B, D).

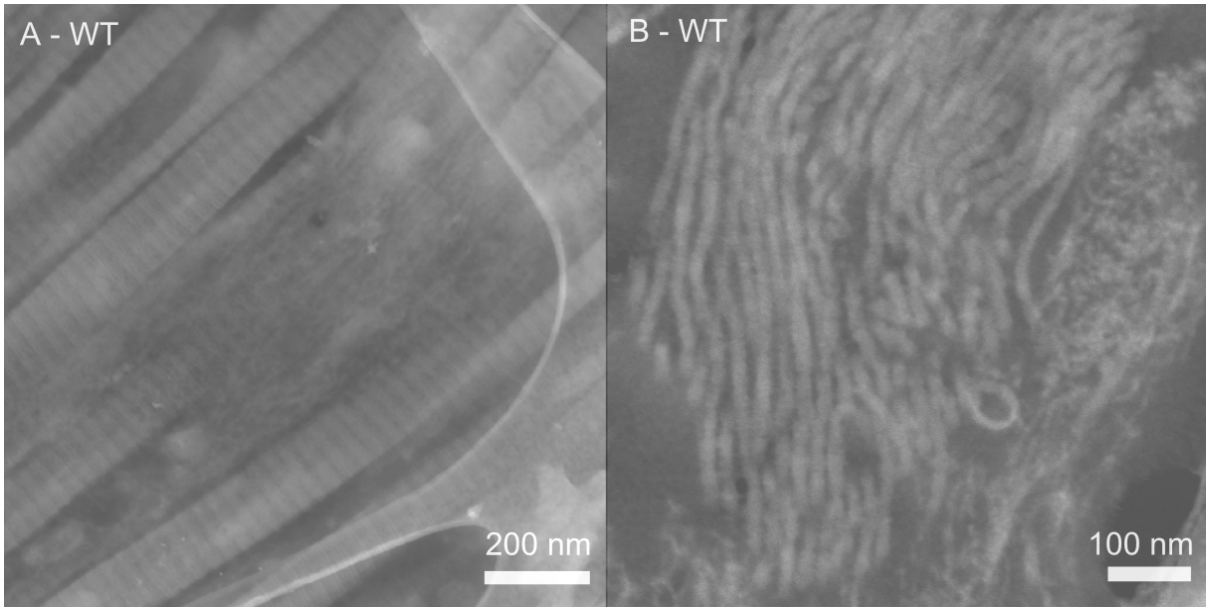


Figure 6.11 Representative ADF-STEM images of a disordered collagen matrix in tail tendon of wild type (WT) mice. (A) Tightly packed bundles of fine fibrils. (B) Bundles of 10nm-thick fibrils exhibiting hints of the banding pattern. These fibrils appear shorter than fibrils observed in OIM (Figure 6.7), which might be a result of sectioning at an oblique angle.

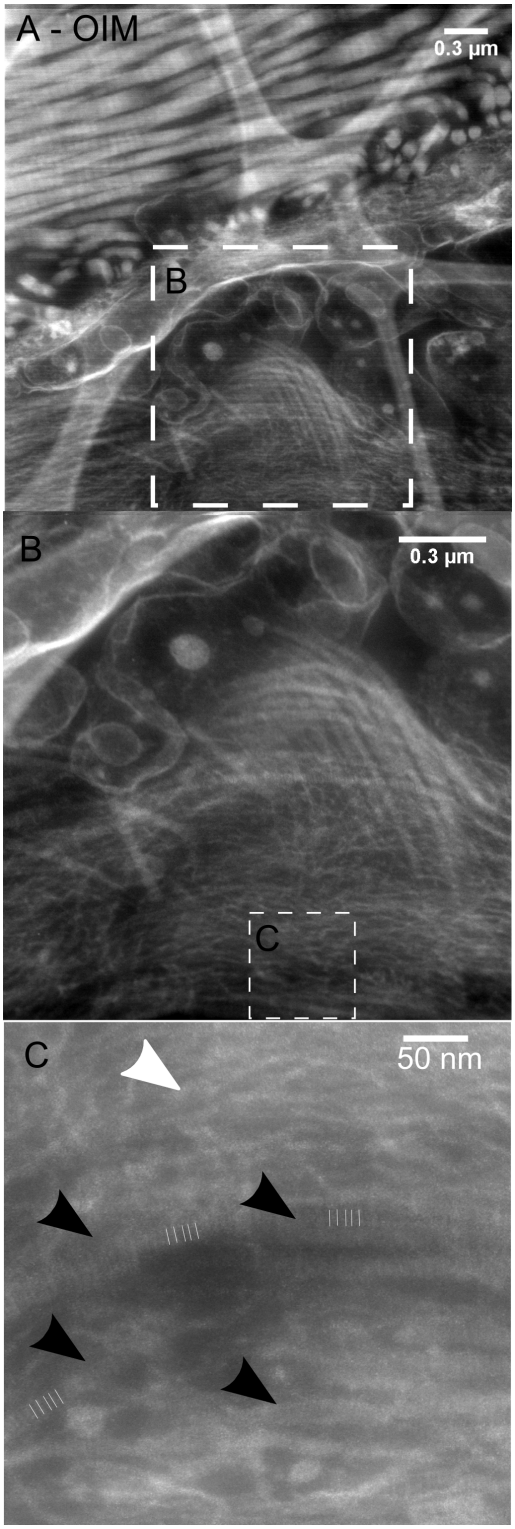


Figure 6.12 Fibril development in tail tendon of OI-affected (OIM) mice. (A) Region consisting of mature (top) and immature (bottom) fibrils. (B) Higher magnification image of the boxed region in A showing disorganised, short filaments. (C) Disorganised filaments (sub-fibrils, white arrowhead) with wider, banded fibrils (black arrowheads, lines are highlighting the faint sub-banding).

6.5. EELS analysis of the chemical composition of the collagen and mineral in wild type (WT) and OI-affected (OIM) models

No significant variation was observed in EELS spectra taken from microtomed sections and sections prepared by FIB milling.

6.5.1. Phosphorus $L_{2,3}$-edge

In the near-edge structure of the phosphorus $L_{2,3}$-edge three main peaks were observed: A, B and C at ~138, ~141 and ~147eV, respectively. These features were followed by a broad feature D with maximum at ~160eV (Figure 6.13). Phosphorus spectra were normalised and aligned to the first peak A, which was set to an energy-loss of 138 eV based on the literature [195].

Peaks A and C were formed due to transitions from core 2p to a p-like (A) and a d-like (C) states, respectively [195]. Peak B was observed in calcium-containing minerals [195]. Peak D was attributed to a cross section maximum of 2p state transitions and multiple scattering [198].

The phosphorus signal was not observed in non-mineralised mouse tail tendons. In mineralised tissues, the phosphorus $L_{2,3}$-edge features closely matched features previously observed in well mineralised turkey tendon (Figure 6.13).

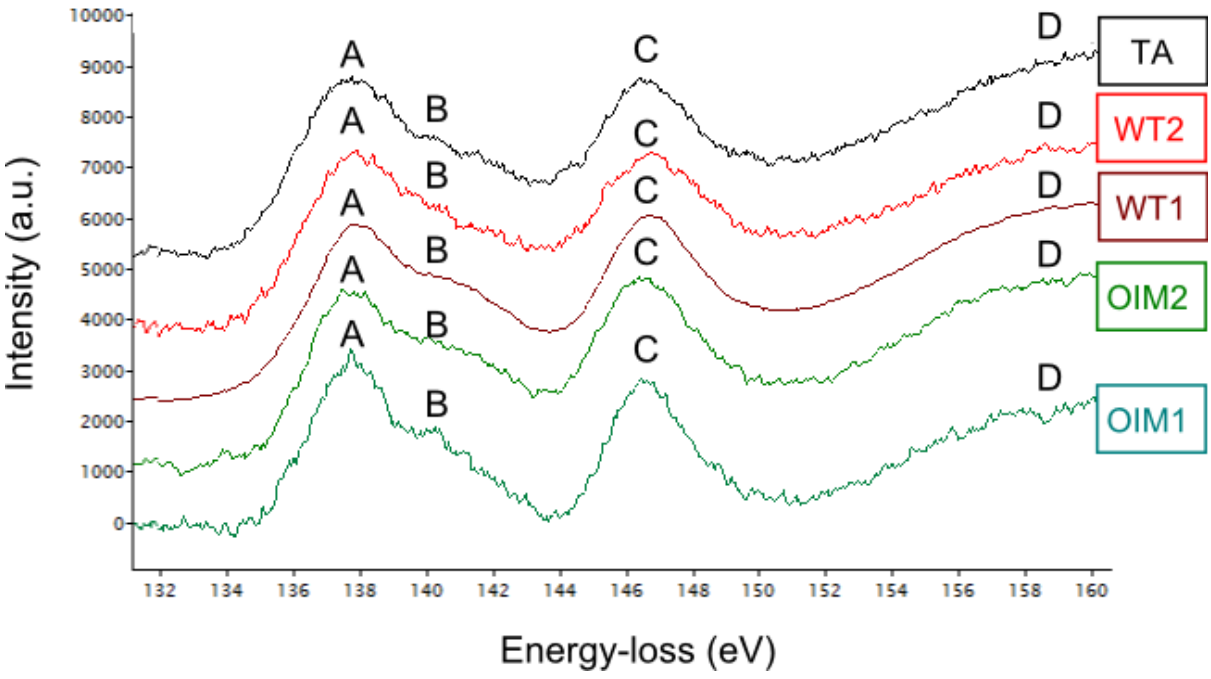


Figure 6.13 The phosphorus $L_{2,3}$ near edge structures of wild type (WT) and OIM mouse bone and well mineralised turkey tendon (TA).

6.5.2. Carbon K-edge

In non-mineralised mouse tail tendon (Figure 6.14), the carbon edge structure consisted of initial double peaks A and B at ~285 and ~286 eV, respectively, followed by a broad peak C starting at ~296 eV. Spectra of non-mineralised tendon were normalised and aligned using peak A, which was set to 285eV based on the literature [204,226]

There are 3 groups of spectra on Figure 6.14 graded by the relative intensity of peak B: (a) TN and WTn1, (b) WTn2 and OIMn1, (c) OIMn2. In group (a), features observed in the carbon K-edge of non-mineralised mouse tissues showed similarities (intense peak B) to spectra previously recorded in non-mineralised turkey tendon tissues (TN on Figure 6.14, see also section 5.3.4.2). In spectra from group (b), peak B is less intense. Spectra from groups (a) and (b) were collected from fibrils showing banding pattern. The change of spectral signature could not be correlated with any change in morphology of the tissue. Spectra represented by group (c), showing the most significant decrease in the intensity of peak B, were recorded only from regions showing sub-fibrils in OIM tail tendon samples.

Peak A and C originated from 1s-π* and 1s-σ* C-C transitions, respectively [204]. The origin of peak B was extensively discussed in Chapter 5 (see section 5.3.4.2) and can be assigned to transitions to molecular orbitals of carbon or carbonyl groups in an aromatic conformation. Spectra collected from regions of disorganised fibrils, in comparison to fully formed fibrils (OIMn2 vs. OIMn1, regions shown on Figure 6.15, spectra shown on Figure 6.14), showed a decrease in the intensity of peak B connected with the presence of aromatic carbon. The decrease of the relative intensity of peak B might be connected with lower number of aromatic rings and suggests a decrease in the levels of phenylalanine, tyrosine or mature, enzymatic, pyridine-based crosslinks.

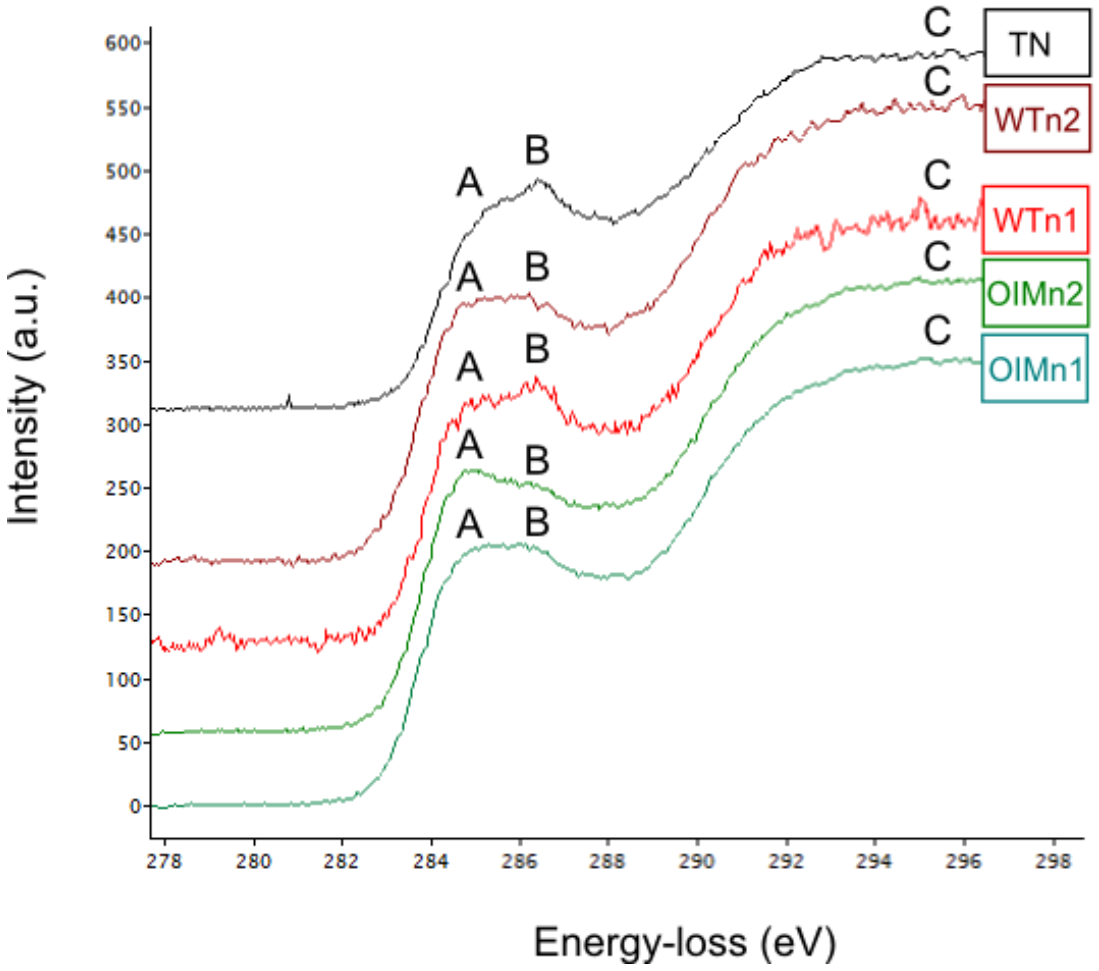


Figure 6.14 The carbon K near edge structures of non-mineralised, osmium tetroxide-stained, wild type (WT) and OIM mouse tail tendon fibrils and non-mineralised, non-stained turkey tendon fibrils (TN). OIMn1 spectra were taken from a mature fibril (Figure 6.15). OIMn2 spectra were taken from a poorly organised region of sub-fibrils.

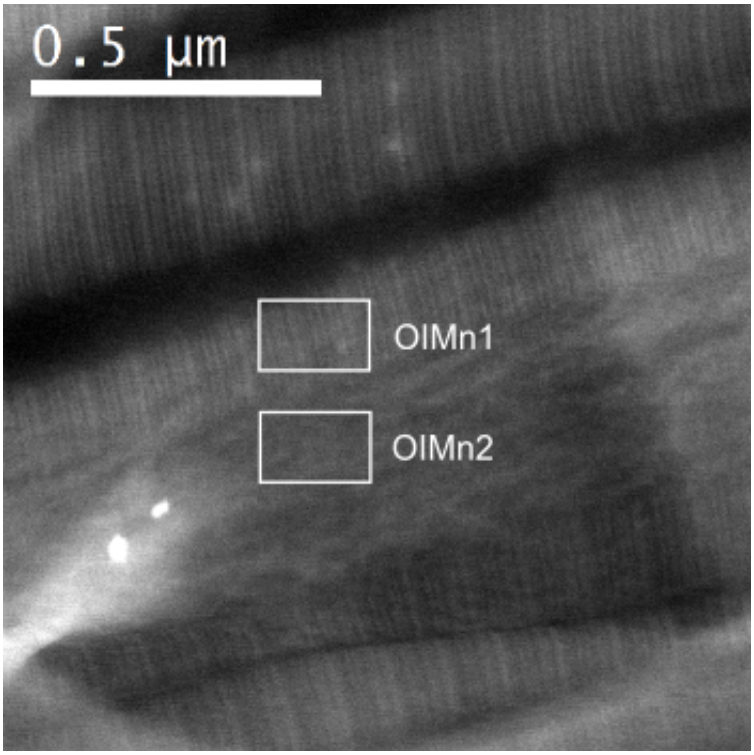


Figure 6.15 Representative ADF-STEM image of longitudinal, osmium-stained OIM mouse tail tendon collagen showing regions, from which spectra OIMn1 and OIMn2 were collected.

In mineralised tissues, the assignment of first peak is open to interpretation due significant experimental noise. In majority of spectra collected from WT and OIM bone, peak A at ~285eV was absent or present only in the form of a more intense shoulder on peak B (WT1, OIM2, Figure 6.16). Spectra of OIM and WT bone (Figure 6.16) usually started with peak B at ~286eV. Peak B was followed by small peaks C at ~287eV and C* at ~288eV, and a pronounced peak D at ~290eV. Peak D was found more frequently in OIM bone. Finally, a broad peak E started at ~292 eV. Spectra of mineralised tissue were normalised to peak B and calibrated to peak D set to standard 290eV based on the literature [177].

Characteristic energies corresponding to different types of molecular bonds are presented in Table 6.2. Peak A was assigned to 1s-π* C-C transitions [204]. Peak B was assigned to transitions in aromatic carbon or carbonyl groups [200,201,227,228]. Assignment of peaks C and C* was not straightforward. Peak C can be attributed to 1s-σ* C-H transitions in an aliphatic [230] or a diamond-like bond [231], 1s-π* C=O transitions in peptide bonds in carbonyl [227,231] or amidyl [230] and 1s-π* C=O transitions in carboxyl [230]. Electron transitions resulting in the formation of peak C* might be connected to C≡N, C=O, C=C or C-H excitations in nitrile, enol, aliphatic or aromatic groups [179,227,228,230]. Peak D was characteristic of carbonate 1s-π*-A transitions [177]. The broad peak E was assigned to 1s-σ* C-C transitions [204].

Table 6.2 Approximate transitions in 285-294eV range in carbon K-edge fine structure and assignments of peaks

Peak	Bonds and example assignments	Energy-loss (eV)
A	Double-bonded carbon C=C, amorphous carbon, graphite , protonated or alkylated aromatic carbon, peptide nucleic acid	284.9-285.5 [200,201,204,228,267,268]
B	Aromatic carbonyl C=O, aromatic C-OH	285.8-286.5 [200,201,227,228,230,269]
B, C	Nitrile C≡N	286.7-286.9 [230]
C	Aromatic C-OH, aliphatic C=O, enol C-OR	287.1-287.4 [200,201,228,230,270–272]
C*	Aromatic carbonyl C=O, amidyl	287.7-288.3 [200,201,228,230,269]
C*	CH_3, CH_2, CH	287.0-288.5 [200,201,228,230,273,274]
C*, D*	Carboxyl COOH, COO, carboxyamide, C=N, C-N	288.0-288.7 [200,201,227,228,230,271,275]
D*	C-OH, alcohol, polysaccharide	289.3-289.5 [200,201,228,230,271,272]
D	Carbonate	290.0-290.2 [177,204,230]

The greatest difference between wild type (WT) and OIM spectra was in the presence and intensity of peak D, which is characteristic of transitions of carbonate groups. Furthermore, in OIM spectra showing the most intense peak D (OIM3, OIM4, Figure 6.16), formation of fine peaks on peak E was observed, which might be assigned to carbonate 1s→σ*-C and π*-C transitions [178]. In WT bone, the carbon edge fine structure is similar to that seen in mineralised turkey tendon (TW, Figure 6.16).

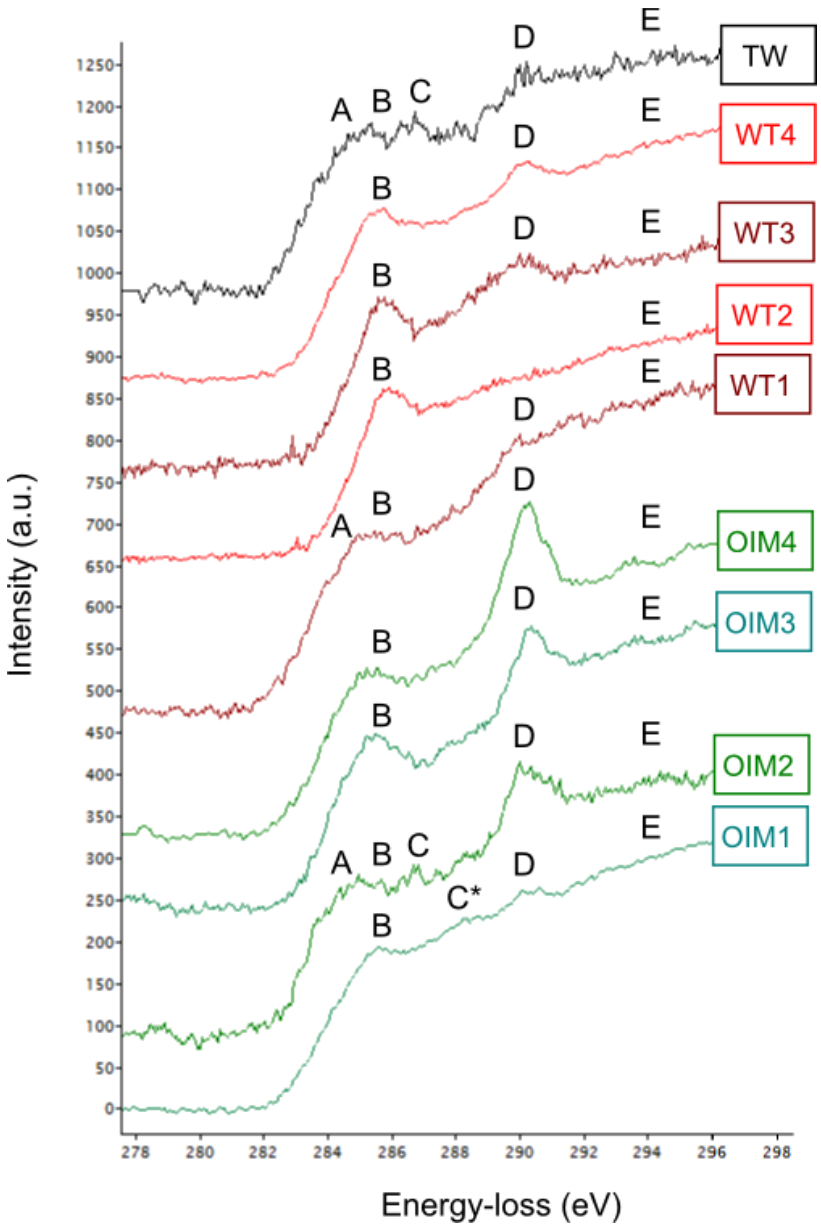


Figure 6.16 The carbon K near edge structures of mineralised bone of wild type (WT) and OIM mice, and well mineralised turkey tendon (TW). The carbonate peak E at ~290eV observed in OIM species is much more intense than in WT.

In attempt to resolve modifications of the carbon K-edge between WT and OIM tissues, monochromated STEM-EELS experiments were performed (Figure 6.17). Spectra were collected from intra- and extrafibrillar regions identified on the transverse sections of WT and OIM bone (II and III on Figure 6.17). Examination of transverse sections of WT and OIM bone revealed fine structure (peaks C, C*, D* at ~287, ~288 and ~289eV, respectively, on Figure 6.17 I), which was difficult to resolve in non-monochromated experiments.

Assignments of peaks A, B, C, C* and D were discussed above and are presented in Table 6.2. Peak D*, which was not observed in the non-monochromated experiments, might originate from transitions in various carbon-oxygen and carbon-nitrogen groups in nucleic acids [179,230,235].

Peaks in the energy range 286-290 eV were less evident (less intense and more obscured by noise) in OIM spectra. These peaks are mostly related to functional groups associated with organic compounds, which suggests a less developed protein structure (e.g. decrease in collagen crosslinking). The intensity of carbonate peak D increased in the intrafibrillar regions of WT and OIM tissues.

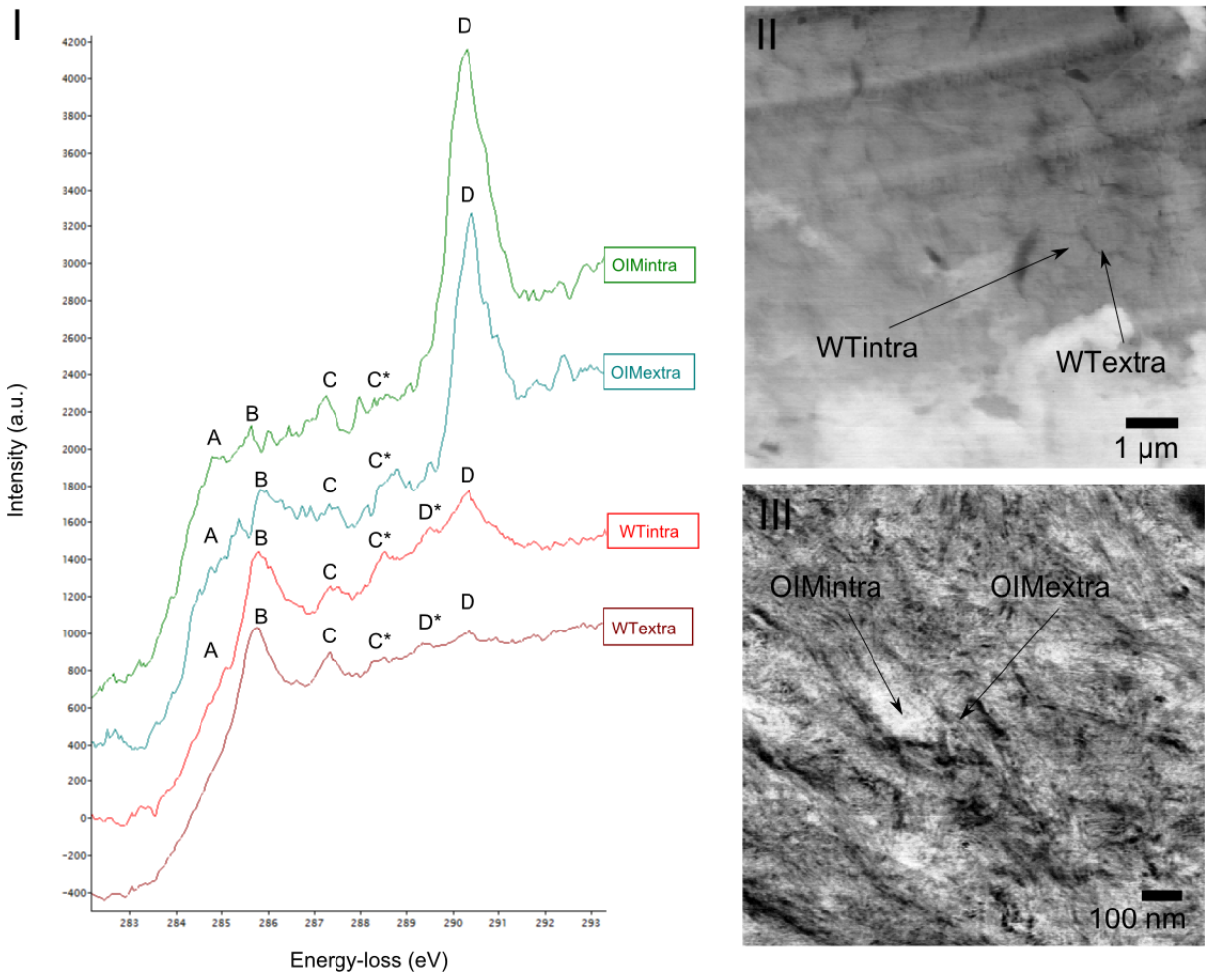


Figure 6.17 (I) The carbon K near edge structures of intra- and extrafibrillar regions of mineralised bone of wild type (WTintra/extra) and OIM (OIMintra/extra) mice taken from transverse sections of the tissue. (II) ADF-STEM image of a transverse WT section showing intra- (WTintra) and extrafibrillar

(WTextra) regions. Additional (see Figure 6.16) peak D* is observed in the WT spectrum. The intensity of the carbonate peak D increases in intrafibrillar regions. (III) ADF-STEM image of a transverse OIM section showing intra- (OIMintra) and extrafibrillar (OIMextra) regions. Peaks in the 286-289eV range are more difficult to resolve in OIM bone.

6.5.3. Calcium $L_{2,3}$-edge

The calcium signal was not present in non-mineralised mouse tail tendons. In mineralised bone, the calcium $L_{2,3}$-edge spectra exhibited characteristic, white line peaks A and B at ~348 and ~351 eV, respectively (Figure 6.18). Calcium spectra were aligned and normalised to the peak A, which was set to 348 eV based on literature [180].

Calcium $L_{2,3}$ edge spectra of OIM and WT bone were comparable with spectra observed in well mineralised turkey tendon (TW, Figure 6.18)

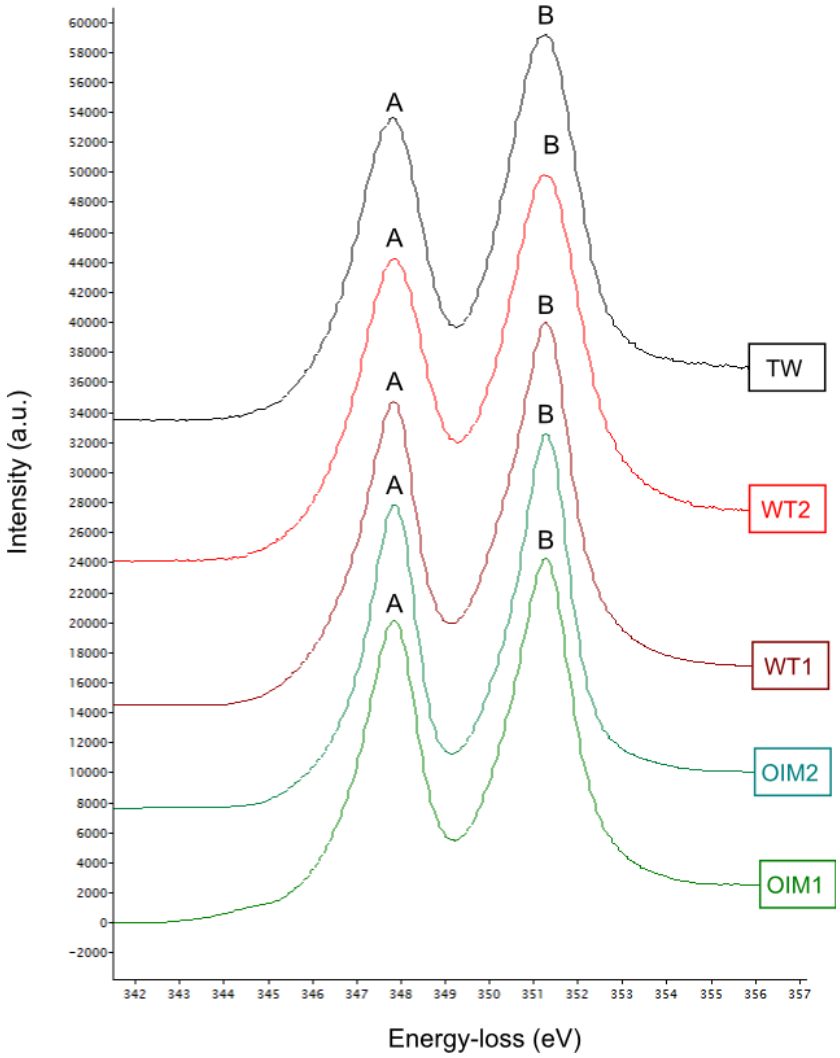


Figure 6.18 The calcium $L_{2,3}$ near edge structures of wild type (WT) and OIM mouse bone and well mineralised turkey tendon (TW).

6.5.4. Nitrogen K-edge

In non-mineralised mouse tail tendon collagen, the nitrogen edge features were difficult to resolve (Figure 6.19). The nitrogen edge in mouse tail collagen exhibited two peaks A and B at ~400 and ~401 eV, respectively, followed by a broad peak C at ~408 eV. The nitrogen K-edge was normalised to most intense peak (A or B). The calibration of energy scale was confirmed by observation of the zero loss peak before and after the acquisition.

As discussed in section 5.3.4.4, peak A is thought to be associated with 1s-π* transitions from nitrogen incorporated in an aromatic ring, especially pyridine [228,232–234], which is essential part of collagen crosslinking. Peak B might be connected with oxidised pyridine [228,232], 1s-π* transitions in the nitrated carbon structure [229,233] or 1s-π* transitions in amide groups (C=ONH) [235]. The broad peak C is attributed more generally to 1s-σ* transitions in amino compounds [228].

The presence of two peaks (A and B) in turkey tendon was not observed in non-mineralised regions. Mouse tail tendon is not mineralised; however, the tail tendon sections were stained with osmium tetroxide, an oxidising agent, which may have an impact on the pyridine-based structures.

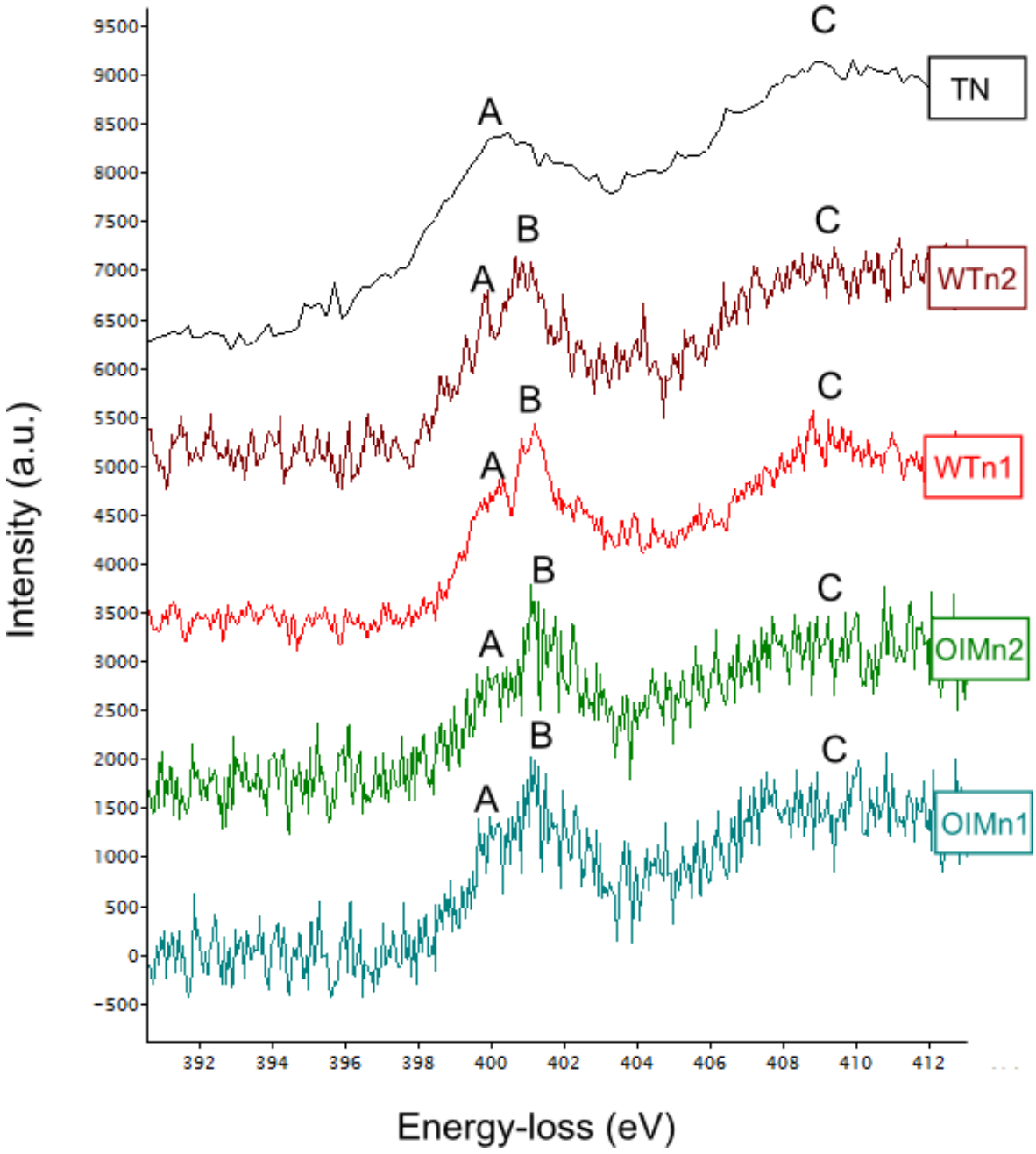


Figure 6.19 The nitrogen K near edge structures of non-mineralised, osmium-stained, wild type (WTn) and OIM (OIMn) mouse tail tendon fibrils and non-mineralised, non-stained turkey tendon fibrils (TN).

The nitrogen K-edge spectra of mineralised OIM and WT bone (Figure 6.20) exhibited more distinct peaks A and B than in tendon. Also a large variation in the relative intensity of peaks A and B is observed in bone (compare WT1 vs. WT2 and OIM1 vs. OIM2, Figure 6.20; OIM spectra taken from regions shown on Figure 6.15). Nitrogen spectra in mineralised tissue

were aligned to the peak A of calcium edge set to 348 eV based on literature [180] and normalised to the most intense peak (A or B).

Monochromated STEM-EELS was employed to resolve the origins of variation seen in the intensity of peaks A and B, which were suspected to originate from changes in the oxidation of pyridine rings (Figure 6.21). Spectra were collected from intra- and extrafibrillar regions of fibrils identified in the transverse sections of WT and OIM bone (II and III on Figure 6.17). There is a difference in the intensity of nitrogen K-edge peaks observed between WT and OIM bone. Peaks in WT spectra are more intense and distinct; peaks in OIM spectra are less intense and obscured by noise. These differences may be connected with relatively lower protein content in OIM tissue.

Spectra collected from the intrafibrillar region exhibited an increase in the intensity of peak B (attributed to oxidised pyridine), while spectra collected from the extrafibrillar regions show an increase in the intensity of peak A (attributed to pyridine). It has been suggested that mineral nucleates inside collagen (in the intrafibrillar spaces) [15]. Changes observed in pyridine oxidation between intra- and extrafibrillar regions may reflect the stage of collagen matrix maturation [61] and the capability to nucleate and proliferate the mineral components [49,60–64].

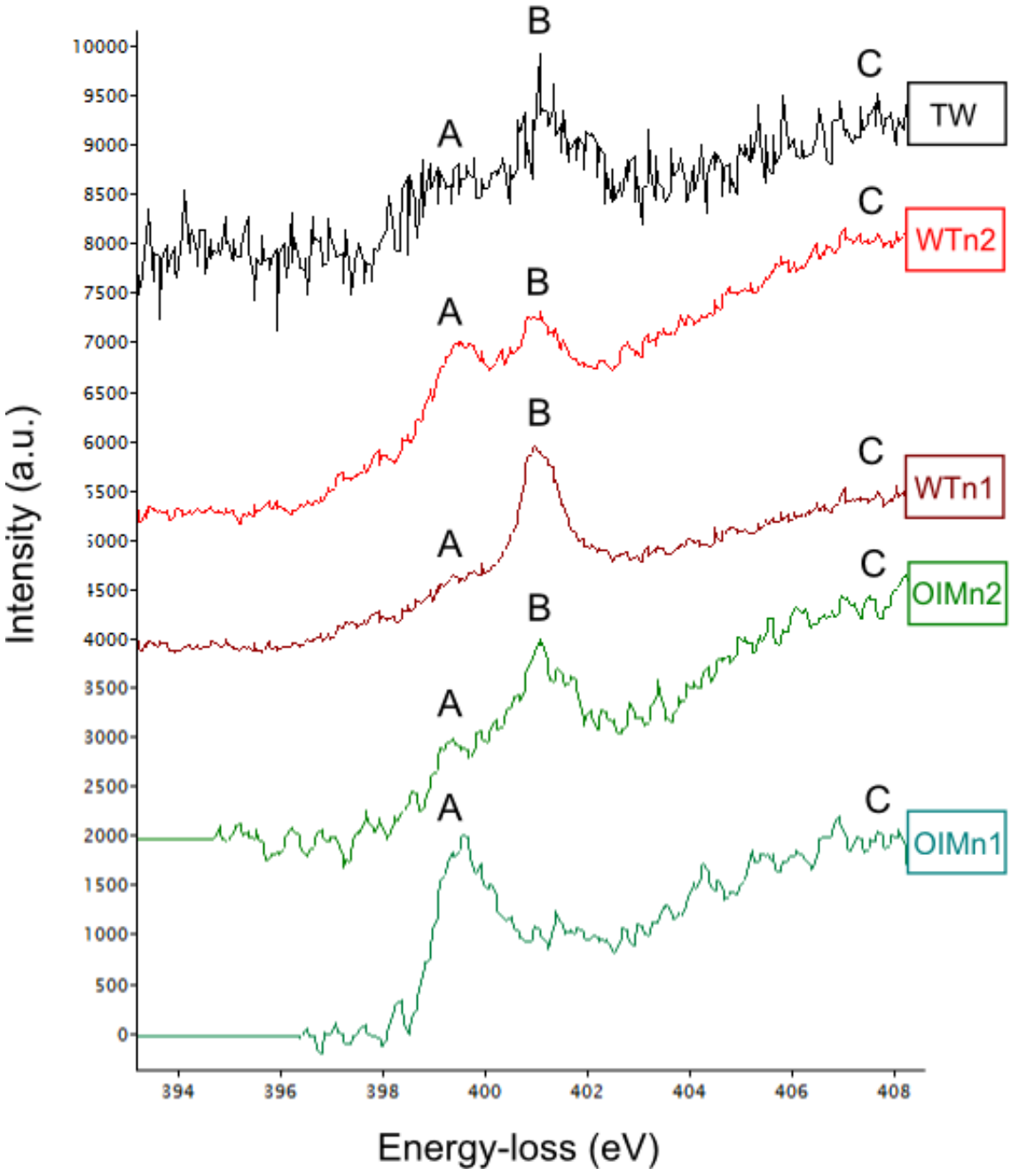


Figure 6.20 The nitrogen K near edge structures of mineralised bone of wild type (WT) and OIM mice and well mineralised turkey tendon (TW).

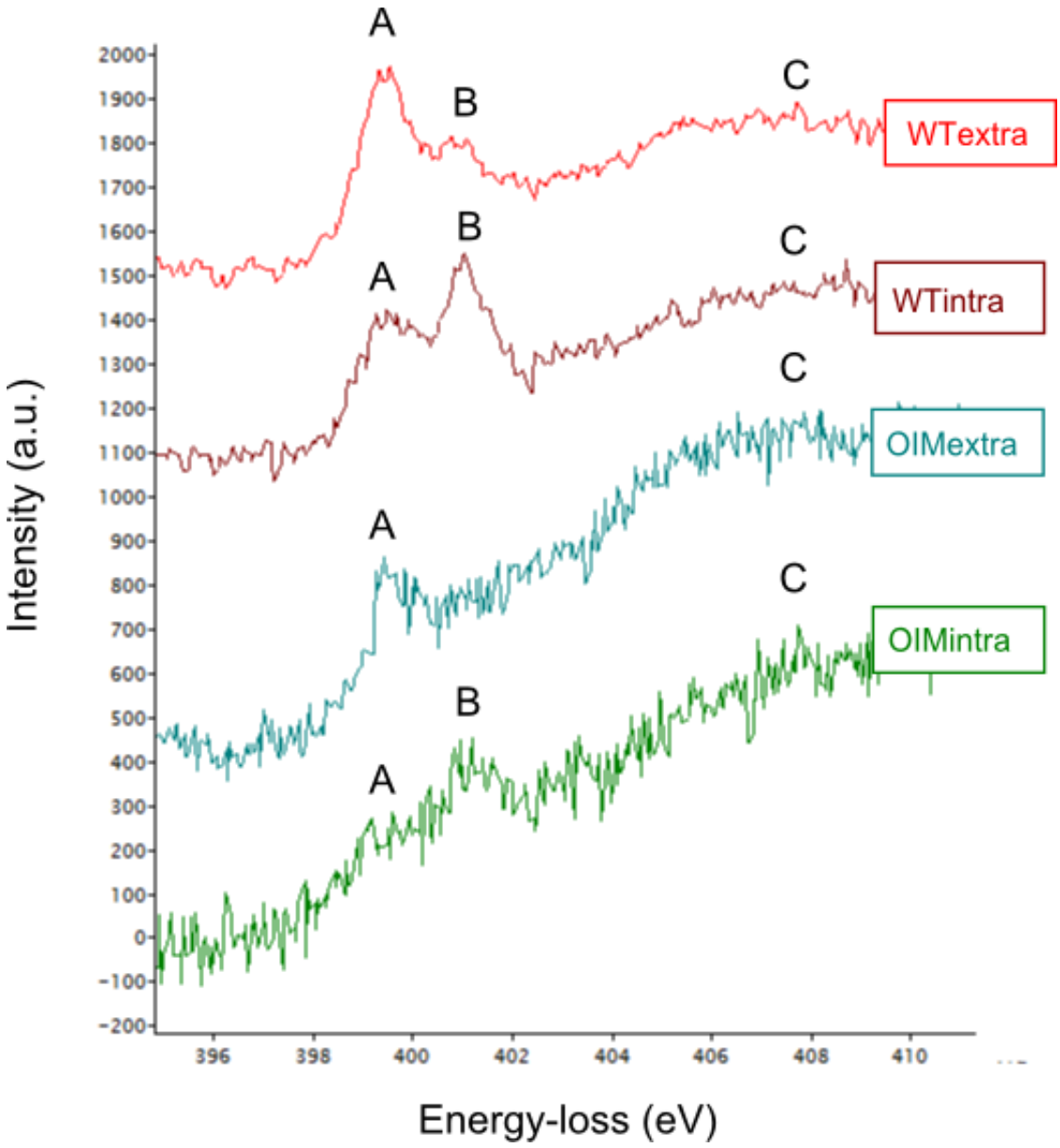


Figure 6.21 The nitrogen K near edge structures of intra- and extrafibrillar regions o of mineralised bone of wild type (WTintra/extra) and OIM (OIMintra/extra) mice taken from transverse sections of the tissue. Spectra were taken from the regions shown on Figure 6.17 (II, III).

6.5.5. Oxygen K-edge

The oxygen signal in non-mineralised tail tendon was not analysed, as the osmium tetroxide stain change the oxidation state of material significantly.

The typical spectrum of mineralised bone of OIM and WT (Figure 6.22) shows a double peak B-C at ~537 and ~539eV, respectively, and a weak peak D at ~545eV. In few spectra, a small

peak A at ~532eV was observed (OIM1, WT1, Figure 6.22). Oxygen spectra of mineralised regions were aligned using peak C set to 539eV (see section 4.3.4). Spectra were normalised to the most intense peak of each individual spectrum.

Feature A was attributed to C=O transitions in carboxyl or amide groups in amino acids [228,230]. Peaks B, C and D originate from transitions in the mineral phase (see section 5.3.4.5). Peaks B and C were assigned to transition in the calcium-oxygen and/or phosphorus-oxygen environment [213]. Peak D was assigned to transitions to 4s- and 4p-like states in calcium-oxygen bonds.

In mineralised WT and OIM bone, the oxygen K-edges structures did not differ from spectra recorded for the well mineralised turkey tendon (TW, Figure 6.22) and consisted of a mixture of features characteristic to collagen and apatite.

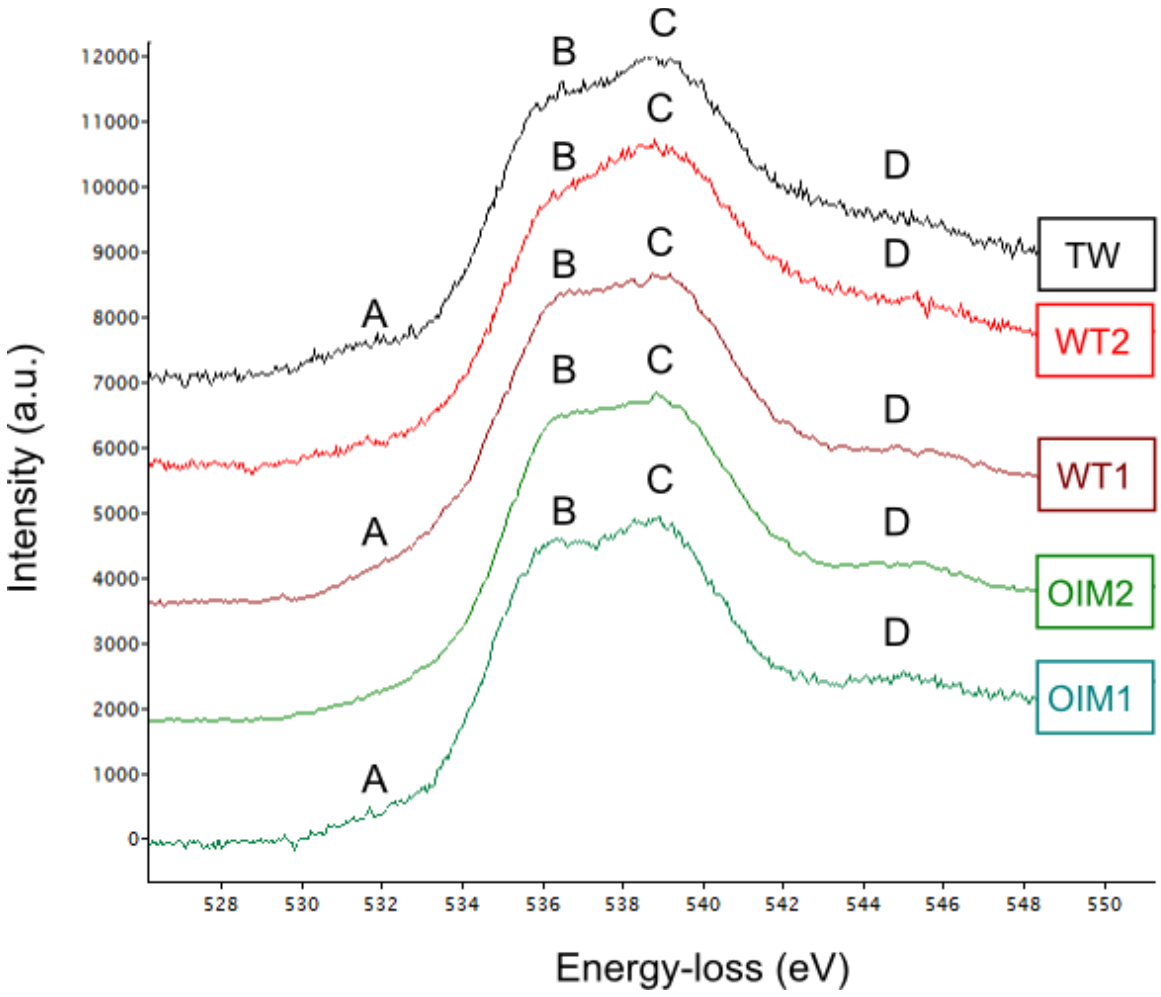


Figure 6.22 The oxygen K near edge structures of mineralised bone of wild type (WT) and OIM mice and well mineralised turkey tendon (TW).

6.6. Discussion & conclusions

OI-affected tissues exhibited many characteristic observed also in the wild type model. In particular, tissues affected by the osteogenesis imperfecta disease were still capable of forming collagen fibrils, which displayed the characteristic banding pattern, identical with those seen in the wild type specimens. However, mature collagen fibrils grew to smaller diameters than fibrils seen in WT.

Regions of disorganised tissues were observed in WT and OIM model. Collagen malformations found in OIM were spread over large areas, while disorganised regions in the WT tissues were localised. Disorganised regions were divided into two hierarchical categories.

1) The first type of collagen malformations were observed at the micro-meter scale (Figure 6.7, Figure 6.8, Figure 6.9). These malformations resembled a loosely packed, collagen structures similar to observed in woven bone. Malformed structures consisted of randomly distributed thin, collagen fibrils, often bent or twisted, devoid of the banding pattern. This is the most extensive malformation of OIM collagen.

2) The second type of collagen malformations was observed at the nano-meter scale (Figure 6.10, Figure 6.12). These malformations consisted of tightly packed collagen assemblies of microribbons and finer filaments, which exhibited a faint banding pattern and resembled structures seen at early stages of fibrillogenesis.

Modifications between WT and OIM tissues were also detected in the chemistry of mineral phase. While mineral nucleating in WT and OIM bone possess the major characteristics of apatite, examination of carbon K-edge revealed a significant presence of carbonate in OIM bone in comparison with the wild type bone. This result suggests that deformations of apatite crystal structure might be caused by the incorporation of carbonate ions and may contribute to brittleness in OIM bone. Carbonate ions are most likely incorporated into hydroxyapatite lattice. Carbonated HA exhibits higher solubility than HA, probably due to microstrains developing in crystal lattice with carbonate ion substitutions [93,94].

However, recent studies suggested that biomineral may have much more complex composition originating from the presence of calcium carbonate [276] and/or citrate bridges [277]. Further investigation is required to identify the source of carbonate ions. It is not know why the carbonate content is higher in OIM tissue. This may be an effect of altered structural organisations of the collagen fibrils (and therefore environment for nucleation), altered functional groups at the nucleation interfaces or altered crosslinking.

There is also evidence of changes in carbonate chemistry between fractured and intact tissue [91]. Lower carbonate content in the damaged regions of bone was connected with apatite

dissolution and removal of carbon-containing mineral from the rupture. Increased solubility of carbonated apatites might be connected with microstrains developing in crystal lattice [92].

Variation observed in the nitrogen K-edge was related to modification of pyridine oxidation states, which may be connected to the maturation of collagen nucleation sites or crosslinks. The increase in the oxidised pyridine signal was associated with intrafibrillar regions of collagen. Modifications of the pyridine oxidation state may reflect changes in collagen chains or crosslinking necessary to initiate mineralisation process or changes occurring during mineralisation process.

Phosphorus and calcium L-edges did not show any significant variation. This was expected as limited sensitivity of these two edges was observed previously in mineral standards (see section 4.3) and turkey tendon (see section 5.3.4).

Changes in oxygen K-edges of OIM and WT bone were subtle and difficult to interpret. In bone, as in well mineralised turkey tendon (see section 5.3.4.5), observed oxygen K-edge structures originate from superposition of signals coming from mineral and protein components. This intrinsic variability makes interpretation of oxygen K-edge challenging. However, examination of oxygen K-edge should not be neglected. As shown in section 4.3.5, oxygen K-edges of mineral standards expressed significant variation in their fine structures, which might be correlated with specific bioceramics and help to differentiate between different minerals (e.g. calcium phosphates and calcium carbonate).

Further characterisation of chemical structure at the nano-meter scale will benefit from examination of additional mineral and collagen standards as well as standards of organic and computational structure predictions. Discerning the origins of fine structures observed in carbon, nitrogen and oxygen K-edges will help to fully understand the role of collagen in the mineralisation process and the significance and impact of mutations in collagen chains in OIM and other bone diseases.

We hypothesise that disruptions of crystal formation and alignment seen in OIM bone tissues originate from modifications of the collagen matrix. Modifications of collagen triple helix may lead to changes in packing of collagen molecules and fibrils. Changes in collagen triple

helix may also result in formation of nucleation sites, which promote nucleation of mineral incorporating larger quantities of carbonate ions.

7.
CONCLUSIONS & FUTURE WORK

This thesis presented a range of TEM preparation and examination techniques and demonstrated their application in the studies of mineralising tissues *in vivo*. In the course of the project, preservation and examination methods were optimised for the nano-meter scale examination of mineralising tissues and an EELS library of bioceramics and mineralised tissues was created. The combination of high pressure freezing and freeze substitution (HPF/FS) with STEM-EELS allowed identification and classification of regions at different stages of mineral development in *in vivo* turkey tendon model. Importantly, these methods were capable of capturing a dynamic mineral nucleation process, especially in the early stages of mineral development. Changes observed in the chemical signature of carbon and nitrogen are good indicators of the collagen transformation prior and/or during the mineralisation process. Modifications of spectral signatures suggest that collagen residues or crosslinks containing aromatic rings play an important role in the mineralisation process, possibly as the primary nucleation sites.

7.1. EELS analysis

The present work showed the benefits of STEM-EELS to perform chemical characterisation of biological materials. Core-loss spectroscopy data collected from bioceramics and mineralising tissues form a library of elemental edges: the phosphorus $L_{2,3}$-edge, the carbon K-edge, the calcium $L_{2,3}$-edge, the nitrogen K-edge and the oxygen K-edge. This spectral data revealed differences in chemical structures of bioceramics (hydroxyapatite, carbonated hydroxyapatite, beta-tricalcium phosphate and calcite), mineralising turkey tendon, WT and OIM mouse bone and will contribute to future classification, identification and analysis of complex mineralising, *in vivo* systems.

EELS spectrum imaging results enabled maps of the relative intensity distribution of the elements of interest to be obtained. Any changes in the near-edge structure (ELNES) of each edge were also investigated.

The application of monochromated STEM-EELS significantly increases the energy resolution of collected spectra. With improved resolution, identification and assignment of peak present in the fine structure of elemental edges could be more informative.

Simultaneous observation of low- and core-loss spectra would provide the benefit of unquestionable calibration of recorded data and application of deconvolution processing for removal of plural scattering effects. The state-of-art microscopes possess the dual EELS capability, which allows recording of low- and core-loss spectra under the same conditions (see also Appendix).

7.2. Damage study

Biological material, like mineralising tissue, is prone to beam-induced damage. This susceptibility needs to be considered and optimisation of experimental conditions should be performed before actual experiment. This optimisation step is crucial, especially in EELS studies, to avoid collection of invalid information.

In the present study, a set of guidelines was presented to facilitate reproduction of the most optimal experimental conditions. Total electron doses should be kept below 10^4 electrons/nm^2. In these conditions, the probability of beam-induced damage is minimised. However, collected spectra should always be examined for signs of introduced modifications. Damage changes are most likely to be reflected in the oxygen K-edge by the presence of an oxidation peak at ~530eV or by formation of peaks characteristic of calcium oxide. Also the carbon K-edge may be used to validate obtained spectra. The presence of a sharp intense peak at ~287eV was connected with beam-induced damage.

The actual safe, low-dose conditions may differ between samples. It is recommended to monitor the oxygen and carbon edges to minimise the damage signal to achieve the best EELS conditions (e.g. achieve high signal-to-noise ratio and reduce the possibility of damage).

7.3. Mineral and protein standards

Mineralised tissues have a complex composite structure consisting of organic and inorganic elements. The calcium phosphate mineral, related to hydroxyapatite, proliferates within the collagen matrix. This is a very simplified view of nano-structure present in mineralising tissues. The exact composition of this complex system is still under investigation and may be dependent on species, age, the individual examined, the examined site and tissue type (tendon, bone, dentin, enamel).

To compensate for this natural variability, a variety of standards and models need to be examined and cross-compared. Selection of models and standards used in the present study is comprehensive, but not exhaustive. Future work needs to address the questions about origins of variations observed in carbon, nitrogen and oxygen K-edges. Such studies should not limit their standards selection to ceramics only, but also include collagen, other proteins, as well as protein-mineral composites and also synthetic organic standards of known chemistry.

To identify mineral composition in biological samples, especially to discern the origin of signal attributed to carbonate, bioceramics composed of calcium phosphate and calcium carbonate and apatites with citrate bridges [277] should be analysed. Collagen models containing high and low quantities of crosslinks, as well as tyrosine- and phenylalanine-rich collagen models, should be examined to confirm the origin of features (possibly related to pyridine) observed in carbon and nitrogen K-edges. Non-collagenous proteins (NCP), such as osteonectin or osteopontin, should be also examined as they contribute to the complexity of the *in vivo* system.

Investigation of mineralising tissues would be also assisted by first principle EELS computational simulations. An insight into the bonding environment of various minerals and proteins would be particularly helpful in the interpretation of carbon and oxygen edges, in which signal from organic and inorganic components is often mixed. Modelling of complex structures, such as apatites and collagen, is a non-trivial task, but necessary for further investigation of mineralising systems. Computational spectral studies would benefit also from preparation of simpler structures, like calcium oxide and calcium carbonate, which would contribute to better understanding of EELS fine structures.

7.4. Mineralised tissue development

Turkey tendon is a well-studied, but challenging model, which helps to characterise the mineralisation process taking place in type I collagen-based tissues. In the present study, regions of interest in turkey tendon were categorised in three groups reflecting the mineralisation stage of tissue (non-mineralised, poorly and well mineralised). The EELS study highlighted the chemical differences between these regions corresponding to the nucleation of mineral (phosphorus, carbon, calcium and oxygen edges) and maturation of the collagen matrix (carbon, nitrogen and oxygen edges).

The main difficulty in examination of turkey tendon arises from disorganised development of the mineralisation process, which may occur simultaneously in different regions and advance with different pace. Other *in vivo* models, like fish fin model, though less relevant, may exhibit a more organised development, which will allow observation of mineral formation in a systematic way.

Nevertheless, the natural inhomogeneity of mineralising turkey tendons might be considered advantageous in some studies. Regions of different architectural and chemical properties could be found and compared directly within one age group and with identical experimental conditions. In the present study, three types of regions (non-, poorly and well mineralised) were identified and characterised. This classification will facilitate further investigation of this complex system with monochromated EELS.

Employment of other methods of microscopic characterisation might offer some additional insight. STEM-EDS might provide more information needed to localise and differentiate mineralising regions. If EDS would be able to detect the presence of mineral-related elements (phosphorus, calcium) in poorly mineralised regions, it would provide a significant help in localisation of aforementioned regions and would provide a simple method of elemental mapping. Application of high resolution TEM (HRTEM) and electron diffraction might be beneficial to discern the crystal structure and its orientation, especially in the poorly mineralised regions. Electron tomography should be also employed to map the 3D distribution of nucleating mineral grains in poorly mineralised regions. The tomography experiment will be particularly challenging due to limited stability of biological material.

7.5. Mineralised tissue disorders

OI is caused by a mutation in the genes coding for collagen, the major structural protein in bone [239]. Advanced microscopy techniques helped to reveal differences in the morphology and chemistry between wild type (WT) and OIM mice tissues *in vivo*. In the present study, deformations of the OIM collagen matrix in non-mineralised tail tendon were observed at high spatial resolution and potential effects of collagen deformation on mineral alignment have been identified. In non-mineralised OIM tissues, extensive regions of loosely packed and significantly bent fibrils were observed at the micro-meter scale, and regions of tightly packed sub-fibrils were found. The diameter of OIM fibrils is also significantly smaller than in WT.

Changes in OIM mineral chemistry (*i.e.* increase in carbonate content) were also observed at the nano-meter scale. The significant increase of carbonate content, which may contribute to bone brittleness, was observed in mineralised OIM tissues may contribute to bone brittleness. Additionally, an increase in the intensity of carbonate signal was detected in the intrafibrillar regions of OIM and WT bone. The increase of the peak, assigned to oxidised pyridine, was also observed in the intrafibrillar regions of OIM and WT bone. No significant variations between OIM and WT tissues were observed in phosphorus, calcium and oxygen edges.

Observation of nano-structural deformations in OIM provides a new insight into the origins and ramifications of bone diseases. Typically bone pathologies are examined at the organ (whole bone) level and at the bulk tissue level. The present study provides a methodology, which might be applied to examination of other abnormal models of mineralising tissues at the nano-meter scale.

The present study revealed significant anomalies in the formation of collagen structures in OIM mouse tail tendons. Future work should examine if demineralisation of OIM bone would expose collagen structure with similar anomalies in micro- and nano-level packing of fibrils. Application of electron tomography and FIB/SEM slice-and-view techniques for 3D visualisation and comparison of normal and malformed regions might provide more information about structural impact of characteristics (total volume, anisotropy, 3D distribution etc.) of the collagen malformation. The direct factors inhibiting or inducing

deformation of collagen fibrils in OIM model are still unknown. A great insight on the origins of these malformations might be provided by combining modelling studies [241] and microscopic observations of fibrillogenesis in OIM *in vitro*.

Monochromated EELS (core and low loss) studies of normal and diseased bone should be continued to unravel their complex chemical structure. Specifically, future studies should aim to establish the origin of carbonate detected in mineralised OIM tissues, to establish the origin and significance of oxidation observed in the nitrogen edge of non-mineralised and mineralised tissues and to improve the energy resolution for detection of fine structures, especially in calcium and phosphorus edges. This study should be facilitated by examination of mineral and protein standards discussed in section 7.3.

Finally, correlation of the structure and chemistry of pathologic bone should now be linked to tissue mechanics at different levels of organisation in bone. This analysis will provide great insight into the fundamental mechanisms by which bone fractures. For example, application of nanoindentation in the SEM could provide a link between failure mechanisms and altered structured features in pathologic bone.

7.6. Final conclusions

Bone has a hierarchical structure and each level of organisation is believed to contribute to the toughness of bone (*i.e.* its ability to resist fracture). Any small changes in composition, structure and bonding between these building blocks may have drastic ramifications for the strength and toughness of bone at larger length scales. However, there are few methods available to characterise the building blocks with the magnifications required.

Over the past four years I have refined super high resolution techniques to map the composition of the mineral/collagen matrix, and to characterise bonding between the collagen fibres and mineral crystals. Findings of present study open the door to understand how the chemistry of the collagen fibres changes in turkey collagen during the mineralisation process and in mice suffering from brittle bone disease. These findings also provided information, which help to establish which functional groups are present at the interface between the mineral and the collagen fibres. Characterising bonding at these interfaces is a long standing

problem, because of the required spatial resolution. However, we are now in a very strong position to study composition of bone at the nano-meter scale.

The results of the present study demonstrated the benefits of monochromated EELS, application of which will be essential in future work. Furthermore, a broad range of collagen and mineral standards needs to be examined to discern the origins of ELNES structures observed. Finally, examination of low loss regions of EELS might provide additional information about the chemistry of this complex mineral-collagen system, whilst reducing the demands on the electron dose used in the experiment.

Future work will use these methods to relate nano-scale changes to changes in mechanics and structure at different hierarchical length-scales in order to identify the salient features of 'healthy' bone. Once we know how these alterations result in whole-bone pathology, we will more readily be able to identify therapies that address bone quality across length scales. We are successfully developing critical assessment tools at the nano-meter scale, which will provide unique fundamental insights into progression of bone pathologies.

Powerful microscopes with the capability to map bonding and compositional variations in bone with molecular scale resolution are indispensable to elucidate fundamental molecular changes to bone tissue in diseased tissues. The EELS technique we have proposed to use is the only method available to analyse these features in tissues at this scale. Further studies will aim to relate changes in the bone's ability to resist fracture to changes in the chemistry and architecture of bone in brittle bone disease and other abnormal models. Acquisition of this knowledge will provide new insights into the origins of bone diseases, which will guide treatment of a range of bone pathologies. More generally this thesis provides a new fundamental understanding into how bone forms, which could provide vital new information to guide novel bone regeneration strategies.

Fractures and malformations of OI bone are the major clinical problem and there is no cure at present for this disease. Existing therapies are focused on prevention of incidents (mainly by increasing bone mass and improving muscle strength *via* exercise) and control over recuperation process. Most pharmaceutical therapies for OI aim to regulate bone mass. However, it has become evident that quantity of bone does not directly correlate with strength or toughness (adding more bad bone is not very effective). Future pharmaceutical strategies

will address the quality (*i.e.* collagen organisation and structure) of the bone tissue and ensure appropriate composition and structure across length scales. This thesis has made a step change in the development of new technologies to assess the nano-structural bone quality.

Appendix

Studies of core loss EELS spectra are challenging in biological systems, which are prone to beam damage and require significant trade-offs in the signal-to-noise ratio.

Low loss (or valence loss) spectra with a good signal to noise ratio can be acquired with significantly lower electron dose than core loss spectra. This approach could provide information about elemental distributions in the frozen, hydrated samples. Additionally, low loss band provides information about optical properties of the material *via* the complex dielectric function. However, processing and analysis of low loss spectra are not trivial [278,279]. Furthermore, discrimination of low loss features can be limited by the energy resolution. Currently the prospects for application of valence loss EELS (VEELS) is under close scrutiny as availability of monochromated microscopes increases.

During the course of the current work of low loss EELS spectra were collected to evaluate the relative thickness of examined regions. Interpretation of low loss spectra was not in scope of this study – they are included for completeness and show some characteristics, which encourage further investigation (Figure 0.1).

Spectra from non-mineralised or low mineralised tissues are dominated by the plasmon peak F at 23.3 eV [280]. Features may be also seen on the low energy shoulder of peak F, especially at 6.3 eV (peak A) [281].

Mineralised tissues exhibit larger variation in displayed features. There are two major peaks visible: a plasmon loss (F) at 23.3 eV and the calcium $M_{2,3}$-edge (G & H) [282]. Peaks B, C, D & E are visible to different extents in each of the mineralised samples, and it is noteworthy that these features are absent when the Ca M-edge is also absent.

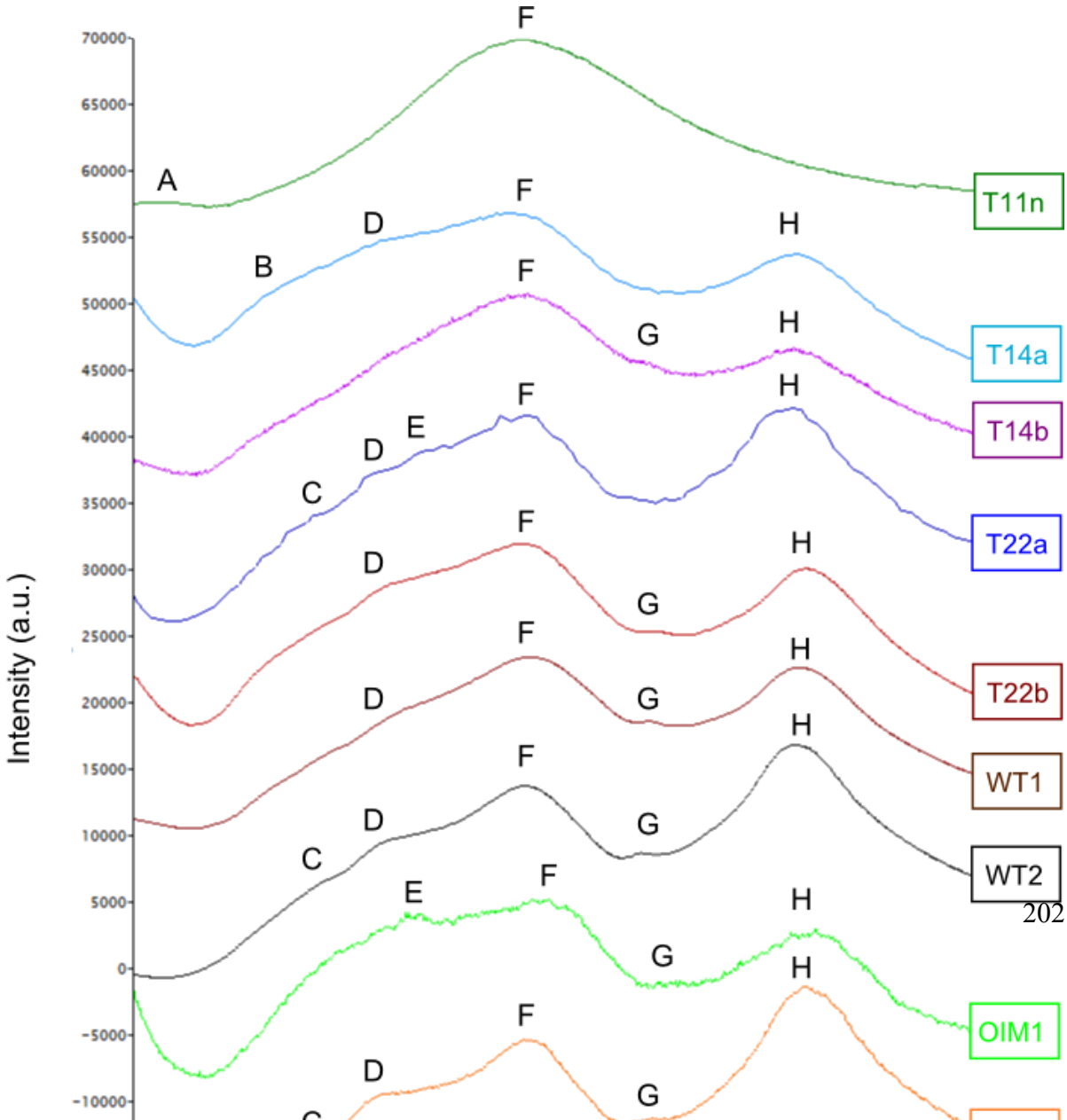

Intensity (a.u.)
70000
65000
60000
55000
50000
45000
40000
35000
30000
25000
20000
15000
10000
5000
0
-5000
-10000
A
B
C
D
E
F
G
H
T11n
T14a
T14b
T22a
T22b
WT1
WT2
OIM1

Figure 0.1 Representative spectra of mineralising tissues collected from the low-loss region of 11 week non-mineralised (T11n) and 14 and 22 week well mineralised (T14, T22) turkey tendon, wild type mouse bone (WT) and OIM mouse bone.

As mentioned before processing and interpretation of VEELS spectra is non-trivial. Initial processing requires removal of the ZLP and deconvolution of spectrum to remove plural scattering.

Further development of VEELS diagnostic methods could be indispensable for identifying alterations in the nano-level of bone, as lower electron doses than in core-loss EELS are sufficient for specimen examination.

Bibliography

[1] Boskey AL. Biomineralization: An Overview. Connect Tissue Res 2003;44:5–9. doi:10.1080/03008200390152007.

[2] Neues F, Epple M. X-ray Microcomputer Tomography for the Study of Biomineralized Endo- and Exoskeletons of Animals. Chem Rev 2008;108:4734–41. doi:10.1021/cr078250m.

[3] Pasteris JD, Wopenka B, Valsami-Jones E. Bone and Tooth Mineralization: Why Apatite? Elements 2008;4:97.

[4] Keaveny TM, Morgan EF, Yeh OC. Bone mechanics. Stand Handb Biomed Eng Des 2004:1–24.

[5] Walsh WR, Ohno M, Guzelsu N. Bone composite behaviour: effects of mineral-organic bonding. J Mater Sci Mater Med 1994;5:72–9.

[6] Glimcher MJ. Bone: nature of the calcium phosphate crystals and cellular, structural, and physical chemical mechanisms in their formation. Rev Mineral Geochem 2006;64:223.

[7] Egerton RF. Electron Energy-Loss Spectroscopy in the Electron Microscope. 2nd ed. 1996.

[8] Thomsen P, Ericson L. Light and transmission electron microscopy used to study the tissue morphology close to implants. Biomaterials 1985;6:421–4.

[9] Porter AE, Patel N, Skepper JN, Best SM, Bonfield W. Effect of sintered silicate-substituted hydroxyapatite on remodelling processes at the bone-implant interface. Biomaterials 2004;25:3303–14.

[10] Grandfield K, McNally EA, Palmquist A, Botton GA, Thomsen P, Engqvist H. Visualizing biointerfaces in three dimensions: electron tomography of the bone-hydroxyapatite interface. J R Soc Interface 2010;7:1497–501. doi:10.1098/rsif.2010.0213.

[11] Hall CE, Jakus MA, Schmitt FO. ELECTRON MICROSCOPE OBSERVATIONS OF COLLAGEN. J Am Chem Soc 1942;64:1234–1234.

[12] Chapman JA, Tzaphlidou M, Meek KM, Kadler KE. The collagen fibril - A model system for studying the staining and fixation of the protein. Electron Microsc Rev 1990;3:143–82.

[13] Arsenault AL. Image Analysis of Collagen-Associated Mineral Distribution in Cryogenically Prepared Turkey Leg Tendons. Calcif Tissue Int 1991;48:56–62.

[14] Holmes DF, Graham HK, Trotter JA, Kadler KE. STEM/TEM studies of collagen fibril assembly. Micron 2001;32:273–85.

[15] Nudelman F, Lausch AJ, Sommerdijk NAJM, Sone ED. In vitro models of collagen biomineralization. J Struct Biol 2013. doi:10.1016/j.jsb.2013.04.003.

[16] Tzaphlidou M. Bone Architecture: Collagen Structure and Calcium/Phosphorus Maps. J Biol Phys 2008;34:39–49. doi:10.1007/s10867-008-9115-y.

[17] Lees S, Prostak KS, Ingle VK, Kjoller K. The loci of mineral in turkey leg tendon as seen by atomic force microscope and electron microscopy. Calcif Tissue Int 1994;55:180–9.

[18] Landis WJ, Hodgens KJ, Song MJ, Arena J, Kiyonaga S, Marko M, et al. Mineralization of Collagen May Occur on Fibril Surfaces: Evidence from Conventional and High-Voltage Electron Microscopy and Three-Dimensional Imaging. J Struct Biol 1996;117:24–35. doi:10.1006/jsbi.1996.0066.

[19] Rubin MA, Jasiuk I, Taylor J, Rubin J, Ganey T, Apkarian RP. TEM analysis of the nanostructure of normal and osteoporotic human trabecular bone. Bone 2003;33:270–82.

[20] Tzaphlidou M. The role of collagen in bone structure: an image processing approach. Micron 2005;36:593–601.

[21] Jantou-Morris V, Horton MA, McComb DW. The nano-morphological relationships between apatite crystals and collagen fibrils in ivory dentine. Biomaterials 2010;31:5275–86. doi:10.1016/j.biomaterials.2010.03.025.

[22] Okuda M, Ogawa N, Takeguchi M, Hashimoto A, Tagaya M, Chen S, et al. Minerals and Aligned Collagen Fibrils in Tilapia Fish Scales: Structural Analysis Using Dark-Field and Energy-Filtered Transmission Electron Microscopy and Electron Tomography. Microsc Microanal 2011;17:788–98. doi:10.1017/S1431927611011949.

[23] Landis WJ, Hodgens KJ, McKee MD, Nanci A, Song MJ, Kiyonaga S, et al. Extracellular vesicles of calcifying turkey leg tendon characterized by immunocytochemistry and high voltage electron microscopic tomography and 3-D graphic image reconstruction. Bone Miner 1992;17:237–41.

[24] Landis WJ, Song MJ, Leith A, McEwen L, McEwen BF. Mineral and organic matrix interaction in normally calcifying tendon visualized in three dimensions by high-voltage electron microscopic tomography and graphic image reconstruction. J Struct Biol 1993;110:39–54.

[25] Landis WJ, Hodgens KJ, Arena J, Song MJ, McEwen BF. Structural relations between collagen and mineral in bone as determined by high voltage electron microscopic tomography. Microsc Res Tech 1996;33:192–202. doi:10.1002/(SICI)1097-0029(19960201)33:2<192::AID-JEMT9>3.0.CO;2-V.

[26] Deshpande AS, Fang P-A, Simmer JP, Margolis HC, Beniash E. Amelogenin-Collagen Interactions Regulate Calcium Phosphate Mineralization in Vitro. J Biol Chem 2010;285:19277–87. doi:10.1074/jbc.M109.079939.

[27] Royce PM, Steinmann B. Connective tissue and its heritable disorders:molecular, genetic and medical aspects. New York: Wiley-Liss; 1993.

[28] Shoulders MD, Raines RT. Collagen structure and stability. Annu Rev Biochem 2009;78:929.

[29] Ricard-Blum S. The Collagen Family. Cold Spring Harb Perspect Biol 2011;3:a004978–a004978. doi:10.1101/cshperspect.a004978.

[30] Branden CI, Tooze J. Introduction to Protein Structure. 2nd ed. Garland Science; 1998.

[31] Berisio R, Vitagliano L, Mazzarella L, Zagari A. Crystal structure of the collagen triple helix model [(Pro-Pro-Gly)10]3. Protein Sci 2009;11:262–70. doi:10.1110/ps.32602.

[32] Rich A, Crick FHC. The molecular structure of collagen. J Mol Biol 1961;3:483–IN4.

[33] Bansal M, Ramakrishnan C, Ramachandran GN. A triple-helical model for (Gly-Pro-Hyp) n with cis peptide units. Biopolymers 1975;14:2457–66.

[34] Ramshaw JAM, Shah NK, Brodsky B. Gly-X-Y Tripeptide Frequencies in Collagen: A Context for Host–Guest Triple-Helical Peptides. J Struct Biol 1998;122:86–91.

[35] Miller MH, Némethy G, Scheraga HA. Calculation of the structures of collagen models. Role of interchain interactions in determining the triple-helical coiled-coil conformation. 2. Poly (glycyl-prolyl-hydroxyprolyl). Macromolecules 1980;13:470–8.

[36] Inouye K, Kobayashi Y, Kishida Y, Sakakibara S, Prockop DJ. Synthesis and physical properties of (hydroxyproline-proline-glycine)10: Hydroxyproline in the X-position decreases the melting temperature of the collagen triple helix. Arch Biochem Biophys 1982;219:198–203.

[37] Fields GB, Prockop DJ. Perspectives on the synthesis and application of triple-helical, collagen-model peptides. Biopolymers 1996;40:345–57.

[38] Persikov AV, Ramshaw JAM, Kirkpatrick A, Brodsky B. Amino Acid Propensities for the Collagen Triple-Helix. Biochemistry (Mosc) 2000;39:14960–7. doi:10.1021/bi001560d.

[39] Miles C. The Role of the α2 Chain in the Stabilization of the Collagen Type I Heterotrimer: A Study of the Type I Homotrimer in oim Mouse Tissues. J Mol Biol 2002;321:797–805. doi:10.1016/S0022-2836(02)00703-9.

[40] Fratzl P. Collagen: Structure and Mechanics. New York: Springer; 2008.

[41] Orgel JPR., Irving TC, Miller A, Wess TJ. Microfibrillar structure of type I collagen in situ. Proc Natl Acad Sci 2006;103:9001. doi:10.1073/pnas.0502718103.

[42] Bear RS. Long x-ray diffraction spacings of collagen. J Am Chem Soc 1942;64:727–727.

[43] Beniash E, Traub W, Veis A, Weiner S. A Transmission Electron Microscope Study Using Vitrified Ice Sections of Predentin: Structural Changes in the Dentin Collagenous Matrix prior to Mineralization. J Struct Biol 2000;132:212–25.

[44] Petruska JA, Hodge AJ. A subunit model for the tropocollagen macromolecule. Proc Natl Acad Sci U S A 1964;51:871.

[45] Hodge AJ. Molecular models illustrating the possible distributions of “holes” in simple systematically staggered arrays of type I collagen molecules in native-type fibrils. Connect Tissue Res 1989;21:137–47.

[46] Sabanay I, Arad T, Weiner S, Geiger B. Study of vitrified, unstained frozen tissue sections by cryoimmunoelectron microscopy. J Cell Sci 1991;100:227–36.

[47] Bornstein P. Covalent cross-links in collagen: A personal account of their discovery. Matrix Biol 2003;22:385–91.

[48] Bailey AJ, Paul RG, Knott L. Mechanisms of maturation and ageing of collagen. Mech Ageing Dev 1998;106:1–56.

[49] Knott L, Bailey AJ. Collagen cross-links in mineralizing tissues: a review of their chemistry, function, and clinical relevance. Bone 1998;22:181–7.

[50] Anastasia L, Rota P, Anastasia M, Allevi P. Chemical structure, biosynthesis and synthesis of free and glycosylated pyridinolines formed by cross-link of bone and synovium collagen. Org Biomol Chem 2013;11:5747. doi:10.1039/c3ob40945g.

[51] Eyre DR, Oguchi H. The hydroxypyridinium crosslinks of skeletal collagens: Their measurement, properties and a proposed pathway of formation. Biochem Biophys Res Commun 1980;92:403–10.

[52] Eyre DR, Weis MA, Wu JJ. Maturation of Collagen Ketoimine Cross-links by an Alternative Mechanism to Pyridinoline Formation in Cartilage. J Biol Chem 2010;285:16675–82. doi:10.1074/jbc.M110.111534.

[53] Robins SP, Duncan A. Cross-linking of collagen. Location of pyridinoline in bovine articular cartilage at two sites of the molecule. Biochem J 1983;215:175–82.

[54] Eyre DR. Collagen: molecular diversity in the body’s protein scaffold. Science 1980;207:1315–22.

[55] Henkel W, Glanville RW, GREIFENDORF D. Characterisation of a type-I collagen trimeric cross-linked peptide from calf aorta and its cross-linked structure. Eur J Biochem 1987;165:427–36.

[56] Robins SP, Duncan A. Pyridinium crosslinks of bone collagen and their location in peptides isolated from rat femur. Enzymology 1987;914:233–9.

[57] Eyre DR, Paz MA, Gallop PM. Cross-linking in collagen and elastin. Annu Rev Biochem 1984;53:717–48.

[58] Aronson D. Cross-linking of glycated collagen in the pathogenesis of arterial and myocardial stiffening of aging and diabetes. J Hypertens 2003;21:3–12.

[59] Nudelman F, Pieterse K, George A, Bomans PHH, Friedrich H, Brylka LJ, et al. The role of collagen in bone apatite formation in the presence of hydroxyapatite nucleation inhibitors. Nat Mater 2010;9:1004–9. doi:10.1038/nmat2875.

[60] Kirsch E, Krieg T, Remberger K, Fendel H, Bruckner P, Muller PK. Disorder of collagen metabolism in a patient with osteogenesis imperfecta (lethal type): increased degree of hydroxylation of lysine in collagen types I and III. Eur J Clin Invest 1981;11:39–47.

[61] Knott L, Tarlton JF, Bailey AJ. Chemistry of collagen cross-linking: biochemical changes in collagen during the partial mineralization of turkey leg tendon. Biochem J 1997;322:535.

[62] Landis WJ, Silver FH, Freeman JW. Collagen as a scaffold for biomimetic mineralization of vertebrate tissues. J Mater Chem 2006;16:1495. doi:10.1039/b505706j.

[63] Wise ER, Maltsev S, Davies ME, Duer MJ, Jaeger C, Loveridge N, et al. The Organic−Mineral Interface in Bone Is Predominantly Polysaccharide. Chem Mater 2007;19:5055–7. doi:10.1021/cm702054c.

[64] Pasteris JD, Wopenka B, Freeman JJ, Rogers K, Valsami-Jones E, van der Houwen JAM, et al. Lack of OH in nanocrystalline apatite as a function of degree of atomic order: implications for bone and biomaterials. Biomaterials 2004;25:229–38. doi:10.1016/S0142-9612(03)00487-3.

[65] Gutsmann T, Fantner GE, Venturoni M, Ekani-Nkodo A, Thompson JB, Kindt JH, et al. Evidence that collagen fibrils in tendons are inhomogeneously structured in a tubelike manner. Biophys J 2003;84:2593–8.

[66] Bozec L, Horton MA. Skeletal tissues as nanomaterials. J Mater Sci Mater Med 2006;17:1043–8. doi:10.1007/s10856-006-0442-x.

[67] Landis WJ. Mineral characterization in calcifying tissues: atomic, molecular and macromolecular perspectives. Connect Tissue Res 1996;34:239–46.

[68] Jäger I, Fratzl P. Mineralized Collagen Fibrils: A Mechanical Model with a Staggered Arrangement of Mineral Particles. Biophys J 2000;79:1737–46. doi:10.1016/S0006-3495(00)76426-5.

[69] Hulmes DJS, Wess TJ, Prockop DJ, Fratzl P. Radial Packing, Order, and Disorder in Collagen Fibrils. Biophys J 1995;68:1661–70.

[70] Burger C, Zhou H, Wang H, Sics I, Hsiao BS, Chu B, et al. Lateral packing of mineral crystals in bone collagen fibrils. Biophys J 2008;95:1985–92. doi:10.1529/biophysj.107.128355.

[71] Alexander B, Daulton TL, Genin GM, Lipner J, Pasteris JD, Wopenka B, et al. The nanometre-scale physiology of bone: steric modelling and scanning transmission electron microscopy of collagen-mineral structure. J R Soc Interface 2012. doi:10.1098/rsif.2011.0880.

[72] Bonar LC, Lees S, Mook HA. Neutron diffraction studies of collagen in fully mineralized bone. J Mol Biol 1985;181:265–70.

[73] Sasaki N, Tagami A, Goto T, Taniguchi M, Nakata M, Hikichi K. Atomic force microscopic studies on the structure of bovine femoral cortical bone at the collagen fibril-mineral level. J Mater Sci Mater Med 2002;13:333–7. doi:10.1023/A:1014079421895.

[74] Balooch M, Habelitz S, Kinney JH, Marshall SJ, Marshall GW. Mechanical properties of mineralized collagen fibrils as influenced by demineralization. J Struct Biol 2008;162:404–10. doi:10.1016/j.jsb.2008.02.010.

[75] Rogers KD, Zioupos P. The bone tissue of the rostrum of a Mesoplodon densirostris whale: a mammalian biomineral demonstrating extreme texture. J Mater Sci Lett 1999;18:651–4.

[76] Skinner HCW. Biominerals. Mineral Mag 2005;69:621–41.

[77] Currey JD, Brear K, Zioupos P. Notch sensitivity of mammalian mineralized tissues in impact. Proc R Soc B Biol Sci 2004;271:517–22. doi:10.1098/rspb.2003.2634.

[78] McConnell D. Applied mineralogy. Apatite, its crystal chemistry, mineralogy, utilization and geologic and biologic occurrences. vol. 5. Springer-Verlag; 1973.

[79] Kay MI, Young RA, Posner AS. Crystal Structure of Hydroxyapatite. Nature 1964;204:1050–2. doi:10.1038/2041050a0.

[80] De Leeuw NH. Computer simulations of structures and properties of the biomaterial hydroxyapatite. J Mater Chem 2010;20:5376. doi:10.1039/b921400c.

[81] Posner AS, Perloff A, Diorio AF. Refinement of the hydroxyapatite structure. Acta Crystallogr 1958;11:308–9. doi:doi:10.1107/S0365110X58000815.

[82] Fletcher DA, McMeeking RF, Parkin D. The United Kingdom chemical database service. J Chem Inf Comput Sci 1996;36:746–9.

[83] Ibrahim DM, Mostafa AA, Korowash SI. Chemical characterization of some substituted hydroxyapatites. Chem Cent J 2011;5:74.

[84] Elliott JC. Calcium Phosphate Biominerals. Rev Mineral Geochem 2002;48:427.

[85] LeGeros R, Legeros J. Phosphate Minerals in Human Tissues. In: Nriagu J, Moore P, editors. Phosphate Miner., Springer Berlin Heidelberg; 1984, p. 351–85.

[86] Legros R, Balmain N, Bonel G. Age-related changes in mineral of rat and bovine cortical bone. Calcif Tissue Int 1987;41:137–44.

[87] Rey C, Renugopalakrishman V, Collins B, Glimcher MJ. Fourier transform infrared spectroscopic study of the carbonate ions in bone mineral during aging. Calcif Tissue Int 1991;49:251–8.

[88] Kuhn LT, Wu Y, Rey C, Gerstenfeld LC, Grynpas MD, Ackerman JL, et al. Structure, Composition, and Maturation of Newly Deposited Calcium-Phosphate Crystals in Chicken Osteoblast Cell Cultures. J Bone Miner Res 2000;15:1301–9.

[89] Leventouri T, Antonakos A, Kyriacou A, Venturelli R, Liarokapis E, Perdikatsis V. Crystal Structure Studies of Human Dental Apatite as a Function of Age. Int J Biomater 2009;2009:1–6. doi:10.1155/2009/698547.

[90] Ouyang H, Sherman PJ, Paschalis EP, Boskey AL, Mendelsohn R. Fourier transform infrared microscopic imaging: effects of estrogen and estrogen deficiency on fracture healing in rat femurs. Appl Spectrosc 2004;58:1–9.

[91] Camacho NP, Rinnerthaler S, Paschalis EP, Mendelsohn R, Boskey AL, Fratzl P. Complementary information on bone ultrastructure from scanning small angle X-ray scattering and Fourier-transform infrared microspectroscopy. Bone 1999;25:287–93.

[92] Paschalis EP, DiCarlo E, Betts F, Sherman P, Mendelsohn R, Boskey AL. FTIR microspectroscopic analysis of human osteonal bone. Calcif Tissue Int 1996;59:480–7.

[93] Ruppel ME, Burr DB, Miller LM. Chemical makeup of microdamaged bone differs from undamaged bone. Bone 2006;39:318–24. doi:10.1016/j.bone.2006.02.052.

[94] Baig AA, Fox JL, Young RA, Wang Z, Hsu J, Higuchi WI, et al. Relationships among carbonated apatite solubility, crystallite size, and microstrain parameters. Calcif Tissue Int 1999;64:437–49.

[95] Rey C, Collins B, Goehl T, Dickson IR, Glimcher MJ. The carbonate environment in bone mineral: a resolution-enhanced Fourier transform infrared spectroscopy study. Calcif Tissue Int 1989;45:157–64.

[96] LeGeros RZ, LeGeros JP. Carbonate analysis of synthetic mineral and biological apatites. J Dent Res 1983;62.

[97] Akkus O, Adar F, Schaffler MB. Age-related changes in physicochemical properties of mineral crystals are related to impaired mechanical function of cortical bone. Bone 2004;34:443–53. doi:10.1016/j.bone.2003.11.003.

[98] Miller LM, Vairavamurthy V, Chance MR, Mendelsohn R, Paschalis EP, Betts F, et al. In situ analysis of mineral content and crystallinity in bone using infrared micro-spectroscopy of the ν< sub> 4</sub> PO< sub> 4</sub>< sup> 3-</sup> vibration. Biochim Biophys Acta BBA-Gen Subj 2001;1527:11–9.

[99] Fratzl P, Gupta HS, Paschalis EP, Roschger P. Structure and mechanical quality of the collagen-mineral nano-composite in bone. J Mater Chem 2004;14:2115. doi:10.1039/b402005g.

[100] Engström A, Zetterström R. Studies on the ultrastructure of bone. Exp Cell Res 1951;2:268–74.

[101] Posner AS. Crystal chemistry of bone mineral. Physiol Rev 1969;49:760.

[102] Nassif N, Martineau F, Syzgantseva O, Gobeaux F, Willinger M, Coradin T, et al. In Vivo Inspired Conditions to Synthesize Biomimetic Hydroxyapatite. Chem Mater 2010;22:3653–63. doi:10.1021/cm903596q.

[103] Boonrungsiman S, Gentleman E, Carzaniga R, Evans ND, McComb DW, Porter AE, et al. The role of intracellular calcium phosphate in osteoblast-mediated bone apatite formation. Proc Natl Acad Sci 2012;109:14170–5. doi:10.1073/pnas.1208916109.

[104] Landis WJ, Silver FH. The structure and function of normally mineralizing avian tendons. Comp Biochem Physiol-Part Mol Integr Physiol 2002;133:1135–57.

[105] Beniash E, Metzler RA, Lam RSK, Gilbert PUPA. Transient amorphous calcium phosphate in forming enamel. J Struct Biol 2009;166:133–43. doi:10.1016/j.jsb.2009.02.001.

[106] Mahamid J, Aichmayer B, Shimoni E, Ziblat R, Li C, Siegel S, et al. Mapping amorphous calcium phosphate transformation into crystalline mineral from the cell to the bone in zebrafish fin rays. Proc Natl Acad Sci 2010;107:6316–21. doi:10.1073/pnas.0914218107.

[107] Bohner M. Physical and chemical aspects of calcium phosphates used in spinal surgery. Eur Spine J 2001;10:114–21. doi:10.1007/s005860100276.

[108] Dey A, Bomans PHH, Müller FA, Will J, Frederik PM, de With G, et al. The role of prenucleation clusters in surface-induced calcium phosphate crystallization. Nat Mater 2010;9:1010–4. doi:10.1038/nmat2900.

[109] Vallet-Regi M, Romero AM, Ragel CV, LeGeros RZ. XRD, SEM-EDS, and FTIR studies of in vitro growth of an apatite-like layer on sol-gel glasses. J Biomed Mater Res 1999;44:416–21.

[110] Heimann R, Wirth R. Formation and transformation of amorphous calcium phosphates on titanium alloy surfaces during atmospheric plasma spraying and their subsequent in vitro performance. Biomaterials 2006;27:823–31. doi:10.1016/j.biomaterials.2005.06.029.

[111] Nudelman F, Bomans PHH, George A, de With G, Sommerdijk NAJM. The role of the amorphous phase on the biomimetic mineralization of collagen. Faraday Discuss 2012;159:357. doi:10.1039/c2fd20062g.

[112] Termine JD, Posner AS. Amorphous/crystalline interrelationships in bone mineral. Calcif Tissue Int 1967;1:8–23.

[113] Bres EF, Moebus G, Kleebe H-J, Pourroy G, Werkmann J, Ehret G. High resolution electron microscopy study of amorphous calcium phosphate. J Cryst Growth 1993;129:149–62.

[114] Silver FH, Landis WJ. Deposition of apatite in mineralizing vertebrate extracellular matrices: A model of possible nucleation sites on type I collagen. Connect Tissue Res 2011;52:242–54. doi:10.3109/03008207.2010.551567.

[115] Lee DD, Glimcher MJ. Three-dimensional spatial relationship between the collagen fibrils and the inorganic calcium phosphate crystals of pickerel (Americanus americanus) and herring (Clupea harengus) bone. J Mol Biol 1991;217:487–501.

[116] Traub W, Arad T, Weiner S. Three-dimensional ordered distribution of crystals in turkey tendon collagen fibers. Proc Natl Acad Sci U S A 1989;86:9822.

[117] Girija EK, Yokogawa Y, Nagata F. Apatite formation on collagen fibrils in the presence of polyacrylic acid. J Mater Sci Mater Med 2004;15:593–9. doi:10.1023/B:JMSM.0000026101.53272.86.

[118] Girija EK, Yokogawa Y, Nagata F. Bone-like apatite formation on collagen fibrils by biomimetic method. Chem Lett 2002;31:702–3.

[119] Katti DR, Pradhan SM, Katti KS. Directional dependence of hydroxyapatite-collagen interactions on mechanics of collagen. J Biomech 2010;43:1723–30.

[120] Wilson EE, Awonusi A, Morris MD, Kohn DH, Tecklenburg MM., Beck LW. Three structural roles for water in bone observed by solid-state NMR. Biophys J 2006;90:3722–31.

[121] Jantou V, Turmaine M, West GD, Horton MA, McComb DW. Focused ion beam milling and ultramicrotomy of mineralised ivory dentine for analytical transmission electron microscopy. Micron 2009;40:495–501. doi:10.1016/j.micron.2008.12.002.

[122] Srot V, Bussmann B, Salzberger U, Koch CT, van Aken PA. Linking Microstructure and Nanochemistry in Human Dental Tissues. Microsc Microanal 2012;18:509–23. doi:10.1017/S1431927612000116.

[123] Mahamid J, Sharir A, Gur D, Zelzer E, Addadi L, Weiner S. Bone mineralization proceeds through intracellular calcium phosphate loaded vesicles: a cryo-electron microscopy study. J Struct Biol 2011.

[124] Schwartz AG, Pasteris JD, Genin GM, Daulton TL, Thomopoulos S. Mineral Distributions at the Developing Tendon Enthesis. PLoS ONE 2012;7:e48630. doi:10.1371/journal.pone.0048630.

[125] Posner AS, Betts F, Blumenthal NC. Properties of nucleating systems. Metab Bone Dis Relat Res 1978;1:179–83.

[126] Mahamid J, Sharir A, Addadi L, Weiner S. Amorphous calcium phosphate is a major component of the forming fin bones of zebrafish: Indications for an amorphous precursor phase. Proc Natl Acad Sci 2008;105:12748–53.

[127] Boskey AL, Posner AS. Conversion of amorphous calcium phosphate to microcrystalline hydroxyapatite. A pH-dependent, solution-mediated, solid-solid conversion. J Phys Chem 1973;77:2313–7.

[128] Landis WJ, Glimcher MJ. Electron diffraction and electron probe microanalysis of the mineral phase of bone tissue prepared by anhydrous techniques. J Ultrastruct Res 1978;63:188–223.

[129] Combes C, Rey C. Amorphous calcium phosphates: Synthesis, properties and uses in biomaterials. Acta Biomater 2010;6:3362–78. doi:10.1016/j.actbio.2010.02.017.

[130] Porter AE, Patel N, Skepper JN, Best SM, Bonfield W. Comparison of in vivo dissolution processes in hydroxyapatite and silicon-substituted hydroxyapatite bioceramics. Biomaterials 2003;24:4609–20.

[131] Bozzola JJ, Russell LD. Electron microscopy: principles and techniques for biologists. Jones & Bartlett Learning.; 1999.

[132] Michael Hoppert. Microscopic techniques in biotechnology. Weinheim: Wiley-VCH Verlag; 2003.

[133] McDonald KL, Morphew M, Verkade P, Müller-Reichert T. Recent advances in high-pressure freezing. Electron Microsc., Springer; 2007, p. 143–73.

[134] Mallein-Gérin F, Garrone R. Tendon collagen fibrillogenesis is a multistep assembly process as revealed by quick-freezing and freeze-substitution. Biol Cell 1990;69:9–16.

[135] H. Kanno, R. J. Speedy, C.A. Angell. Supercooling of Water to -92°C Under Pressure. Science 1975;189:880–1. doi:10.1126/science.189.4206.880.

[136] Studer D, Humbel BM, Chiquet M. Electron microscopy of high pressure frozen samples: bridging the gap between cellular ultrastructure and atomic resolution. Histochem Cell Biol 2008;130:877–89. doi:10.1007/s00418-008-0500-1.

[137] Dahl R, Staehelin LA. High-pressure freezing for the preservation of biological structure: Theory and practice. J Electron Microsc Tech 1989;13:165–74. doi:10.1002/jemt.1060130305.

[138] Moor H. Theory and Practice of High Pressure Freezing. Cryotech. Biol. Electron Microsc., Springer Berlin Heidelberg; 1987, p. 175–91.

[139] Studer D, Hennecke H, Müller M. High-pressure freezing of soybean nodules leads to an improved preservation of ultrastructure. Planta 1992;188:155–63.

[140] White DL, Andrews SB, Faller JW, Barrnett RJ. The chemical nature of osmium tetroxide fixation and staining of membranes by X-ray photoelectron spectroscopy. Biochim Biophys Acta BBA-Biomembr 1976;436:577–92. doi:http://dx.doi.org/10.1016/0005-2736(76)90442-9.

[141] Hodge AJ, Petruska JA. Recent studies with the electron microscope on ordered aggregates of the tropocollagen macromolecule. Asp. Protein Struct., New York: Academic Press; 1963, p. 289–300.

[142] Hayat MA. Principles and techniques of electron microscopy: biological applications. Cambridge: Cambridge University Press; 2000.

[143] Williams DB, Carter C. Transmission electron microscopy: a textbook for materials science. New York: Springer; 2009.

[144] Egerton RF, Li P, Malac M. Radiation damage in the TEM and SEM. Micron 2004;35:399–409.

[145] Eddisford P, Brown A, Brydson R. Identifying and quantifying the mechanism of electron beam induced damage and recovery in hydroxyapatite. J Phys Conf Ser 2008;126. doi:10.1088/1742-6596/126/1/012008.

[146] Isabell TC, Fischione PE, O'Keefe C, Guruz MU, Dravid VP. Plasma cleaning and its applications for electron microscopy. Microsc Microanal 1999;5:126–35.

[147] Keyse RJ, Goodhew P, Lorimer, G. W. Introduction to Scanning Transmission Electron Microscopy. Springer-Verlag; 1998.

[148] Müllejans H, Bruley J. Electron energy-loss spectroscopy (EELS) ; comparison with X-ray analysis. J Phys IV 1993;03:C7–2083 – C7–2092. doi:10.1051/jp4:19937332.

[149] Brydson R. Electron Energy Loss Spectroscopy. Garland Science; 2001.

[150] Lerotic M, Jacobsen C, Schäfer T, Vogt S. Cluster analysis of soft X-ray spectromicroscopy data. Ultramicroscopy 2004;100:35–57. doi:10.1016/j.ultramic.2004.01.008.

[151] Bosman M, Watanabe M, Alexander DTL, Keast VJ. Mapping chemical and bonding information using multivariate analysis of electron energy-loss spectrum images. Ultramicroscopy 2006;106:1024–32. doi:10.1016/j.ultramic.2006.04.016.

[152] Jutten C, Herault J. Blind separation of sources, part I: An adaptive algorithm based on neuromimetic architecture. Signal Process 1991;24:1–10.

[153] De la Peña F, Berger M-H, Hochepied J-F, Dynys F, Stephan O, Walls M. Mapping titanium and tin oxide phases using EELS: An application of independent component analysis. Ultramicroscopy 2011;111:169–76. doi:10.1016/j.ultramic.2010.10.001.

[154] Hyperspy: Hyperspectral data analysis toolbox. 2013.

[155] Tiemeijer PC. Measurement of Coulomb interactions in an electron beam monochromator. Ultramicroscopy 1999;78:53–62.

[156] Monochromator manual Titan V1.0. 2008.

[157] Rose H, Wan W. Aberration correction in electron microscopy. Part. Accel. Conf. 2005 PAC 2005 Proc. Of, 2005, p. 44–8.

[158] Suryanarayana C, Grant Norton M. X-Ray diffraction: a practical approach. Springer; 1998.

[159] Peters F, Schwarz K, Epple M. The structure of bone studied with synchrotron X-ray diffraction, X-ray absorption spectroscopy and thermal analysis. Thermochim Acta 2000;361:131–8.

[160] Smith BC. Fundamentals of Fourier transform infrared spectroscopy. 1st ed. CRC Press; 1996.

[161] Rogers KD, Daniels P. An X-ray diffraction study of the effects of heat treatment on bone mineral microstructure. Biomaterials 2002;23:2577–85.

[162] Brown WE, Chow LC. Chemical properties of bone mineral. Annu Rev Mater Sci 1976;6:213–36.

[163] Kaplan FS, Hayes WC, Keaveny TM, Boskey A, Einhorn TA, Iannotti JP. Form and Function of Bone. In: Simon SR, editor. Orthop. Basic Sci. Ed. Sheldon R Simon, American Academy of Orthopaedic Surgeons; 1994.

[164] Arsenault AL. A comparative electron microscopic study of apatite crystals in collagen fibrils of rat bone, dentin and calcified turkey leg tendons. Bone Miner 1989;6:165–77. doi:10.1016/0169-6009(89)90048-2.

[165] Phillips C, Bradley D, Schlotzhauer C, Bergfeld M, Libreros-Minotta C, Gawenis L, et al. Oim mice exhibit altered femur and incisor mineral composition and decreased bone mineral density. Bone 2000;27:219–26.

[166] Camacho NP, Hou L, Toledano TR, Ilg WA, Brayton CF, Raggio CL, et al. The material basis for reduced mechanical properties in oim mice bones. J Bone Miner Res 1999;14:264–72.

[167] Tai K, Dao M, Suresh S, Palazoglu A, Ortiz C. Nanoscale heterogeneity promotes energy dissipation in bone. Nat Mater 2007;6:454–62. doi:10.1038/nmat1911.

[168] Vanleene M, Saldanha Z, Cloyd KL, Jell G, Bou-Gharios G, Bassett JHD, et al. Transplantation of human fetal blood stem cells in the osteogenesis imperfecta mouse leads to improvement in multiscale tissue properties. Blood 2010;117:1053–60. doi:10.1182/blood-2010-05-287565.

[169] Shackelford JF. Bioceramics: Applications of Ceramic and Glass Materials in Medicine (Materials Science Forum). 1999.

[170] Vallet-Regí M. Ceramics for medical applications. J Chem Soc Dalton Trans 2001:97–108. doi:10.1039/b007852m.

[171] Dorozhkin SV, Epple M. Biological and medical significance of calcium phosphates. Angew Chem Int Ed 2002;41:3130–46.

[172] Thamaraiselvi TV, Rajeswari S. Biological evaluation of bioceramic materials-a review. Carbon 2004;24:172.

[173] Fathi MH, Hanifi A, Mortazavi V. Preparation and bioactivity evaluation of bone-like hydroxyapatite nanopowder. J Mater Process Technol 2008;202:536–42. doi:10.1016/j.jmatprotec.2007.10.004.

[174] Hossein Fathi M, Mortazavi V, Roohani Esfahani SI. Bioactivity Evaluation of Synthetic Nanocrystalline Hydroxyapatite. Dent Res J 2009;5.

[175] Kapoor S, Batra U. Preparation and Bioactivity Evaluation of Bone like Hydroxyapatite-Bioglass Composite. Int J Chem Biol Eng 2010;3:24–8.

[176] Ritchie RO, Buehler MJ, Hansama P. Plasticity and toughness in bone. Phys Today 2009;62:41. doi:10.1063/1.3156332.

[177] Metzler R, Abrecht M, Olabisi R, Ariosa D, Johnson C, Frazer B, et al. Architecture of Columnar Nacre, and Implications for Its Formation Mechanism. Phys Rev Lett 2007;98. doi:10.1103/PhysRevLett.98.268102.

[178] Zhou D, Metzler RA, Tyliszczak T, Guo J, Abrecht M, Coppersmith SN, et al. Assignment of Polarization-Dependent Peaks in Carbon K-Edge Spectra from Biogenic and Geologic Aragonite. J Phys Chem B 2008;112:13128–35. doi:10.1021/jp803176z.

[179] Benzerara K, Yoon TH, Tyliszczak T, Constantz B, Spormann AM, Brown GE. Scanning transmission X-ray microscopy study of microbial calcification. Geobiology 2004;2:249–59.

[180] Brandes JA, Wirick S, Jacobsen C. Carbon K-edge spectra of carbonate minerals. J Synchrotron Radiat 2010;17:676–82. doi:10.1107/S0909049510020029.

[181] Fleet ME, Liu X. Calcium L2,3-edge XANES of carbonates, carbonate apatite, and oldhamite (CaS). Am Mineral 2009;94:1235–41. doi:10.2138/am.2009.3228.

[182] Chao W, Harteneck BD, Liddle JA, Anderson EH, Attwood DT. Soft X-ray microscopy at a spatial resolution better than 15 nm. Nature 2005;435:1210–3. doi:10.1038/nature03719.

[183] Hitchcock AP, Dynes JJ, Johansson G, Wang J, Botton G. Comparison of NEXAFS microscopy and TEM-EELS for studies of soft matter. Micron 2008;39:311–9. doi:10.1016/j.micron.2007.09.008.

[184] Gonzalez-Jimenez ID, Cats K, Davidian T, Ruitenbeek M, Meirer F, Liu Y, et al. Hard X-ray Nanotomography of Catalytic Solids at Work. Angew Chem Int Ed 2012;51:11986–90. doi:10.1002/anie.201204930.

[185] Wirth R. Water in minerals detectable by electron energy-loss spectroscopy EELS. Phys Chem Miner 1997;24:561–8.

[186] Jarcho M, Bolen CH, Thomas MB, Bobick J, Kay JF, Doremus RH. Hydroxylapatite synthesis and characterization in dense polycrystalline form. J Mater Sci 1976;11:2027–35.

[187] Akao M, Aoki H, Kato K. Mechanical properties of sintered hydroxyapatite for prosthetic applications. J Mater Sci 1981;16:809–12.

[188] Gibson IR, Bonfield W. Novel synthesis and characterization of an AB-type carbonate-substituted hydroxyapatite. J Biomed Mater Res 2002;59:697–708. doi:10.1002/jbm.10044.

[189] Klein CPAT, De Groot K, Driessen AA, Van der Lubbe HBM. A comparative study of different β-whitlockite ceramics in rabbit cortical bone with regard to their biodegradation behaviour. Biomaterials 1986;7:144–6.

[190] Prevéy PS. X-ray diffraction characterization of crystallinity and phase composition in plasma-sprayed hydroxyapatite coatings. J Therm Spray Technol 2000;9:369–76.

[191] Vignoles M, Bonel G, Holcomb DW, Young RA. Influence of preparation conditions on the composition of type B carbonated hydroxyapatite and on the localization of the carbonate ions. Calcif Tissue Int 1988;43:33–40. doi:10.1007/BF02555165.

[192] Fleet ME, Liu X. Coupled substitution of type A and B carbonate in sodium-bearing apatite. Biomaterials 2007;28:916–26. doi:10.1016/j.biomaterials.2006.11.003.

[193] Garvie LAJ. Can electron energy-loss spectroscopy (EELS) be used to quantify hydrogen in minerals from the O K edge? Am Mineral 2009;95:92–7. doi:10.2138/am.2010.3290.

[194] Arenal R, de la Peña F, Stéphan O, Walls M, Tencé M, Loiseau A, et al. Extending the analysis of EELS spectrum-imaging data, from elemental to bond mapping in complex nanostructures. Ultramicroscopy 2008;109:32–8. doi:10.1016/j.ultramic.2008.07.005.

[195] Kruse J, Leinweber P, Eckhardt K-U, Godlinski F, Hu Y, Zuin L. Phosphorus L2,3 -edge XANES: overview of reference compounds. J Synchrotron Radiat 2009;16:247–59. doi:10.1107/S0909049509000211.

[196] Hansen PL, Brydson R, McComb DW. p → p-like transitions at the silicon L2,3-edges of silicates. Microsc Microanal Microstruct 1992;3:213–9. doi:10.1051/mmm:0199200302-3021300.

[197] McComb DW, Brydson R, Hansen PL, Payne RS. Qualitative interpretation of electron energy-loss near-edge structure in natural zircon. J Phys Condens Matter 1992;4:8363.

[198] Sutherland DGJ, Kasrai M, Bancroft GM, Liu ZF, Tan KH. Si L-and K-edge x-ray-absorption near-edge spectroscopy of gas-phase Si (CH3)x(OCH3) 4-x: Models for solid-state analogs. Phys Rev B 1993;48:14989.

[199] Srot V, Wegst UGK, Salzberger U, Koch CT, Hahn K, Kopold P, et al. Microstructure, chemistry, and electronic structure of natural hybrid composites in abalone shell. Micron 2013;48:54–64. doi:10.1016/j.micron.2013.02.010.

[200] Cody GD, Ade H, Wirick S, Mitchell GD, Davis A. Determination of chemical-structural changes in vitrinite accompanying luminescence alteration using C-NEXAFS analysis. Org Geochem 1998;28:441–55.

[201] Braun A, Kubatova A, Wirick S, Mun SB. Radiation damage from EELS and NEXAFS in diesel soot and diesel soot extracts. J Electron Spectrosc Relat Phenom 2009;170:42–8. doi:10.1016/j.elspec.2007.08.002.

[202] Lam RSK, Metzler RA, Gilbert PUPA, Beniash E. Anisotropy of Chemical Bonds in Collagen Molecules Studied by X-ray Absorption Near-Edge Structure (XANES) Spectroscopy. ACS Chem Biol 2012;7:476–80. doi:10.1021/cb200260d.

[203] Metzler RA, Kim IW, Delak K, Evans JS, Zhou D, Beniash E, et al. Probing the Organic−Mineral Interface at the Molecular Level in Model Biominerals. Langmuir 2008;24:2680–7. doi:10.1021/la7031237.

[204] Garvie LAJ, Craven AJ, Brydson R. Use of electron-energy loss near-edge fine structure in the study of minerals. Am Mineral 1994;79:411–25.

[205] Benzerara K, Tyliszczak T, Brown Jr GE. Study of Interactions Between Microbes and Minerals by Scanning Transmission X-Ray Microscopy (STXM). AIP Conf. Proc., vol. 882, 2007, p. 726.

[206] Leapman RD, Grunes LA, Fejes PL. Study of the L_ 2,3 edges in the 3d transition metals and their oxides by electron-energy-loss spectroscopy with comparisons to theory. Phys Rev B 1982;26:614.

[207] Van der Laan G, Kirkman IW. The 2p absorption spectra of 3d transition metal compounds in tetrahedral and octahedral symmetry. J Phys Condens Matter 1992;4:4189.

[208] Aronova MA, Sousa AA, Leapman RD. EELS characterization of radiolytic products in frozen samples. Micron 2011;42:252–6. doi:10.1016/j.micron.2010.10.009.

[209] Mkhoyan KA, Silcox J, Mcguire MA, Disalvo FJ. Radiolytic purification of CaO by electron beams. Philos Mag 2006;86:2907–17. doi:10.1080/14786430600658025.

[210] Bres EF, Hutchison JL, Senger B, Voegel J-C, Frank RM. HREM study of irradiation damage in human dental enamel crystals. Ultramicrotomy 1991;35:305–22. doi:http://dx.doi.org/10.1016/0304-3991(91)90083-I.

[211] Brès EF, Michel J, Reyes-Gasga J, Mussi A, Rey C. Damage in apatite during TEM observation. Acta Microsc., vol. 20, Mérida Yucatán, México: 2011.

[212] Metzler R, Zhou D, Abrecht M, Chiou J-W, Guo J, Ariosa D, et al. Polarization-dependent imaging contrast in abalone shells. Phys Rev B 2008;77. doi:10.1103/PhysRevB.77.064110.

[213] Grunes LA, Leapman RD, Wilker CN, Hoffmann R, Kunz AB. Oxygen K near-edge fine structure: An electron-energy-loss investigation with comparisons to new theory for selected 3d transition-metal oxides. Phys Rev B 1982;25:7157.

[214] De Groot F, Grioni M, Fuggle J, Ghijsen J, Sawatzky A, Petersen H. Oxygen 1s x-ray-absorption edges of transition-metal oxides. Phys Rev B 1989;40:5715–23.

[215] Gregori G, Kleebe H-J, Mayr H, Ziegler G. EELS characterisation of β-tricalcium phosphate and hydroxyapatite. J Eur Ceram Soc 2006;26:1473–9. doi:10.1016/j.jeurceramsoc.2005.02.007.

[216] SCOTT DB, NYLEN MU. Improved Preservation of Tendon for Electron Microscopy through Wet Freeze-drying. Nature 1959;183:1205–6. doi:doi:10.1038/1831205a0.

[217] Landis WJ, Librizzi JJ, Dunn MG, Silver FH. A study of the relationship between mineral content and mechanical properties of turkey gastrocnemius tendon. J Bone Miner Res 1995;10:859–67. doi:10.1002/jbmr.5650100606.

[218] Bigi A, Castellani PP, Cojazzi G, Roveri N. Age related changes in the thermal transition of Turkey leg flexor tendon collagen. J Therm Anal Calorim 1992;38:505–14.

[219] Arsenault AL. Crystal-collagen relationships in calcified turkey leg tendons visualized by selected-area dark field electron microscopy. Calcif Tissue Int 1988;43:202–12.

[220] Traub W, Arad T, Weiner S. Growth of mineral crystals in turkey tendon collagen fibers. Connect Tissue Res 1992;28:99–111.

[221] White SW, Hulmes DJS, Miller A, Timmins PA. Collagen–mineral axial relationship in calcified turkey leg tendon by X-ray and neutron diffraction. Nature 1977;266:421–5. doi:doi:10.1038/266421a0.

[222] Wenk HR, Heidelbach F. Crystal alignment of carbonated apatite in bone and calcified tendon: results from quantitative texture analysis. Bone 1999;24:361–9.

[223] Weiner S, Traub W. Organization of hydroxyapatite crystals within collagen fibrils. FEBS Lett 1986;206:262–6.

[224] Prostak KS, Lees S. Visualization of crystal-matrix structure. In situ demineralization of mineralized turkey leg tendon and bone. Calcif Tissue Int 1996;59:474–9.

[225] Qu J, Thoreson AR, Chen Q, An K-N, Amadio PC, Zhao C. Tendon gradient mineralization for tendon to bone interface integration: BONE INTERFACE INTEGRATION. J Orthop Res 2013:n/a – n/a. doi:10.1002/jor.22412.

[226] Alexander D, Anderson J, Forró L, Crozier P. The Real Carbon K-Edge. Microsc Microanal 2008;14. doi:10.1017/S1431927608086509.

[227] Boese J, Osanna A, Jacoben C, Kirz J. Carbon edge XANES spectroscopy of amino acids and peptides. J Spectrosc Relat Phenom 1997;85:9–15.

[228] Lehmann J, Solomon D, Brandes J, Fleckenstein H, Jacobsen C, Thieme J. Synchrotron-based near-edge X-ray spectroscopy of natural organic matter in soils and sediments. Biophys-Chem Process Involv Nat Nonliving Org Matter Environ Syst 2009:729–81.

[229] Bhattacharyya S, Lubbe M, Bressler PR, Zahn DRT, Richter F. Structure of nitrogenated amorphous carbon films from NEXAFS. Diam Relat Mater 2002;11:8–15.

[230] Westphal SW, Yabuta H. Quantitative Organic and Light Element analysis of Comet 81P/Wild 2 particles using C-, N-, and O-μ-XANES n.d.

[231] Ray SC, Tsai HM, Chiou JW, Bose B, Jan JC, Kumar K, et al. X-ray absorption spectroscopy (XAS) study of dip deposited a-C:H(OH) thin films. J Phys Condens Matter 2004;16:5713–9. doi:10.1088/0953-8984/16/32/008.

[232] Vairavamurthy A, Wang S. Organic Nitrogen in Geomacromolecules: Insights on Speciation and Transformation with K-edge XANES Spectroscopy. Environ Sci Technol 2002;36:3050–6. doi:10.1021/es0155478.

[233] Leinweber P, Kruse J, Walley FL, Gillespie A, Eckhardt K-U, Blyth RIR, et al. Nitrogen K-edge XANES – an overview of reference compounds used to identify `unknown' organic nitrogen in environmental samples. J Synchrotron Radiat 2007;14:500–11. doi:10.1107/S0909049507042513.

[234] Matsui T, Yudasaka M, Kikuchi R, Ohki Y, Yoshimura S. Two kinds of nitrogen atoms in nitrogen-substituted, highly crystalline graphite prepared by chemical vapor deposition. Appl Phys Lett 1994;65:2145. doi:10.1063/1.112774.

[235] Gordon ML, Cooper G, Morin C, Araki T, Turci CC, Kaznatcheev K, et al. Inner-Shell Excitation Spectroscopy of the Peptide Bond: Comparison of the C 1s, N 1s, and O 1s Spectra of Glycine, Glycyl-Glycine, and Glycyl-Glycyl-Glycine. J Phys Chem A 2003;107:6144–59. doi:10.1021/jp0344390.

[236] Murugan R, Rao KP, Kumar TS. Heat-deproteinated xenogeneic bone from slaughterhouse waste: physico-chemical properties. Bull Mater Sci 2003;26:523–8.

[237] Habraken WJEM, Tao J, Brylka LJ, Friedrich H, Bertinetti L, Schenk AS, et al. Ion-association complexes unite classical and non-classical theories for the biomimetic nucleation of calcium phosphate. Nat Commun 2013;4:1507. doi:10.1038/ncomms2490.

[238] Martin E, Shapiro JR. Osteogenesis imperfecta: epidemiology and pathophysiology. Curr Osteoporos Rep 2007;5:91–7.

[239] Forlino A, Cabral WA, Barnes AM, Marini JC. New perspectives on osteogenesis imperfecta. Nat Rev Endocrinol 2011;7:540–57. doi:10.1038/nrendo.2011.81.

[240] Gautieri A, Vesentini S, Redaelli A, Buehler MJ. Single molecule effects of osteogenesis imperfecta mutations in tropocollagen protein domains. Protein Sci 2008:NA – NA. doi:10.1002/pro.21.

[241] Gautieri A, Uzel S, Vesentini S, Redaelli A, Buehler MJ. Molecular and mesoscale mechanisms of osteogenesis imperfecta disease in collagen fibrils. Biophys J 2009;97:857–65.

[242] Chipman SD, Sweet HO, McBride DJ, Davisson MT, Marks SC, Shuldiner AR, et al. Defective pro alpha 2 (I) collagen synthesis in a recessive mutation in mice: a model of human osteogenesis imperfecta. Proc Natl Acad Sci U S A 1993;90:1701.

[243] Kuznetsova N, McBride Jr D, Leikin S. Osteogenesis Imperfecta Murine: Interaction Between Type I Collagen Homotrimers. J Mol Biol 2001;309:807–15. doi:10.1006/jmbi.2001.4682.

[244] Kuznetsova NV, McBride Jr. DJ, Leikin S. Changes in Thermal Stability and Microunfolding Pattern of Collagen Helix Resulting from the Loss of a2(I) Chain in Osteogenesis Imperfecta Murine. J Mol Biol 2003;331:191–200.

[245] Landis WJ. The strength of a calcified tissue depends in part on the molecular structure and organization of its constituent mineral crystals in their organic matrix. Bone 1995;16:533–44.

[246] Vogel BE, Doelz R, Kadler KE, Hojima Y, Engel J, Prockop DJ. A Substitution of Cysteine for Glycine 748 of the 01 Chain Produces a Kink at This Site in the Procollagen I Molecule and an Altered N-Proteinase Cleavage Site over 225 nm Away. J Biol Chem 1988;263:19249–55.

[247] VALLI M, ZOLEZZI F, MOTTES M, ANTONIAZZI F, STANZIAL F, TENNI R, et al. Gly85 to Val substitution in proα1 (I) chain causes mild osteogenesis imperfecta and introduces a susceptibility to protease digestion. Eur J Biochem 1993;217:77–82.

[248] Baker AT, Ramshaw JA, Chan D, Cole WG, Bateman JF. Changes in collagen stability and folding in lethal perinatal osteogenesis imperfecta. The effect of alpha 1 (I)-chain glycine-to-arginine substitutions. Biochem J 1989;261:253–7.

[249] Chang S-W, Shefelbine SJ, Buehler MJ. Structural and Mechanical Differences between Collagen Homo- and Heterotrimers: Relevance for the Molecular Origin of Brittle Bone Disease. Biophys J 2012;102:640–8. doi:10.1016/j.bpj.2011.11.3999.

[250] McBride DJ, Choe V, Shapiro JR, Brodsky B. Altered collagen structure in mouse tail tendon lacking the [alpha] 2 (I) chain1. J Mol Biol 1997;270:275–84.

[251] Tenni R, Cetta G, Dyne K, Rossi A, Quacci D, Lenzi L, et al. Type I procollagen in the severe non-lethal form of osteogenesis imperfecta. Hum Genet 1988;79:245–50.

[252] Bank RA, Tekoppele JM, Janus GJ, Wassen MH, Pruijs HE, van der Sluijs HA, et al. Pyridinium Cross-Links in Bone of Patients with Osteogenesis Imperfecta: Evidence of a Normal Intrafibrillar Collagen Packing. J Bone Miner Res 2000;15:1330–6.

[253] Carriero A, Zimmermann EA, Paluszny A, Tang SY, Bale H, Busse B, et al. How tough is Brittle Bone? Investigating Osteogenesis Imperfecta in Mouse Bone. J Bone Miner Res 2014.

[254] Vetter U, Fisher LW, Mintz KP, Kopp JB, Tuross N, Termine JD, et al. Osteogenesis imperfecta: Changes in noncollagenous proteins in bone. J Bone Miner Res 1991;6:501–5.

[255] Fratzl P, Paris O, Landis WJ, Klaushofer K. Mineral crystals are smaller and less oriented in osteogenesis imperfecta mouse model, as revealed by small-angle X-ray scattering. Bone, vol. 16, 1995, p. 407.

[256] Vanleene M, Porter A, Guillot P-V, Boyde A, Oyen M, Shefelbine S. Ultra-structural defects cause low bone matrix stiffness despite high mineralization in osteogenesis imperfecta mice. Bone 2012;50:1317–23. doi:10.1016/j.bone.2012.03.007.

[257] Vetter U, Eanes ED, Kopp JB, Termine JD, Robey PG. Changes in apatite crystal size in bones of patients with osteogenesis imperfecta. Calcif Tissue Int 1991;49:248–50.

[258] Fratzl P, Paris O, Klaushofer K, Landis WJ. Bone mineralization in an osteogenesis imperfecta mouse model studied by small-angle x-ray scattering. J Clin Invest 1996;97:396.

[259] Grabner B, Landis WJ, Roschger P, Rinnerthaler S, Peterlik H, Klaushofer K, et al. Age-and genotype-dependence of bone material properties in the osteogenesis imperfecta murine model (oim). Bone 2001;29:453–7.

[260] Dubey DK, Tomar V. Effect of osteogenesis imperfecta mutations in tropocollagen molecule on strength of biomimetic tropocollagen-hydroxyapatite nanocomposites. Appl Phys Lett 2010;96:023703. doi:10.1063/1.3279158.

[261] Kozloff KM, Carden A, Bergwitz C, Forlino A, Uveges TE, Morris MD, et al. Brittle IV Mouse Model for Osteogenesis Imperfecta IV Demonstrates Postpubertal Adaptations to Improve Whole Bone Strength. J Bone Miner Res 2004;19:614–22. doi:10.1359/JBMR.040111.

[262] Rey C, Kim H-M, Gerstenfeld L, Glimcher MJ. Characterization of the apatite crystals of bone and their maturation in osteoblast cell culture: Comparison with native bone crystals. Connect Tissue Res 1996;35:343–9.

[263] Wallace JM, Orr BG, Marini JC, Holl MMB. Nanoscale morphology of Type I collagen is altered in the Brtl mouse model of osteogenesis imperfecta. J Struct Biol 2011;173:146–52.

[264] Gajko-Galicka A. Mutations in type I collagen genes resulting in osteogenesis imperfecta in humans. ACTA Biochim Pol-Engl Ed- 2002;49:433–42.

[265] Cassella JP, Stamp TCB, Ali SY. A morphological and ultrastructural study of bone in osteogenesis imperfecta. Calcif Tissue Int 1996;58:155–65.

[266] Jiang F, Hörber H, Howard J, Müller DJ. Assembly of collagen into microribbons: effects of pH and electrolytes. J Struct Biol 2004;148:268–78. doi:10.1016/j.jsb.2004.07.001.

[267] Hitchcock AP, Fischer P, Gedanken A, Robin MB. Antibonding s* valence MOs in the inner shell and outer shell spectra of the fluorobenzenes. J Phys Chem 1987;91:531–40.

[268] Robin MB, Ishii I, McLaren R, Hitchcock AP. Fluorination e€ffects on the inner shell spectra of unsaturated molecules. J Electron Spectrosc Relat Phenom 1988;47:53–92.

[269] Hitchcock AP, Urquhart SG, Rightor EG. Inner-shell spectroscopy of benzaldehyde, terephthalaldehyde, ethylbenzoate, terephthaloyl chloride and phosgene: models for core excitation of poly (ethylene terephthalate). J Phys Chem 1992;96:8736–50.

[270] Francis JT, Hitchcock AP. Inner-shell spectroscopy of p-benzoquinone, hydroquinone, and phenol: distinguishing quinoid and benzenoid structures. J Phys Chem 1992;96:6598–610.

[271] Ishii I, Hitchcook AP. The oscillator strengths for C1< i> s</i> and O1< i> s</i> excitation of some saturated and unsaturated organic alcohols, acids and esters. J Electron Spectrosc Relat Phenom 1988;46:55–84.

[272] Sham TK, Yang BX, Kirz J, Tse JS. K-edge near-edge x-ray-absorption fine structure of oxygen- and carbon-containing molecules in the gas. Phys Rev A 1989;40:652–68.

[273] Hitchcock AP. Carbon K-shell excitation of gaseous and condensed cyclic hydrocarbons: C3H6, C4H8, C5H8, C5H10, C6H10, C6H12, and C8H8. J Chem Phys 1986;85:4849. doi:10.1063/1.451719.

[274] Hitchcock AP, Ishii I. Carbon K-shell excitation spectra of linear and branched alkanes. J Electron Spectrosc Relat Phenom 1987;42:11–26.

[275] Ishii I, Hitchcock AP. A quantitative experimental study of the core excited electronic states of formamide, formic acid, and formyl fluoride. J Chem Phys 1987;87:830. doi:10.1063/1.453290.

[276] Müller WEG, Schröder HC, Schlossmacher U, Grebenjuk VA, Ushijima H, Wang X. Induction of carbonic anhydrase in SaOS-2 cells, exposed to bicarbonate and consequences for calcium phosphate crystal formation. Biomaterials 2013;34:8671–80. doi:10.1016/j.biomaterials.2013.07.096.

[277] Davies E, Muller KH, Wong WC, Pickard CJ, Reid DG, Skepper JN, et al. Citrate bridges between mineral platelets in bone. Proc Natl Acad Sci 2014;111:E1354–63. doi:10.1073/pnas.1315080111.

[278] Mkhoyan KA, Babinec T, Maccagnano SE, Kirkland EJ, Silcox J. Separation of bulk and surface-losses in low-loss EELS measurements in STEM. Ultramicroscopy 2007;107:345–55. doi:10.1016/j.ultramic.2006.09.003.

[279] Stöger-Pollach M. Optical properties and bandgaps from low loss EELS: Pitfalls and solutions. Micron 2008;39:1092–110. doi:10.1016/j.micron.2008.01.023.

[280] Aronova MA, Kim YC, Zhang G, Leapman RD. Quantification and thickness correction of EFTEM phosphorus maps. Ultramicroscopy 2007;107:232–44. doi:10.1016/j.ultramic.2006.07.009.

[281] Katti KS, Qian M, Frech DW, Sarikaya M. Low-loss Electron Energy-loss Spectroscopy and Dielectric Function of Biological and Geological Polymorphs of CaCO3. Microsc Microanal 1999;5:358–64.

[282] Hofer F, Wilhelm P. EELS microanalysis of the elements Ca to Cu using M2,3 edges. Ultramicroscopy 1993;49:189–97.

List of Figures

Figure 1.1 The hierarchical structure of the bone. (A) The whole bone sectioned longitudinally to show cortical (shaft) and trabecular bone (end). (B) A wedge of a bone cross-section depicting the osteon distribution in cortical bone. (C) A single osteon. (D) A collagen fibre. (E) Collagen fibrils. (F) Schematic organisation of collagen molecules and apatite mineral inside a microfibril (not to scale). (G) A single apatite crystal platelet. (H) A projection of the atomic structure of apatite. (I) A collagen triple helix molecule (tropocollagen) with side groups and crosslinks. [3].....14

Figure 2.1 Models of collagen structure hierarchy from the basic amino acid sequence to the collagen molecule. (A) Example of Gly-Pro-Hyp amino acid sequence. (B) Ball model of polypeptide chain fragment. (C) Fragment of collagen molecule (tropocollagen) twisted together from three polypeptide chains. [27].....18

Figure 2.2 Example of proline *cis-trans* isomerisation [28].....21

Figure 2.3 An example of banding in mouse cortical bone. (A) Bright-field (BF)-TEM micrograph of a thin, focused ion beam (FIB) milled bone section. Image acquired at 120kV on JEOL 2000FX. (B) Part of the line profile taken from the boxed region in insert A. Four D-periods were plotted with the corresponding periodic spacing ranging from 65 to 71 nm. 23

Figure 2.4 Schematic 2D quarter-stagger representation of the collagen microfibril arrangement (A) explaining collagen fibril banding (B). The overlap (with five molecules), and gap (with four molecules) regions, alternately arranged, form a characteristic pattern.…24

Figure 2.5 Collagen molecules with N- and C-termini labelled. Tropocollagen is organised in a staggered fashion and reinforced with crosslinks. [27,48–50].....25

Figure 2.6 Initial intra- and extracellular action of two enzymes leading to creation of lysyl-based aldehydes essential for crosslink development. Inside the cell, lysyl hydroxylase (LH) affects selected lysine (Lys) residues attaching hydroxyl groups to their side chains and thus creating hydroxylysine (Hys). Outside the cell, lysyl oxidase performs further modifications

of the Lys and Hys residues resulting in formation of lysine aldehyde (Aly) and hydroxylysine aldehyde (HAly). [27,50].....25

Figure 2.7 Crosslink formation *via* the HAly pathway proposed by Eyre. [50].....27

Figure 2.8 Two proposed models of mature crosslink organisation within collagen fibril. [57] 28

Figure 2.9 Example of glucose-derived saccharide crosslink formation leading to creation of vesperlysine [48].....29

Figure 2.10 Various structural models of collagen fibril. (A) Landis model. Collagen molecules and apatite crystals arranged in Hodge model fashion. Top to bottom: collagen fibrils alone, collagen fibrils with mineral nucleating in gaps, mineral growing from gaps between fibrils [67]. (B) Jäger and Fratzl model. Apatite platelets (absent) and collagen molecules arranged in concentric layers [68]. (C) Burger *et al.* model. Apatite crystals (grey) randomly distributed among the collagen molecules (white) [70]. (D) Jantou-Morris *et al.* model. Extrafibrillar mineral crust formed around fibril [21]. (E) Alexander *et al.* model. Bent collagen molecules with various crystal alignments. The crystals align separately in each gap [71].....32

Figure 2.11 The atomic structure of two unit cells of hydroxyapatite with labelled Ca_I and Ca_{II} sites; O = red, Ca = green, P = orange, H = white; a, b, c – unit cell dimensions; α, β, γ – unit cell angles. (A) A view on the (001) plane. (B) A view on the (-110) plane. (C) A view on the (001) plane indicating the P and OH sites. This structural model is based on work of Posner *et al.* [81] and was acquired from The United Kingdom Chemical Database Service [82].....34

Figure 3.1: A flow chart showing the embedding procedure.....44

Figure 3.2 Representative ADF-STEM images of non-stained and bulk stained collagen fibrils. (A) An 11 week old, non-stained turkey tendon collagen. (B) An 8 month old, bulk stained mouse tail tendon collagen.....45

Figure 3.3 Part of water phase diagram showing the melting point (T_m) and the homogeneous nucleation temperature (T_n) as a function of pressure. At 210 MPa, the melting temperature is at a minimum as well as the nucleation temperature. The possibility of supercooling is maximized. At high pressure (i.e above 200 MPa), water crystallizes as ice II and III, rather than ice I.....47

Figure 3.4 Bright-field TEM images of unstained mouse bone sectioned by (A) ultramicrotomy and (B) FIB milling. White arrows indicate the direction of the fibrils. In ultramicrotomed section, the majority of mineral crystals is aligned along the fibrils. In FIB milled section, the orientation of crystals is less homogeneous.....49

Figure 3.5 Schematic of a conventional TEM.....51

Figure 3.6 Schematics of perfect and aberrant lenses. (A) A perfect system focusing a point source into point. (B) Astigmatism – the lens spreading a round object into ellipsoid. (C) Chromatic aberration – the lens focusing electrons according to their energy. (D) Spherical aberration – the lens overfocusing off-axis electrons.....53

Figure 3.7 Schematic showing electron-sample interactions used in electron microscopy imaging and analysis [143].....54

Figure 3.8 Illustration of the mass-thickness effect on image contrast in bright field TEM. The objective aperture enhances contrast by removal of strongly scattered electrons.....58

Figure 3.9 (A) Bright-field image of mouse bone and (B) the corresponding diffraction pattern showing arcs resulting from diffraction from the (002) crystal planes of hydroxyapatite indicating the alignment of the crystals (dotted arrow). The central spot in (B) is covered by the beam stop to increase contrast and protect the camera from over-saturation. 59

Figure 3.10 Schematic showing the scattering of an incident electron wave in a crystal lattice. The black spheres represent lattice points [143].....60

Figure 3.11 Schematic showing the TEM microscope operation in diffraction mode. The objective aperture is removed [143].....61

Figure 3.12 BF-TEM image of 22 week old mineralised turkey tendon before (A) and after exposure (B) to the electron beam at 200kV. The electron dose was not recorded in this experiment. The region of interest was exposed for several minutes. After prolonged exposure to the electron beam radiation, the distinctive banding pattern (A) is lost (B), possibly due to amorphisation of the crystal structure.....62

Figure 3.13 Effects of free carbohydrate accumulation on non-mineralised collagen of a 14 week turkey tendon. Clusters (solid arrows) are formed by a stationary beam. Lines (dashed arrows) are formed during collection of EELS line profiles.....64

Figure 3.14 Schematics of an operating STEM probe, rastering across the specimen. The beam is scanned and kept parallel to optic axis (dashed line) by deflection coils [143].....65

Figure 3.15 Comparison of the same region of 14 week turkey tendon imaged in TEM and STEM mode. In TEM image banding is hardly visible parallel to the arrow. In STEM mode, banding (along the black arrow) is more visible. White arrow heads point the gap regions. The collection angles have been adjusted to angles characteristic for mineral diffraction.....66

Figure 3.16 Schematic showing STEM detectors collecting electrons scattered at different angles [143]. α is the probe convergence angle. θ_1, θ_2 and θ_3 are the collection angles of respective detectors. Detectors are often mounted on retractable strips to allow access to other tools, such as the EELS spectrometer.....67

Figure 3.17 Schematic of the EELS spectrometer. The magnetic prism deflects electrons according to the energy of the electrons. Slower electrons are deflected to higher angles (dashed line) than faster ones (solid line). [143].....69

Figure 3.18 Schematics of electron energy-loss spectra. (A) Zero loss peak and low loss region with features arising from plasmon scattering. (B) Extended spectrum with core loss region. The intensity of the core loss structures is relative low in comparison to the 0-50eV region. The structure of the core loss edge is presented by an example of an oxygen-K edge. Core edges are labelled according to their corresponding ionised shell (K – 1s, L – 2s/2p, M - 3s/3p/3d, N – 4s/4p/4d/4f and O).....70

Figure 3.19 Schematics of Titan microscope.....76

Figure 4.1 Representative XRD patterns of selected mineral standards used in STEM-EELS studies. The lower crystallinity shown in carbonated HA (lowest A/B ratio) is due to the lower heat treatment temperature and lower Ca/P ratio.....85

Figure 4.2 Phosphorus $L_{2,3}$-edge structures of hydroxyapatite (HA), carbonated hydroxyapatite (CHA) and beta-tricalcium phosphate (bTCP). All phosphate-containing minerals displayed a characteristic pattern of two main peaks: peak A and peak C, followed by a broad peak D.....89

Figure 4.3 Carbon K-edge structures of carbonated hydroxyapatite (CHA), calcite (CAL), an impurity (IMP) and amorphous carbon (AC). The carbonate-containing minerals (CHA, CAL, IMP) display a sharp peak D at 290 eV and a less intense peak H at 302 eV. The IMP edge was obtained *via* ICA (Figure 4.4).....90

Figure 4.4 The original calcite impurity carbon K-edge spectrum acquired from a crystal grain deposited on an amorphous carbon film, accompanied by the amorphous carbon film (AC) and impurity (IMP) spectra reconstructed by the ICA method.....92

Figure 4.5 Calcium $L_{2,3}$-edge structures of hydroxyapatite (HA), carbonated hydroxyapatite (CHA), beta-tricalcium phosphate (bTCP), calcite (CAL) and impurity (IMP). All specimens displayed two peaks B and D characteristic to calcium L-edge. All minerals containing carbonate groups showed a small shift of peak D towards higher energies in comparison to pure calcium phosphates (HA, bTCP). Only CAL displayed additional peaks A and C characteristic of multiplet splitting.....94

Figure 4.6 Damage markers seen in the oxygen K-edge. CAL (calcite) and HA (hydroxyapatite) display an additional peak at 530 eV when exposed to an electron dose above 10^4 electrons/nm^2. The spectrum obtained from HA exposed to an electron dose above 10^5 electrons/nm^2 (HA into CaO) is consistent with CaO spectra presented in the literature [209]. CaO exhibits new peaks marked as B* and E*. The origin of oxygen K ELNES is discussed in section 4.3.5.....96

Figure 4.7 Oxygen K-edge structures of hydroxyapatite (HA), carbonated hydroxyapatite (CHA), beta-tricalcium phosphate (bTCP), calcite (CAL) and impurity found in calcite

(IMP). Calcium carbonates (CAL, IMP) display a characteristic peak B. Calcium phosphates (HA, CHA, bTCP) display a characteristic double peak C-D.....98

Figure 5.1 Schematics showing a turkey leg with tendons (grey).The mineralisation front proceeds in the direction indicated by the dashed arrow.....104

Figure 5.2 Bright field TEM images of non-mineralised (A, C, E) and mineralised (B, D, F) turkey tendon.....110

Figure 5.3 Transverse structure of mineralised (A, B, C in ADF-STEM) and non-mineralised (D in BF-TEM) regions of 14 week old turkey tendon imaged at different magnifications. Fibres (red, dashed regions) are built from smaller fibrils (blue, dotted regions) and wrapped into collagen sheets formed from collagen fibrils arranged perpendicular to the long axis of fibre. A faint periodic banding pattern is visible in the wrapping region in B, C and D.....113

Figure 5.4 Bright-field, mass-thickness contrast TEM image of grains (indicated by arrows) associating with 11 week old turkey tendon. Grains form larger agregates and align along the gap region and along the surface of the collagen fibril.....114

Figure 5.5 ADF-STEM image of 22 week old turkey tendon displaying features characteristic of mineralising tissues. Banding pattern with characteristic periodicity is clearly visible. The needle-like (edge-on) crystal are superimposed on banded regions. The long axes of the needles followed the long axes of the collagen fibrils. Disorganised areas were also observed, where crystals do not follow the collagen orientation, but instead form disordered globules. 116

Figure 5.6 14 week old turkey tendon microtomed and imaged in ADF-STEM mode on the Titan at 300kV. The tissue cut at an oblique angle to the fibril plane revealed (possibly due to rotation of some crystals) plate-like mineral crystals and a needle-like crystals which are probably platelets oriented edge-on.....117

Figure 5.7 Tomographic reconstruction of a mineral plate inside the gap region of turkey tendon. Acquisitions were collected in STEM-HAADF mode from the 22 week turkey. (A) An orthogonal section through a segment of a reconstructed volume showing a fragment through a banded fibril. (B) A mineral platelet (thresholded and segmented) from within the

gap region. (C, D) Reconstructed plates superimposed on slide A. The edges of the plates are marked with lines.....118

Figure 5.8 TEM image of banded collagen fibrils from non-mineralised regions of 11, 14 and 22 week old (A, B, C, respectively) turkey tendon (left) and corresponding diffraction patterns (right) collected from selected region (dashed circle) consistent with amorphous material.....120

Figure 5.9 TEM images of mineralised turkey tendon (left) and corresponding SAED patterns (right; with major plane reflections indexed) collected from regions defined by the dashed circles in their corresponding images.....121

Figure 5.10 (A) TEM image of synthetic hydroxyapatite crystals. Needle-like crystals are randomly distributed in the clusters. (B) A SAED pattern obtained from selected region (dashed circle in A) indexed using a hydroxyapatite standard.....122

Figure 5.11 BF-TEM image of a 14 week old turkey tendon showing the transition from non-mineralised (left) to mineralised (right) regions.....124

Figure 5.12 Representative features seen in non-mineralised regions taken from a 14 week old turkey (TN). (A) ADF-STEM image shows banded fibrils with mineral absent. Dotted arrow indicates the direction of the periodic banding pattern. (B) SAED shows a diffused halo characteristic of amorphous material. (C) An EELS spectrum of a non-mineralised turkey tendon collagen fibril showing characteristic carbon (starting at 285 eV), nitrogen (at 400 eV) and oxygen (at 530 eV) edges.....125

Figure 5.13 Representative features seen in the poorly mineralised regions taken from a 14 week old turkey (TP). (A) ADF-STEM image shows banded fibrils with ellipsoidal grains (black arrows). In regions with these grains, the banding contrast is difficult to resolve. The dotted arrow indicates the direction of banding. (B) SAED taken from the fibril shows a diffused halo attributed to amorphous material. (C) EELS spectrum shows presence of carbon (starting at 285 eV), calcium (E, at 345 eV) nitrogen (at 400 eV) and oxygen (F, at 530 eV) edges. The phosphorus signal (D) could not be properly examined due to the poor signal-to-

noise, but irregular features (black arrows) in the spectrum between 130-160eV suggest presence of phosphorus.....127

Figure 5.14 (A) ADF-STEM image of a poorly mineralised fibril showing calcium-containing globules and grains. False-colour calcium intensity map (a.u.) of (B) a large globule and (C) a single grain. Regions with higher intensities of the calcium signal are “hotter” (red and orange), while regions with low intensities are “colder” (blue and violet).....128

Figure 5.15 TEM images of a poorly mineralised region of 14 week old turkey tendon showing (A) large globules and (B) needle-like grains. The insert shows the corresponding SAED pattern characteristic of an amorphous material.....129

Figure 5.16 Representative features seen in well mineralised regions taken from 14 week old turkey (TW). (A) ADF-STEM image shows banded fibrils with needle-like crystals. Dotted arrow indicates the direction of banding. (B) SAED acquisition shows a ring pattern typical for apatite. The (002) plane reflections are indexed. (C) EELS spectrum shows the presence of phosphorus (starting at 125 eV), carbon (at 285 eV), calcium (at 345 eV), nitrogen (at 400 eV) and oxygen (at 530 eV) edges.....130

Figure 5.17 The phosphorus $L_{2,3}$ near edge structures of 14 week old well mineralised turkey tendon (TW) and the characteristic standards (HA – hydroxyapatite, CHA – carbonated HA). All turkey tendon patterns were consistent with patterns recorded for hydroxyapatite and carbonated hydroxyapatite. Turkey tendon regions in non-mineralised and in poorly mineralised regions did not exhibit a fully resolved phosphorous signal and have been omitted for clarity.....132

Figure 5.18 The carbon K near edge structures of turkey tendon fibrils (collected from 14 week old specimen), carbonated HA (CHA) and amorphous carbon (AC). The amorphous carbon (AC) spectrum is consistent with spectra collected from resin and carbon film. The AC spectrum has two peaks: a smaller peak A at ~284 eV and a broad peak E above 292 eV. Spectra collected from turkey tendon (TN, TP, TW1, TW2) display an additional peak B at ~286 eV. The mineralised regions show also a formation of peak C at ~287 eV (TW2). In some acquisitions, (TW2), a carbonate peak D at ~290 eV is seen.....134

Figure 5.19 The calcium $L_{2,3}$ near edge structures of 14 week old mineralised turkey tendon (TP, TW) and hydroxyapatite (HA) and carbonated HA (CHA) standards. All calcium edge spectra exhibit two characteristic white line peaks: A at ~348 eV and B at ~351 eV.....135

Figure 5.20 The nitrogen K near edge structures of non-mineralised (TN) and mineralised (TP, TW) 14 week old turkey tendon fibrils. In the nitrogen spectra, three peaks can be observed: A at ~400 eV, B at ~401 eV and a broad peak C at ~408 eV.....137

Figure 5.21 The oxygen K near edge of non-mineralised (TN) and mineralised (TP, TW) 14 week old turkey tendon fibrils, and hydroxyapatite (HA) and carbonated HA (CHA) standards. In mineralised tissues, a mixture of features characteristic of the mineral and collagen can be seen.....139

Figure 5.22 Representative normalised intensity line profiles (white arrows;) of elemental signals (phosphorous $L_{2,3}$, carbon K, calcium $L_{2,3}$, nitrogen K, oxygen K) and intensity of ADF-STEM micrographs (int). Profiles were collected for 14 week turkey tendon. Scale bar (blue)=100nm. Arrow heads are consistent with the direction of X axis on the plots and line markers on arrows correspond to the border lines on particular plots.....140

Figure 5.23 Representative EDS spectrum collected from mineralised turkey tendon showing carbon, nitrogen, oxygen, phosphorous and calcium peaks. The spectrum was collected from the 14 week old turkey tendon.....142

Figure 5.24 Changes in Ca/P ratio between turkey tendon (T11 - 11 week old, T14 - 14 week, T22 - 22 week) and hydroxyapatite standard (HA). The Ca/P ratio increases with age towards values characteristic for hydroxyapatite.....143

Figure 5.25 XRD spectra of the ground turkey tendon powders (T11 - 11 week old, T14 - 14 week, T22 - 22 week) before TGA. The major peaks are labelled, showing corresponding crystal plane indices.....144

Figure 5.26 XRD spectra of the incinerated turkey tendon powders (T11 - 11 week old, T14 - 14 week, T22 - 22 week) and the hydroxyapatite standard. The major peaks are labelled with corresponding crystal plane indices.....145

Figure 5.27 Percentage mass reduction of incinerated the tissue samples: three turkey tendons (T11 - 11 week old, T14 - 14 week, T22 - 22 week).....146

Figure 5.28 Schematic showing the progression of mineralisation in the turkey tendon model. (A) A non-mineralised fibril. (B) The mineral ions are delivered into the collagen matrix either as amorphous calcium phosphate vesicles/globules, which dissolve and release the ions, or free ions are transported in the body fluids. (C) Mineral ions start to aggregate forming mineral grains in the gap regions. The periodic banding contrast starts to reverse. (D) Mineral grains crystallise into aligned crystals inside, and outside, the fibril. During development some of the extrafibrillar crystals may lose their alignment and rearrange into disorganised globules.....150

Figure 6.1 Representative BF-TEM images of FIB-milled wild type (A) and osteogenesis imperfecta (C) bone with corresponding SAED patterns (B, D). White arrows indicate the direction of the fibrils. WT regions exhibited a distinctive banding pattern (A) and characteristic arcs of (002) plane reflections from HA in the SAED patterns (B). Banding in OIM tissues is often absent and the fibrils appear disorganised (C), but faint arcs of (002) plane reflections can still be observed (D).....158

Figure 6.2 Representative BF-TEM images of microtomed wild type (WT, A, B) and OI-affected (OIM, C, D) bone regions with corresponding indexed SAED patterns. Dashed circles show regions without a distinctive banding pattern (A, C), which still show oriented (002) arcs. In the more disorganised regions (B, D), full rings are formed. White arrows on the SAED patterns indicate the most intense regions of rings.....160

Figure 6.3 Changes in the length of the (002) arcs between wild type (WT) and osteogenesis imperfecta (OIM) specimens (n=30, for each group). WT and OIM arcs have a similar mean length, but the distribution of OIM arc length is much wider.....161

Figure 6.4 Representative BF- TEM images of WT (A) and OIM (B) bone at low magnification. Fibrils in OIM bone appear more totuous and tend to branch and change direction more across smaller length scales than in the control WT tissue. This is a characteristic architecture of ‘woven’ fibrils.....162

Figure 6.5 Representative ADF-STEM images of longitudinal sections of osmium-stained, non-mineralised tail tendon of wild type (WT, A) and OI-affected (OIM, B) mice with corresponding intensity line profiles (C). White arrows indicate the direction of the line profiles. The sub-banding pattern originates from accumulation of osmium in the bands. Bands are labelled as in work of Chapman [12] and attributed to the gap and overlap regions. 163

Figure 6.6 Representative ADF-STEM images of transverse sections of mature, osmium-stained, non-mineralised tail tendon of wild type (WT, A) and OI-affected (OIM, B). (C) Comparison of fibril cross-sectional area (n=150).....165

Figure 6.7 Representative ADF-STEM images of longitudinal, irregularly oriented, poorly packed collagen fibrils of OI-affected (OIM) mice. Fibrils are grouped into loose bundles (A) and may bend extensively (B).....167

Figure 6.8 Representative ADF-STEM images of disorganised collagen fibrils (transverse sections) of OIM mouse tail tendon showing circular assemblies of collagen (A). Some assemblies seen in non-mineralised tail tendon (B) resemble circular formations seen in mineralised bone (C). Features in the mineralised tissue appear smaller, which suggest that mineral growth might limit the growth of the collagen assemblies.....168

Figure 6.9 Representative ADF-STEM image of loosely packed collagen fibrils and circular collagen assemblies of OI-affected (OIM) mouse tail tendon.....169

Figure 6.10 Representative ADF-STEM images of longitudinal sections of OIM collagen fibrils. Regions containing mature fibrils coexist with regions of tightly packed microribbons (A, C). In disorganised regions, a faint banding pattern can be observed (dashed boxes, B, D). 171

Figure 6.11 Representative ADF-STEM images of a disordered collagen matrix in tail tendon of wild type (WT) mice. (A) Tightly packed bundles of fine fibrils. (B) Bundles of 10nm-thick fibrils exhibiting hints of the banding pattern. These fibrils appear shorter than fibrils observed in OIM (Figure 6.7), which might be a result of sectioning at an oblique angle....172

Figure 6.12 Fibril development in tail tendon of OI-affected (OIM) mice. (A) Region consisting of mature (top) and immature (bottom) fibrils. (B) Higher magnification image of the boxed region in A showing disorganised, short filaments. (C) Disorganised filaments (sub-fibrils, white arrowhead) with wider, banded fibrils (black arrowheads, lines are highlighting the faint sub-banding).....173

Figure 6.13 The phosphorus $L_{2,3}$ near edge structures of wild type (WT) and OIM mouse bone and well mineralised turkey tendon (TA).....175

Figure 6.14 The carbon K near edge structures of non-mineralised, osmium tetroxide-stained, wild type (WT) and OIM mouse tail tendon fibrils and non-mineralised, non-stained turkey tendon fibrils (TN). OIMn1 spectra were taken from a mature fibril (Figure 6.15). OIMn2 spectra were taken from a poorly organised region of sub-fibrils.....177

Figure 6.15 Representative ADF-STEM image of longitudinal, osmium-stained OIM mouse tail tendon collagen showing regions, from which spectra OIMn1 and OIMn2 were collected. 178

Figure 6.16 The carbon K near edge structures of mineralised bone of wild type (WT) and OIM mice, and well mineralised turkey tendon (TW). The carbonate peak E at ~290eV observed in OIM species is much more intense than in WT.....180

Figure 6.17 (I) The carbon K near edge structures of intra- and extrafibrillar regions of mineralised bone of wild type (WTintra/extra) and OIM (OIMintra/extra) mice taken from transverse sections of the tissue. (II) ADF-STEM image of a transverse WT section showing intra- (WTintra) and extrafibrillar (WTextra) regions. Additional (see Figure 6.16) peak D* is observed in the WT spectrum. The intensity of the carbonate peak D increases in intrafibrillar regions. (III) ADF-STEM image of a transverse OIM section showing intra- (OIMintra) and extrafibrillar (OIMextra) regions. Peaks in the 286-289eV range are more difficult to resolve in OIM bone.....182

Figure 6.18 The calcium $L_{2,3}$ near edge structures of wild type (WT) and OIM mouse bone and well mineralised turkey tendon (TW).....183

Figure 6.19 The nitrogen K near edge structures of non-mineralised, osmium-stained, wild type (WTn) and OIM (OIMn) mouse tail tendon fibrils and non-mineralised, non-stained turkey tendon fibrils (TN).....185

Figure 6.20 The nitrogen K near edge structures of mineralised bone of wild type (WT) and OIM mice and well mineralised turkey tendon (TW).....187

Figure 6.21 The nitrogen K near edge structures of intra- and extrafibrillar regions o of mineralised bone of wild type (WTintra/extra) and OIM (OIMintra/extra) mice taken from transverse sections of the tissue. Spectra were taken from the regions shown on Figure 6.17 (II, III).....188

Figure 6.22 The oxygen K near edge structures of mineralised bone of wild type (WT) and OIM mice and well mineralised turkey tendon (TW).....190

Figure 0.1 Representative spectra of mineralising tissues collected from the low-loss region of 11 week non-mineralised (T11n) and 14 and 22 week well mineralised (T14, T22) turkey tendon, wild type mouse bone (WT) and OIM mouse bone.....203

List of Tables

Table 2.1 Basic amino acids found in type I collagen peptide chains.....20

Table 2.2 Calcium phosphate biominerals considered in mineralisation process, or as synthetic bone replacements and their corresponding Ca/P ratios.....37

Table 2.3 Recent (2010-2012) TEM studies of bone mineralisation.....41

Table 3.1Typical Titan settings and parameters used in the present study.....77

Table 4.1 List of standards used in the EELS study. Mineral standards were prepared by Dr. Robert Friedrichs (Cambridge University).....83

Table 4.2 A/B ratios in ascending order for CHA produced using various Ca/P and heat treatment temperatures. The two extreme A/B ratios were used in the TEM-EELS study.….86

Table 5.1 Length of gap, overlap, their sum and period measured separately in freeze-substituted (FS) and room temperature embedded (RT) 22 week old turkey tendon.....111

Table 5.2 Length of gap, overlap, their sum and period measured separately in non-mineralised and mineralised regions 22 week old turkey tendon, prepared by freeze-substitution.....112

Table 5.3 Weight percentage of water, protein and carbonate content in examined samples147

Table 6.1 Length of gap, overlap and the full period measured separately in osmium tetroxide-stained, non-mineralised tail tendon of wild type (WT) and OI-affected (OIM) mice, prepared by high pressure freezing and freeze-substitution (n=20).....164

Table 6.2 Approximate transitions in 285-294eV range in carbon K-edge fine structure and assignments of peaks.....179